Quantum Noise and Radiation Pressure Effects in High Power Optical Interferometers

by

Thomas Randall Corbitt

B.S. Physics, Georgia Institute of Technology, 2001

Submitted to the Department of Physics
in partial fulfillment of the requirements for the degree of

Doctor of Philosophy in Physics

at the

MASSACHUSETTS INSTITUTE OF TECHNOLOGY

August 2008

Author .....
Department of Physics
August 1, 2008

Certified by .....
Nergis Mavalvala
Associate Professor
Thesis Supervisor

Accepted by .....
Thomas J. Greytak
Associate Department Head for Education

Quantum Noise and Radiation Pressure Effects in High Power Optical Interferometers

by

Thomas Randall Corbitt

Submitted to the Department of Physics
on August 1, 2008, in partial fulfillment of the
requirements for the degree of
Doctor of Philosophy in Physics

Abstract

In recent years, a variety of mechanical systems have been approaching quantum limits to their sensitivity of continuous position measurements imposed by the Heisenberg Uncertainty Principle. Most notably, gravitational wave interferomters, such as the Laser Interferometer Gravitational wave Observatory (LIGO), operate within a factor of 10 of the standard quantum limit. Here we characterize and manipulate quantum noise in a variety of alternative topologies which may lead to higher sensitivity GW detectors, and also provide an excellent testbed for fundamental quantum mechanics. Techniques considered include injection and generation of non-classical (squeezed) states of light, and cooling and trapping of macroscopic mirror degrees of freedom by manipulation of the optomechanical coupling between radiation pressure and mirror motion. A computational tool is developed to model complex optomechanical systems in which these effects arise. The simulation tool is used to design an apparatus capable of demonstrating a variety of radiation pressure effects, most notably ponderomotive squeezing and the optical spring effect. A series of experiments were performed, designed to approach measurement of these effects. The experiments use a 1 gram mirror to show progressively stronger radiation pressure effects, but only in the classical regime. The most significant result of these experiments is that we use radiation pressure from two optical fields to shift the mechanical resonant frequency of a suspended mirror from 172 Hz to 1.8 kHz, while simultaneously damping its motion. The technique could prove useful in advanced gravitational wave interferometers by easing control issues, and also has the side effect of effectively cooling the mirror by removing its thermal energy. We show that with improvements, the technique may allow the quantum ground state of the mirror to be approached. Finally, we discuss future prospects for approaching quantum effects in the experiments.

Thesis Supervisor: Nergis Mavalvala
Title: Associate Professor

Acknowledgments

This thesis would not be possible without the support of many people. First, I would like to thank my supervisor Nergis Mavalvala. Without her, I likely would never have made it to MIT in the first place. Her knowledge, advice, patience and unwavering support have made me a better scientist and a better person.

I express my gratitute to Edmund Bertschinger and Erik Katsavounidis for their service on my thesis committee. They have provided guidance and constructive criticism that has greatly improved this thesis.

I have had the pleasure to work with many intelligent and friendly graduate students, postdocs and research associates at MIT, including Chris Wipf, Tim Bodiya, Nicolas Smith, Sarah Ackley, Keisuke Goda, Eugeniy Mikhailov, Dave Ottaway, Edith Innerhofer and Jason Pelc. These people have made my time at MIT both enjoyable and productive. I would also like to thank the technicians in the lab, Myron MacInnis and Bob Laliberte, without whom the experiments would never have happened. I'd also like to thank our administrative assistant, Marie Woods, for her never-ending aid and organization.

I would also like to thank several people outside of MIT for their scientific mentoring and support. Stan Whitcomb (Caltech) has provided guidance and advice on my work based on his experience. Daniel Sigg (LIGO Hanford) has provided invaluable help with many aspects of the experiment. Yanbei Chen (Caltech) has provided appreciated insight into the fundamentals of our experiments, along with Kentaro Somiya (Albert Einstein Institute) and other members of the MQM telecon group.

Finally, I thank my fiancée Bess, my parents and the rest of my family for their love and support. They make it all worthwhile.

-Thomas August 1, 2008

Contents

List of Figures

List of Tables

Chapter 1

Quantum noise in gravitational wave detectors

1.1 Introduction

With several gravitational wave (GW) observatories worldwide completed, or nearing completion [1], we are on the verge of the direct detection of gravitational waves from astrophysical sources. The Laser Interferometer Gravitational wave Observatory (LIGO), the US component of the worldwide effort, has completed an extended science data taking run at its target sensitivity. Meanwhile, design, planning and construction, are underway for next-generation detectors. The initial detectors have maximal strain sensitivity between 50 Hz and 4 kHz as shown in Fig. 1-1, and are limited by seismic vibrations at low frequency, and shot noise (poissonian noise in the number of photons detected) at high frequencies. Improvements to the initial detectors, which include more powerful lasers, more effective seismic isolation, new optical topologies, and higher quality mechanical components to reduce thermal noise, are expected to further increase the sensitivity by a factor of 10, and to extend the frequency range down to 10 Hz, as in Advanced LIGO [2, 3], for example. It is expected that the sensitivity of the future detectors will be predominately limited by quantum noise that arises from the measurement process. One of the most important features of next generation detectors is that they will operate at sufficiently high laser powers that the radiation pressure acting on the suspended mirrors will become a dominant force. The effects of the radiation pressure will manifest primarily in two ways: the shot noise of

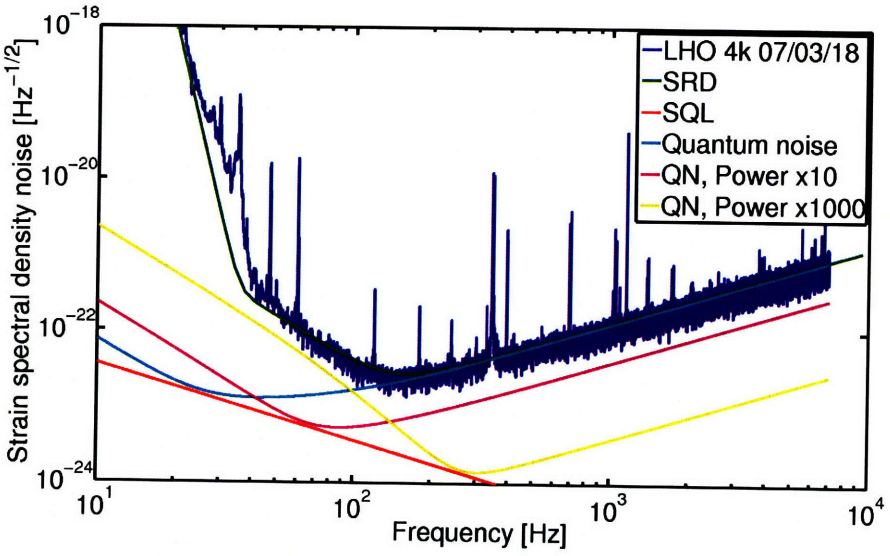

Figure 1-1: Initial LIGO strain noise spectral density. Shown in blue is the measured strain spectral noise density of the LIGO Hanford 4km interferometer taken on March 18, 2007. The design sensitivity is shown in green, the Standard Quantum Limit (SQL) in red and the calculated quantum noise in cyan. Also shown is the quantum noise for 10x and 1000x higher input power. The calculated quantum noise does not reach the SQL because a heterodyne readout scheme is being used, which introduces slightly excess shot noise [4].

the laser light will drive the mirror position and limit the sensitivity, and optical feedback effects will radically alter the mechanical dynamics of the mirrors. The work presented in this thesis was performed with the goal of exploring these effects.

The work presented in this thesis is focused on reducing the effects of quantum noise. This chapter is organized as follows. First, we derive the input/output relations for an ideal Michelson interferometer, and derive the quantum noise components that limit the sensitivity to gravitational radiation. We then discuss techniques to reduce the quantum noise, which include more advanced optical topologies and the injection of non-classical light fields. This chapter is adapted from Ref [5].

1.2 Quantum noise in a Michelson interferometer

It is instructive to use a simple Michelson interferometer to demonstrate how quantum noise enters a gravitational wave interferometer, and how it may be minimized. The configuration consists of a laser incident on a beamsplitter, split into two arms, and reflected back to the beamsplitter. The mirrors are suspended so that they are free to move under the influence of

gravitational waves. The distance between the beamsplitter and the two mirrors is assumed to be nearly identical, so that the returning beams to the beamsplitter interfere destructively at the antisymmetric port, and all the laser light returns towards the laser. The calculation technique is similar to that presented in Ref. [6] for a Michelson interferometer with arm cavities.

We may write the electric field entering the bright port of the beamsplitter as

$$E_{sym}(t) = E_0 \cos(\omega_0 t) + \delta E_{sym}, \tag{1.1}$$

where the first term represents the coherent laser field, and δE_{sym} its fluctuations, which could be quantum or classical in origin, $E_0 = \sqrt{\frac{4\pi I_0}{Ac}}$, I_0 is the incident laser power, and A is the effective cross sectional area of the laser field. However, because the output of the Michelson interferometer is operated on a dark fringe (see Figure 1-2), the fluctuations of the electric field entering from the symmetric, bright port do not enter the final measurement, as they interfere destructively at the dark port, so we set $\delta E_{sym} = 0$ for simplicity. It has been shown [7, 8] that the lowest energy state of the electric field introduces vacuum fluctuations into the dark port of the interferometer, as required by quantum mechanics. Taking the beamsplitter to be precisely 50% transmissive, we may then write the electric field of the vacuum at the frequency of the laser as

$$\begin{aligned} E_{asm}(t) = \cos(\omega_0 t)\sqrt{\frac{4\pi\hbar\omega_0}{Ac}} \int_0^\infty \left(a_1 e^{-i\Omega t} + a_1^\dagger e^{+i\Omega t}\right) \frac{d\Omega}{2\pi} + \\ \sin(\omega_0 t)\sqrt{\frac{4\pi\hbar\omega_0}{Ac}} \int_0^\infty \left(a_2 e^{-i\Omega t} + a_2^\dagger e^{+i\Omega t}\right) \frac{d\Omega}{2\pi}, \end{aligned} \tag{1.2}$$

where a_1 and a_2 are quadrature operators for the electric field (see Chapter 4 or Refs. [6–8]). For simplicity, we assume that the distance between the beamsplitter and each mirror is an integer number of wavelengths, so that the laser field remains in the cosine quadrature at each mirror. The electric field incident on M_1 is therefore

$$E_1(t) = \frac{1}{\sqrt{2}} \left[E_{sym}(t) + E_{asm}(t)\right], \tag{1.3}$$

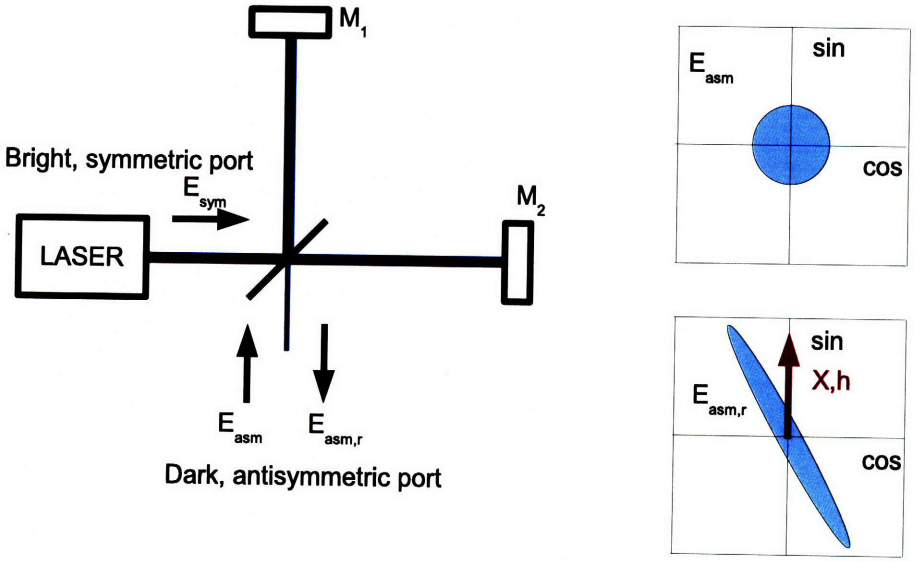

Figure 1-2: A Michelson interferometer showing the input and output fields. A laser beam is split by a beamsplitter into two beams of equal power, which travel through arms of length L, before being reflected back to the beamsplitter where they are interfered. The microscopic positions of the mirrors are arranged so that the bulk of the laser light is returned towards the laser (the bright port), and the light exiting this port is sensitive to the symmetric, $X_1 + X_2$, motion of the mirrors. The fields exiting the dark port are sensitive to the antisymmetric motion $X_1 - X_2$. In the top right axes, we show the vacuum fluctuations entering the dark port, represented as uncertainty in phase space (the magnitude of the field in the sine and cosine quadratures) of the electric field. Entering the dark port, the vacuum fluctuations are equally large in each quadrature. In the bottom right axes, we show how the interferometer transforms the electric field. First, the uncertainty in the electric field has been modified by the radiation pressure, and has been transformed into a squeezed state, signifying that the uncertainty is no longer equal in all quadratures as shown in Eq. 1.15. Second, the mirror motions have been imprinted on the electric field in the sine quadrature also shown in Eq. 1.15.

and the electric field incident on M_2 is

$$E_2(t) = \frac{1}{\sqrt{2}} \left[E_{sym}(t) - E_{asm}(t) \right], \tag{1.4}$$

where we have ignored an overall time shift $\delta t = \omega_0 L/c$. The time shift only creates a multiple of 2π phase shift, and does not change our calculation. Any displacement $X_1(t)$ of M_1 creates a phase shift of the reflected electric field such that

$$E_{1r}(t) = \frac{1}{\sqrt{2}} \left[E_{sym}(t - \frac{2X_1(t)}{c}) + E_{asm}(t - \frac{2X_1(t)}{c}) \right]. \tag{1.5}$$

Proper operation of the interferometer requires that $\frac{2\omega_0 X_1(t)}{c} \ll 1$, so we may make the approximation

$$E_{1r}(t) \approx \frac{1}{\sqrt{2}} \left[E_0 \cos(\omega_0 t) - 2E_0 \frac{\omega_0 X_1(t)}{c} \sin(\omega_0 t) + E_{asm}(t) \right], \tag{1.6}$$

and likewise for M_2,

$$E_{2r}(t) \approx \frac{1}{\sqrt{2}} \left[E_0 \cos(\omega_0 t) - 2E_0 \frac{\omega_0 X_2(t)}{c} \sin(\omega_0 t) - E_{asm}(t) \right]. \tag{1.7}$$

The field that exits the dark port is then

$$E_{asm,r}(t) = \frac{1}{\sqrt{2}} \left[E_{1r}(t) - E_{2r}(t) \right] = E_{asm}(t) + E_0 \frac{\omega_0 \left[X_2(t) - X_1(t) \right]}{c} \sin(\omega_0 t). \tag{1.8}$$

We now examine the terms that enter into $X_{1,2}(t)$. There are three primary terms: classical displacements, including as seismic and thermal noise, quantum back-action, and gravitational-wave induced motion. The back-action noise arises from the vacuum fluctuations $E_{asm}(t)$ that enter from the dark port, creating intensity fluctuations of the laser field, which then exert a fluctuating force on the mirrors and drive its motion. From Eq. 1.3, the fluctuating power (averaged over ω_0) incident on M_1 may be written as

$$\delta I_1(t) = \sqrt{I_0 \hbar \omega_0} \int_0^\infty \left(a_1 e^{-i\Omega t} + a_1^\dagger e^{+i\Omega t} \right) \frac{d\Omega}{2\pi}. \tag{1.9}$$

At this point, we transform into the frequency domain, taking the Fourier transform, we

obtain

$$\delta\tilde{I}_1 = \sqrt{I_0\hbar\omega_0}a_1. \tag{1.10}$$

The intensity fluctuations exert a fluctuating force $\tilde{F}_1 = 2\delta\tilde{I}_1/c$ on the mirror. The mirror behaves essentially as a free mass at the frequencies of interest (far greater than the mirror's suspension frequency), with mechanical susceptibility $(M\Omega)^{-2}$, where Ω is the Fourier frequency of motion. The radiation pressure therefore creates the displacements

$$\tilde{X}_{1,ba} = \frac{2\sqrt{I_0\hbar\omega_0}}{cM\Omega^2}a_1 \tag{1.11}$$

$$\tilde{X}_{2,ba} = -\frac{2\sqrt{I_0\hbar\omega_0}}{cM\Omega^2}a_1 \tag{1.12}$$

of each mirror. We may then write the total differential displacement as

$$\tilde{X}_1 - \tilde{X}_2 = \frac{4\sqrt{I_0\hbar\omega_0}}{cM\Omega^2}a_1 + \tilde{X}_{cl,1} - \tilde{X}_{cl,2} + L\tilde{h}, \tag{1.13}$$

where $\tilde{X}_{cl}$ is the classical displacement noise, L is the length of the arms, and h is the gravitational wave strain. We define the output quadratures $b_{1,2}$ of the output field $E_{asm,r}$ according to

$$\begin{aligned} E_{asm,r}(t) = \quad & \cos \quad (\omega_0 t)\sqrt{\frac{4\pi\hbar\omega_0}{Ac}}\int_0^\infty \left(b_1 e^{-i\Omega t} + b_1^\dagger e^{+i\Omega t}\right)\frac{d\Omega}{2\pi} + \\ & \sin \quad (\omega_0 t)\sqrt{\frac{4\pi\hbar\omega_0}{Ac}}\int_0^\infty \left(b_2 e^{-i\Omega t} + b_2^\dagger e^{+i\Omega t}\right)\frac{d\Omega}{2\pi}. \end{aligned} \tag{1.14}$$

Under this formalism,

$$\begin{aligned} b_1 &= a_1 \\ b_2 &= a_2 - \kappa a_1 - \sqrt{\frac{I_0\omega_0}{\hbar c^2}}\left(\tilde{X}_{cl,1} - \tilde{X}_{cl,2} + L\tilde{h}\right), \end{aligned} \tag{1.15}$$

where $\kappa = \frac{4I_0\omega_0}{c^2M\Omega^2}$ is the radiation pressure coupling coefficient. The b_2 quadrature may be measured using a homodyne or heterodyne readout scheme (see Ref. [4] for details and a comparison between the two). Assuming an ideal detection of the b_2 quadrature, which may be accomplished by homodyne detection, and neglecting any classical noise, we obtain

the strain spectral noise density of the detected field

$$S_h = \left(1+\kappa^2\right)\frac{\hbar c^2}{4I_0\omega_0 L^2} = \left(1/\kappa+\kappa\right)\frac{h_{SQL}^2}{2} \tag{1.16}$$

where

$$h_{SQL} = \sqrt{\frac{4\hbar}{M\Omega^2 L^2}} \tag{1.17}$$

is the "Standard Quantum Limit" (SQL) for strain sensitivity. We note that the SQL given here differs from that given in Ref. [6] because we only use two mirrors, rather than four, so the reduced mass for the system is twice as large. The SQL is a necessary result of the Heisenberg Uncertainty Principle (HUP). As the positions of the mirrors are measured at one instant, the HUP requires uncertainty in the momentum of the mirrors (back-action) in proportion to the inverse of the uncertainty of the position measurement. The uncertainty in the momentum then disrupts future measurements of the mirror position. The initial uncertainty in the position of the mirror is represented in Eq. 1.16 by the $1/\kappa$ term, while the back-action noise is represented by the κ term. For any continuous measurement, the optimal performance is achieved when the measurement strength (the input power) is chosen to balance the two noise terms (see Figure 1-1 for example). In our case, this is achieved when the input power is set to

$$I_{SQL} = \frac{Mc^2\Omega^2}{4\omega_0}. \tag{1.18}$$

The SQL may be overcome, however, and we demonstrate various ways to beat the limit by manipulating the quadrature fields. At present, no interferometers have operated in the $\kappa > 1$ regime at frequencies for which quantum noise is significant. Note that because of the frequency dependence of κ, this should always occur for small Ω, but the effects of the back-action noise are hidden underneath seismic or other classical noise and have never been directly detected. We proceed to discuss methods to reduce the effects of quantum noise.

1.3 Quantum noise mitigation

In this section, we discuss techniques, both currently employed and planned for the future, to reduce the effects of quantum noise. We defer a discussion of the use of squeezed light injected to the dark port to Section 1.4.

1.3.1 Cavities and power recycling

With only a Michelson interferometer, unrealistically high levels of laser power would be required to approach $\kappa \approx 1$ near the GW frequency band. For example, with the 10 kg mirrors used in LIGO, approximately 50 MW of input laser power would be required to reach $\kappa = 1$ at 100 Hz. By placing an additional highly reflective mirror in each arm of the Michelson interferometer in order to form an optical cavity, the laser power may circulate in the arms many times before escaping. In the limit that the transmission of the input mirror T is the dominant optical loss in the cavity (which is usually the case, for reasons that we discuss), then each photon takes on order $4/T$ roundtrips within the cavity, and the signal at the output is increased by a factor of the same order. We see from Eq. 1.16 that we obtain an increase of order $(4/T)^2$ in the effective power. While this technique does not allow the SQL to be circumvented, it does allow for κ to be dramatically increased without increasing the input power level, and so it has become standard in most GW interferometers. Ideally, one would operate the cavity such that the light continues to circulate within the cavity, until it is lost to imperfections in the mirror coatings or diffraction, in order to make $4/T$ as large as possible. This "impedance matching" is achieved when the transmission of the input mirror, T, is equal to the round trip optical loss resulting from imperfections. However, an important limitation generally prevents us from operating in that regime. The bandwidth (or linewidth) of the cavity describes how quickly the cavity may respond to external disturbances, as limited by the light travel time multiplied by the effective number of round trips each photon makes within the cavity. If the mirror motion induced by gravitational waves exceeds the bandwidth of the cavity, the slow response of the cavity acts to average the GW signal, generating a low pass filter in the cavity response. The corner frequency of this low pass filter, equivalent to the cavity's half-linewidth, is given by

$$\gamma = \frac{Tc}{4L}. \tag{1.19}$$

Considering the LIGO arm lengths of 4 km, and the expected optical losses of order 100 ppm, one could ideally operate with $T = 10^{-4}$, leading to $\gamma = 2\pi \times 0.3$ Hz. However, since the desired peak sensitivity is near 100 Hz, the transmission of the input mirrors is limited to 3% so that $\gamma \approx 2\pi \times 100$ Hz. In this regime, almost all of the laser power is reflected back towards the laser.

Since most of the light returns toward the laser, a partially transmitting power-recycling mirror (PRM) may be placed between the laser source and the beam splitter to 'recycle' the light back into the interferometer [9] (see Fig. 1-3(a)). This technique allows the power recycling cavity to be impedance matched, without the bandwidth constraints present with arm cavities, so that the available laser power is optimized given the constraints of the optical losses. In the Initial LIGO interferometers, a 10 W laser is increased to approximately 200 W in the power recycling, and increased further to approximately 15 kW in the arm cavities, within a factor of about 25 of the required power to reach the SQL at 100 Hz, despite beginning with a 10 W laser.

1.3.2 Signal tuned interferometers

The optical configuration currently planned to achieve quantum-limited performance in Advanced LIGO uses the Resonant Sideband Extraction (RSE) technique [10], in addition to power-recycling. In RSE, an additional partially transmitting mirror, the signal extraction mirror (SEM), is placed between the antisymmetric port of the beam splitter and photodetector (see Fig 1-3(b)). The reflectivity of this signal extraction mirror and its microscopic position (on the scale of the wavelength of the laser light, $1.064\,\mu$m) significantly influence the frequency response of the interferometer [11]. The resonance condition of the signal extraction cavity – comprising the SEM and the input test-mass (ITM) mirrors of the arm cavities – and the reflectivity of the SEM, control the frequency of peak response and the bandwidth of the detector, respectively.

With cavities on resonance, the peak response is for signals at 0 frequency (DC). The signal-recycling cavity allows one to utilize arm cavities with bandwidths significantly less than the frequency of the desired signal to measure (which allows for higher power buildup in the arm cavities) by detuning the resonance of the signal recycling cavity to the desired frequency. This detuning has the profound consequence, however, that the frequency response of the detuned configuration is no longer symmetric around the carrier frequency. As a consequence, only one of the two (upper or lower) GW-induced sidebands is exactly on resonance in the signal-recycling cavity. In general, the upper and lower GW sidebands contribute asymmetrically to the total output field, which makes the GW signal appear simultaneously in both quadratures of the output field [12]. Furthermore, use of the detuned RSE to optimize the detector response has exposed some surprising features that

are due to the dynamical correlations of the shot noise and radiation pressure noise [12]. These shot noise–radiation pressure noise correlations – which are manifestations of quantum non-demolition (QND) in that the correlations lead to below-SQL noise limits – lead to an optomechanical coupling that significantly modifies the dynamics of the interferometer mirrors, introducing an additional resonance at which the sensitivity also peaks (see, e.g., the dark solid (blue) curve in Fig. 1-5) [12, 13]. We further discuss these correlations and optomechanical couplings effects in Chapter 2.

Signal-tuned interferometers are already used in the GEO600 detector, and are part of the baseline plan for the Advanced LIGO detectors.

1.3.3 Ponderomotive squeezing and the variational readout

Ponderomotive squeezing arises from the naturally occurring correlation of light intensity fluctuations to mirror position fluctuations upon reflection of light from a mirror. Recall from Eq. 1.16 that the intensity fluctuations couple to the phase fluctuations with coupling constant κ. In the case that the phase quadrature is measured, the only effect of this coupling is excess radiation pressure noise. However, if one allows for an arbitrary quadrature

$$b_\theta = b_1 \cos\theta + b_2 \sin\theta \tag{1.20}$$

to be measured (which may be accomplished by varying the phase of the local oscillator in the homodyne readout), then more complex features may be revealed. Suppose that we choose θ so as to eliminate the radiation pressure term (a_1),

$$\theta_Z = \arctan\frac{1}{\kappa}, \tag{1.21}$$

then

$$b_{\theta_Z} = \left[a_2 - 2\sqrt{\frac{I_0\omega_0}{\hbar c^2}}\left(\tilde{X}_{cl,1} - \tilde{X}_{cl,2} + L\tilde{h}\right)\right]\sin\theta_Z. \tag{1.22}$$

In this regime, only shot noise, the classical noise, and the GW signal remain, and all terms have been reduced by a factor $\sin\theta_Z$. The resulting noise spectral density for the GW signal is

$$S_h = \frac{h_{SQL}^2}{2\kappa}, \tag{1.23}$$

which is precisely what would be expected from shot noise alone. In this way, the effects of radiation pressure noise may be completely eliminated by taking advantage of the correlations with the intensity quadrature. It is critical to note that the detected quantum noise at this quadrature is below the shot noise level. This is allowed under quantum mechanics, as long as the Heisenberg Uncertainty Principle, related by the commutation relations between b_1 and b_2, is satisfied. In our case, this requires that the noise in the quadrature orthogonal to b_{θ_Z} exceed shot noise by at least the factor that b_{θ_Z} is below it. This type of output state is called a squeezed state (see Figure 1-2, and we discuss it in greater detail in Section 1.4.

We point out that κ and therefore θ_Z is frequency dependent, and we may only choose a single homodyne phase for detection, so it would at first appear impossible to achieve the cancellation of radiation pressure noise at all frequencies simultaneously. However, it has been pointed out [6] that by using filter cavities at the dark port before performing the homodyne detection (see Figure 1-3), the frequency dependent cancellation may be obtained. This scheme is called the "variational readout." Achieving this cancellation in practice is extremely difficult because the filter cavities require linewidths comparable to the frequency at which the interferometer reaches the SQL, of order 100 Hz. The filter cavity must also have very low optical loss, as any loss introduces additional uncorrelated vacuum fields that destroy the a_1 correlations. These requirements lead to very long filter cavities, ranging from 15 m to 4 km in length. Additionally, optical losses intrinsic to the interferometer itself destroy the correlations, limiting the potential benefit of this technique.

1.3.4 Speed meters

The principle of a speed meter is most easily understood in terms of the HUP applied to position and momentum. We have highlighted how the momentum disturbance from position measurements disrupts future measurements. This back-action obviously does not make position a good QND observable. While a measurement of momentum certainly perturbs the position of a test particle as required by the HUP, that position kick does not influence the time evolution of the momentum, and hence there is no back-action. Momentum measurements are thus inherently back-action evading [1] , provided no position information is collected. Interferometric measurements that measure the speed – similar in

[1] Momentum is a constant of the motion for a free particle; it commutes with itself at different times and is, therefore, a good QND variable.

behavior to the momentum – of the mirrors were first proposed by Braginsky et al. [14] and refined into more practical designs by Purdue and Chen [15].

Many Michelson-based variants of interferometric speed meters rely on the addition of a "sloshing" cavity at the output port of an otherwise position sensitive interferometer. The role of the "sloshing" cavity is to completely cancel the momentum "kick" due to the position measurement at an earlier time by providing an equal and opposite "kick" by the fields stored in the sloshing cavity. Optically, this occurs due to a π phase shift in the coupling constant that connects the sloshing cavity field to the interferometer field. This behavior is analogous to that of two weakly coupled oscillators: when a mode other than a normal mode of the system is excited, energy "sloshes" between the two oscillators, with a π phase shift after each "slosh" cycle. A schematic representation of a sample speed meter interferometer is shown in Fig. 1-3(d). The unused port of the readout mirror that connects the sloshing cavity (sc) to the signal extraction cavity (sec) can with be plugged (with the dashed mirror), or it can be used for squeezed vacuum injection. We do not include noise curves corresponding to various speed meter configurations here, but these appear in Ref. [15].

1.4 Squeezing

The vacuum fields that enter the dark port of the interferometer are the source of shot noise. Recall that equal magnitudes of noise are present in both the sine and cosine quadratures of the electric field of the vacuum. However, the magnitude of noise in each quadrature is only limited by their commutation relations, as described by the Heisenberg Uncertainty Principle. It is possible in principle to reduce, for example, the magnitude of the noise in the sine quadrature, while increasing the noise in the cosine quadrature, thereby "squeezing" the uncertainty of the vacuum field in phase space. This may be done prior to the vacuum noise entering the interferometer (contrary to ponderomotive squeezing, which is the squeezing produced by the interferometer itself) as shown in Figure 1-3.

Since the earliest experiments to generate squeezed states of light were carried out in the 1980's [16,17], there has been steady progress in both the degree of squeezing achieved [18] as well as the stability and long-term operation of squeezing experiments [19]. The use of squeezed light in various applications has nudged squeezed state generation from delicate

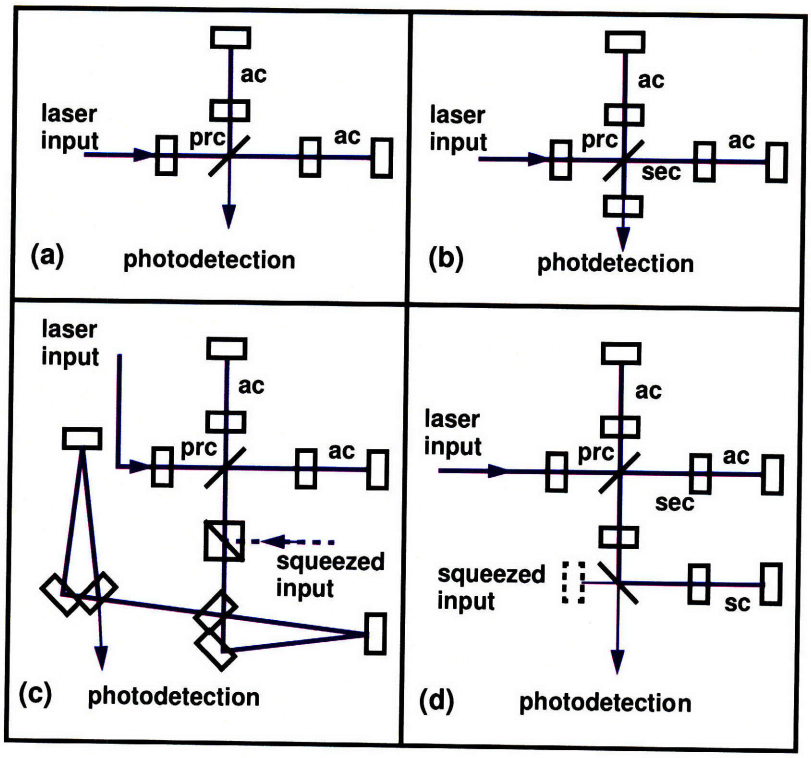

Figure 1-3: Schematic representations of some sample interferometer configurations. In all cases shown except (c) we have chosen extensions of a power-recycled Michelson interferometer with Fabry-Perot cavities in each arm as the basic interferometer; this configuration is shown in (a). (a) Power-recycled Michelson interferometer with Fabry-Perot arm cavities (PRFPMI); (b) Signal-tuned PRFPMI; (c) PRFPMI with variational readout and (optional) squeezed input; and (d) PRFPMI-based speed meter with (optional) squeezing. Acronyms used: ac = arm cavity, prc = power-recycling cavity, sec = signal extraction cavity, sc = sloshing cavity.

laboratory set-ups with millisecond durations to the realm of stable sources of strongly squeezed light that operate robustly for several hours at a time. The present state of the science for CW squeezed light is about 10 dB of squeezing at 5 MHz [20], and 4 dB at 10 Hz [21]. Demonstrations of squeezing-enhanced interferometers on both tabletop experiments [22, 23] and suspended prototype interferometers [24] have been performed, and plans to squeeze a 4 km LIGO interferometers are currently being developed. With these advancements, all of the requirements for squeezing GW interferometers placed on the squeezed state source have been satisfied.

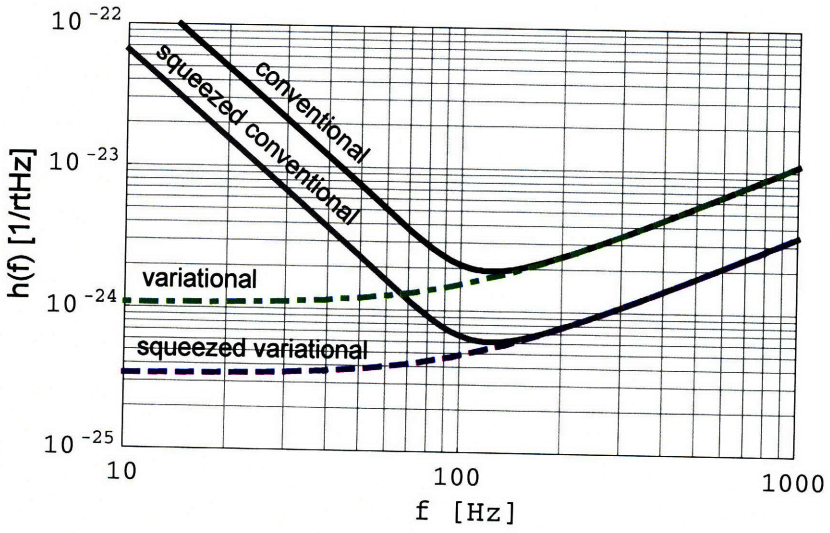

Figure 1-4: Noise curves for a power-recycled interferometer (with initial LIGO parameters) with squeezing and with a variational readout [6]. The solid dark (black) curve uses the standard, or baseline, initial LIGO parameters but power at the beamsplitter that gives SQL-limited performance at 100 Hz, i.e. ($I_0 = I_{SQL} \simeq 10$ kW; the solid light (gray) curve is the sensitivity for the same interferometer but with squeezing injected at a *frequency-dependent* optimal squeeze angle; the dash-dot (green) curve is for the same interferometer but using a *frequency-dependent* homodyne readout that measures the optimal quadrature at each frequency; the lighter dashed curve (blue) uses a variational readout as well as 10 dB of squeezing injected. No losses are included in the noise curves plotted here, but the treatment including losses can be found in Ref. [6].

1.4.1 Applications of squeezing to gravitational-wave interferometers

In this section we describe some of the effects of using squeezed light in GW interferometers. We assume availability of 10 dB of vacuum squeezing available from DC to 10 kHz. Here we do not include losses, but the effect of losses are described in Sec. 1.4.2. We consider the use of squeezed light in a few typical GW detector configurations.

Power-recycled interferometers

Several variations have been proposed to turn these "conventional" interferometers into QND devices. The sensitivity curves for these are shown in Fig. 1-4.

- In the *squeezed-input interferometer* squeezed vacuum is injected into the antisymmetric port of the interferometer. Squeezing has the effect of increasing the fluctuations in one quadrature, while decreasing fluctuations in the other. Since radiation-pressure noise and shot noise dominate in different frequency regions and depend on different

input quadratures, the squeeze angle that achieves optimal performance is frequency dependent. One possible configuration is choosing a frequency independent squeeze angle that decreases shot noise and increases radiation pressure noise. This configuration is equivalent to an unsqueezed interferometer with an increase to the laser power by the squeeze factor [8]. To obtain a broadband performance increase, two long (required for low losses) filter cavities can produce the required frequency dependent squeeze angle from a fixed squeeze angle source. In this configuration, the noise is reduced by the squeeze factor at all frequencies.

- In the squeezed-variational interferometer, two filter cavities are used to perform a frequency dependent homodyne detection of the signal. This detection method eliminates radiation-pressure noise from the signal by taking advantage of correlations between the shot noise and radiation-pressure noise. As a result, squeezing must reduce only the shot noise, and the radiation-pressure noise may be disregarded, which results in a frequency independent squeeze angle, and the noise is reduced by the squeeze factor at all frequencies.

Signal tuned interferometers

It is constructive to consider the detuned RSE interferometers planned for Advanced LIGO and show that there are reasonable gains to be made even with frequency-independent squeezing.

The detuning of the signal recycling cavity has the effect of mixing the quadratures in the input/output relations of the interferometer. This allows the shot noise and radiation pressure noise to become correlated, producing the two resonances typical (see Figure 1-5) of signal recycled interferometers [12].

To improve the performance of this configuration, we inject squeezed vacuum into the dark port. The mixing of the quadratures results in a modification of the optimal squeeze angle from the power-recycled case. It has been shown that this frequency-dependent squeeze angle can be produced by kilometer scale filter cavities [6,25]. Due to the inherent difficulty of using long filter cavities, we consider the case of a fixed squeeze angle in the Advanced LIGO configuration.

For Advanced LIGO, the signal recycling cavity is detuned to place the resonances near

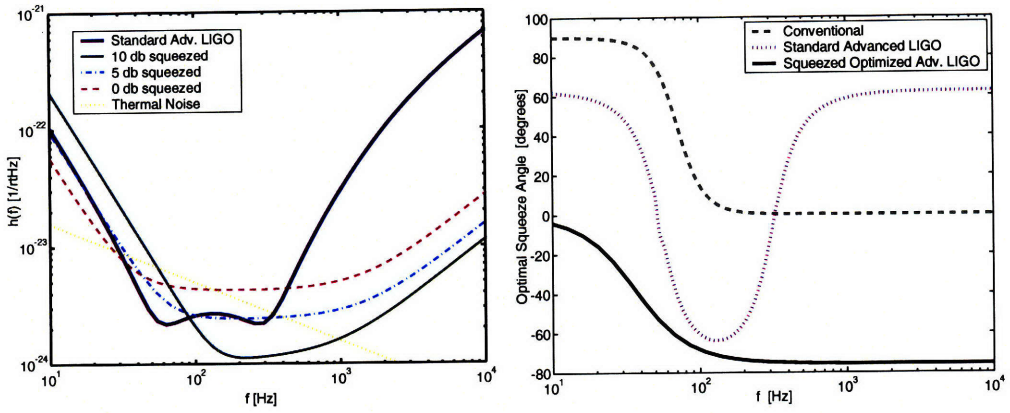

Figure 1-5: Left panel: Noise curves for Advanced LIGO with different levels of squeezing included. The dark solid curve is the standard, or baseline, Advanced LIGO sensitivity when limited by quantum noise; the dashed (purple) curve corresponds to a broadband configuration that is better suited for squeezing (but no squeezing is injected); the dash-dot (cyan) curve is for the broadband configuration with 5 dB of squeezing; the lighter solid curve (green) has 10 dB of squeezing injected. The dotted (yellow) curve is an estimate of the thermal noise, assuming 40 kg silica test masses limited by internal thermal noise [2]. Right panel: The optimal squeeze angle for three interferometer considered. The dashed curve (gray) is for a conventional power-recycled interferometer; the dotted curve (purple) is for the standard (baseline) Advanced LIGO configuration; the solid (black) curve is for the optimized broadband Advanced LIGO configuration.

100 Hz to achieve the best performance in the GW frequency band. This results in the optimal squeeze angle being strongly frequency dependent and broadband improvements impossible. By choosing the optimal squeeze angle for a particular frequency band, narrow-band improvements can be achieved, at the cost of worse performance at other frequencies. To increase the broadband performance, we must modify the detuning of the signal recycling cavity so as to reduce the variance of the optimal squeeze angle. We choose a detuned signal extraction cavity, such that carrier light with angular frequency ω_l obtains a net phase shift of $\frac{\pi}{2}$ in one pass through the cavity. In this configuration, the optimal squeeze angle varies much less than in the standard configuration. We choose a squeeze angle to optimize the noise performance at 200 Hz. This choice allows us to improve the performance over the bulk of our frequency range. The performance of the squeezed configuration is comparable to the unsqueezed configuration in the frequency range 10 Hz to 300 Hz, and dramatically better at 300 Hz to 10 kHz.

1.4.2 The role of losses

Optical losses play an important role in the performance of a squeezed interferometer. There are two mechanisms that must be considered simultaneously when evaluating the effects of losses: (i) The dissipation leads to smaller signals, which is a purely classical effect; and (ii) A lossy port allows ordinary (unsqueezed) vacuum to enter and superpose on the squeezed field in the interferometer, thus destroying the effects of the squeezing.

In general, the significance of the different losses in an interferometer or associated injection/readout scheme depends on the interferometer configuration. Squeezed light injection losses are obviously problematic, since they correspond to pure degradation of the level of squeezing. The sensitivity to optical losses in an interferometer depends on the build-up of signal and noise fields in the various part of the interferometer. In the variational and/or squeezed-variational interferometer of Fig. 1-3(c), for example, the losses in the arm cavities dominate the overall performance of the detector [6].

In this section we consider the effect of losses in the signal-tuned interferometer described in Sec. 1.4.1, as an example. The effects of the losses are strongly dependent on the buildup of the noise fields in the signal extraction cavity and in the arm cavities. There are four types of losses we consider:

- *Injection losses* are losses associated with the injection of squeezed light into the dark port. This effectively limits the squeezing magnitude, and we assume that these are included in the squeezing magnitudes used, and are subsequently ignored.

- *Detection losses* are due to quantum inefficiencies in the detection of the signal light. These losses allow a small amount of vacuum fluctuations to leak into the measurement, decreasing its precision. The vacuum fluctuations are small relative to the radiation pressure noise at low frequencies, and thus have little effect where radiation pressure noise dominates. The vacuum fluctuations are significant relative to shot noise, however, and hurt performance at high frequencies where shot noise dominates.

- *Signal recycling losses* are produced by the beamsplitter, signal recycling mirror, and the anti-reflective coatings on the initial test masses. These losses are either amplified or suppressed depending on the buildup of the noise fields in the signal extraction cavity. The frequency-dependent phase shift experienced by the noise fields in interacting with the arm cavities results in the signal recycling cavity being resonant at

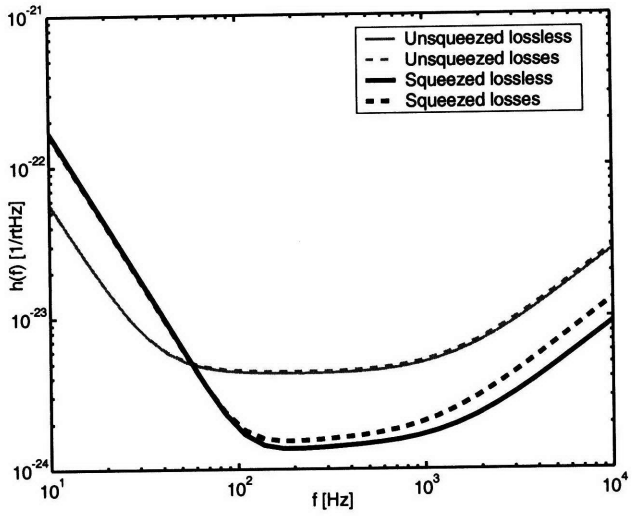

Figure 1-6: Noise curves for a squeezed input signal-tuned interferometer (with broadband Advanced LIGO parameters) including losses. The solid gray curve is for the broadband Advanced LIGO configuration shown as the dashed (purple) curve in Fig. 1-5; the dashed gray curve is the sensitivity for the same interferometer but with additional losses (see below) ; the solid black curve is for the lossless interferometer squeezing injected (same as the lighter solid (green) curve of Fig. 1-5; the dashed curve black curve includes losses. The losses assumed in these curves are 50 ppm per high-reflection surface, 200 ppm per anti-reflection surface and photodetection efficiency of 98%.

high frequencies, and anti-resonant at low frequencies; thus the effects of the losses are amplified at high frequencies and suppressed at low frequencies.

- *Arm cavity losses* are incurred in the arm cavities due to diffraction and absorption. Due to the suppression of the noise fields at low frequencies in the signal recycling cavity, and to the suppression of the noise fields at high frequencies in the arm cavities, the noise fields do not resonate strongly in the arm cavities. This effect reduces the importance of arm cavity losses.

While not apparent from Fig. 1-6, we have determined that the dominant losses in this configuration arise from the signal recycling cavity, and that the effects of the losses are the worst at frequencies above 300 Hz, and limit the amount of squeezing that is beneficial at these frequencies. The losses are largely unimportant at frequencies below 300 Hz. As mentioned above, the effect of these losses is amplified or suppressed, depending on the resonance condition in the signal extraction cavity.

1.5 Overview

We have attempted to give a very broad survey of our understanding of quantum noise in GW interferometers. With regard to laser interferometer gravitational-wave detectors, the stage was set in the late 1970s and early 1980s by the work of Caves, Thorne, Braginsky et al., and many others, which introduced the conceptual and mathematical formulation of the problem of quantum noise limits in macroscopic measurements and the possibility of circumventing them by quantum non-demolition techniques, using squeezed light, for example. These ideas were deemed not to be realizable in GW detectors at the time [2]. In the following decade, there were significant enough advances in the generation of non-classical states of light [16,17,19,26] and their use to make modest gains in interferometric measurements below the quantum limit [22,27], that once again renewed interest in the topic at the turn of the millennium. The work of Buonanno and Chen [12,13], building on that of Kimble et al. [6], led to better understanding of the important role that naturally occurring quantum correlations can play in advanced GW detectors with higher power, hence non-negligible back action noise. At the present time, we have entered an era of vigorous activity and interest in the possibility of sub-SQL measurement techniques that aim to take advantage of (i) squeezed-state generation and injection; (ii) the naturally occurring ponderomotive squeezing in interferometers; (iii) other back-action evading measurement techniques based on speed meters [15]; and a variety of other techniques that we have not described here.

The remaining chapters in this thesis are organized as follows: In Chapter 2, we describe a scheme to filter the squeezed light in order to give the squeezing a frequency dependent amplitude, rather than the frequency dependent squeeze angle already discussed. We argue that this technique is easier, and analyze the benefits that it could provide to the detection of GWs from astrophysical sources. Chapter 3 provides an overview of the theory of optomechanical coupling in detuned cavities, and discusses the effects arising from this coupling. Chapter 4 presents a mathematical technique to calculate the propagation of classical and quantum optical fields in complex interferometers, including optomechanical coupling. Chapter 5 develops an experimental design for a small-scale experiment capable of

[2] In the Conclusions section of his 1981 paper [8], Caves wrote: "The squeeze-state technique outlined in this paper will not be easy to implement... Difficult or not [it] might turn out at some stage to be the only way to improve sensitivity of detectors designed to detect gravitational waves..."

demonstrating a number of the optomechanical effects discussed, including ponderomotive squeezing and radiation pressure noise. Chapter 6 describes a series of experiments that have been performed in the context of the design presented in Chapter 5, and demonstrate a number of strong optomechanical effects. Chapter 7 discusses how these experiments may have other applications in exploring how quantum mechanics influence macroscopic objects, in the context of optical cooling and trapping. In Chapter 8, we conclude with an outlook for the future of these experiments.

Chapter 2

Filter cavities for squeezed light

We explore the use of Fabry-Pérot cavities as high-pass filters for squeezed light, and show that they can increase the sensitivity of interferometric gravitational-wave detectors without the need for long (kilometer scale) filter cavities. We derive the parameters for the filters, and analyze the performance of several possible cavity configurations in the context of a future gravitational-wave interferometer with squeezed light (vacuum) injected into the output port. This chapter is adapted from Ref. [28].

2.1 Introduction

To achieve broadband noise reduction using squeezed light, it is necessary to produce squeezing with a frequency-dependent squeeze angle. Kimble et al. [6] recognized that squeezed vacuum reflected from appropriately detuned filter cavities could match the required squeeze angle over a broad range of frequencies and give broadband performance below the SQL. Squeezing in signal-tuned interferometers was analyzed in Refs. [5, 29, 30]. Frequency-dependent squeezing using optical cavities offers excellent performance, but it is likely to be difficult and costly to implement because it requires long (kilometer scale) filter cavities to reduce losses so that the squeezing is not destroyed in the process [6, 29].

Here we propose using an alternative type of filter cavity that, instead of giving a frequency-dependent squeeze angle, act as high-pass filters for the squeeze amplitude. In using this design, we reduce the harmful effects of squeezing with a constant squeeze angle and the need for a low-loss cavity, while retaining the benefits of squeezing at high frequencies. The premise of our filter is that at high frequencies the input beam is entirely reflected

by the filter cavity and the squeezing is preserved, while at low frequencies, it is entirely transmitted and the cavity losses cause ordinary vacuum to replace the (anti-) squeezed vacuum noise. The cavities have a visibility of nearly unity. In general, we attempt to choose a transition frequency above which the squeezing is preserved and below which we destroy the anti-squeezing. For any realistic cavity, however, there is a transition region in which the squeezing is also partially destroyed. The use of multiple cavities allows manipulation, and hence optimization, of this transition region.

In this chapter we evaluate the performance of these filter cavities and propose configurations that reduce the extent of the transition region. We initially consider the use of a single filter cavity, [Fig. 2-1 (b)]; in Section 2.6, we consider the extension to multiple cavities. In each case the filter cavities are placed between the squeeze source and unused output port of the beam splitter, as shown in Fig. 2-1 (a). We evaluate the performance using three astrophysical criteria *simultaneously*: (i) the signal-to-noise ratio (SNR) for detecting a stochastic background of gravitational-waves, (ii) the signal-to-noise ratio (SNR) for inspiraling neutron star binaries, and (iii) the strain sensitivity at higher frequencies, where pulsars are expected to be detectable.

2.2 Filter description

We consider a triangular cavity with three mirrors, as shown in Fig. 2-1 (b), where R_i, T_i and A_i are the power reflectivity, transmission and loss, respectively, of each mirror such that

$$R_i + T_i + A_i = 1, \text{ with } i = 1, 2, 3. \tag{2.1}$$

The field incident on the the cavity comprises a carrier at frequency, ω_0, and sidebands at frequencies, $\omega_0 \pm \Omega$. When the cavity is resonant with the carrier frequency, ω_0, the roundtrip length of the cavity, l, is an integer number of carrier half-wavelengths and the $\omega_0 + \Omega$ component of the incident field experiences a frequency-dependent phase shift, $\Phi = \frac{\Omega l}{c}$ for a single round trip of the cavity. Cavity amplitude reflection and transmission coefficients are then given by

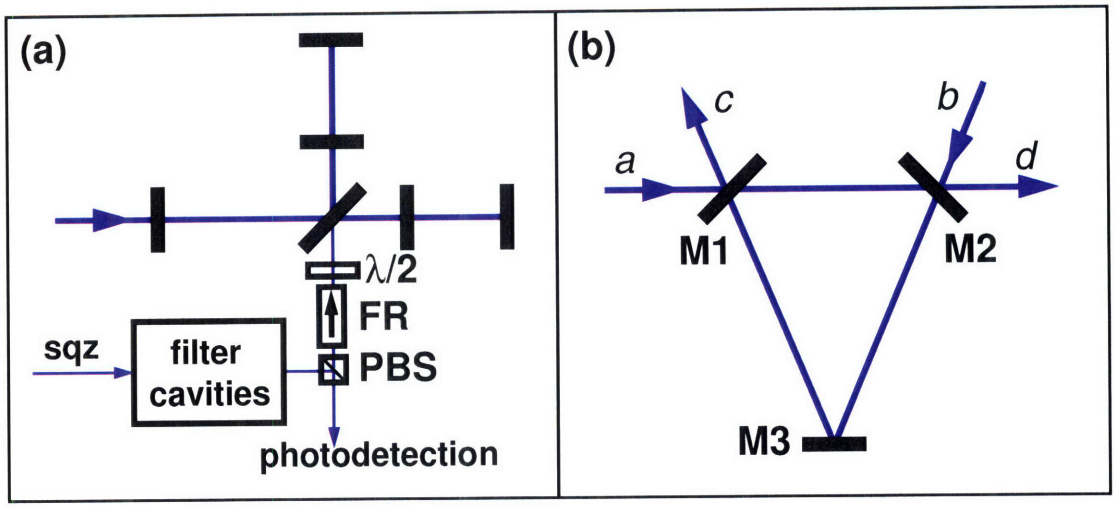

Figure 2-1: Panel (a) displays the placement of the filter in a squeezed-input interferometer. Panel (b) shows the single filter configuration, where a is the beam to be filtered, b is unsqueezed vacuum, c is the filtered beam and d is the transmitted beam.

$$\rho(\Omega) = \frac{c}{a} = \sqrt{R_1} - \frac{T_1\sqrt{R_2 R_3}\, e^{2i\Phi}}{1 - \sqrt{R_1 R_2 R_3}\, e^{2i\Phi}}, \tag{2.2}$$

$$\tau(\Omega) = \frac{d}{a} = \frac{\sqrt{T_1 T_2}\, e^{i\Phi}}{1 - \sqrt{R_1 R_2 R_3}\, e^{2i\Phi}}. \tag{2.3}$$

To make the cavity act as a high-pass filter for the reflected light at frequency Ω (relative to the carrier frequency, ω_0), a cavity with no reflected light at $\Omega = 0$ is desired, so we require that $\rho(0) = 0$. We constrain the values of R_1 and $R_2 R_3$ at a fixed value of A_1 by choosing a value for the half-linewidth of the cavity

$$\gamma_f \equiv \frac{c}{4l}(1 - R_1 R_2 R_3), \tag{2.4}$$

$$R_1 = \sqrt{1 - \frac{4l\gamma_f}{c}}\,(1 - A_1), \tag{2.5}$$

$$R_2 R_3 = \frac{\sqrt{1 - \frac{4l\gamma_f}{c}}}{(1 - A_1)}, \tag{2.6}$$

resulting in a reflected beam of the form

$$\rho(\Omega) = \frac{\sqrt{R}(1 - e^{2i\Phi})}{1 - \sqrt{1 - \frac{4l\gamma_f}{c}}e^{2i\Phi}} \approx \frac{\Omega}{i\gamma_f + \Omega}. \tag{2.7}$$

Eqn. (2.7) shows that the performance of the cavity depends only on its linewidth. $R_2 R_3$ must be less than $1 - A_2 - A_3 \approx 1 - 2A_1$, which requires $A_1 < \frac{2l\gamma_f}{3c}$. The finesse of the cavity is $\mathcal{F} = \frac{\pi c}{2l\gamma}$.

2.3 Filtered squeezed states

Since the cavity is not detuned from resonance and there is no rotation of the quadratures, it is straightforward to extend this result to the Caves-Schumaker two-photon formalism [31,32]. Referring to Fig. 2-1 (b), a and b are the (complex) amplitudes of fields at sideband frequency, Ω, incident on mirror M1 and M2, respectively. The field reflected from the cavity, c, has the form

$$c_i = \rho a_i + \tau b_i + \sqrt{1 - |\rho|^2 - |\tau|^2}\, v_i\,, \tag{2.8}$$

where $i = 1, 2$ and the v_i are the quadrature field amplitudes of the unsqueezed vacuum that leaks in due to the losses in the cavity. In the case where the light incident on M2 is also unsqueezed vacuum [1], the reflected field takes the form

$$c_i = \rho a_i + \sqrt{1 - |\rho|^2}\, v_i. \tag{2.9}$$

Now suppose squeezed vacuum is incident on the cavity, i.e. a is squeezed. Since $\rho(\Omega)$ has the response of a high pass filter, we see from Eqn. (2.9) that at low frequencies where $\rho(\Omega < \gamma_f) \sim 0$, the second term dominates and the filter output field, c, is in an ordinary vacuum state given by v, while at high frequencies where $(1 - |\rho|^2) \sim 0$, the output field contains primarily the squeezed input vacuum, a.

The reflected beam is, in general, not a pure squeezed state [2]. Two parameters characterize the effects of the cavity on the squeezed state: the attenuation factor, α, and

[1] Since the vacuum fluctuations entering the cavity due to losses and those due to finite transmissivity are uncorrelated, we add them in quadrature.

[2] A "pure" squeezed state refers to the case where the variance of the noise in one quadrature increases by exactly the same amount as that in the orthogonal quadrature is reduced, i.e. the area of the noise ellipse is unity. When excess noise is present in one quadrature, this condition is not satisfied.

the vacuum leakage, β. The attenuation factor measures the effect on the anti-squeezed quadrature, while the vacuum leakage measures the effect on the squeezed quadrature by measuring the vacuum noise that enters the beam. Defining $x = \Omega/\gamma_f$, we find

$$\alpha = \quad |\rho|^2 \quad \approx \frac{x^2}{1+x^2}, \tag{2.10}$$

$$\beta = \quad 1-|\rho|^2 \quad \approx \frac{1}{1+x^2}, \tag{2.11}$$

$$\alpha+\beta = \quad 1. \tag{2.12}$$

We define the corner frequency, $\xi = x_{1/2}\gamma_f$, of the filter to be the frequency at which $\alpha = \beta = \frac{1}{2}$, which gives $x_{1/2} \approx 1$. The parameters α and β as a function of (normalized) frequency are plotted as the solid curves in Fig. 2-2. Discussion of multiple filters, also shown in Fig. 2-2, is deferred to Section 2.6.

2.4 Application to gravitational-wave interferometers

2.4.1 Conventional interferometer

It is instructive to study the performance of the amplitude filter cavity with a conventional GW interferometer operated at the optimum power required to reach the standard quantum limit at $\Omega = \gamma$ [6]. Here γ is the linewidth of the arm cavities of the interferometer, distinct from γ_f, which is the linewidth of the filter cavity. Though γ may be adjusted to optimize the detector performance under certain circumstances, we restrict ourselves to $\gamma = 2\pi \times 100$ Hz.

A phase-squeezed vacuum beam is filtered by the cavity and then injected into the otherwise unused output port of the interferometer, as shown in Fig. 2-1 (a). To maintain the same input/output relations as developed in Ref. [6], the interferometer input (cavity output) beam is given in the form [3]

$$a_1' = \sqrt{\alpha}\, e^{R} a_1 + \sqrt{\beta}\, v_1 \tag{2.13}$$

$$a_2' = \sqrt{\alpha}\, e^{-R} a_2 + \sqrt{\beta}\, v_2. \tag{2.14}$$

For an interferometer with arm lengths, L, mirror masses, m, and injection squeeze factor,

[3] A unitary transformation was applied to the operator equation $a_i' = \sqrt{\alpha}\, a_i + \sqrt{\beta}\, v_i$ acting on a squeezed state $|\mathrm{sqz}\rangle$, such that $a_{1,2} \to e^{\pm R} a_{1,2}$ and $|\mathrm{sqz}\rangle \to |0\rangle$.

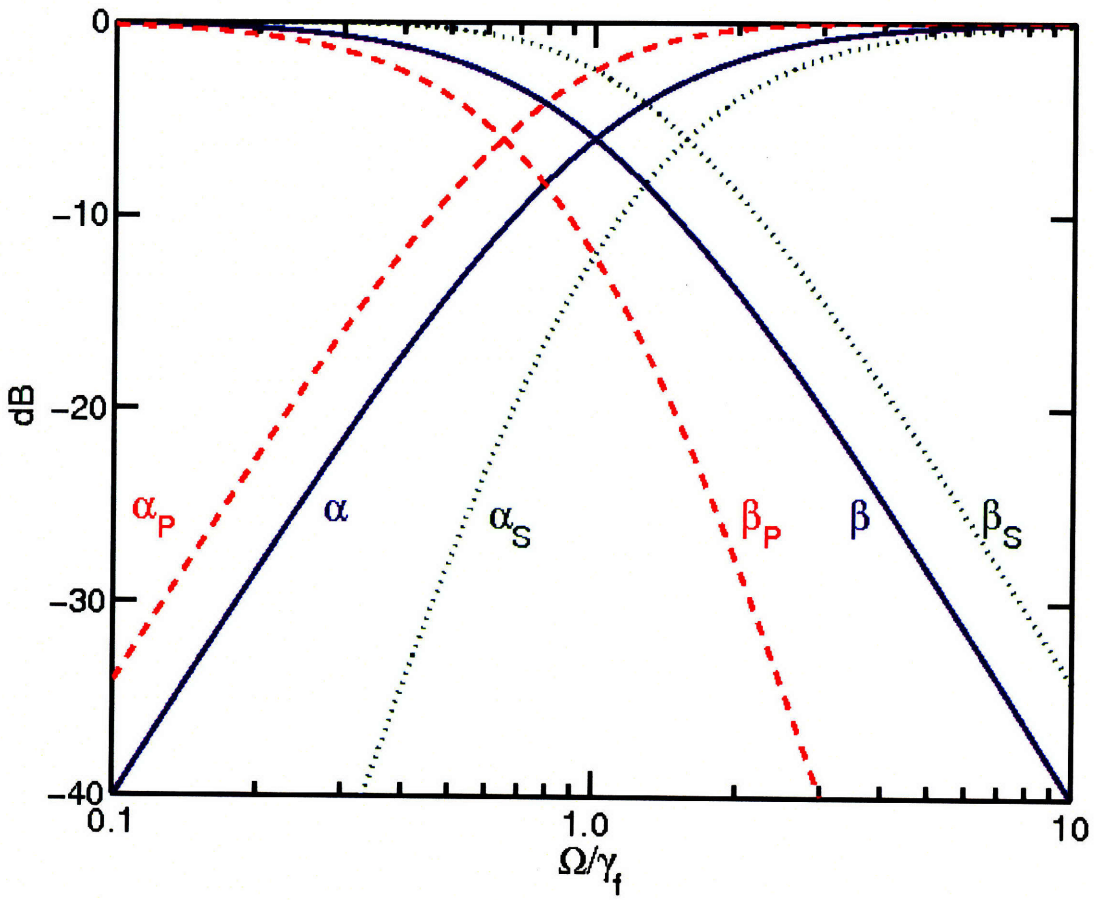

Figure 2-2: A plot of the attenuation, α, and maximum possible squeezing, β for a single (blue, solid), series (red, dashed) and parallel (green, dotted) filter. The subscripts S and P refer to series and parallel filters, respectively; these filter configurations are described in Section 2.6. The series filter increases the effective corner frequency and the attenuation factor, while the parallel filter decreases the effective corner frequency but increases the maximum squeezing.

R, this leads to the noise spectral density

$$S_h = \frac{h_{SQL}^2}{2\kappa}\left[\alpha\left(\mathrm{e}^{-2R} + \kappa^2 \mathrm{e}^{2R}\right) + \beta\left(1+\kappa^2\right)\right], \tag{2.15}$$

where

$$h_{SQL} \equiv \sqrt{\frac{8\hbar}{m\,\Omega^2\,L^2}} \tag{2.16}$$

is the noise spectral density of the dimensionless gravitational-wave strain at the standard quantum limit for an interferometer with uncorrelated shot noise and radiation-pressure noise, and

$$\kappa = \frac{2\left(I_0/I_{SQL}\right)\,\gamma^4}{\Omega^2\left(\gamma^2+\Omega^2\right)} \tag{2.17}$$

is the effective coupling constant that relates the output signal to the motion of the interferometer mirrors [6].

In Fig. 2-3, we plot the noise spectral densities for a conventional interferometer with squeezed input parameter $\mathrm{e}^{-2\,R} = 0.1$, using different filter cavity configurations. The unfiltered squeezed input gives significantly higher noise at $\Omega < \gamma$. When the squeezed input is filtered by a single filter, there is a frequency band $\Omega/\gamma > 1.5$ in which the sensitivity is worse than the the unfiltered squeezed case, and a corresponding range $\Omega/\gamma < 1$ in which the sensitivity is worse than the unsqueezed case. We refer to this band around $\Omega/\gamma \sim 1$ as the "transition region"; it is a consequence of the frequency response of the filter. In Section 2.6 we examine some methods to reduce the frequency extent of this transition region such that the low-frequency noise of the squeezed input interferometer approaches that of an interferometer with no squeezing, while preserving the noise reduction at high frequencies.

It is also possible to define a critical frequency above which squeezing is desirable, and below which it is deleterious [4]. Inserting $\alpha + \beta = 1$ into eqn. (2.15) for S_h, we get

$$S_h = \frac{h_{SQL}^2}{2\kappa}\left\{\alpha\left[\left(\mathrm{e}^{2R}-1\right)\,\kappa^2 - \left(1-\mathrm{e}^{-2R}\right)\right] + \left(1+\kappa^2\right)\right\}. \tag{2.18}$$

The coefficient of the term in α switches sign at the critical frequency, $\Omega/\gamma = 1.44$, which corresponds to the frequency at which the curves in Fig. 2-3 cross. Since $\beta = 0$ and $\alpha = 1$ when no filtering is applied, we always have $\alpha < 1$ in the filtered case. More generally then,

[4]The critical frequency was first pointed out by Yanbei Chen.

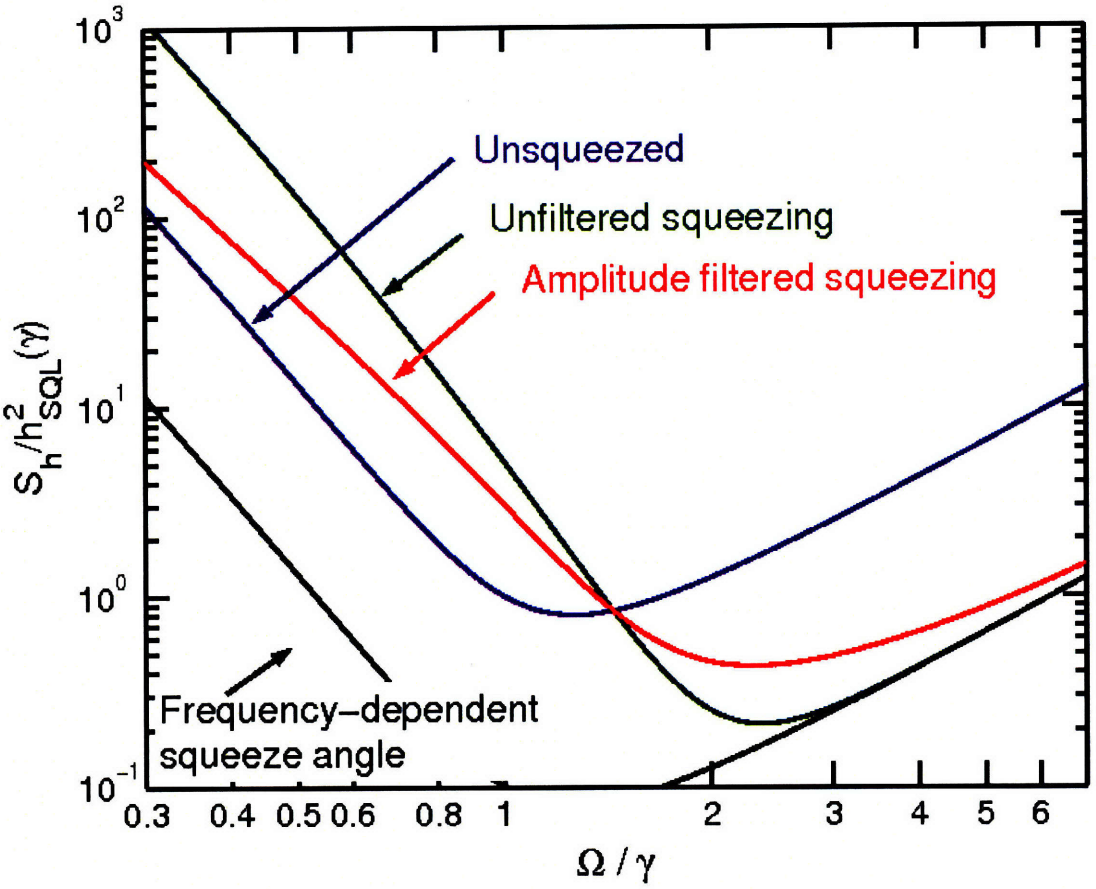

Figure 2-3: The noise spectral density, normalized by h_{SQL}, for a *conventional* interferometer with (i) no squeezed input ("Unsqueezed"); (ii) squeezed vacuum injected ("Unfiltered Squeezing"); (iii) squeezed input filtered by a filter cavity ("Amplitude filtered squeezing"); and (iv) frequency-dependent squeeze angle ("Frequency-dependent squeeze angle").

the noise for the unfiltered case is better at frequencies higher than the critical frequency (where κ is small), and worse at frequencies below the critical frequency. Moreover, at the critical frequency, the coefficient of α in eqn. (2.18) is zero and the value of α does not matter. This also explains why the curves for a variety of filter configurations in Fig. 2-4 all cross at a single frequency. It becomes evident in Section 2.5, however, that in optimizing the filter performance using astrophysical criteria, the critical frequency does not play a significant role.

2.4.2 Signal-recycled interferometer

The amplitude filter cavities can also be used in conjunction with a squeezed-input signal-recycled interferometer. The introduction of signal recycling has the effect of mixing the quadratures in the input/output relations of the interferometer. This allows the shot noise and radiation-pressure noise to become correlated, typically producing two resonances [12]: the lower frequency dip is due to an optical-mechanical coupling and the higher frequency one is a purely optical resonance due to the storage time of the gravitational wave signal in the interferometer. The mixing of the quadratures results in the optimal squeeze angle having a strong frequency dependence compared to the conventional interferometer [29]. The sensitivity curve can be shaped by an appropriate choice of the reflectivity of the signal extraction mirror (SEM) and the detuning of the signal extraction cavity (SEC) [30]. The noise curves shown in Fig. 2-4 are for a narrowband signal-recycled interferometer where the detuning of the SEC is chosen to place the optical resonance at 200 Hz. An alternative choice of detuning, where the carrier light with angular frequency ω_l obtains a net phase shift of $\frac{\pi}{2}$ in one pass through the cavity, gives a broadband response. This choice reduces the variation of the optimal squeeze angle with frequency and allows for improvement in the performance over a large frequency range. The broadband interferometer with squeezed input does not, however, benefit from the amplitude filtering unless the squeezed state is not pure. We, therefore, limit our discussion to the narrowband case shown in Fig. 2-4. Furthermore, we discuss the narrowband signal-recycled interferometer in term of real frequency, in Hz, since the normalization to an arm cavity inverse storage time is not meaningful when the gravtitational-wave signal storage time depends on both the arm cavity and the (detuned) signal extraction cavity.

The performance of the squeezed configuration is comparable to the unsqueezed configuration in the frequency range 10 Hz to 300 Hz, and considerably better between 300 Hz to 10 kHz.

2.5 Filter performance

To evaluate the performance of these amplitude filters with parameters that can be realized we invoke some simple astrophysical arguments. The amplitude filters are best suited to optimizing the gravitational-wave detector performance at high frequencies without com-

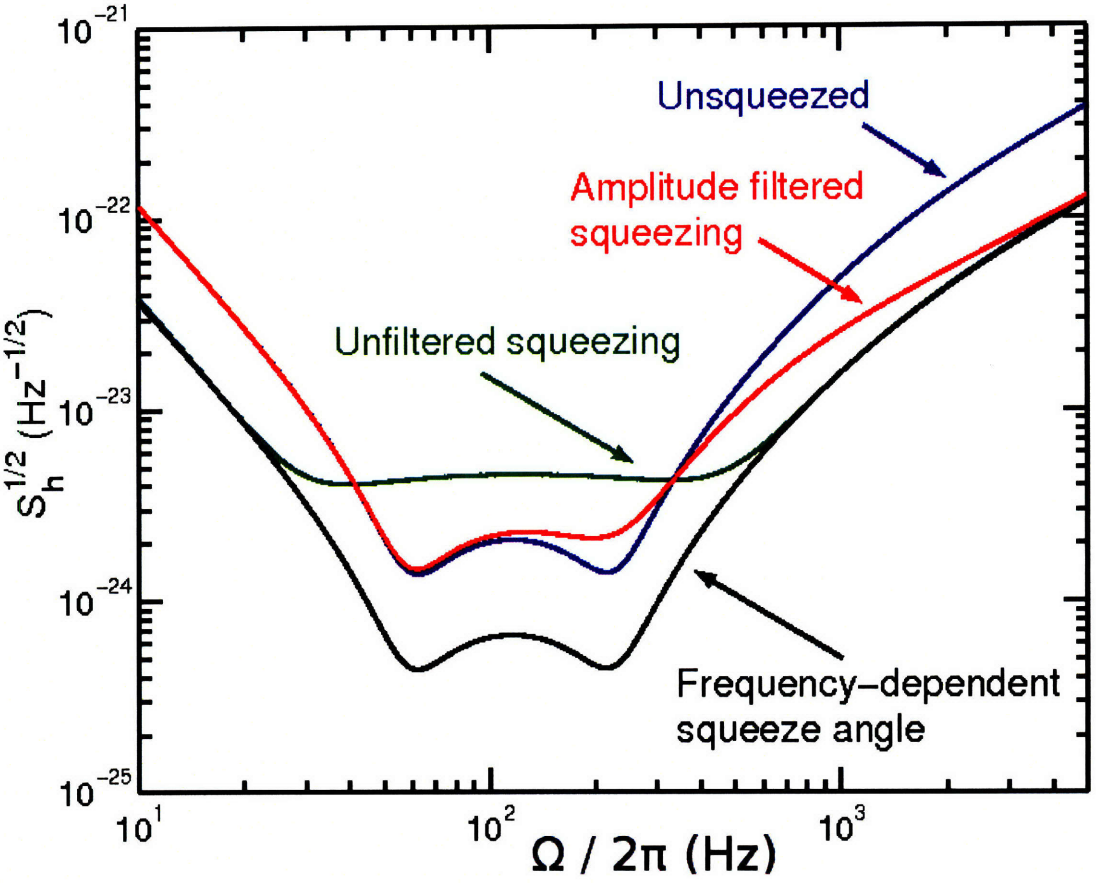

Figure 2-4: The square root of the noise spectral density for a *signal-recycled* narrowband Advanced LIGO interferometer with (i) no squeezing ("Unsqueezed"); (ii) squeezed vacuum injected directly into the output port of the beamsplitter ("Unfiltered squeezing"); (iii) squeezed vacuum injected after filtering with an amplitude filter cavity ("Amplitude filtered squeezing"); and (iv) squeezed vacuum injected after filtering to get a "Frequency-dependent squeeze angle".

promising the low-frequency performance as severely as a fixed squeeze angle input with no filtering. To this end, three frequency bands are of interest: (i) high frequencies $\Omega/\gamma \sim 10$ where we expect to carry out searches for GW emission from pulsars, for example; (ii) the minimum in S_h around $\Omega/\gamma \sim 1$ which is important for detection of radiation from inspiraling binary systems; and (iii) low frequencies $\Omega/\gamma < 1$ which are especially important for detection of a stochastic gravitational-wave background of cosmological origin by correlating the outputs of two spatially separated terrestrial detectors [5]. The performance in each of these frequency bands is characterized by the signal from the targeted source compared with the noise in the detectors. In Table 2.1, we compare the sensitivity or signal-to-noise ratio (SNR) for pulsars, binary neutron star inspirals and a stochastic background for several amplitude filter cavity configurations with a conventional interferometer with varying input power levels.

Most generally, the square of the signal-to-noise ratio (assuming optimum filtering) is given by [33].

$$\left(\frac{S}{N}\right)^2 \propto \int_0^{+\infty} \frac{|h(f)|^2}{S_h(f)}\, df \tag{2.19}$$

where $h(f)$ is the Fourier transform of the strain signal from the source and $S_h(f)$ is the single-sided noise spectral density of the detector.

For *periodic* sources such as a pulsar at a fixed frequency Ω_s, and ignoring any other modulation effects, the SNR can be expressed as

$$\left(\frac{S}{N}\right)^2_{per} \propto \int_0^{+\infty} \frac{\delta(2\pi f - \Omega_s)}{S_h(f)}\, df \tag{2.20}$$

where $\delta(2\pi\Omega_s)$ is a Dirac delta function. For our purposes it is convenient to assume $\Omega_s = 10\,\gamma$, and the signal-to-noise ratio is simply proportional to the inverse of the detector noise spectral density at that frequency.

For the *inspiral* phase of binary neutron star systems, the Newtonian quadrupole approximation gives $|h(f)|^2 \propto f^{-7/3}$. We estimate the SNR for inspiraling neutron stars by

$$\left(\frac{S}{N}\right)^2_{ins} \propto \int_{10\ \mathrm{Hz}}^{+\infty} \frac{1}{f^{7/3}\, S_h(f)}\, df \tag{2.21}$$

[5] We recall that $\gamma = 2\pi \times 100$ Hz for the conventional interferometer considered here.

where $S_h(f)$ is given by the curves in Figures 2-3 and 2-4 and a lower cut-off frequency of $\Omega/\gamma = 0.1$ is used to account for seismic noise [6].

For a *stochastic background* of cosmological origin, the spectrum of gravitational-waves is given by

$$|h(f)|^2 = \frac{3H_0^2}{10\pi^2} f^{-3} E_{gw}(f) \tag{2.22}$$

where H_0 is the present day Hubble expansion rate and $E_{gw}(f)$ is the gravitational-wave energy density per logarithmic frequency, divided by the critical energy density required to close the Universe. Assuming that $E_{gw}(f) =$ constant $= E_0$, and that the waves are isotropic, unpolarized, stationary and Gaussian, we arrive at $|h(f)|^2 \propto f^{-3/2}$. Limits on the stochastic background can be set by cross-correlating the outputs of two detectors. To ensure that noise in the detectors is not correlated by shared local effects, we use two widely separated detectors, e.g. detectors at the two LIGO Observatories, which are nearly co-planar and co-aligned but separated by a distance $d_s = 3001$ km. The cross-correlation depends on an additional quantity, $\eta(f)$, the overlap reduction function, which characterizes the reduction in sensitivity due to the separation time delay and relative orientation of the detectors. For the LIGO detectors in Louisiana and Washington, $\eta(f)$ can be expressed in terms of Bessel functions, J_i: $\eta(f) = -0.124842\, J_0\,(2\pi f d_s/c) - 2.90014\, J_1\,(2\pi f d_s/c) + 3.00837\, J_2\,(2\pi f d_s/c)$ [34], which gives $\eta(f = 0 \text{ Hz}) \approx 0.9$ with a sharp reduction above 50 Hz. The square of the signal-to-noise ratio for the stochastic background obtained by cross-correlating two detectors with noise spectra, $S_{h1}(f)$ and $S_{h2}(f)$, is given by

$$\left(\frac{S}{N}\right)^2_{sb} \propto \int_{-\infty}^{+\infty} \frac{\eta(f)^2}{f^6\, S_{h1}(f)\, S_{h2}(f)}\, df \tag{2.23}$$

$$\approx \int_{-\infty}^{+\infty} \frac{\eta(f)^2}{f^6\, S_h^2(f)}\, df \tag{2.24}$$

The result of Eqn. (2.24) assumes that the noise spectra of the two detectors are Gaussian, stationary and identical, i.e. $S_{h1}(f) = S_{h2}(f)$, and that optimal filtering was used [35].

[6] Strictly speaking, there is also an upper cut-off frequency associated with the innermost stable circular orbit (ISCO) of the binary system. Above $f_{ISCO} \approx 4400 \text{ Hz}\,(M/M_\odot)^{-1}$, where $M/M_\odot$ is the total mass of the binary system per solar mass, the binary system enters the merger phase and the spectrum of $|h(f)|^2$ is not expected to retain a $f^{-7/3}$ dependence. This upper cut-off frequency does not affect the estimate of the SNR here.

Configuration	$\frac{\gamma_f}{\gamma}$	Stochastic	NS Inspiral	Periodic
Conventional interferometer	–	1.00	1.00	1.00
Unfiltered fixed-angle squeeze	–	0.32	1.16	3.16
Single filter	1	0.89	1.00	3.03
Single filter	5	0.99	0.98	1.89
Series filter	$1/\sqrt{2}$	0.98	1.02	3.03
Series filter	$5/\sqrt{2}$	1.00	1.01	1.86
Parallel filter	$\sqrt{2}$	0.89	1.09	1.12
Parallel filter	$5\sqrt{2}$	0.99	0.98	2.24
FD squeeze	–	3.16	3.16	3.16

Table 2.1: Comparison of performance of a conventional interferometer with different filter configurations using three criteria: the signal-to-noise ratios for detecting (i) a stochastic background of gravitational-waves, (ii) the inspiral phase of a neutron star binary system (NS SNR), and (iii) a periodic source at $\Omega/\gamma = 10$ (which is simply the inverse strain spectral density, $1/\sqrt{S_h}$, at that frequency). We use the square root of the SNRs defined in Eqns. (2.20), (2.21) and (2.22) with S_h corresponding to the various interferometer and filter configurations listed. All SNRs are normalized to that of a conventional interferometer with no squeezing. The series and parallel filter configurations are described in Section 2.6.

Table 2.1 and Fig. 2-3 show that the best overall configuration is no doubt the frequency-dependent squeeze angle. Assuming that the interferometers are operated at the maximum power possible, then the only way to improve the high frequency noise is to use squeezing. If no filtering is used, the binary inspiral SNR is significantly reduced. If an amplitude filter is used in conjunction with the squeezed input, a moderate reduction in binary inspiral SNR is traded off against the benefits of squeezing at higher frequencies. The choice of bandwidth of the filter influences this trade off. Furthermore, the amplitude filtered squeezing can be used to increase sensitivity to binary inspirals by lowering the power, and using the squeezing to not completely worsen the high frequency noise. In the likely event that the multiple kilometer-scale filter cavities needed to achieve the frequency-dependent squeeze angle are not feasible in the upcoming generation of interferometers, amplitude filters such as the ones we propose are promising candidates for broadband improvement in the detector sensitivity.

To explore the feasibility of these filter cavities further, we give some physical parameters for the amplitude filter cavities. For a conventional interferometer with initial LIGO

Configuration	$\frac{\gamma_f}{100\text{ Hz}}$	NS Inspiral	$\frac{1}{\sqrt{S_h}}\left(\frac{\Omega}{2\pi} = 1\text{ kHz}\right)$	$\frac{1}{\sqrt{S_h}}\left(\frac{\Omega}{2\pi} = 10\text{ kHz}\right)$
SR IFO	–	1.00	1.00	1.00
Unfiltered	–	0.654	3.16	3.08
Single filter	3	0.854	2.39	3.07
Single filter	5	0.924	1.89	3.05
Single filter	10	0.974	1.35	2.96
FD squeeze	–	3.16	3.16	3.16

Table 2.2: Comparison of performance of a narrowband signal-recycled interferometer with different filter configurations using two criteria: The signal-to-noise ratio for (i) inspiraling neutron star binaries (NS Inspiral), and (ii) periodic sources radiating at 1 kHz and 10 kHz, respectively. All SNRs are normalized to that of a signal-recycled interferometer with no squeezing.

parameters $\gamma \simeq 2\pi \times 100$ Hz. From Table 2.1, we see that $\gamma < \gamma_f < 5\gamma$, implying that the filter cavity linewidth is typically equal to, or a few times larger, than the arm cavity linewidth, or $500\,\text{Hz} > \gamma_f/(2\pi) > 100\,\text{Hz}$. For a 10 meter long filter cavity, this would correspond to a finesse of 15000 to 75000, or average losses of 70 to 14 parts-per-million per mirror. If the filter cavities can be made longer (upto ~ 30 m is feasible in the output train of LIGO), the limit on the mirror losses can be accordingly relaxed.

For completeness we evaluate the performance of a narrowband signal-recycled interferometer as well. As with the conventional interferometer, the narrowband signal-recycled configuration of Fig. 2-4 and Table 2.2 benefits at all frequencies from squeezed input with a frequency-dependent squeeze angle. We intentionally use a narrowband configuration to highlight the differences between it and the conventional interferometer. It is evident from Fig. 2-4 that for the narrowband signal-recycled configuration, the amplitude filter gives significant improvement for detection of neutron star binary inspirals (the SNR is most sensitive to detector noise in the minimum between 40 and 400 Hz), but would certainly deteriorate the detector performance for the stochastic background (the overlap reduction function strongly favors frequencies below 50 Hz). In Table 2.2 it is interesting to note that the filter cavity can provide substantial benefit at high frequencies even with considerably higher resonance bandwidths, e.g. 1 kHz.

2.6 Extension to multiple filters

In this section we explore methods to reduce the frequency extent of the transition region between the reduced noise at high frequencies (due to squeezing) and the increased noise at low frequencies, that can be made to approach the noise level of an interferometer with no squeezing.

2.6.1 Series filters

The most straightforward way to reduce the transition region is to connect two filters in series, as shown in Fig. 2-5(a). Extending Eqns. 2.7, 2.11 and 2.12, we find

$$\alpha_S = |\rho|^4 \approx \frac{x^4}{x^4 + 2x^2 + 1}, \tag{2.25}$$

$$\beta_S = 1 - |\rho|^4 \approx \frac{2x^2 + 1}{x^4 + 2x^2 + 1}, \tag{2.26}$$

$$x_{1/2} \approx \left(\sqrt{2} + 1\right)^{\frac{1}{2}}. \tag{2.27}$$

Comparing the solid curves with the dotted curves in Fig. 2-2, we see that the addition of the second filter has the effect of increasing the attenuation factor, while shifting the vacuum leakage by a factor of $\sqrt{2}$ in frequency at frequencies $\Omega > \gamma$. By reducing the linewidth of both filters by a factor $\sqrt{2}$, we obtain nearly the same vacuum leakage along with an increased attenuation factor, thereby reducing the size of the transition region. For ease of comparison, in the "series filter" curve of Fig. 2-6 the linewidth of each filter cavity is reduced by $\sqrt{2}$ compared to an equivalent single filter. We also note that further gains could be made by double-passing the input squeezed light through each filter, or, alternatively, reducing the number of filters required, and hence reducing the complexity.

2.6.2 Parallel filters

To decrease the vacuum leakage, we inject the filtered beam from one filter into the input port of another filter, as shown in Fig. 2-5 (b). We assume that the input light in each filter is squeezed in the same quadrature. We also assume that the filters are *lossless* for simplicity. The output from the combined filters is

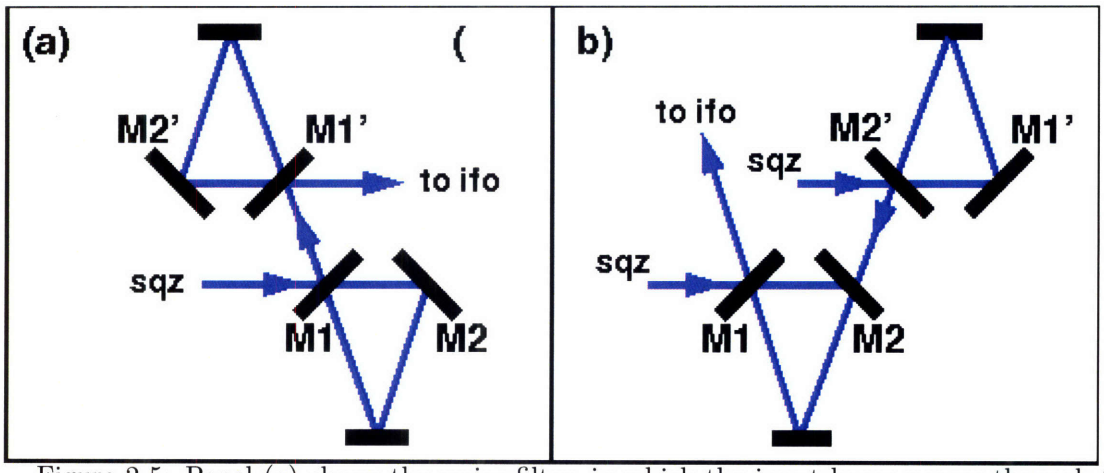

Figure 2-5: Panel (a) shows the series filter, in which the input beam passes through two filters. Panel (b) shows the parallel filter, in which a filtered beam is injected instead of vacuum.

$$c_i = \rho\,(a_i + \tau b_i) + \tau^2 v_i \tag{2.28}$$

where a_i is the field injected in the first filter, and b_i is the field injected into the second filter. Using the relation that $|\rho|^2 + |\tau|^2 = 1$ for a lossless filter, we find that

$$\alpha_P = \left|\rho\right|^2\left(2 - \left|\rho\right|^2\right) \approx \frac{x^4 + 2x^2}{x^4 + 2x^2 + 1}, \tag{2.29}$$

$$\beta_P = \left(1 - \left|\rho\right|^2\right)^2 \approx \frac{1}{x^4 + 2x^2 + 1}, \tag{2.30}$$

$$x_{1/2} \approx \left(\sqrt{2} - 1\right)^{\frac{1}{2}}. \tag{2.31}$$

As shown in the dashed curves of Fig. 2-2, the parallel filter has the effect of decreasing the vacuum leakage, while shifting the attenuation factor by a factor of $\sqrt{2}$ in frequency at frequencies $\Omega < \gamma$. By increasing the linewidth of both filters by a factor $\sqrt{2}$, we can obtain nearly the same attenuation factor along with reduced vacuum leakage, once again reducing the size of the transition region.

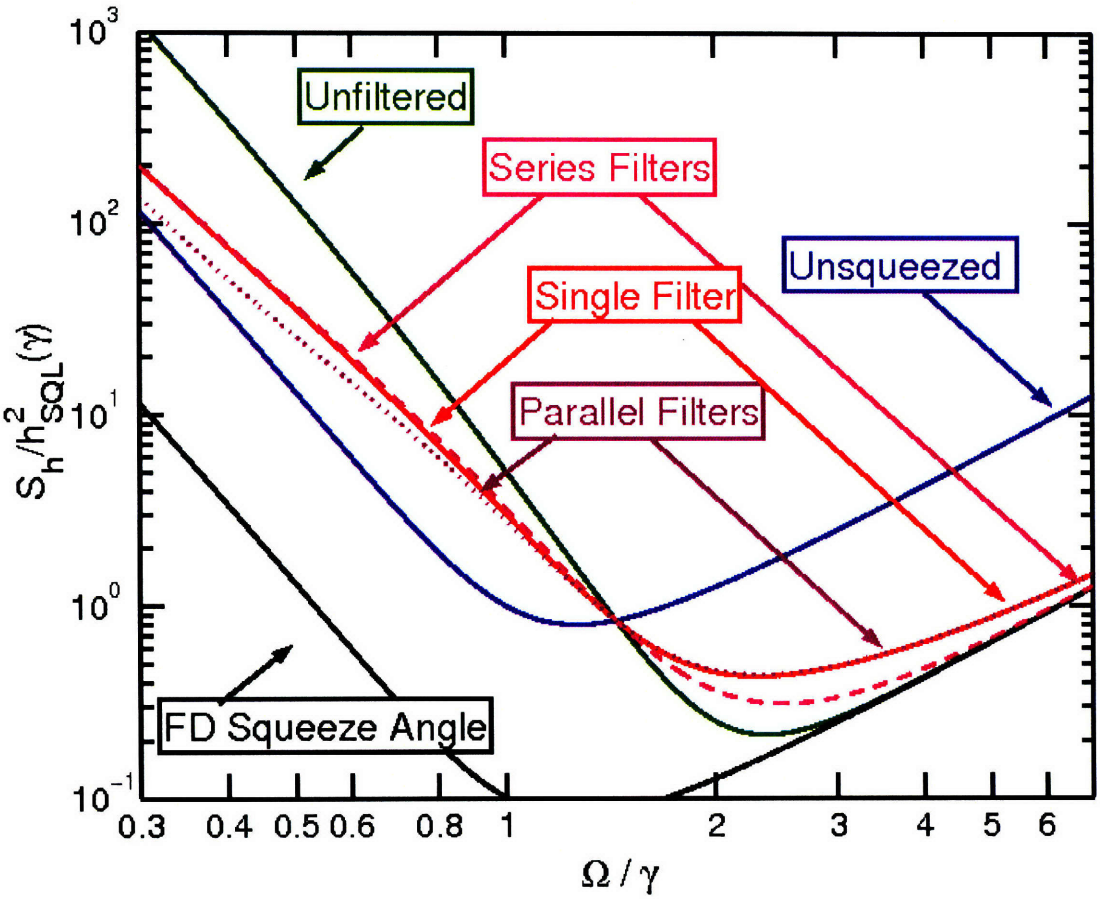

Figure 2-6: The square root of the noise spectral density is shown for a conventional interferometer with (i) no squeezed input ("Unsqueezed"), (ii) Squeezed vacuum injected ("Unfiltered"); Squeezed input filtered by (iii) a single filter cavity ("Single Filter"), (iv) series filter cavities ("Series Filter"), (v) parallel filter cavities ("Parallel Filter"); and (vi) frequency-dependent squeeze angle ("FD Squeeze Angle").

2.6.3 Filter performance

It is instructive to evaluate the sensitivity of the interferometer with squeezed input filtered by the multiple cavity configurations. For conciseness, we apply multiple filters only to the conventional interferometer described in Section 2.4.1. The performance measures are listed in the series and parallel filter sections of Table 2.1, where we apply the same criteria as those described in Section 2.5, namely, the signal-to-noise ratios for detecting gravitational radiation from (i) a stochastic background using widely separated detectors, (ii) an inspiraling neutron star binary system, and (iii) a perfectly periodic source at $\Omega/\gamma = 10$.

2.7 Summary

Recognizing the operational complexity of using kilometer-scale filter cavities in conjunction with a squeezed input in long-baseline gravitational-wave interferometers, we have proposed an alternative type of filter cavity that acts as a high-pass filter for the squeeze amplitude. We evaluate the performance of these amplitude filters with parameters that can be realized and find them to be effective in improving the high-frequency performance of a squeezed input gravitational-wave detector without drastically compromising the low-frequency sensitivity. From Table. 2.1, we see that that significant improvements can be achieved with the amplitude-filtered squeezed input interferometer compared with an interferometer with no squeezing, or with a frequency-independent squeezed-input interferometer, depending on the target astrophysical source and the interferometer and filter parameters. The amplitude filters do not give the broadband improvement afforded by the (multiple) kilometer-scale filter cavities that give a frequency-dependent squeeze angle, but they are an attractive alternative since they are a few meters in length and require finesses well under 10^5, making them more feasible in the output train of gravitational-wave detectors. Moreover, the amplitude filters can suppress noise in excess of the anti-squeezed quantum-limited noise. We also point out that some of the broadband benefit afforded by the frequency-dependent squeeze angle – or any other filtering scheme – is likely to be compromised by other noise sources, e.g., thermal noise, which were not considered in this work.

Chapter 3

Optomechanical coupling

In this chapter, we derive the equations governing classical optomechanical coupling in detuned cavities. The effects of weak ponderomotive forces have been studied experimentally decades ago [36,37], and been proposed for use in GW interferometers relatively recently [38]. Cavities provide a way to couple the motion of a mirror to the radiation pressure that is exerted on it. It is convenient to interpret this coupling in terms of a spring constant. We begin by deriving the optomechanical spring constant, and then apply it to a variety of mechanical regimes to demonstrate its effects. Due to the calculational complexity, we defer discussions of the behavior of the quantum noise in these systems to Chapter 4, where we introduce a computational model.

3.1 Adiabatic optical spring constant

First, let us consider a cavity as shown in Figure 3-1, with a partially transmissive, stationary input mirror, and a perfectly reflecting, movable end mirror, pumped with a laser beam. If the distance between the mirrors and the frequency of the laser are arranged so that the light entering the cavity is in phase with the light already inside the cavity, then the intracavity field is resonantly enhanced.

When operated slightly detuned from this resonance, an optical feedback mechanism occurs in which the intracavity power is linearly dependent on the position of the mirrors, which acts to couple mirror motion to intensity fluctuations (see Figure 3-2), which then push on the mirror via radiation pressure. The feedback can profoundly modify the dynamics of both the mechanical and optical systems at high power levels. To model these

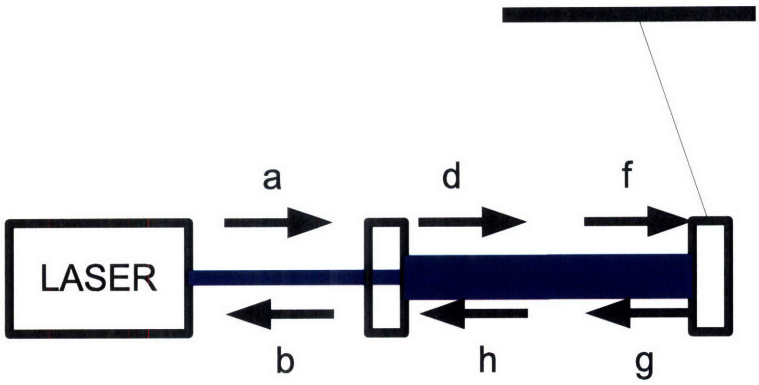

Figure 3-1: A cavity is pumped by a laser of power I_0 and frequency ω_0 from the left side. The input mirror has power transmissivity $T = \tau^2 = \sqrt{1-\rho^2}$ and is immovable. The end mirror, with mass M is perfectly reflective and moves freely.

effects, we assume that the motion of the mirror is small, and break the intracavity fields into a constant, pumping field, which is solely determined by the steady state positions of the mirrors and the input power, and the fluctuating fields that vary in time. To find the steady state fields, we relate the fields at each position:

$$d = \tau a - \rho h \tag{3.1}$$

$$f = e^{i\theta} d \tag{3.2}$$

$$g = -f \tag{3.3}$$

$$h = e^{i\theta} g \tag{3.4}$$

$$b = \rho a + \tau h \tag{3.5}$$

$$\theta = \frac{\omega_0 L}{c} \, mod \, 2\pi, \tag{3.6}$$

where ρ and τ are the amplitude reflectivity and transmissivity, such that $\rho^2 + \tau^2 = 1$. Solving these equations for the field incident on the end mirror, we find

$$b = \frac{\tau e^{i\theta}}{1 - \rho e^{2i\theta}} a. \tag{3.7}$$

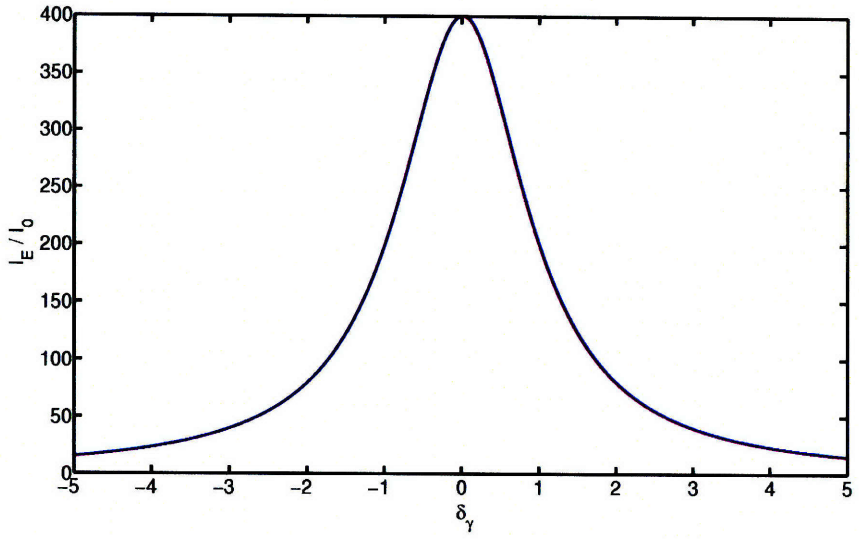

Figure 3-2: The intracavity power incident on the end mirror for $T = 0.01$ is shown as a function of δ_γ. The radiation pressure exerted on the end mirror is proportional to the intracavity power.

The force on the mirror is proportional to the intensity of the field:

$$|b|^2 = \frac{4}{T}\frac{1}{1+\delta_\gamma^2}|a|^2, \tag{3.8}$$

$$\delta_\gamma = \frac{\theta c}{L\gamma}, \tag{3.9}$$

$$\gamma = \frac{Tc}{4L}, \tag{3.10}$$

$$T = \tau^2, \tag{3.11}$$

where δ_γ is the detuning of the cavity in units of its linewidth, and we have approximated to first order in T and second order in θ. The power incident on the end mirror is then

$$I_E = \frac{4}{T}\frac{1}{1+\delta_\gamma^2}I_0. \tag{3.12}$$

Recall that the radiation pressure exerted on the mirror is $2I_E/c$, so that for any small and adiabatic (sufficiently slow that the response of the cavity may be regarded as instantaneous) displacements around an equilibrium position, the mirror experiences a change in force

$$\delta F = \frac{2}{c}\frac{dI_E}{dL}\delta L. \tag{3.13}$$

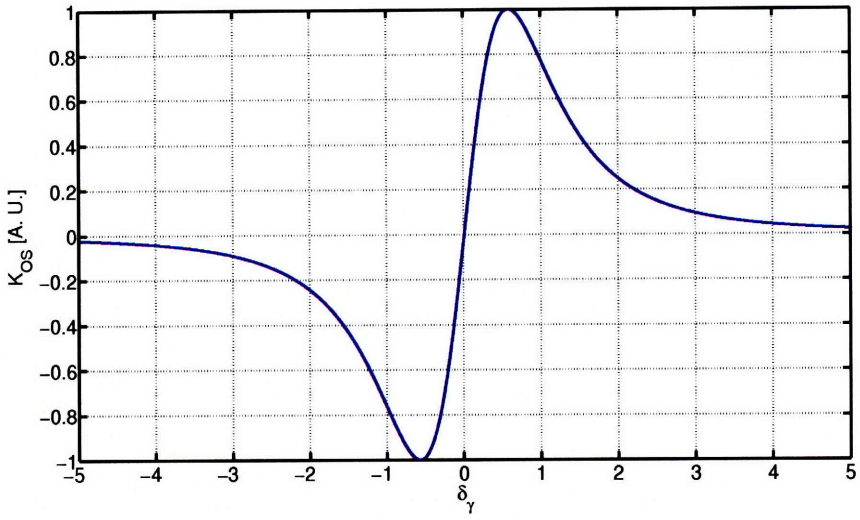

Figure 3-3: The adiabatic spring constant is shown. The spring constant vanishes for $\delta_\gamma = 0$, and changes signs depending on the sign of the detuning. The maximum amplitude of spring constant is achieved for $\delta_\gamma = \pm 1/\sqrt{3}$.

The change in force is equivalent to having the cavity mirrors connected with by a spring with spring constant

$$K = -\frac{2}{c}\frac{dI_E}{dL} = -\frac{64 I_0 \omega_0}{T^2 c^2}\frac{\delta_\gamma}{(1+\delta_\gamma^2)^2}, \tag{3.14}$$

which is shown in Figure 3-3.

3.2 Full optical spring constant

In the above calculation, we have assumed that the mirror motion is slow and that the intracavity fields respond instantaneously. This is a poor assumption when the frequency of motion is comparable to the response time of the cavity γ^{-1}. To calculate the full time dependent response, we first assume that the carrier is in the cosine quadrature at the end mirror (which may always be arranged by adjusting the phase of the input field). We perform the calculations in the frequency domain, using the notation presented in Chapter 1 for the fluctuating fields, and taking the convention

$$\mathbf{a} = \begin{pmatrix} a_1 \\ \\ a_2 \end{pmatrix}. \tag{3.15}$$

We may relate the field operators and the mirror motion X with

$$\mathbf{a} = 0 \tag{3.16}$$

$$\mathbf{d} = -\rho\mathbf{h} \tag{3.17}$$

$$\mathbf{f} = \mathbf{R}(\theta)e^{i\phi}\mathbf{d} \tag{3.18}$$

$$\mathbf{g} = -\mathbf{f} + 2\sqrt{\frac{I_E\omega_0}{\hbar c^2}}\begin{pmatrix} 0 \\ 1 \end{pmatrix} X \tag{3.19}$$

$$\mathbf{h} = \mathbf{R}(\theta)e^{i\phi}\mathbf{g} \tag{3.20}$$

$$-M\Omega^2 X = F_0 + \frac{2\sqrt{I_E\hbar\omega_0}}{c}\begin{pmatrix} 1 \\ 0 \end{pmatrix}^T \mathbf{f} \tag{3.21}$$

$$\phi = \frac{\Omega L}{c}, \tag{3.22}$$

where

$$\mathbf{R}(\Theta) = \begin{pmatrix} \cos\Theta & -\sin\Theta \\ \sin\Theta & \cos\Theta \end{pmatrix}, \tag{3.23}$$

and F_0 is ambient force noise on the mirror.

In the general case of a cavity not on resonance, the fields propagating in free space mix the quadratures (the R terms act to rotate the quadratures), which allow the phase disturbance from mirror motion to couple into intensity fluctuations. We point out that if the cavity is on resonance ($\theta = 0$), then this does not occur. We have assumed the input fluctuations $\mathbf{a}$ are 0, because we are focusing only on the change in dynamics of the mirror and not on the quantum noise. We may rearrange these equations to find the equation of motion for the mirror:

$$-M\Omega^2 X = F_0 + K_{OS}X, \tag{3.24}$$

where

$$K_{OS}(\Omega) = -\frac{8I_E\omega_0\rho}{c^2}e^{i\phi}\begin{pmatrix} 1 \\ 0 \end{pmatrix}^T \mathbf{R}(\theta)\left(\mathbf{I} - \rho\mathbf{R}(2\theta)e^{2i\phi}\right)^{-1} e^{i\phi}\mathbf{R}(\theta)\begin{pmatrix} 0 \\ 1 \end{pmatrix}, \tag{3.25}$$

$$= -\frac{8I_E\omega_0\rho e^{i\phi}}{c^2}\frac{\sin 2\theta}{1 + \rho^2 e^{4i\phi} - 2\rho e^{2i\phi}\cos 2\theta} \tag{3.26}$$

is the optical spring constant. We may simplify this expression, by making the assumptions $\phi \ll 1$, $\theta \ll 1$, expanding ρ to first order in T, the denominator to second order in ϕ and third order in θ to obtain

$$K_{OS} = \frac{K_0}{\delta_\gamma^2 + (1 + i\Omega_\gamma)^2}, \tag{3.27}$$

where $\Omega_\gamma = \Omega/\gamma$ and

$$K_0 = -\frac{16 I_E \omega_0 \delta_\gamma}{Tc^2}, \tag{3.28}$$

$$= -\frac{64 I_0 \omega_0}{T^2 c^2} \frac{\delta_\gamma}{1 + \delta_\gamma^2}. \tag{3.29}$$

We note that the form of the full spring constant is identical to the form of a damped harmonic oscillator with resonant frequency $\Omega_{\gamma,0} = \sqrt{1 + \delta_\gamma^2}$ and quality factor $\Omega_{\gamma,0}/2$. This resonant frequency is for the optical spring constant, not for the mirror motion itself. The full spring constant contains both real and imaginary terms. The real component corresponds to the usual frictionless spring constant, and the imaginary component corresponds to a viscous damping force. Note that if we set $\Omega = 0$, the imaginary component vanishes, and we recover the adiabatic spring constant given in Eq. 3.14. The effects of the spring constant are different depending on the magnitude of the real and imaginary components relative to their mechanical counterparts, and relative to which mode of mirror motion is considered. It is convenient to form two divisions of the coupling: the optical spring regime, and the parametric instability regime.

3.3 Optical spring regime

In the derivation of the optical spring constant above, we neglected any mechanical spring constant present in the system. It is, however, straightforward to include a mechanical spring:

$$-M\Omega^2 X = -(K_M + K_{OS})X + M\Omega\Gamma_M X + F_0, \tag{3.30}$$

where K_M is the mechanical spring constant, and Γ_M is the mechanical damping rate. The mechanical spring could be a pendulum suspension of a mirror, as used in LIGO, or an acoustic mode of vibration of the mirror. In general, the radiation pressure couples to

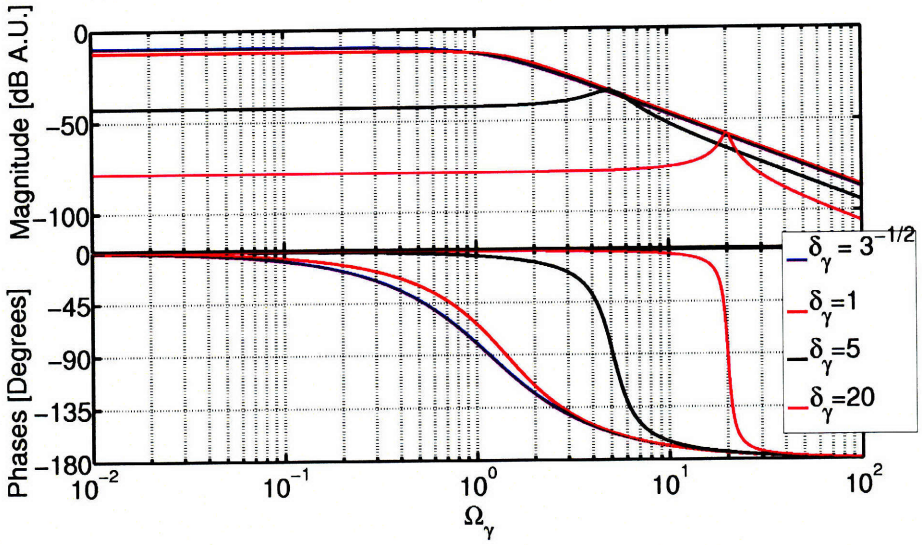

Figure 3-4: Bode plots of spring constants for $\delta_\gamma = 1/\sqrt{3}, 1, 5, 20$ are shown.

any available degree of freedom of the mirror, but each of the modes may be considered independently.

First, we consider the case that the real part of the optical spring constant dominates the mechanical spring constant, or $|K_{OS}| \gg K_M$. If the cavity is operated with $\delta_\gamma < 0$, the optical spring constant is anti-restoring, indicating that the radiation pressure reinforces any position disturbance. This configuration is, therefore, unstable and in general undesirable, so we limit our consideration to the case that $\delta_\gamma > 0$ and the radiation pressure is a restoring force. For this configuration, the primary effect of the optical spring constant is to shift the mechanical resonant frequency of the mirror to

$$\Theta = \sqrt{\frac{K_M^2 + K_{OS}^2}{M}}. \tag{3.31}$$

The consequences of this change are revealed when we consider the effects of force (or GW) disturbances:

$$X/F_0 = \frac{1}{-\Omega^2 + \Theta^2 + M\Omega\Gamma_M}. \tag{3.32}$$

At the new resonant frequency of the optomechanical oscillator, the mechanical motion is amplified, and it has been shown that this amplification may reduce the quantum noise level of the detector, even below the free mass SQL [12]. Below the new resonant frequency,

the optical response to external disturbances is reduced by a factor

$$\frac{\Theta^2 - \Omega^2}{\Omega_M^2 - \Omega^2}. \tag{3.33}$$

The reduction modifies the coupling of quantum noise which we discuss in Chapter 5, and also provides some practical benefits that will be discussed in Chapter 6.

3.4 Parametric instability and cold damping

The optical spring may also profoundly impact the dynamics of the system if its imaginary component, which corresponds to damping forces, dominates the mechanical damping forces. It is usually desirable to minimize damping effects in experiments in order to reduce the effects of thermal noise in the measurement. This leads to oscillators with extremely high quality factors that routinely exceed 10^6. Therefore, even a small imaginary component in the optical spring constant can overwhelm the mechanical damping, even if the change in resonant frequency of the oscillator is negligible. The optical damping rate is given by

$$\Gamma_{OS} = \frac{\mathrm{Imag}(K_{OS})}{M\Omega} = \frac{-2K_0}{M\gamma} \times \frac{1}{(1+\delta_\gamma^2 - \Omega_\gamma^2)^2 + 4\Omega_\gamma^2}. \tag{3.34}$$

We point out that the sign of the damping constant opposes the sign of the optical spring. This indicates that when the optical spring forms a restoring force, the imaginary component forms an anti-damping force. Therefore, in most cases, the system experiences an unstable force – either anti-restoring or anti-damping. There is a special case, which occurs for frequencies $\Omega_\gamma > 1 + \delta_\gamma^2$, in which the force experienced by a mode at that frequency may be both restoring and damping (see the phase behavior at high frequency in Figure 3-4 for example). However, this regime may not be described as a simple spring constant because the spring constant itself is strongly frequency dependent.

There is a large variety of systems for which the mode of mirror motion is extremely stiff so that $K_M > |K_{OS}|$, but $\Gamma_M < \Gamma_{OS}$. In this case, the resonant frequency of the mode is essentially unchanged by the optical spring, but the damping of the mode may be dramatically altered. Depending on the side of the detuning, the optical damping may either reinforce the mechanical damping (cold damping) and reduce the quality factor of the mode, or oppose the mechanical damping which results in parametric instabilities if

the optical damping exceeds the mechanical damping. This often occurs for the acoustic internal modes in macroscopic mirrors [48], and for vibrational modes of micromechanical oscillators [68, 70, 72]. The effect is further discussed in Chapter 6.

The theory of the optical spring effect developed here will be central to the experiments described in Chapters 5 and 6 and 7.

Chapter 4

Computational basis

We present a mathematical framework for simulation of optical fields in complex GW interferometers. The simulation framework uses the two-photon formalism [31,32] for optical fields and includes radiation pressure effects, an important addition required for simulating signal and noise fields in next-generation interferometers with high circulating power. We present a comparison of results from the simulation with analytical calculation and show that accurate agreement is achieved. This chapter is adapted from Ref. [39]. The technique is an extension to the basic calculations presented in Chapters 1 and 2.

4.1 Introduction

The need for optical field simulation for GW interferometer design has been addressed in the past with a variety of simulation tools, both in the frequency domain (e.g., *twiddle* [40] and *finesse* [41]) and in the time domain (e.g., the *LIGO end-to-end simulation program* [42]). Although time-domain simulations can study issues associated with large mirror displacements and non-linear effects, e.g., the lock acquisition of the interferometer, they are computationally costly; in addition, full time-domain simulations are also less straightforward to quantize. In order to study the performance of gravitational-wave detectors, it suffices to stay in the linear regime near the operation point. For such a linear problem, frequency-domain simulations are dramatically simpler than time-domain ones; it is straightforward to obtain frequency-domain transfer functions, and, therefore, noise spectra. In addition, since the system is linear, the propagation of quantum Heisenberg operators are identical to those of classical field amplitudes, therefore, it suffices to build

an essentially classical propagator.

In low-power situations where radiation-pressure-induced mirror motion is negligible and no non-linear optical elements (e.g., squeezers) are used, when linearizing over mirror displacements, propagation of electromagnetic fields at different frequencies are independent, and the transfer functions can be established for each different frequency separately. One only needs to take into account that, for the inputs to this linear system: (i) mirror motion (with frequency Ω) creates phase modulation of the carrier (with frequency ω_0), which is equivalent to generating two equally spaced sidebands on the carrier frequency (at $\omega_0 \pm \Omega$, where ω_0 is the carrier frequency and we denote $\omega_0 + \Omega$ and $\omega_0 - \Omega$ as the upper and lower sidebands, respectively) with opposite amplitudes, and that (ii) laser noise can usually be decomposed into amplitude noise and phase noise, with the former contributing equally to the upper and lower sidebands, and the latter oppositely. These considerations have been the conceptual foundations of previous frequency-domain simulation programs.

For high-power interferometers, the above strategy must be modified: the radiation-pressure forces acting on the mirrors, at frequency Ω, depend on both upper and lower sideband fields; the induced mirror motion again contributes to both sidebands — this makes it necessary to propagate pairs of upper and lower sidebands simultaneously. The mathematical formalism most convenient for this problem, at least in the case of only one carrier frequency, is the Caves-Schumaker *two-photon formalism* [31,32]. In this chapter, we adopt this formalism and present a mathematical framework for calculating the propagation of fields in an arbitrary optical system that includes the dynamical response of the mirrors to the light field. Namely, we divide complex interferometers into inter-connected elementary subsystems, and provide a general procedure for building a set of linear equations for all optical fields propagating between these systems – based on each individual system's *input-output relation*, i.e., transformation matrices relating output fields to input ones and the incoming GW. We also describe the way in which these subsystems are connected to each other. Solving these equations provides us with the optical fields, in terms of vacuum fluctuations entering the system from open ports, laser noise, and incoming GWs. While this mathematical framework, and the resulting numerical simulation tool, were developed to model quantum correlation effects in gravitational-wave interferometers, the method is general and can be used in any system where optical fields couple to mechanical oscillation modes.

This chapter is organized as follows: In Sec. 4.2 we introduce the mathematical framework for the simulation, and illustrate it with a simple example; in Sec. 4.3 we provide input-output relations of basic optical elements that may be present in a laser interferometer, ignoring radiation-pressure effects and the presence of gravitational waves — by re-formatting well-known results in optics; in Sec. 4.4, we take radiation-pressure-induced mirror motion into account, and provide input-output relations for movable mirrors and beamsplitters (up to linear order in mirror motion), which have not been obtained before in the most general form; in Sec. 4.5, we take into account the presence of GWs by introducing modulation of cavity lengths, and treat the corresponding effect on light propagation up to linear order in $L/\lambda_{\rm GW}$ (with L the length of the interferometer). In Appendix A the formulation is applied to a novel interferometer designed to extract squeezed vacuum states that are created by a strong opto-mechanical coupling; and, finally, conclusions are summarized in Section 4.6.

4.2 Mathematical framework

4.2.1 Two-photon quantum optical formalism

We use the two-photon formalism developed by Caves and Schumaker [31,32] to describe GW interferometers with significant radiation-pressure effects. In this formalism, any quasi-monochromatic optical field with frequency near the carrier frequency ω_0 is written as

$$\begin{aligned} E(t) &= E_1(t)\cos(\omega_0 t) + E_2(t)\sin(\omega_0 t) \\ &= \left[\begin{array}{cc} \cos\omega_0 t & \sin\omega_0 t \end{array}\right] \left[\begin{array}{c} E_1(t) \\ E_2(t) \end{array}\right], \end{aligned} \tag{4.1}$$

where $E_1(t)$ and $E_2(t)$ are called *quadrature fields*, which vary on timescales much longer than that of the optical oscillation, $1/\omega_0$. The quadrature formalism replaces $E(t)$ by

$$\mathbf{E} = \left[\begin{array}{c} E_1(t) \\ E_2(t) \end{array}\right]. \tag{4.2}$$

The DC components of $E_{1,2}(t)$ can be regarded as monochromatic carrier light. In particular, carrier light with amplitude $De^{i\varphi}$ is represented as

$$De^{i\varphi} \Leftrightarrow \left(De^{i\varphi}\right) e^{-i\omega_0 t} \Leftrightarrow D \begin{pmatrix} \cos\varphi \\ \sin\varphi \end{pmatrix} . \tag{4.3}$$

AC components of $E_{1,2}(t)$, which we denote by $A_{1,2}(t)$, are called *sideband fields*, which are usually more convenient to study once transformed into the frequency domain,

$$\tilde{A}_{1,2}(\Omega) = \int_{-\infty}^{+\infty} A_{1,2}(t) e^{i\Omega t} dt \,. \tag{4.4}$$

In quantum two-photon optics, it is convenient to use a particular normalization for sideband fields:

$$A_{1,2}(t) = \sqrt{\frac{4\pi\hbar\omega_0}{\mathcal{A}c}} \int_0^{+\infty} \frac{d\Omega}{2\pi} \left[a_{1,2}(\Omega) e^{-i\Omega t} + H.c.\right] . \tag{4.5}$$

In this way, we have a convenient set of commutation relations (for $\Omega \ll \omega_0$) [31,32]:

$$[a_1, a_1'] = [a_2, a_2'] = [a_1, a_1'^{\dagger}] = [a_2, a_2'^{\dagger}] = 0 \,, \tag{4.6a}$$

$$[a_1, a_2'^{\dagger}] = -[a_2, a_1'^{\dagger}] = 2\pi i \delta(\Omega - \Omega') \,. \tag{4.6b}$$

Here we have denoted $a_{1,2} \equiv a_{1,2}(\Omega)$, $a'_{1,2} \equiv a_{1,2}(\Omega')$.

4.2.2 General prescription

As mentioned above, the presence of opto-mechanical coupling dictates that we propagate the upper and lower sidebands simultaneously, which means that for each frequency Ω, we have to work with the two-dimensional linear space spanned by the upper $[a(\omega_0 + \Omega)]$ and lower $[a(\omega_0 - \Omega)]$ sidebands [1]. Within the *two-photon formalism*, developed by Schumaker and Caves [31,32], and outlined above, instead of $a(\omega_0 \pm \Omega)$, the two *quadrature fields* $a_{1,2}(\Omega)$

[1] Strictly speaking, we must consider the four-dimensional linear space spanned by $a(\omega_0 + \Omega)$, $a(\omega_0 - \Omega)$ and their Hermitian conjugates, $a^{\dagger}(\omega_0 + \Omega)$, $a^{\dagger}(\omega_0 - \Omega)$. However, the fact that the sideband fields are real functions in the time domain limits us to a two-dimensional subspace.

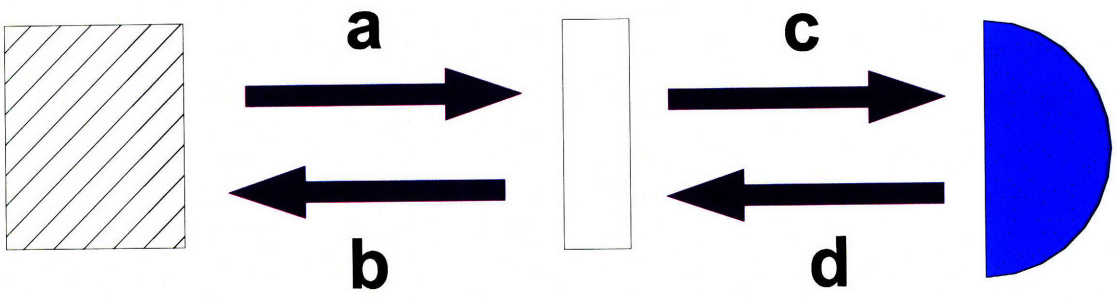

Figure 4-1: A sample configuration is shown. A beam block is connected to a mirror, which is in turn connected to a detector. Input fields incident on the mirror, **a** and **d**, are related to the output fields, **b** and **c**, by matrix operators derived in Sections 4.2, 4.3 and 4.4.

are chosen as the basis vectors. For simplicity of notation, we generally denote

$$\mathbf{a} \equiv \begin{pmatrix} a_1 \\ a_2 \end{pmatrix} \tag{4.7}$$

and suppress the dependence of **a** on Ω.

We consider optomechanical systems formed by the following elementary subsystems: movable mirrors, beamsplitters and free space propagators. We also include a "linear squeezer", which turns an ordinary vacuum state into a two-mode squeezed field with arbitrary squeeze factor and squeeze angle. Auxiliary to these optical elements, we introduce the beam block and the photodetector to deal with open ports which are either left undetected and those detected with unit quantum efficiency; we also introduce the laser as an optical element, which injects monochromatic carrier light and laser noise into the interferometer. Quadrature optical fields undergo linear transformations when propagating through such elementary systems, and quadrature fields with different Ω's propagate independently from each other. These linear transformations are described mathematically by the *input-output relation*, namely a set of equations relating the output fields to the input ones, including vacuum fluctuations, the carrier laser and laser fields, as well as to incoming GWs. We provide these input-output relations in Secs. 4.3–4.5.

However, we note that propagation of sideband quadratures ($\Omega \neq 0$), although independent from each other, all depend on the propagation of the carrier quadratures ($\Omega = 0$), i.e., the amplitude and phase of the carrier incident on each subsystem. Fortunately, the propagation of the carrier is *not* affected by that of the sidebands, and can be carried out

independently at the beginning. This said, we begin to formulate our general method of simulation.

We build the following system of linear equations (for each sideband frequency Ω)

$$\begin{bmatrix} \mathcal{M}_{11} & \cdots & \mathcal{M}_{1N} \\ \vdots & \cdots & \vdots \\ \mathcal{M}_{N1} & \cdots & \mathcal{M}_{NN} \end{bmatrix} \begin{bmatrix} \mathbf{a}^{(1)} \\ \vdots \\ \mathbf{a}^{(N)} \end{bmatrix} = \begin{bmatrix} \mathbf{u}^{(1)} \\ \vdots \\ \mathbf{u}^{(N)} \end{bmatrix}, \tag{4.8}$$

where $\mathbf{a}^{(i)}$, $i = 1, \ldots, N$ are the N quadrature fields (each of them a two-dimensional vector) propagating in every part of the system, $\mathbf{u}^{(i)}$, $i = 1, \ldots N$ are N generalized input quadrature fields (each of them again a two-dimensional vector). The $\mathcal{M}_{ij}$, $i, j = 1, \ldots N$ are 2×2 matrices which depend on the details of the optical system, and the $\mathbf{u}^{(i)}$ can be written schematically as

$$\mathbf{u}^{(i)} = \mathbf{v}^{(i)} + \mathbf{l}^{(i)} + \mathbf{H}^{(i)} h \,, \tag{4.9}$$

where $\mathbf{v}^{(i)}$ arises from vacuum fluctuations entering from the detection port or other lossy ports (Secs. 4.2.3, 4.3 and 4.4), $\mathbf{l}^{(i)}$ from the laser (Sec. 4.2.3), and $\mathbf{H}^{(i)} h$ from GW-induced phase modulation, with h the GW amplitude (Sec. 4.5); depending on the location of this generalized input field, some or all of the above three contributions could also be zero. Henceforth, we shall consider each pair of quadrature fields as one object. Inverting the matrix $\mathcal{M}_{ij}$ gives $\mathbf{a}^{(i)}$ in terms of $\mathbf{u}^{(i)}$, and hence all of the necessary transfer functions.

Now let us provide a universal prescription for constructing Eq. (4.8), suitable for modelling generic systems. We break this procedure into two steps:

1. Suppose we have n elementary subsystems mentioned above, with the k^{th} subsystem having p_k ports. The entire system then has $P \equiv \sum_{k=1}^{n} p_k$ ports. Because we formally include beam blocks and photodetectors as subsystems, none of our ports are formally open, i.e., left unconnected to some other port. This means that we have $P/2$ pairs of connections. For each pair of connections, we have two fields, one propagating in each direction. This means we have a total of P fields (each in turn has two quadrature components).

2. For each system k, with p_k ports, we also have p_k input fields and p_k output fields, and the input-output relation provides us p_k equations. All subsystems together then

provide us with P equations (each with two components), exactly the number needed.

4.2.3 Example with beam block, photodetector and a mirror

Next we illustrate the generic construction procedure with a simple example, which also clarifies the formal roles of beam blocks, photodetectors, and lasers. We first propagate fields between three basic elements of an optical train: a beam block, a partially reflecting mirror, and a photodetector. Referring to Fig. 4-1, the beam block is connected to the mirror, which is in turn connected to a detector. For simplicity, we assume that the mirror is lossless and fixed in position.

As a first step, we identify the fields in consideration. The beam block and the photodetector are 1-port systems, the mirror is a 2-port system; we have a total of 4 ports, and $4/2 = 2$ connections. There are two fields associated with each connection; we label them $\mathbf{a}$, $\mathbf{b}$, and $\mathbf{c}$, $\mathbf{d}$, respectively, as done in Fig. 4-1. Note that each field in turn has two quadrature components, so the system is 8-dimensional, and we need 8 scalar equations.

Now we have to provide the input-output relations for each object. For the mirror with amplitude reflectivity ρ and transmissivity τ, and neglecting radiation pressure effects, we have

$$\begin{pmatrix} \mathbf{b} \\ \mathbf{c} \end{pmatrix} = \begin{pmatrix} -\rho & \tau \\ \tau & \rho \end{pmatrix} \begin{pmatrix} \mathbf{a} \\ \mathbf{d} \end{pmatrix} \equiv \mathbf{M}_{\mathrm{Mir}} \begin{pmatrix} \mathbf{a} \\ \mathbf{d} \end{pmatrix}. \tag{4.10}$$

Note that Eq. (4.10) contains 4 scalar equations, and that ρ and τ are really 2×2 scalar matrices, $\rho\mathbf{I}$, and $\tau\mathbf{I}$ (this is true because our mirror does not mix quadratures) — we have suppressed the identity matrix $\mathbf{I}$ for simplicity. To comply with the format of Eq. (4.8), we write

$$\begin{pmatrix} -\rho & -1 & 0 & \tau \\ \tau & 0 & -1 & \rho \end{pmatrix} \begin{pmatrix} \mathbf{a} \\ \mathbf{b} \\ \mathbf{c} \\ \mathbf{d} \end{pmatrix} = \begin{pmatrix} 0 \\ 0 \end{pmatrix}. \tag{4.11}$$

The photodetector and beam block simply act as as source of vacuum fluctuations (independent from the input fields):

$$\mathbf{a} = \mathbf{v}^{(1)}, \qquad \mathbf{d} = \mathbf{v}^{(2)}, \tag{4.12}$$

Here we assume implicitly that the photodetector is detecting the field $\mathbf{c}$ with unit quantum efficiency. In order to model imperfect photodetectors, we could add a mirror with zero reflectivity and non-zero loss in front of the ideal photodetector.

Combining Eqs. (4.11) and (4.12), we have

$$\underbrace{\begin{pmatrix} -1 & 0 & 0 & 0 \\ -\rho & -1 & 0 & \tau \\ \tau & 0 & -1 & \rho \\ 0 & 0 & 0 & -1 \end{pmatrix}}_{\mathcal{M}} \begin{pmatrix} \mathbf{a} \\ \mathbf{b} \\ \mathbf{c} \\ \mathbf{d} \end{pmatrix} = \begin{pmatrix} -\mathbf{v}^{(1)} \\ 0 \\ 0 \\ -\mathbf{v}^{(2)} \end{pmatrix}, \tag{4.13}$$

which are the 8 scalar equations we need. Inverting $\mathcal{M}$ gives us each of the propagating fields in terms of the input vacuum fields.

Now suppose the beam block is replaced by a laser source, coupled to the spatial mode of $\mathbf{a}$ field, then we only need to replace the vacuum field $\mathbf{v}^{(1)}$ in Eqs. (4.12) and (4.13) by the laser field, $\mathbf{l}^{(1)}$: at $\Omega = 0$, carrier quadratures, while at $\Omega \neq 0$, it gives the laser noises.

Here we note that all diagonal elements of $\mathcal{M}$ are equal to -1 — this is in fact not a coincidence, but a universal feature of our construction procedure. In order to understand this, we need to realize that every field $\mathbf{a}^{(k)}$ is the output field of exactly one subsystem. In the input-output relation of that unique subsystem, there is exactly one line that relates $\mathbf{a}^{(k)}$ to the input fields of this subsystem, which reads:

$$\mathbf{a}^{(k)} = [\text{terms not involving } \mathbf{a}^{(k)}]\,. \tag{4.14}$$

This equation corresponds to, after moving $\mathbf{a}^{(k)}$ to the right-hand side of the equation, moving any non-$\mathbf{a}^{(j)}$, $j = 1, \ldots, N$ terms to the left-hand side, and swapping left and right,

$$\begin{pmatrix} \cdots & \underbrace{-1}_{k^{\text{th}}\text{ column}} & \cdots \end{pmatrix} \begin{pmatrix} \mathbf{a}^{(1)} \\ \vdots \\ \mathbf{a}^{(k)} \\ \vdots \\ \mathbf{a}^{(N)} \end{pmatrix} = \ldots . \tag{4.15}$$

It is obvious that the lines of equation found by this way for different $\mathbf{a}^{(k)}$'s are different. As a consequence, we can arrange to have the line corresponding to $\mathbf{a}^{(k)}$ appear on the k^{th} row of $\mathcal{M}$, and thus have all its diagonal elements equal to -1.

4.3 Matrices for static optical elements

In this section, we derive the matrices for some standard objects used in simulating quantum noise in a GW interferometer. Here we neglect radiation pressure effects and the presence of GWs (they are dealt with in Secs. 4.4 and 4.5, respectively). As a consequence, our derivation only involves some re-formatting of previously well-known results.

4.3.1 Mirrors

Field transformations due to a mirror were introduced in the example of Section 4.2. The transformation matrix for a lossless mirror is given in Eq. (4.10). We now derive more complete equations for the mirror that include losses. We ascribe a power loss A to the mirror in Fig. 4-1 such that $\rho^2 + \tau^2 + A = 1$. The introduction of losses gives rise to an additional vacuum field of amplitude $\sqrt{A/(1-A)}$ that is added to each input of the mirror. The $(1-A)^{-1}$ factor accounts for part of the loss field being lost to the mirror. This can be verified by having shot-noise-limited fields, $\mathbf{a}$ and $\mathbf{d}$, incident on the mirror. The field returning to the beam block

$$-\rho\left(\mathbf{a}+\sqrt{\frac{A}{1-A}}\mathbf{v}^{(3)}\right)+\tau\left(\mathbf{d}+\sqrt{\frac{A}{1-A}}\mathbf{v}^{(4)}\right) \tag{4.16}$$

must also be at the shot noise level, such that

$$\rho^2\left(1+\frac{A}{1-A}\right)+\tau^2\left(1+\frac{A}{1-A}\right)=\frac{1-A}{1-A}=1. \tag{4.17}$$

The new equations governing the mirror are

$$\begin{pmatrix}\mathbf{b}\\ \mathbf{c}\end{pmatrix}=\begin{pmatrix}-\rho & \tau\\ \tau & \rho\end{pmatrix}\begin{pmatrix}\mathbf{a}+\sqrt{\frac{A}{1-A}}\mathbf{v}^{(3)}\\ \mathbf{d}+\sqrt{\frac{A}{1-A}}\mathbf{v}^{(4)}\end{pmatrix} \tag{4.18}$$

where $\mathbf{v}^{(3)}$ and $\mathbf{v}^{(4)}$ are the vacuum fluctuations that enter due to the presence of loss.

Figure 4-2: The fields entering and exiting a region of free space are shown. Propagation operators are characterized by the propagation distance (and orientation relative to the source polarization, in the case of the GW signal).

Equation (4.18) may be rewritten as

$$\begin{pmatrix} \mathbf{b} \\ \mathbf{c} \end{pmatrix} = \begin{pmatrix} -\rho & \tau \\ \tau & \rho \end{pmatrix} \begin{pmatrix} \mathbf{a} \\ \mathbf{d} \end{pmatrix} + \sqrt{A} \begin{pmatrix} \mathbf{v}^{(3)\prime} \\ \mathbf{v}^{(4)\prime} \end{pmatrix}, \tag{4.19}$$

where

$$\mathbf{v}^{(3)\prime} \equiv \sqrt{\frac{1}{1-A}} \left(-\rho\, \mathbf{v}^{(3)} + \tau\, \mathbf{v}^{(4)} \right) \tag{4.20}$$

$$\mathbf{v}^{(4)\prime} \equiv \sqrt{\frac{1}{1-A}} \left(\tau\, \mathbf{v}^{(3)} + \rho\, \mathbf{v}^{(4)} \right). \tag{4.21}$$

$\mathbf{v}^{(3)\prime}$ and $\mathbf{v}^{(4)\prime}$ are uncorrelated vacuum fields in this representation. We can subsequently write the mirror's contribution to Eq. (4.8) as

$$\begin{pmatrix} -\rho & -1 & 0 & \tau \\ \tau & 0 & -1 & \rho \end{pmatrix} \begin{pmatrix} \mathbf{a} \\ \mathbf{b} \\ \mathbf{c} \\ \mathbf{d} \end{pmatrix} = \begin{pmatrix} -\sqrt{A}\mathbf{v}^{(3)\prime} \\ -\sqrt{A}\mathbf{v}^{(4)\prime} \end{pmatrix}. \tag{4.22}$$

This method may also be used to inject losses in beamsplitters or cavities.

4.3.2 Free space propagation

Since optical cavities are present in virtually all optical configurations of GW interferometers, we must give a transformation matrix for them as an element of our arbitrary optical

train. To do so we introduce an operator to transform the field as it propagates through free space between any two other optical elements (in the case of an optical cavity, these would be mirrors). Using the convention of Fig. 4-2, the matrix for propagation through a length L transforms input fields $\mathbf{a}$ and $\mathbf{d}$ according to

$$\begin{pmatrix} \mathbf{b} \\ \mathbf{c} \end{pmatrix} = \mathbf{M}_{\mathrm{Prop}} \begin{pmatrix} \mathbf{a} \\ \mathbf{d} \end{pmatrix} \tag{4.23}$$

where the matrix for the propagator is

$$\mathbf{M}_{\mathrm{Prop}} \equiv e^{i\phi} \begin{pmatrix} 0 & \mathbf{R}_{\Theta} \\ \mathbf{R}_{\Theta} & 0 \end{pmatrix}. \tag{4.24}$$

Here

$$\Theta \equiv \frac{\omega_0 L}{c}, \tag{4.25}$$

$$\phi \equiv \frac{\Omega L}{c}, \tag{4.26}$$

are the one-way phase shift on the carrier light at frequency, ω_0, and on modulation sidebands at frequency, Ω, respectively, and

$$\mathbf{R}_{\Theta} \equiv \begin{pmatrix} \cos\Theta & -\sin\Theta \\ \sin\Theta & \cos\Theta \end{pmatrix} \tag{4.27}$$

is the rotation operator on quadrature fields.

4.3.3 Beamsplitters

Another essential optical element of an interferometer is the beamsplitter. We consider a beamsplitter with amplitude reflectivity and transmissivity, ρ and τ, respectively. The beamsplitter transforms the input fields, shown in Figure 4-3, according to the matrix equation

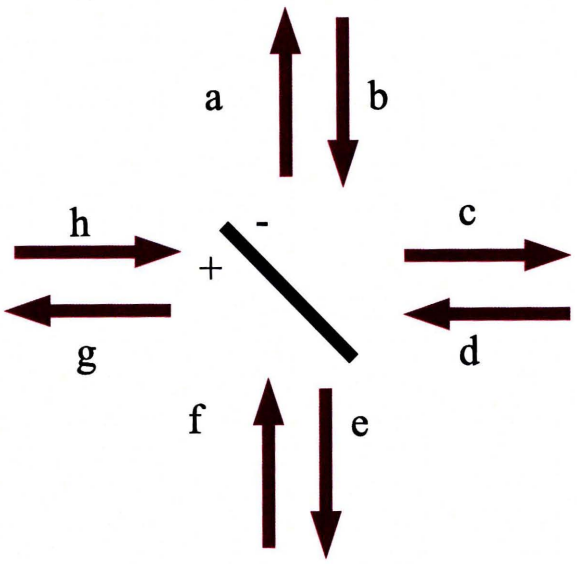

Figure 4-3: Treating the beamsplitter as a four-port device, definitions for the fields, including sign conventions, are shown.

$$\begin{pmatrix} \mathbf{a} \\ \mathbf{c} \\ \mathbf{e} \\ \mathbf{g} \end{pmatrix} = \mathbf{M}_{BS} \begin{pmatrix} \mathbf{d} \\ \mathbf{b} \\ \mathbf{h} \\ \mathbf{f} \end{pmatrix} \tag{4.28}$$

where

$$\mathbf{M}_{BS} \equiv \begin{pmatrix} -\rho & 0 & 0 & \tau \\ 0 & -\rho & \tau & 0 \\ 0 & \tau & \rho & 0 \\ \tau & 0 & 0 & \rho \end{pmatrix}. \tag{4.29}$$

In presence of optical loss, assuming $\rho^2+\tau^2+A=1$, and going through similar arguments to Sec. 4.3.1, we simply add a column vector of vacuum fields $-\sqrt{A}\mathbf{v}^{(i)}$ $(i=1,2,3,4)$ onto the right-hand side of Eq. (4.28).

4.3.4 Correlators

The correlator module of the simulation allows for the inclusion of squeezed light or vacuum fields in the interferometer. It is essentially a one-way device: only fields entering from one direction are transformed; fields entering from the other direction pass through the correlator unmodified. Taking **a** to be the input field, the field at the output of the correlator, **b**, is defined by

$$\mathbf{b} = \mathbf{S}(r, \phi)\, \mathbf{a}, \tag{4.30}$$

where $\mathbf{S}(r, \phi)$ is the squeeze operator with squeeze factor r and squeeze angle ϕ:

$$\mathbf{S}(r, \phi) \equiv \begin{pmatrix} \cosh r + \sinh r \cos 2\phi & \sinh r \sin 2\phi \\ \sinh r \sin 2\phi & \cosh r - \sinh r \cos 2\phi \end{pmatrix}. \tag{4.31}$$

4.4 Radiation pressure

Sideband quadrature fields create amplitude modulations to the carrier field, and the associated power modulation drives the motion of optical elements, which, in turn, phase modulates the carrier, thereby creating sideband quadrature fields. Details of this sideband-to-sideband conversion depend on the phases (this determines which quadrature gets converted into which) and amplitudes (this determines the conversion strength) of the carrier field propagating in different parts of the interferometer. Therefore, it is necessary to separate the fields into carrier ($\Omega = 0$) and sideband ($\Omega \neq 0$) components at this point. The radiation pressure force due to the carrier field itself is a time independent force and can be ignored (in reality they are balanced by a static force exerted on the optical elements, e.g., the pendulum restoring force on a suspended mirror). The effect of interest is the time-dependent part of the force, due to sideband components, which is the subject of this section. As a foundation, we must first of all calculate the phase and amplitude of the carrier fields at each location. But this we can already do by building the general equation (4.8) out of input-output relations of static optical elements, which have already been derived in Sec. 4.3, and solving it.

Before incorporating radiation pressure into the treatment of specific systems, let us study the electromagnetic momentum flux carried by optical fields in the two-photon for-

malism. In quadrature representation, we decompose the total quadrature field $\mathbf{E}_j^{\text{total}}$ (here $\mathbf{E}_j$ can be **a**, **b**, **c** or **d** for the configuration in Fig. 4-1) into the following two terms:

$$\mathbf{E}_j^{\text{total}} = \mathbf{E}_j^{\text{carrier}} + \mathbf{E}_j^{\text{sb}} \,. \tag{4.32}$$

The monochromatic carrier field in Eq. (4.32) can be written more explicitly in terms of power I_j, phase θ_j and effective beam area $\mathcal{A}$ as

$$\mathbf{E}_j^{\text{carrier}} = \sqrt{\frac{8\pi I_j}{\mathcal{A}c}} \begin{pmatrix} \cos\theta_j \\ \sin\theta_j \end{pmatrix}, \tag{4.33}$$

while the sideband field can be written as an integral over all sideband frequencies:

$$\mathbf{E}_j^{\text{sb}}(t) = \sqrt{\frac{4\pi\hbar\omega_0}{\mathcal{A}c}} \int_0^{+\infty} \frac{d\Omega}{2\pi} \Big[\mathbf{j}(\Omega) e^{-i\Omega t} + H.c.\Big]. \tag{4.34}$$

The total momentum flow carried by the field is

$$\frac{\mathcal{A}}{4\pi} \left(\mathbf{E}_j^{\text{carrier}} + \mathbf{E}_j^{\text{sb}}\right)^2 . \tag{4.35}$$

Removing the static (dc) and optical frequency (ω_0) components, the Fourier transform of the time-averaged (over a time scale much shorter than the GW period, but much longer than $1/\omega_0$) AC momentum flow carried by this field is

$$\dot{P}_j(\Omega) = \sqrt{\frac{\hbar\omega_0}{c^2}} \mathbf{D}_j^T \mathbf{j}(\Omega) \,, \tag{4.36}$$

where we have defined

$$\mathbf{D}_j \equiv \sqrt{\frac{\mathcal{A}c}{4\pi}}\, \mathbf{E}_j^{\text{carrier}} = \sqrt{2I_j} \begin{pmatrix} \cos\theta_j \\ \sin\theta_j \end{pmatrix} \tag{4.37}$$

as the carrier quadrature field, and $\mathbf{j}(\Omega)$ is the sideband component at angular frequency Ω.

In the remainder of this Section we derive explicit input-output relations for mirrors and beamsplitters, including radiation pressure effects. Our results are more general than previously obtained results by allowing the carrier fields incident from different ports to

have different phases.

4.4.1 Mirrors

Let us once again consider the mirror in Fig. 4-1. Assuming that the mirror behaves as a free particle with mass M when no radiation-pressure forces are exerted (valid for suspended mirrors when frequencies greater than the pendulum resonant frequency are considered), the Fourier transform for the equation of motion for the mirror is

$$-M\Omega^2 X = \sum_j \eta_j \dot{P}_j \tag{4.38}$$

where X is the displacement of the mirror *induced by all the sideband fields* (X is positive to the left in Fig. 4-1, and the j refer to $\mathbf{a}, \mathbf{b}, \mathbf{c}, \mathbf{d}$). The summation is performed over all the fields entering and exiting the mirror; the coefficients $\eta_a = \eta_b = -1$ and $\eta_c = \eta_d = 1$ account for the directions of propagation. The displacement of the mirror due to the radiation pressure forces, X, can be written explicitly as [see Eq. (4.36)]

$$X = \frac{1}{M\Omega^2}\sqrt{\frac{\hbar\omega_0}{c^2}} \left[\begin{pmatrix} \mathbf{D}_a^T & -\mathbf{D}_d^T \end{pmatrix} \begin{pmatrix} \mathbf{a} \\ \mathbf{d} \end{pmatrix} + \begin{pmatrix} \mathbf{D}_b^T & -\mathbf{D}_c^T \end{pmatrix} \begin{pmatrix} \mathbf{b} \\ \mathbf{c} \end{pmatrix} \right]. \tag{4.39}$$

Given a (time-dependent) displacement $X(t)$ of the mirror, the input-output relation can be written as (if $\dot{X} \ll c$)

$$E_b^{\text{total}}(t) = -\rho E_a^{\text{total}}\left[t + \frac{2X(t)}{c}\right] + \tau E_d^{\text{total}}(t) \tag{4.40a}$$

$$E_c^{\text{total}}(t) = \tau E_a^{\text{total}}(t) + \rho E_d^{\text{total}}\left[t - \frac{2X(t)}{c}\right]. \tag{4.40b}$$

c in the argument of E_j^{total} for the j-th field is the speed of light and should be distinguished from c in the subscript of E_j^{total}, which refers to the field $\mathbf{c}$. In quadrature representation,

to leading order in X and in the sideband field amplitudes, we have,

$$\begin{aligned} & E_j^{\text{total}}\left[t \mp \frac{2X(t)}{c}\right] \\ \Leftrightarrow \quad & \mathbf{E}_j^{\text{carrier}} + \mathbf{E}_j^{\text{sb}}(t) \pm \frac{2\omega_0 X(t)}{c}\mathbf{R}_{\Theta=\pi/2}\mathbf{E}_j^{\text{carrier}}, \\ = \quad & \mathbf{E}_j^{\text{carrier}} + \mathbf{E}_j^{\text{sb}}(t) \mp \frac{2\omega_0 X(t)}{c}\left[\mathbf{E}_j^{\text{carrier}}\right]^* . \end{aligned} \tag{4.41}$$

Here * refers to a rotation by $\pi/2$, as described by $-\mathbf{R}_{\Theta=\pi/2}$ in Eq. (4.41). Accordingly, for any quadrature field $\mathbf{v}$, we define

$$\mathbf{v}^* \equiv \begin{pmatrix} v_2 \\ -v_1 \end{pmatrix}, \quad \text{for } \mathbf{v} = \begin{pmatrix} v_1 \\ v_2 \end{pmatrix}. \tag{4.42}$$

Equation (4.41) implies that time delays, or phase modulations, create sideband quadratures orthogonal to the carrier, as illustrated in terms of phasors in Fig. 4-4. The sideband part, i.e., the AC components in Eqs. (4.40a) and (4.40b), can be obtained using Eq. (4.41):

$$\begin{pmatrix} \mathbf{b} \\ \mathbf{c} \end{pmatrix} = \mathbf{M}_{\text{mirror}} \begin{pmatrix} \mathbf{a} \\ \mathbf{d} \end{pmatrix} - \frac{2\rho\omega_0 X}{c\sqrt{\hbar\omega_0}} \begin{pmatrix} \mathbf{D}_a^* \\ \mathbf{D}_d^* \end{pmatrix}. \tag{4.43}$$

Inserting Eq. (4.39) into Eq. (4.43) gives

$$\begin{aligned} & \left[\mathbf{I} + \Pi \begin{pmatrix} \mathbf{D}_a^* \\ \mathbf{D}_d^* \end{pmatrix} \begin{pmatrix} \mathbf{D}_b^T & -\mathbf{D}_c^T \end{pmatrix}\right] \begin{bmatrix} \mathbf{b} \\ \mathbf{c} \end{bmatrix} \\ = \quad & \left[\mathbf{M}_{\text{mirror}} - \Pi \begin{pmatrix} \mathbf{D}_a^* \\ \mathbf{D}_d^* \end{pmatrix} \begin{pmatrix} \mathbf{D}_a^T & -\mathbf{D}_d^T \end{pmatrix}\right] \begin{bmatrix} \mathbf{a} \\ \mathbf{d} \end{bmatrix}. \end{aligned} \tag{4.44}$$

where

$$\Pi \equiv \frac{2\rho\omega_0}{M\Omega^2 c^2} \tag{4.45}$$

is a quantity with units of inverse power or W^{-1}. [For lossy mirrors with $\rho^2 + \tau^2 + A = 1$, we simply insert a column vector $-\sqrt{A}\mathbf{v}^{(i)}$, $i = 1, 2$ onto the right-hand sides of Eq. (4.43) and (4.44), Cf. Sec. 4.3.1.]

To solve for $\mathbf{b}$ and $\mathbf{c}$, the matrix on the left hand side of Eq. (4.44) must be inverted. It

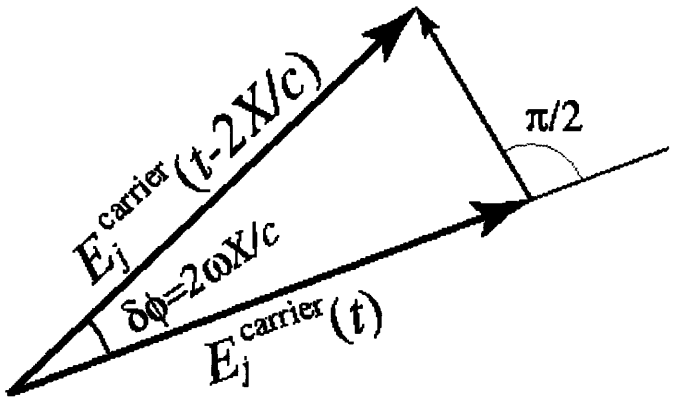

Figure 4-4: Here we show that the phase modulation sideband generated by the radiation pressure force is perpendicular to the carrier field, which is why the generated signal has a $\mathbf{D}^*$ dependence.

is straightforward to find a complete set of eigenvectors for this matrix, they are:

$$[\xi_1, \xi_2, \xi_3, \xi_4] = \left[\begin{pmatrix} \mathbf{D}_b^* \\ 0 \end{pmatrix}, \begin{pmatrix} 0 \\ \mathbf{D}_c^* \end{pmatrix}, \begin{pmatrix} \mathbf{D}_c \\ \mathbf{D}_b \end{pmatrix}, \begin{pmatrix} \mathbf{D}_a^* \\ \mathbf{D}_d^* \end{pmatrix} \right] . \tag{4.46}$$

Since the first three vectors are orthogonal to $\begin{pmatrix} \mathbf{D}_b^T & -\mathbf{D}_c^T \end{pmatrix}$, the three corresponding eigenvalues are $\lambda_1 = \lambda_2 = \lambda_3 = 1$; the last eigenvalue is

$$\begin{aligned} \lambda_4 &= 1 + \Pi \left[\mathbf{D}_b^T \mathbf{D}_a^* - \mathbf{D}_c^T \mathbf{D}_d^* \right] \\ &= 1 + 2\tau \Pi \mathbf{D}_d^T \mathbf{D}_a^* \\ &= 1 + \frac{8\rho\tau\omega_0 \sqrt{I_a I_d}}{M\Omega^2 c^2} \sin(\theta_a - \theta_d) . \end{aligned} \tag{4.47}$$

Inverting the eigenvalue λ_4 yields a pair of resonant frequencies at

$$\pm\Omega_{\mathrm{M}} = \pm \left[\frac{-8\rho\tau\omega_0 \sqrt{I_a I_d}}{M c^2} \sin(\theta_a - \theta_d) \right]^{1/2} . \tag{4.48}$$

Physically, this resonance comes about because the sideband fields generated by mirror motion can exert radiation pressure back onto the mirror. Let us for a moment consider classical motion of the mirror. As was mentioned after Eq. (4.43), for any given input carrier field, the sideband field generated upon reflection from the moving mirror is $\pi/2$ phase shifted relative to the input carrier, so the sideband does not beat with the reflected

carrier to induce any force on the mirror [see Eq. (4.36)] — force can only be induced by beating this motion-induced sideband field with the transmitted carrier, which must have non-zero amplitude and must have a phase difference other than $\pi/2$ relative to the sideband. This explains why the resonant frequency vanishes if either $\rho = 0$ or $\tau = 0$ (no reflected or transmitted field), or if $\theta_a - \theta_d = N\pi$ (no phase difference between the two input fields).

When the two input carrier fields, $\mathbf{D}_a$ and $\mathbf{D}_d$, have the same phase (or differ by $N\pi$), the phasors corresponding to $\mathbf{D}_a$, $\mathbf{D}_b$, $\mathbf{D}_c$ and $\mathbf{D}_d$ all become parallel to each other. This is true for almost all interferometers that have been treated explicitly analytically. This case is rather special from a mathematical point of view, since the matrix we are inverting does *not* have a complete set of eigenvectors. Fortunately, the inverse is just

$$\begin{aligned} &\left[\mathbf{I} + \Pi \begin{pmatrix} \mathbf{D}_a^* \\ \mathbf{D}_d^* \end{pmatrix} \begin{pmatrix} \mathbf{D}_b^T & -\mathbf{D}_c^T \end{pmatrix}\right]^{-1} \\ = &\left[\mathbf{I} - \Pi \begin{pmatrix} \mathbf{D}_a^* \\ \mathbf{D}_d^* \end{pmatrix} \begin{pmatrix} \mathbf{D}_b^T & -\mathbf{D}_c^T \end{pmatrix}\right], \quad \text{if } \mathbf{D}_a \parallel \mathbf{D}_d; \end{aligned} \tag{4.49}$$

since

$$\left[\begin{pmatrix} \mathbf{D}_a^* \\ \mathbf{D}_d^* \end{pmatrix} \begin{pmatrix} \mathbf{D}_b^T & -\mathbf{D}_c^T \end{pmatrix}\right]^2 = 0, \quad \text{if } \mathbf{D}_a \parallel \mathbf{D}_d. \tag{4.50}$$

(This identity originates from the fact that the sideband field is orthogonal to the carrier field about which it is generated.) Using this fact, we can further simplify the input-output relation to

$$\begin{pmatrix} \mathbf{b} \\ \mathbf{c} \end{pmatrix} = \left[\mathbf{M}_{\text{mirror}} - 2\rho\Pi \begin{pmatrix} \mathbf{D}_a^* \\ \mathbf{D}_d^* \end{pmatrix} \begin{pmatrix} \mathbf{D}_a^T & -\mathbf{D}_d^T \end{pmatrix} \begin{pmatrix} \rho & -\tau \\ \tau & \rho \end{pmatrix}\right] \begin{pmatrix} \mathbf{a} \\ \mathbf{d} \end{pmatrix}, \quad \text{if } \mathbf{D}_a \parallel \mathbf{D}_d. \tag{4.51}$$

[Here for simplicity we have assumed the mirror to be lossless.] In practice, although Eq. (4.44) does not give the output fields $\mathbf{b}$ and $\mathbf{c}$ explicitly in terms of the input fields $\mathbf{a}$ and $\mathbf{d}$, it can be incorporated to the matrix $\mathcal{M}$ (and into $\mathbf{u}^{(i)}$, in presence of optical losses) without any trouble [cf. Eq. (4.8)]: its inversion takes place *automatically* when $\mathcal{M}^{-1}$ is

calculated. [However, doing so makes it impossible to have -1 all along the diagonal of $\mathcal{M}$.] Alternatively, the variable X may be added to our system of variables, with Eq. (4.39) providing the additional equation necessary. The equations governing a mirror may then be replaced with Eq. (4.43) to include the dependence on X. In this way, the -1 diagonal components are preserved, without the need to invert additional matrices.

4.4.2 Beamsplitter

Referring to the fields shown in Fig. 4-3, the displacement due to radiation pressure on a beamsplitter (normal to its reflective face) is

$$X_{\mathrm{N}} = \frac{X_x + X_y}{\sqrt{2}} = \frac{1}{M\Omega^2}\sqrt{\frac{\hbar\omega_0}{2c^2}} \times$$

$$\left[\begin{pmatrix} \mathbf{D}_a^T & \mathbf{D}_c^T & -\mathbf{D}_e^T & -\mathbf{D}_g^T \end{pmatrix} \begin{pmatrix} \mathbf{a} \\ \mathbf{c} \\ \mathbf{e} \\ \mathbf{g} \end{pmatrix} + \begin{pmatrix} \mathbf{D}_d^T & \mathbf{D}_b^T & -\mathbf{D}_h^T & -\mathbf{D}_f^T \end{pmatrix} \begin{pmatrix} \mathbf{d} \\ \mathbf{b} \\ \mathbf{h} \\ \mathbf{f} \end{pmatrix} \right]. \tag{4.52}$$

where X_x is the displacement along the x-axis and X_y is the displacement along the y-axis. Similar to the case of a cavity mirror, this motion induces phase fluctuations on the impinging fields upon reflection, and introduces additional terms in the input-output relation. Following a procedure similar to the one with which we obtain Eq. (4.43), we get

$$\begin{pmatrix} \mathbf{a} \\ \mathbf{c} \\ \mathbf{e} \\ \mathbf{g} \end{pmatrix} = \mathbf{M}_{\mathrm{BS}} \begin{pmatrix} \mathbf{d} \\ \mathbf{b} \\ \mathbf{h} \\ \mathbf{f} \end{pmatrix} - \frac{\sqrt{2}\rho\omega_0 X_{\mathrm{N}}}{c\sqrt{\hbar\omega_0}} \begin{pmatrix} \mathbf{D}_d^* \\ \mathbf{D}_b^* \\ \mathbf{D}_h^* \\ \mathbf{D}_f^* \end{pmatrix}. \tag{4.53}$$

Inserting Eq. (4.52) into Eq. (4.53) gives

$$\left[\mathbf{I}+\frac{\Pi}{2}\begin{pmatrix}\mathbf{D}_d^*\\ \mathbf{D}_b^*\\ \mathbf{D}_h^*\\ \mathbf{D}_f^*\end{pmatrix}\begin{pmatrix}\mathbf{D}_a^T & \mathbf{D}_c^T & -\mathbf{D}_e^T & -\mathbf{D}_g^T\end{pmatrix}\right]\begin{pmatrix}\mathbf{a}\\ \mathbf{c}\\ \mathbf{e}\\ \mathbf{g}\end{pmatrix}=$$

$$\left[\mathbf{M}_{\mathrm{BS}}-\frac{\Pi}{2}\begin{pmatrix}\mathbf{D}_d^*\\ \mathbf{D}_b^*\\ \mathbf{D}_h^*\\ \mathbf{D}_f^*\end{pmatrix}\begin{pmatrix}\mathbf{D}_d^T & \mathbf{D}_b^T & -\mathbf{D}_h^T & -\mathbf{D}_f^T\end{pmatrix}\right]\begin{pmatrix}\mathbf{d}\\ \mathbf{b}\\ \mathbf{h}\\ \mathbf{f}\end{pmatrix} \tag{4.54}$$

Equation (4.54) is quite similar in nature to Eq. (4.44); optical losses can also be incorporated in a similar fashion, by adding $-\sqrt{A}\mathbf{v}^{(i)}$, $i=1,2,3,4$ on to its right-hand side, where $\rho^2+\tau^2+A=1$. Again, in the generic case where

$$\begin{pmatrix}\mathbf{D}_a^T & \mathbf{D}_c^T & -\mathbf{D}_e^T & -\mathbf{D}_g^T\end{pmatrix}\begin{pmatrix}\mathbf{D}_d^*\\ \mathbf{D}_b^*\\ \mathbf{D}_h^*\\ \mathbf{D}_f^*\end{pmatrix}\neq 0\,, \tag{4.55}$$

the matrix on the LHS of Eq. (4.54) has eight linearly independent eigenvectors, of which seven have unit eigenvalue, while the eighth has

$$\begin{aligned}\lambda_8 &= 1+\frac{\Pi}{2}\begin{pmatrix}\mathbf{D}_a^T & \mathbf{D}_c^T & -\mathbf{D}_e^T & -\mathbf{D}_g^T\end{pmatrix}\begin{pmatrix}\mathbf{D}_d^*\\ \mathbf{D}_b^*\\ \mathbf{D}_h^*\\ \mathbf{D}_f^*\end{pmatrix}\\ &= 1+\tau\Pi(\mathbf{D}_f^T\mathbf{D}_d^*+\mathbf{D}_h^T\mathbf{D}_b^*)\\ &= 1+\frac{4\rho\tau\omega_0}{M\Omega^2c^2}\left[\sqrt{I_fI_d}\sin(\theta_f-\theta_d)+\sqrt{I_hI_b}\sin(\theta_h-\theta_b)\right]\,,\end{aligned} \tag{4.56}$$

which corresponds to an opto-mechanical resonance at angular frequency

$$\pm\Omega_{\mathrm{BS}} = \pm\left\{-\frac{4\rho\tau\omega_0}{Mc^2}\left[\sqrt{I_hI_b}\sin(\theta_h-\theta_b)+\sqrt{I_fI_d}\sin(\theta_f-\theta_d)\right]\right\}^{1/2}. \tag{4.57}$$

In the special case of

$$\begin{pmatrix} \mathbf{D}_a^T & \mathbf{D}_c^T & -\mathbf{D}_e^T & -\mathbf{D}_g^T \end{pmatrix} \begin{pmatrix} \mathbf{D}_d^* \\ \mathbf{D}_b^* \\ \mathbf{D}_h^* \\ \mathbf{D}_f^* \end{pmatrix} = 0\,, \tag{4.58}$$

i.e., all input carrier fields are in phase with each other (modulo π) we get

$$\begin{pmatrix} \mathbf{a} \\ \mathbf{c} \\ \mathbf{e} \\ \mathbf{g} \end{pmatrix} = \left[\mathbf{M}_{\mathrm{BS}} - \rho \mathrm{II} \begin{pmatrix} \mathbf{D}_d^* \\ \mathbf{D}_b^* \\ \mathbf{D}_h^* \\ \mathbf{D}_f^* \end{pmatrix} \begin{pmatrix} \mathbf{D}_d^T & \mathbf{D}_b^T & -\mathbf{D}_h^T & -\mathbf{D}_f^T \end{pmatrix} \begin{pmatrix} \rho & & & -\tau \\ & \rho & -\tau & \\ & \tau & \rho & \\ \tau & & & \rho \end{pmatrix} \right] \begin{pmatrix} \mathbf{d} \\ \mathbf{b} \\ \mathbf{h} \\ \mathbf{f} \end{pmatrix}, \quad \text{if } \mathbf{D}_b \parallel \mathbf{D}_d \parallel \mathbf{D}_f \parallel \mathbf{D}_h\,. \tag{4.59}$$

For simplicity, we assume the beamsplitter to be lossless in the above equation. This is particularly true for the *beamsplitter* in Michelson- and Sagnac-type GW interferometers [29]. Similar to the case of the mirror, for the purposes of simulation, we incorporate the position of the beamsplitter as an additional variable in $\mathcal{M}$, in order to preserve the -1 diagonal elements and to avoid the inversion of additional matrices.

4.5 Gravitational wave signal and the output field

4.5.1 Gravitational wave contribution

In our set of optical elements, only optical cavities have significant propagation distances, so we model the effect of GWs by introducing a phase shift to the carrier light as it passes through a cavity. To calculate the propagation of these fields, all that must be done is to add a source term in the equation governing the cavity. Referring to the fields in Fig. 4-2, the cavity field becomes

$$\begin{aligned}\mathbf{c} &= e^{i\phi}\mathbf{R}_\Theta\mathbf{a} - \eta\frac{\omega_0 L h}{2c\sqrt{\hbar\omega_0}}\mathbf{D}_c^* \\ &= \mathbf{R}_\Theta\left[e^{i\phi}\mathbf{a} - \eta\frac{\omega_0\, L\, h}{2\, c\sqrt{\hbar\,\omega_0}}\mathbf{D}_a^*\right]\end{aligned} \tag{4.60}$$

where h is the Fourier transform of the GW amplitude. An h-dependent term is also added to the equation relating $\mathbf{b}$ and $\mathbf{d}$ using $\mathbf{D}_d^*$ in place of $\mathbf{D}_a^*$. The parameter η takes values from -1 to 1 depending on the orientation of the cavity and the polarization state of the incoming GW. For example, for a linearly polarized incoming GW, and for an optimally aligned Michelson interferometer, we have $\eta = 1$ for one and -1 for the other.

It is straightforward to incorporate Eq. (4.60) into the general equation Eq. (4.8). In particular, the term containing h on RHS contributes to the GW part of the general input field $\mathbf{u}$, i.e., to the third term of Eq. (4.9), with

$$\mathbf{H} = -\eta\frac{\omega_0 L}{2c\sqrt{\hbar\omega_0}}\,\mathbf{D}_c^*, \tag{4.61}$$

4.5.2 Photodetection: signal and noise

For our purposes, the photodetector serves two roles: first, it represents an open port, from which vacuum fluctuations enter the interferometer; second, it determines the measurement point. For the former, the input-output relation of a photodetector, as it contributes to the matrix $\mathcal{M}$ and the generalized input vector $\mathbf{u}^{(i)}$, is trivial and has been discussed in Sec. 4.2.3. Here we focus on the latter. At zero frequency, there is only contribution to $\mathbf{b}$ from the carrier laser, while at non-zero sideband frequencies, the detected fields at a photodetector comprise three components: the GW signal, classical laser noise, and noise due to vacuum fluctuations in the detected mode. The outgoing field being detected, $\mathbf{b}$, has the general form [see Eqs. (4.8) and (4.9)]:

$$\begin{aligned}\mathbf{b} &= \sum_i \left[\mathcal{M}^{-1}\right]_{bi}\left[\mathbf{v}^{(i)} + \mathbf{l}^{(i)} + \mathbf{H}^{(i)}h\right] \\ &\equiv \sum_i \mathcal{T}_{bi}\left[\mathbf{v}^{(i)} + \mathbf{l}^{(i)} + \mathbf{H}^{(i)}h\right].\end{aligned} \tag{4.62}$$

The summation is performed over all fields. We note that contributions to $\mathbf{v}^{(i)}$ exist only for fields that emerge from beam blocks or lossy optical elements, those to $\mathbf{l}^{(i)}$ exist only for the field that emerges from the laser, and those to $\mathbf{H}^{(i)}$ only for fields that emerge from cavities.

We suppose homodyne detection at quadrature angle, ζ, is performed such that the measured field is

$$\mathbf{b}_\zeta = b_1 \cos\zeta + b_2 \sin\zeta. \tag{4.63}$$

For a complete simulation, ζ should be the phase of the carrier that emerges at this port. However, in theoretical studies, we could also assign another value to ζ, assuming that the local-oscillator phase is modified by some other means the simulation does not address.

For the detected field, the quantum noise spectral density is (see, e.g., Sec. III of Ref. [6])

$$\left(N_Q^2\right)_b = \sum_i \left[\begin{array}{cc} \cos\zeta & \sin\zeta \end{array}\right] \mathcal{T}_{bi} S_{\mathbf{v}_i} \mathcal{T}_{bi}^\dagger \left[\begin{array}{c} \cos\zeta \\ \sin\zeta \end{array}\right]. \tag{4.64}$$

Because $\mathbf{v}_i$ is always proportional to a vacuum field, we have used $S_{\mathbf{v}_i}$ to denote the noise spectral density which is identical for all its quadratures. Here we have added the *power* of different loss contributions, since we assume the vacuum fields to be independent to each other. In general, laser noise is neither quantum-limited, nor are the magnitudes of phase and amplitude fluctuations equal; there could also be correlations between the laser amplitude and phase noise, even as the laser field enters the system. Taking these into account, we have a laser noise spectral density of

$$\left(N_L^2\right)_b = \left[\begin{array}{cc} \cos\zeta & \sin\zeta \end{array}\right] \mathcal{T}_{bl} \mathcal{S}_L \mathcal{T}_{bl}^\dagger \left[\begin{array}{c} \cos\zeta \\ \sin\zeta \end{array}\right], \tag{4.65}$$

where l corresponds to the input laser field, and

$$\mathcal{S}_L \equiv \left[\begin{array}{cc} S_{11} & S_{12} \\ S_{12} & S_{22} \end{array}\right] \tag{4.66}$$

describes noise of the laser as it first enters the interferometer, with $S_{11(22)}$ being the noise spectral density of the first (second) quadrature, and S_{12} the cross spectral density between the two quadratures. [In the usual convention of having input laser in the first quadrature,

1 corresponds to the amplitude quadrature, hence amplitude noise, while 2 corresponds to the phase quadrature, hence phase noise.] The transfer function for the GW signal is

$$H_b \equiv \sum_i \begin{bmatrix} \cos\zeta & \sin\zeta \end{bmatrix} \mathcal{T}_{bi} \mathbf{H}^{(i)} . \tag{4.67}$$

Note that GW contributions from different parts of the system add up coherently. The displacement (strain) noise spectral density from quantum noise is then given by

$$S_h = \frac{N_Q^2 + N_L^2}{|H|^2} . \tag{4.68}$$

The mathematical formulation described in Sections 4.2 through 4.5 was encoded into a simulation program written in C++. In Appendix A we describe tests of the simulation code for a complex interferometer configuration, where the simulation results were compared with analytic calculations with excellent agreement.

4.6 Summary

The main purpose of this work was to develop a mathematical framework for the simulation of quantum fields in a complex interferometer that includes radiation pressure effects. We work in the linear regime around the operation point of this interferometer; in this regime, after adopting the Heisenberg picture of quantum mechanics, the quantum equations of motion (Heisenberg operators) of observables are identical to classical ones.

During the development of this framework, we augmented previous treatments of mirrors (and beamsplitters) by allowing the carrier phases at the four (eight) ports to be different. This extension gives rise to the optical spring effect even without detuned optical cavities.

Based on this mathematical framework, we developed a simulation code that can allow arbitrary optical topologies, and applied it to specific examples of the interferometer shown in Fig. A-1 and also one described in Chapter 5. This interferometer was shown to be capable of squeezing the vacuum modes that enter – and subsequently exit – the differential port of the beamsplitter. We introduced optical spring effects by detuning the arm cavities as a means of mitigating the detrimental effects of thermal noise. We studied not only the quantum noise, but also laser noise couplings from the symmetric (input or bright) port to the output (antisymmetric or dark) port. Good agreement was found between numerical

results given by this code and analytical ones derived independently. This agreement makes us confident that the simulation is working correctly for this rather complex interferometer.

During our study of the laser noise couplings, we found a novel method of evading the laser noise by introducing artificial but controlled asymmetries. This is crucial for the practical implementation of this interferometer, and is likely to find applications in many other experiments.

Chapter 5

Ponderomotive squeezer design

We propose an experiment to extract ponderomotive squeezing from an interferometer with high circulating power and low mass mirrors as shown in Figure 5-1. In this interferometer, optical resonances of the arm cavities are detuned from the laser frequency, creating a mechanical rigidity that dramatically suppresses displacement noises. After taking into account imperfection of optical elements, laser noise, and other technical noise consistent with existing laser and optical technologies and typical laboratory environments, we expect the output light from the interferometer to have measurable squeezing of 5 dB, with a frequency-independent squeeze angle for frequencies below 1 kHz. This design provides an experimental test of quantum-limited radiation pressure effects, which have not previously been tested. The apparatus serves as the basis for the experimental work presented in the following chapters. This chapter is adapted from Ref. [43].

5.1 Optical configuration

We begin by motivating the use of detuned cavities and optical springs for extraction of ponderomotive squeezing. We argue that the ideal configuration is to observe squeezing below the resonant frequency of the optical spring. First, consider that in the case of a suspended mass, the radiation pressure coupling constant above the suspension frequency scales as $\kappa(\Omega) \propto \Omega^{-2}$. Recall from Eq. 1.21 that in the absence of any filter cavities, the squeezed quadrature is frequency dependent. We also point out that for large κ, the squeezing is observed only a small range of quadratures (see Figure 5-2). One may show

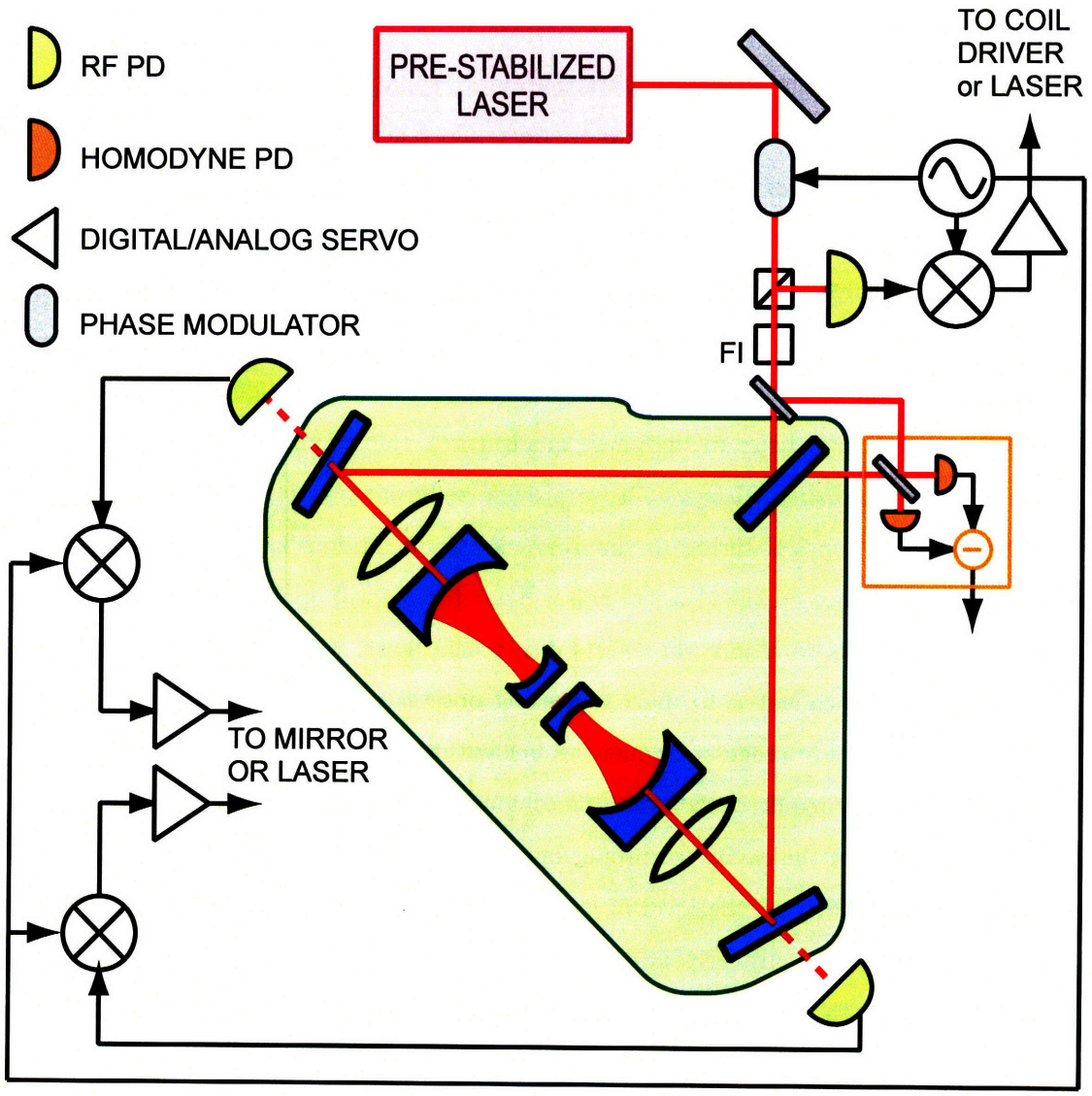

Figure 5-1: Schematic of a an interferometer designed to extract ponderomotively squeezed light due to radiation-pressure-induced motion of the low-mass end mirrors. Light from a highly amplitude- and phase-stabilized laser source is incident on the beamsplitter. High-finesse Fabry-Perot cavities in the arms of the Michelson interferometer are used to build up the carrier field incident on the end mirrors of the cavity. All interferometer components in the shaded triangle are mounted on a seismically isolated platform in vacuum. The input optical path comprises a pre-stabilized 10 Watt laser, equipped with both an intensity stabilization servo and a frequency stabilization servo. FI is a Faraday Isolator.

that sub-shot noise levels are observed over a range

$$\delta\zeta = \arctan\frac{2}{\kappa} \approx \frac{2}{\kappa}, \tag{5.1}$$

which becomes a challenging experimental hurdle for large κ. For the cavity parameters and input power presented in this Chapter, we would reach $\kappa \approx 10^3$ near 300 Hz. Ironically, more modest levels of squeezing are more easily observed than extremely large values. Furthermore, we wish to minimize the effect of classical motion of the mirror. Since this motion couples into the phase quadrature of the output, and so we must optimize the measurement quadrature to reduce the combined effect of the classical noise and the quantum noise. Figure 5-3 shows that in the regime where classical noise is significant (when classical noise exceeds shot noise in the phase quadrature), that having a large κ is desirable to having more squeezing. However, if we provide sufficient power levels to achieve large κ, but then use an optical spring to suppress the mirror motion back to a smaller κ, we reduce our dependence on the classical noise. Therefore, a stiff optical spring allows us to use high power levels to reduce the effects of classical noise, while maintaining a modest and frequency independent κ to make squeezing observable over a broad and frequency independent quadrature range at frequencies below the optical spring resonance.

Cavities typically require high levels of mechanical stability with length fluctuations less than the linewidth of the cavity for proper operation. For the cavities proposed here, this requires length stability at the level of 0.1 nm. However, to achieve low thermal noise, the mirrors are individually suspended and typically have RMS motions on the order of 1 micron (most of the motion occurs at frequencies below 10 Hz). This gap in stability is typically overcome by the use of control systems that detect and stabilize the motion in complex feedback systems. However, with a ponderomotive squeezer, one is presented with two problems: (i) if the output light is used in the feedback system, it cannot be used as a source for squeezed states; and (ii) noise introduced by the feedback destroys the squeezed state. Recall that the optical spring virtually connects the two cavity mirrors by a stiff material, which greatly reduces their relative motion, providing a useful method for overcoming the stabilization gap without the need for external feedback. The optical anti-damping does, however, require active stabilization, but this may be accomplished in a narrow frequency range around the resonance, the effects of which may be minized in the

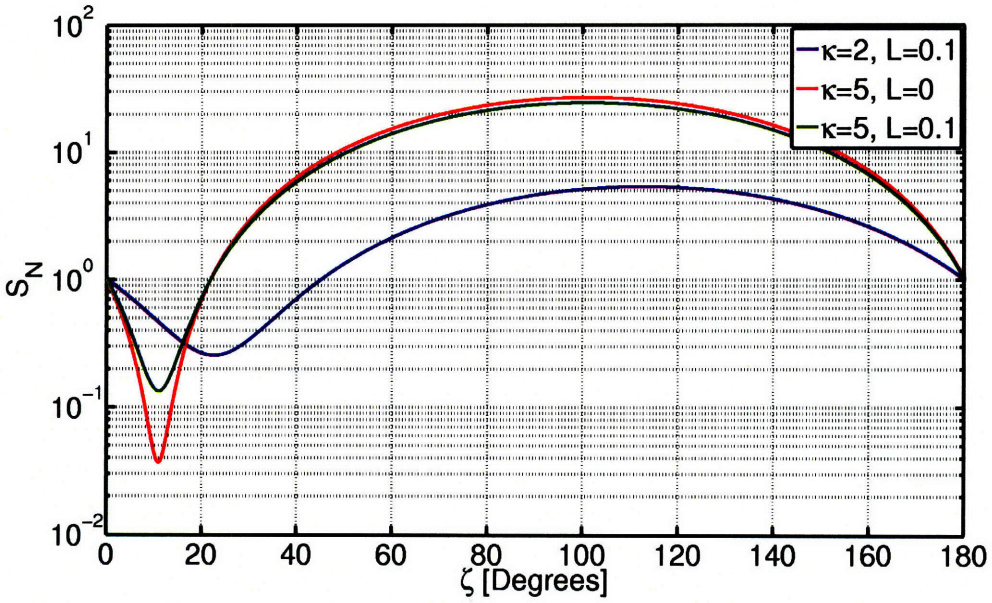

Figure 5-2: The noise of an output field of the form $b_\zeta = (\cos\zeta - \kappa\sin\zeta)a_1 + \sin\zeta a_2$ is shown, where ζ is the measurement quadrature; a_1 and a_2 are assumed to be vacuum fields, and L refers to optical loss. The range of quadratures over which squeezing is observable degrades as κ increases. Going from the blue curve to the red curve may be achieved by increasing the input power, which gives greater levels of squeezing, but over a smaller range of quadratures.

squeezing frequency band. We discuss this limitation in Section 5.3.3.

5.1.1 Quadrature coupling and squeezing

This section demonstrates the basic principles behind the ponderomotive squeezer. However, a full calculation of the vacuum states in an imperfect interferometer are prohibitive to derive here. Instead, for the calculations presented later, we rely on the simulation tool described in Chapter 4.

Assuming no external forces acting on the mirrors, and solving Eqs. 3.16 to 3.22 while allowing for non-zero **a**, one obtains

$$\mathbf{b} = \mathbf{R}(\alpha)\begin{pmatrix} 1 & 0 \\ -2\kappa(\Omega) & 1 \end{pmatrix}\mathbf{R}(\alpha)\mathbf{a}, \tag{5.2}$$

where

$$\alpha = \arctan\left(\frac{1+\rho}{1-\rho}\tan\theta\right). \tag{5.3}$$

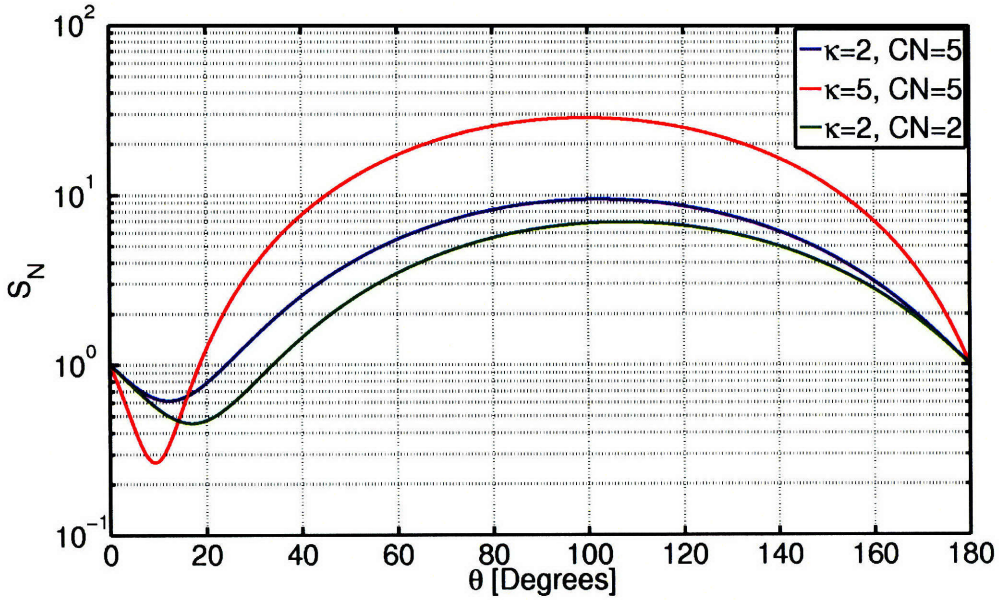

Figure 5-3: The noise of an output field of the form $b_\zeta = (\cos\zeta - \kappa\sin\zeta)a_1 + \sin\zeta a_2 + C\sin\zeta$ is shown, where ζ is the measurement quadrature, a_1 and a_2 are assumed to be vacuum fields, and C is assumed to exceed shot noise by the levels described in the legend. If one introduces the optical spring, reducing both κ and the classical noise level, squeezing over a broader quadrature range with reduced dependence on classical noise. A loss of 10% is assumed for all curves.

The rotation terms act only to rotate the quadratures and are irrelevant to our discussion of squeezing, so they are disregarded. Under the same approximations as used to obtain Eq. 3.27, and further looking only at the low frequency behavior $\Omega \ll \Theta$ where Θ is the opto-mechanical resonant frequency from Eq. 3.31, we obtain the coupling constant

$$\kappa(\Omega) = \frac{1}{\delta_\gamma}. \tag{5.4}$$

Clearly, κ couples the output amplitude and phase quadratures, and gives rise to squeezing in the output state.

In order to quantify squeezing, we look at the quadrature field measured by a homodyne detector, which is given by

$$\overline{2b(t)\cos(\omega_0 t - \Phi - \zeta)} = (A + b_1)\cos\zeta + b_2 \sin\zeta\,, \tag{5.5}$$

where ζ is the homodyne angle, with a convention in which $\zeta = 0$ corresponds to the simple amplitude detection of the output field. The fluctuating part of the output quadrature is

$$b_1 \cos\zeta + b_2 \sin\zeta = a_A[\cos\zeta - 2\kappa \sin\zeta] + a_P \sin\zeta\,, \tag{5.6}$$

with a spectral density of

$$S_\zeta(\Omega) = 1 + 2\kappa^2 - 2\kappa[\sin 2\zeta + \kappa \cos 2\zeta] \equiv \xi_\zeta^2(\Omega)\,. \tag{5.7}$$

Note that for vacuum state we have $S_\zeta(\Omega) = 1$.

By minimizing $\xi_\zeta(\Omega)$ over quadratures, we obtain the amplitude squeeze factor

$$\xi_{\min}(\Omega) = \frac{1}{|\kappa(\Omega)| + \sqrt{1 + \kappa^2(\Omega)}}\,, \tag{5.8}$$

which is achieved at

$$\zeta_{\min}(\Omega) = \frac{1}{2}\arctan\frac{1}{\kappa(\Omega)}\,. \tag{5.9}$$

We have a constant $\kappa = 1/\delta_\gamma$, which means we have a frequency independent squeezed

state. The amplitude squeeze factor and squeeze angle of this state are:

$$\xi_{\min}\left[\Omega \ll |\Theta|\right] = \frac{|\delta_\gamma|}{1+\sqrt{\delta_\gamma^2+1}}, \tag{5.10}$$

$$\zeta_{\min}\left[\Omega \ll |\Theta|\right] = \frac{1}{2}\arctan\delta_\gamma\,. \tag{5.11}$$

Consequently, we obtain a frequency-independent ponderomotively squeezed source with squeeze factor $\xi_{\min}$ (which depends only on the detuning parameter δ_γ), and bandwidth Θ. Although the squeeze factor $\xi_{\min}$ can be lowered indefinitely by taking $\delta_\gamma \to 0$, the bandwidth Θ also drops in this process as we reduce the magnitude of the optical spring.

As discussed in the introduction, such a squeezed state can be transformed into frequency dependent squeezed states by optical filters [6,28,29,44,45]. Technically, the independence in frequency makes it easier to reduce laser noise, allowing broad-band squeezing, as we shall discuss in Section 5.3.4; it also simplifies our readout scheme.

5.1.2 Radiation-pressure-driven instabilities

The quasistatic approximation we used in this section cannot describe the ponderomotive damping associated with optical rigidity. Recall from Eq. 3.27 that the full optical spring constant is given by

$$K(s) = -K_0\,\frac{1}{(1+i\Omega_\gamma)^2+\delta_\gamma^2}, \tag{5.12}$$

where

$$K_0 = \frac{4\omega_0 I_0\,\delta_\gamma}{c^2}\left[\frac{4}{T}\,\frac{1}{1+\delta_\gamma^2}\right]^2, \tag{5.13}$$

The effects of the damping force associated with the imaginary component of the optical spring is usually evident in two ways. The first is that the center-of-mass motion of the mirrors, already frequency shifted by the optical spring, is made dynamically unstable as a result of the anti-damping force. Approximating Eq. 5.12, one may show that for $\Omega_\gamma \ll 1$, which is usually valid for the optical spring, that the damping is given by

$$\Gamma \approx \frac{2\Theta^2}{\gamma\,(1+\delta_\gamma)^2}. \tag{5.14}$$

The optical spring instability can be suppressed by a narrowband feedback system acting in a restricted band around Θ, while leaving the frequency band of interest $\Omega \ll \Theta$ uncontrolled. The control system for suppressing this instability is detailed in Section 5.3.3.

High circulating power in the detuned cavities, coupled with high quality factor mechanical modes of the mirrors, may give rise to another type of radiation-pressure induced instability [47]. The internal modes of the mirrors, while very stiff, have very small damping rates due to their high Q's. The small damping rates can potentially be overwhelmed by the optical anti-damping detailed above, leading to these modes becoming unstable. This instability, which has been experimentally observed and characterized for the acoustic modes of the input mirror of our experiment [48], is well outside the bandwidth of the proposed squeezing experiment, and stabilizing it with a narrowband velocity damping loop has little effect on the experiment. The modes of the end mirror are likely to be too high in frequency (compared to the cavity linewidth) to become unstable.

Radiation-pressure-induced torques can also lead to angular instability. Fabry-Perot cavities with suspended mirrors are susceptible to a dynamical tilt instability [49]: as the cavity mirrors tilt, the beam spots also walk away from the center of the mirrors, which induces a torque that drives the mirrors further away. This effect is considered in detail in Section 5.2.1.

5.1.3 Optical losses

When a cavity with non-zero losses is considered, the noise spectrum at the ζ quadrature becomes

$$S_\zeta^{\text{loss}}(\Omega) = \frac{\mathcal{T}_I\, S_\zeta(\Omega) + \mathcal{A}}{\mathcal{T}_I + \mathcal{A}}, \tag{5.15}$$

where $S_\zeta(\Omega)$ is the lossless noise spectrum of Eq. (5.7), and $\mathcal{A}$ is the total loss per bounce in the cavity. Assuming that $\mathcal{A}/\mathcal{T}_I \ll \xi_{\text{min}}$ and $\mathcal{A} \ll \mathcal{T}_I$, we have

$$\xi_{\text{min}}^{\text{loss}}(\Omega) \approx \xi_{\text{min}}(\Omega) + \frac{\mathcal{A}}{2\,\mathcal{T}_I}. \tag{5.16}$$

With the parameters assumed in Table 5.2, we expect optical losses to be a significant limitation, but we do not expect that they will preclude the observation of squeezing.

5.2 Experimental design

In this section we describe the optical and mechanical design of a realistic experimental apparatus capable of producing observable ponderomotive squeezing. The interferometer configuration shown in Fig. 5-1 is the baseline design for the experiment. The interferometer is similar to that used in GW detection: a Michelson interferometer with Fabry-Perot cavities in each arm. All the mirrors of the interferometer are suspended as pendulums. While squeezed light could be produced with the use of a single cavity and suspended mirror, the use of interferometry is necessary to introduce common mode rejection of the laser noise, which would otherwise mask the squeezed light. Moreover, dark fringe operation of the Michelson interferometer allows for keeping the DC power below photodetector saturation levels [1].

We consider the design features most critical to the goal of achieving measurable levels of squeezing. The optical design, described in Section 5.2.1, includes:

- A powerful input laser beam with stringent but achievable requirements on frequency and intensity stability to mitigate the effects of laser noise coupling;
- A Michelson interferometer with good contrast for common-mode rejection of laser noise at the output;
- Fabry-Perot cavities with
  - high finesse to realize the large optical power incident on the suspended mirror,
  - substantial detuning (comparable to the cavity linewidth) to create the optical spring,
  - a geometric design that mitigates the effects of radiation-pressure-induced angular instability;
- An efficient readout chain to detect the squeezing.

The mechanical design of the mirror oscillator, also crucial to the performance of the interferometer, is described in Section 5.2.5.

[1] An alternative would be to use much lower input power and much higher finesse cavities, which is generally not feasible.

Parameter	Symbol	Value	Units
Light wavelength	λ_0	1064	nm
Input mirror trans.	$\mathcal{T}_I$	8×10^{-4}	–
Input mirror mass	M_I	0.25	kg
End mirror mass	M_E	1	g
Arm cavity finesse	$\mathcal{F}$	8×10^3	–
Loss per bounce	$\mathcal{A}/2$	5×10^{-6}	–
Input power	I_0	4	W
Arm cavity detuning	δ	1.8×10^4	rad/sec
BS refl. imbalance	$\Delta_{\rm BS}$	0.01	–
Mich. phase imbalance	$\Delta\alpha_{\rm M}$		
Mich. loss imbalance	$\Delta\epsilon_{\rm M}$		
Input mirror mismatch	Δ_T	25×10^{-6}	–
Detuning mismatch	Δ_δ	10^{-6}	λ_0
Arm cavity loss mismatch	Δ_ϵ	5×10^{-6}	–
Laser intensity noise	–	10^{-8}	$\mathrm{Hz}^{-1/2}$
Laser phase noise	–	10^{-6}	–
Susp. resonant freq.	Ω_0	0.7	Hz
Susp. mech. Q	Q	10^5	–
Parallel coating loss angle	$\phi_\parallel$	4×10^{-4}	
Perpendicular coating loss angle	$\phi_\perp$	4×10^{-4}	
Substrate Young's modulus	Y	7.3×10^{10}	$\mathrm{N\,m^{-2}}$
Coating Young's modulus	Y'	1.1×10^{11}	$\mathrm{N\,m^{-2}}$
Coating thickness	d	10	μm
Beam radius	w	1	mm
Detection loss	ϵ_{det}	0.1	
Temperature	T	293	K

Table 5.1: Select interferometer parameters and the nominal values we assume for them.

5.2.1 Optical design

The optical configuration is shown in Fig. 5-1, and upper section of Table 5.1 lists the optical parameters that we assume in designing the experiment.

5.2.2 Detuned arm cavities

The optical spring is the predominant feature of the detuned arm cavity. In particular, when a cavity is detuned, the optical spring modifies the response function of the differential mode from a free mass (here we ignore the pendulum frequency) to a harmonic oscillator with resonant frequency Θ. Our frequency band of interest is $\Omega \ll \Theta$, in which the response of cavity lengths to external disturbances (e.g., driven by seismic and/or thermal forces) is suppressed by Θ^2/Ω^2, and the (ideal) output state is a frequency-independent squeezed vacuum with squeeze factor as a function of $\delta_\gamma = \delta/\gamma$ [Eq. (5.10)]. Based on this qualitative understanding, in order to obtain a substantial squeeze factor up to around 1 kHz, we need to choose an optical configuration such that Θ is at least several kHz, and δ of the same order of magnitude as γ. This lead us to a high-power, low-mass, substantially detuned arm cavity.

We have chosen to realize our optical-spring squeezer by a Michelson interferometer with Fabry-Perot cavities formed by a large, suspended mirror as the input mirror (IM), and a small, light, highly reflective mirror as the end mirror (EM). The EM is chosen to be 1 g, as light as we deem possible with current experimental techniques. We note that the optical spring could also be created with a detuned signal recycling mirror, as is done in Advanced LIGO [12], but that would require an additional mirror and optical cavity, increasing the complexity of the system. The suspensions are primarily necessary to allow the mirrors to behave as free masses in the experimental frequency band, but also have the added benefit of isolation from seismic noise. To achieve these benefits, a pendulum resonant frequency of 0.7 Hz is chosen. The arm cavities must be placed in vacuum chambers due to the high finesse and circulating power, and also to meet the length stability requirements. The mechanical design of the suspension of the end mirror is discussed in the next section.

Next we discuss the optical parameters of system. We first set an "ideal" target squeeze factor of 17 dB, i.e., the squeeze factor of the system in absence of optical losses and technical noises. This allows for the contribution of the vacuum fluctuations from the anti-symmetric

port to the total noise to be small. This determines $\delta_\gamma \approx 0.31$. As a next step, we fix the finesse of the arm cavity, which should be high because we would like to have the optical-spring resonance Θ as high as possible, for a better noise suppression. Although this could be achieved by increasing input power alone, it is much more efficient to increase the finesse, because $\Theta \propto \sqrt{I_0}/\mathcal{T}$, see Eq. (3.27), note that we need to maintain δ_γ for a fixed target squeeze factor); a higher *input power* is also undesirable because of the associated increase in amplitude and phase noise. On the other hand, cavities with too high a finesse limit the output squeeze factor through increased optical losses, and also increase the instability from the optical spring. In the end, we set the transmission of the input mirror to be 800 ppm, which, if assumed to be the dominant loss in the cavity, gives a finesse of 8×10^3. In this system, for a 4 W input laser power, we have a circulating power of roughly 9 kW, and $\Theta \approx 2\pi \times 5$ kHz.

5.2.3 Angular instability

Our discussion of the optical properties of the cavities so far has been restricted to the longitudinal resonances. In this section we consider the geometrical properties of the cavity, necessary to avoid angular instability due to radiation-pressure-induced torque [49]. For a cavity with two spherical mirrors, the equations of motion of the two mirrors are rather straightforward, if the motion frequency is much lower than the cavity bandwidth (which is trivially true in our case). Suppose $\theta_{I,E}$ are the tilt angles of two mirrors with radii of curvature $R_{I,E}$, separated by L, then the equations of motion of $\theta_{I,E}$ are given by (here and henceforth we denote IM by I and EM by E)

$$\begin{pmatrix} \ddot{\theta}_I \\ \ddot{\theta}_E \end{pmatrix} = \mathbf{M} \begin{pmatrix} \theta_I \\ \theta_E \end{pmatrix}, \tag{5.17}$$

with

$$\mathbf{M} = \frac{1}{1 - g_I g_E} \begin{pmatrix} g_E \omega_I^2 & -\omega_I^2 \\ -\omega_E^2 & g_I \omega_E^2 \end{pmatrix} - \begin{pmatrix} \omega_I^2 & \\ & \omega_E^2 \end{pmatrix}. \tag{5.18}$$

k	r (cm)	d (cm)	M_k (g)	J_k (g·cm^2)	$\omega_k/(2\pi)$ (Hz) $W = 9\,\mathrm{kW}$
IM	4.25	2.00	250	1211	0.11
EM	0.60	0.30	1.00	0.098	12.4

Table 5.2: Moments of inertia of the mirrors along their tilt axes. we model the mirrors as a cylinder with radius r and thickness T, and $J = Mr^2/4 + MT^2/12$. Circulating powers of 9 kW are assumed.

Here $\Omega_{I,E}$ are the resonant frequencies of the tilt degrees of freedom of the mirrors in the absence of radiation pressure,[2] and $g_{I,E}$ are the g-factors, defined by

$$g_k = 1 - \frac{L}{R_k}, \qquad k = I, E. \tag{5.19}$$

The angular frequencies $\omega_{I,E}$ are given by

$$\omega_k^2 \equiv \frac{2I_c L}{cJ_k}, \quad k = I, E, \tag{5.20}$$

where J_k are the moments of inertia of each mirror along the tilt axis under consideration. These frequencies set the time scales of tilt-induced dynamics associated with each mirror. In Table 5.2, we list the relevant parameters for our IM and EM, along with the resulting ω_k. Note that ω_{E} does seem to be in a regime (a few Hz) where we have to worry about tile instability. As pointed out by Sidles and Sigg [49], in the absence of external restoring forces, (i.e., as $\Omega_{I,E} \to 0$), we have

$$\det \mathbf{M} = -\omega_I^2 \omega_E^2/(1 - g_I g_E) < 0, \tag{5.21}$$

which means $\mathbf{M}$ always has one positive eigenvalue (pure instability) and one negative eigenvalue (stable resonant mode). On the other hand, the $\Omega_{I,E}$ terms, if large enough, stabilize the system.

Let us first examine the case without external restoring force. The resonant frequencies are in general given by

[2]We consider two types of tilt angles, *pitch* and *yaw*, described in Section 5.2.5 for our mirrors. In the ideal situation, pitch and yaw are orthogonal degrees of freedom and can be considered separately. The resonant frequencies of the IMs and EMs when they are "free" masses, $\Omega_{I,E}$, do, however, differ from each other, as does the pitch and yaw mode frequencies for each optic.

$$\omega_{\pm}^2 = \frac{1}{2(1-g_I g_E)}\Big[-(g_E\omega_I^2+g_I\omega_E^2) \pm\sqrt{(g_E\omega_I^2+g_I\omega_E^2)^2+4(1-g_I g_E)\omega_I^2\omega_E^2}\Big]. \tag{5.22}$$

Noticing that we have $\omega_{\rm I}^2/\omega_{\rm E}^2 \approx 8\times 10^{-5} \ll 1$, we can expand the unstable resonant frequency up to the leading order in $\omega_{\rm I}^2/\omega_{\rm E}^2$. We also have to require that $g_{\rm E}$ is not very close to 0 ($|g_{\rm E}| \gg \omega_{\rm I}^2/\omega_{\rm E}^2$). Now if we pay attention only to ω_-^2, which is the unstable resonant frequency, then we have

$$\omega_-^2 = \begin{cases} -\dfrac{g_{\rm I}\omega_{\rm E}^2}{1-g_{\rm I}g_{\rm E}} & g_{\rm I}, g_{\rm E} > 0 \\ \\ \dfrac{\omega_{\rm I}^2}{g_{\rm E}} & g_{\rm I}, g_{\rm E} < 0\,. \end{cases} \tag{5.23}$$

This confirms, in our special case, that cavities with negative g factors are less unstable, as argued by Sidles and Sigg [49]. Moreover, each mirror itself, when the other mirror is held fixed, is stable in the case of negative g-factors (since diagonal elements in $\mathbf{M}$ are both negative).

Now let us study the stability when external restoring forces are available. In general the resonant frequencies ω are given by

$$\det\left[\mathbf{M}+\omega^2\mathbf{I}\right] = 0\,. \tag{5.24}$$

The stability condition can be stated more formally as having $\mathbf{M}$ negative definite, which means requiring

$$(1-g_I g_E)\omega_I^2 - g_E\omega_I^2 > 0 \tag{5.25}$$

$$(1-g_I g_E)\omega_E^2 - g_I\omega_E^2 > 0 \tag{5.26}$$

$$\det\mathbf{M} > 0\,, \tag{5.27}$$

with

$$\begin{aligned} & \det \mathbf{M} > 0 \\ \Leftrightarrow \quad & \left[\omega_I^2 - \frac{g_E \omega_I^2}{1 - g_I g_E}\right]\left[\omega_E^2 - \frac{g_I \omega_E^2}{1 - g_I g_E}\right] > \frac{\omega_I^2 \omega_E^2}{(1 - g_I g_E)^2} \,. \end{aligned} \tag{5.28}$$

For negative g-factor cavities, which start out to be less unstable, the stabilization is easy: Eqs. (5.25) and (5.26) are automatically satisfied (since the diagonal elements are already negative in absence of external restoring force), while Eq. (5.28) can be satisfied without requiring any EM external stabilization, if

$$\Omega_{\mathrm{I}} > \omega_{\mathrm{I}} / |g_{\mathrm{I}}| \,, \tag{5.29}$$

Stabilization is less straightforward for positive g-factor cavities: $\Omega_{I,E}$ must be at least of the same order as $\omega_{I,E}$, unless we fine-tune $g_{I,E}$. For example, Eqs. (5.25) and (5.26) already impose

$$\Omega_{I,E} > \sqrt{\frac{g_{2,1}}{1 - g_1 g_E}}\, \omega_{I,E} \,, \tag{5.30}$$

which suggests that Ω_{E} must be at least comparable to ω_{E}, unless we make g_{I} very small, which is undesirable due to decreased stability of spatial optical modes. Defining

$$\Omega_{I,E}^2 = (1 + \sigma_{I,E}) \frac{g_{E,I}\, \omega_{I,E}^2}{1 - g_I g_E} \,, \quad (g_{I,E} > 0) \,, \tag{5.31}$$

the stability condition can be written as

$$\sigma_{\mathrm{I}} > 0 \,, \ \sigma_{\mathrm{E}} > 0 \,, \ \sigma_{\mathrm{I}} \sigma_{\mathrm{E}} > \frac{1}{g_I g_E} \,. \tag{5.32}$$

For stability reasons, we propose using negative g-factor cavities. To minimize the angular instability and simultaneously maximize the beam spot size at the mirrors in order to reduce the effects of the coating thermal noise, as discussed in Section 5.3.2, we propose cavities of length $L \sim 1$ m, with the mirrors having a radius of curvature slightly greater than 0.5 m, in order to have $g \sim -0.8$.

From Eq. (5.29), we find a stabilizing IM frequency of 0.12 Hz, which is trivially satisfied, to be sufficient to stabilize the system without an active control system.

5.2.4 Optical readout

Ideally, the squeezed field would be measured at the antisymmetric port with a homodyne detector. In this setup, a strong local oscillator (LO) field is mixed on a beamsplitter with the squeezed field, and the two resulting fields are measured by photodiodes and the resulting photocurrents are subtracted, eliminating the component of the signal due to the LO alone. This scheme is advantageous because it allows for an arbitrary quadrature of the squeezed field to be measured, simply by changing the phase of the LO. The disadvantage of this scheme, however, is that the LO field must be much stronger than the carrier component of the squeezed field. Due to mismatches in the system, a portion of the carrier light couples out the antisymmetric port. With the parameters for contrast defect and other optical imperfection listed in Table 5.1, we expect the carrier light at the output to be on the order of 1 mW. While a LO level that is an order of magnitude larger is readily achievable, we begin to reach the saturation limits of our photodetectors.

An alternative readout scheme is to simply measure the squeezed field with a photodetector. In this scheme, only the amplitude fluctuations of the light exiting the antisymmetric port may be measured. However, our optimization scheme for laser noise, as described in Sec 5.3.4, has the side effect of aligning the squeezed quadrature with the amplitude quadrature of the light exiting the antisymmetric port. While this limits us to measuring only the amplitude fluctuations of the light, this is precisely the quadrature in which the squeezing occurs. The homodyne readout scheme is preferable, but the direct readout is a viable alternative to avoid power constraints.

In practice, since we wish to control the interferometer degrees of freedom, we use the detection scheme shown in Fig. 5-7. A small fraction of the antisymmetric port light ($R \ll 1$ in power) is sampled to generate an error signal for the control loop, while the majority is preserved for injection into an interferometer or for detection of squeezing using either the homodyne or direct detection methods described above.

5.2.5 Mechanical design

Both the input and end mirrors of the cavities are suspended from pendulums. The input mirrors have a mass of 250 g and a 75 mm diameter; they are identical to the suspended optics used in the input modecleaner of the initial LIGO detectors [50]. Greater care must be

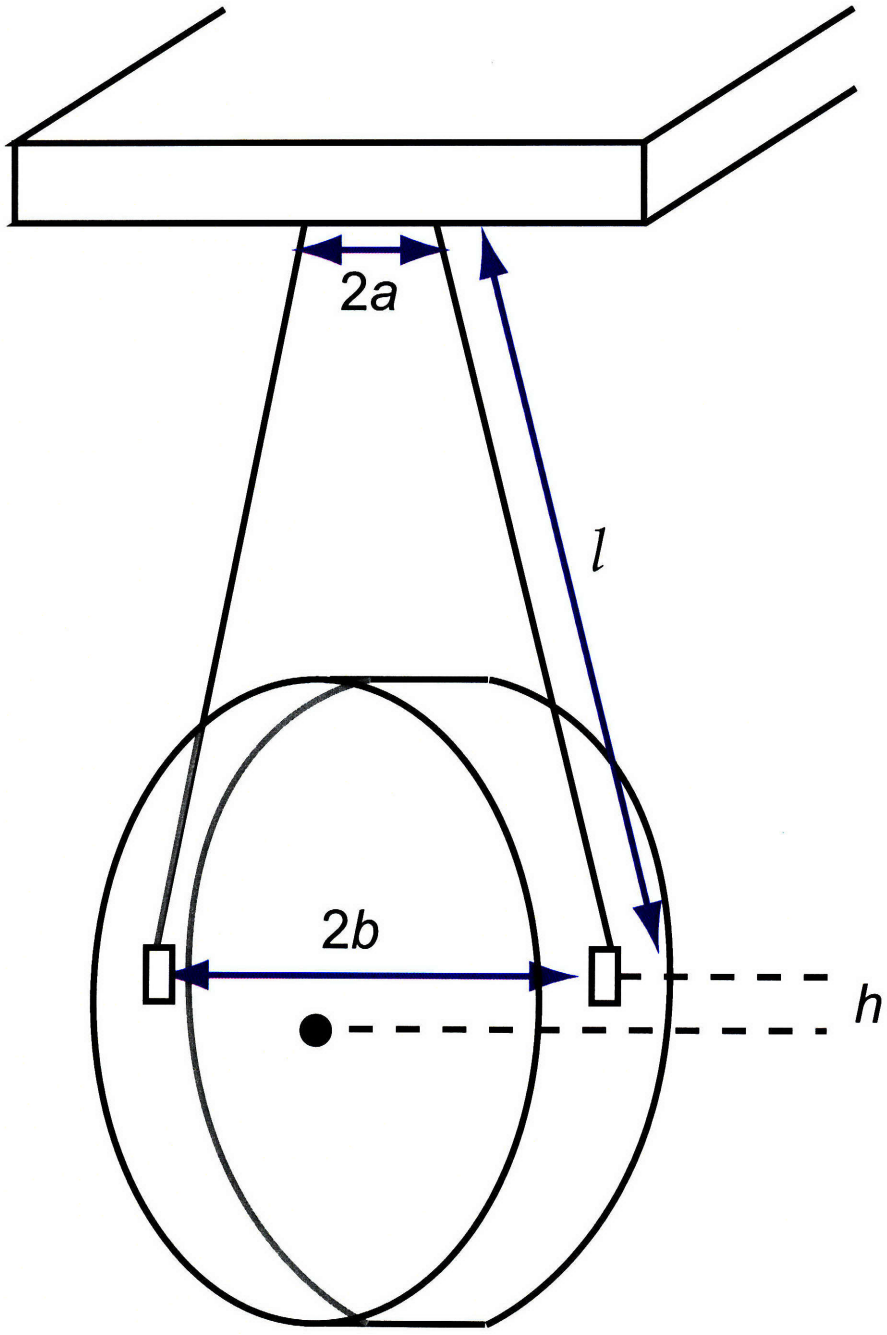

Figure 5-4: Front and side view of the end mirror suspension. The dot represents the center of mass of the mirror. The fibers are attached to a point a distance h, which could be negative, above the mirror center of mass. The distance between the attachment points at the mirror is $2b$, and at the top of the suspension is $2a$. Not drawn to scale.

taken in the suspension of the end mirrors of the cavities, however – due to their small mass of 1 g, the EMs have greater susceptibility to thermal noise. We use a monolithic fused silica suspension, in which thin fused silica fibers are welded to the side of the mirror substrate using a CO_2 laser. This technique has been demonstrated to produce a pendulum mode Q of approximately 10^7 [51]. The suspension design consists of two fibers, each approximately $10\,\mu$m in diameter, welded or glued to the mirror, as shown in Fig. 5-4.

To maintain high circulating power in the arm cavities, and minimize interference from higher-order spatial modes, alignment of the mirror is critical. Controlling the pitch (rotation about the horizontal diameter of the mirror) is a particularly important consideration, since we expect large pitch angles due to static displacement of the EM with 9 kW of laser power impinging on it. The frequency of the pitch mode is determined by the location of the attachment point between the fiber and the mirror substrate, and the diameter of the fiber [52]. For our regime of fiber lengths, typically 0.5 m, the frequency of the pitch mode frequency, is approximately

$$\omega_{pitch} = \sqrt{\frac{T\,(h+\Delta)}{J_{pitch}}}, \tag{5.33}$$

assuming $\Delta + h \ll l$, where Δ is the characteristic length at which the fiber bends above its attachment point, h is the distance of the attachment point from the mirror center of mass, l is the length of the suspension wire, T is the tension in the fiber, and J_{pitch} is the moment of inertia for the pitch degree of freedom (given in Table 5.2). A higher frequency, ω_{pitch}, requires a larger force to control the pitch of the mirror. Minimizing the necessary force, and hence $\Delta + h$ is desirable to limit the actuator range. For fibers with a diameter of $100\,\mu$m, $\Delta \approx 8.5$ mm, while for $10\,\mu$m, $\Delta \approx 8.5 \times 10^{-2}$ mm. In the $100\,\mu$m case, it would be impossible to make $\Delta + h$ smaller than a few millimeters, while for the $10\,\mu$m case, it can be made very small by choosing h appropriately. Consideration of the necessary torques that must be supplied, and the torques that may be generated by actuators, as well as the ability to create and work with thin fibers, leads to a choice of fiber diameter of approximately $10\,\mu$m. Taking $\Delta + h = 100\,\mu$m, $J_{pitch} = 0.098$ g cm^2, $T = 98$ dyne, we get $\omega_{pitch} \approx 2\pi \times 0.50$ Hz. The yaw frequency, again assuming that $\Delta + h \ll l$, is

$$\omega_{yaw} = \sqrt{\frac{2\,T\,a\,b}{l\,J_{yaw}}} \tag{5.34}$$

where $2a$ is the separation between attachment points of the fibers at the top end of the suspension, $2b$ is the distance between the attachment points on either side of the mirror, and J_{yaw} is the moment of inertia for the yaw degree of freedom. For $a = 6$ mm, $b = 3$ mm, $J_{yaw} = 0.098$ dyne, we get $\omega_{yaw} \approx 2\pi \times 0.43$ Hz.

Control of the longitudinal motion of the end mirror is a difficult task. When the 9 kW of power in the cavity is incident on the end mirror, the mirror feels a constant force, which must be balanced. We choose to balance the constant (dc) radiation pressure force with gravity. When the mirror is displaced by a few millimeters from its equilibrium (with no laser light present), for a given (fixed) pendulum length, the gravitational restoring force is equal to the constant radiation pressure force. In order to lock the cavity at full power, we propose the following scheme: First, we use an electromagnetic actuator to offset the mirror the required distance from its equilibrium position. Next, we lock the cavities with very small circulating powers, such that the radiation pressure forces are negligible. We slowly increase the power in the system, which increases the radiation pressure forces on the mirrors. Simultaneously, we reduce the pulling force of the actuator, which is counteracted by the increasing radiation pressure force, keeping the mirror at a fixed position. When the power reaches its design value, the mirror is held in place by a balance of the radiation pressure, gravitational restoring, and electromagnetic forces. This provides a way of controlling the longitudinal degree of freedom of the mirror.

5.3 Noise couplings

In this section, we estimate the contribution of expected noise sources to the total noise budget. These include thermal noise from the suspended mirrors (including thermal noise from the optical coatings on the substrates), as well as laser intensity and phase noise. In Figs. 5-5 and 5-6, we show the spectral density of the dominant noise sources both in terms of noise power relative to the vacuum level in a given quadrature, and also in terms of (free mass) displacement, which does not include the suppression from the optical spring. Furthermore, we shall see that the coupling of laser noise has a very strong dependence on the quadrature to be measured. Careful choice of the measurement quadrature is critical to successful extraction of the squeezing; this is analyzed in Section 5.3.4.

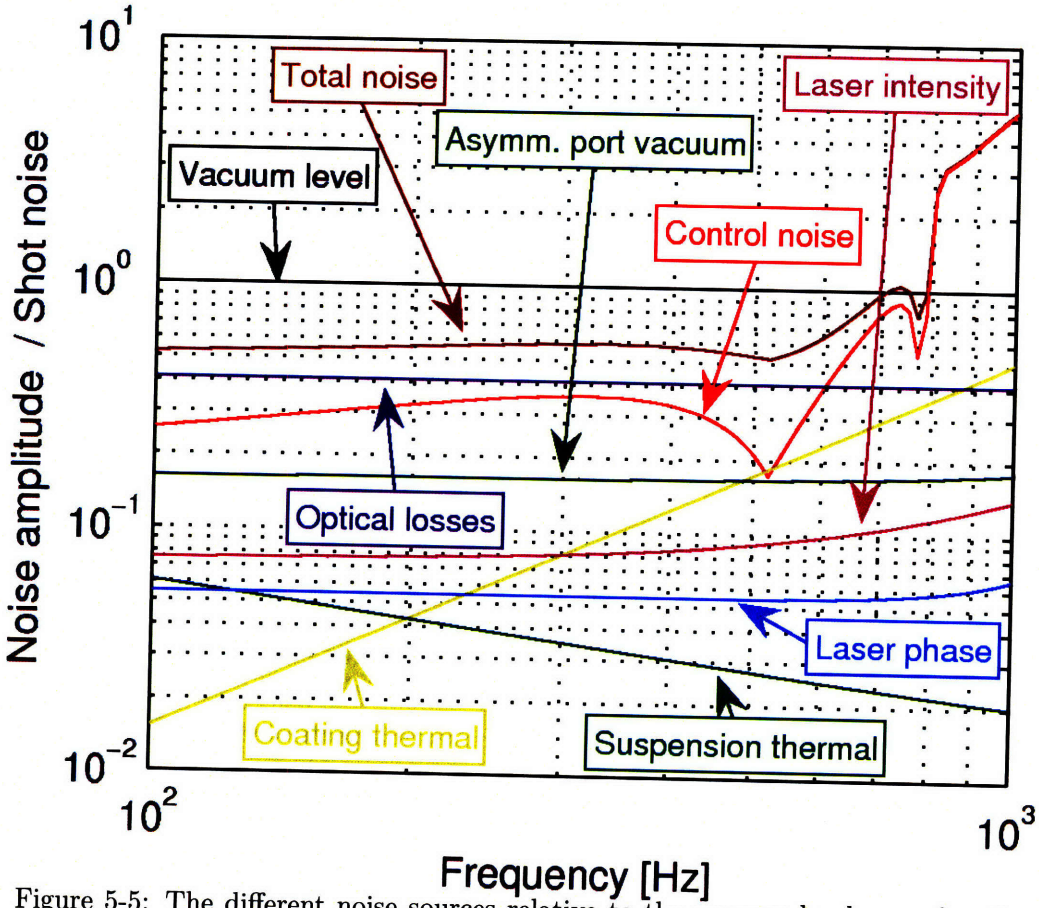

Figure 5-5: The different noise sources relative to the vacuum level, as a function of frequency. The dominant noise below 1 kHz is optical losses, which are primarily comprised of detection losses (10%) and the optimization losses (13% in one arm).

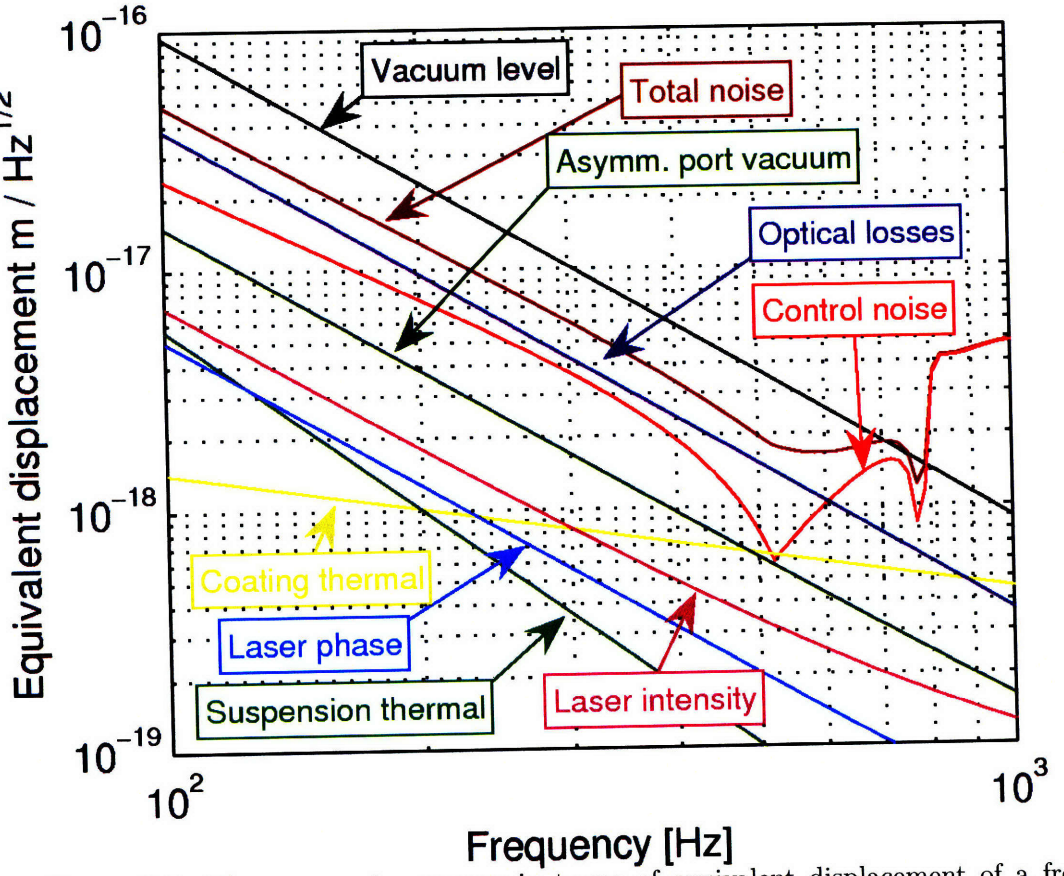

Figure 5-6: The same noise sources in terms of equivalent displacement of a free mass (the displacement noise that each noise source would exhibit if the optical spring were not present). We estimate that a sensitivity of $5 \times 10^{-16}\mathrm{m\,Hz^{-1/2}}$ is necessary to measure squeezing at 100 Hz, and the required sensitivity drops as frequency to the second power at higher frequencies.

5.3.1 Suspension thermal noise

Applying the Fluctuation Dissipation Theorem [53] to an object of mass M that is suspended from a pendulum with mechanical quality factor Q and resonant frequency Ω_R, we get the free mass displacement noise spectrum [54]

$$S_{susp}(\Omega) = \frac{4\,k_B\,T}{M\,\Omega\,Q}\frac{\Omega_R^2}{\left(\Omega_R^2-\Omega^2\right)^2+\frac{\Omega_R^4}{Q^2}}, \tag{5.35}$$

where T is the temperature and k_B is the Boltzmann constant. The monolithic fused silica suspension, described in Section 5.2.5, is used primarily to reduce ϕ. Metal wires and alternative methods of attachment have higher losses, which would make the suspension thermal noise more severe. As shown in the curve labelled "Suspension thermal" in Fig. 5-5, the monolithic fused silica suspension places the suspension thermal noise at a level where it does not have any measurable effect on the experiment.

5.3.2 Internal and coating thermal noise

The free mass displacement noise spectrum due to internal and coating thermal noise has been approximated as [55]

$$\begin{aligned} S_{ICTN}(f) = \quad & \frac{2k_BT}{\pi^{3/2}f}\frac{1}{wY}\Bigg[\phi_{substrate} \\ + \quad & \frac{d}{w\sqrt{\pi}}\left(\frac{Y'}{Y}\phi_{\parallel}+\frac{Y}{Y'}\phi_{\perp}\right)\Bigg]. \end{aligned} \tag{5.36}$$

We assume that $\phi_{substrate} \ll \frac{d}{w\sqrt{\pi}}\left(\frac{Y'}{Y}\phi_{\parallel}+\frac{Y}{Y'}\phi_{\perp}\right)$, so that the dominant thermal noise is due to the optical coating. Using the parameters listed in Table 5.1, we calculate the coating thermal noise shown in Fig. 5-5. We note that the coating thermal noise is potentially a limiting noise source near 1 kHz.

5.3.3 Control system noise

As discussed in Section 5.1.2, the optomechanical resonance is unstable, i.e., the amplitude of its oscillations grow in time. This instability must be controlled by use of a feedback loop that stabilizes the unstable resonance by a damping-like control force.

Defining $s = j\,\Omega$, the transfer function $P(s)$ of the pendulum, including the optical

spring effect, is given by

$$P(s) = \left[s^2 + \frac{\Theta^2 \gamma^2}{(\gamma + s)^2 + \delta^2} \right]^{-1} . \tag{5.37}$$

This transfer function is straightforward to interpret; it is the transfer function of an ideal spring, with a spring constant that is filtered by the cavity pole. In the limiting case that $\gamma \gg s$ and $\gamma \gg \delta$, the transfer function of an ideal pendulum is obtained. This transfer is unstable because it has poles in the right half plane (the real part of the pole is greater than 0).

To stabilize this resonance, we apply a velocity damping force via a feedback control system; a schematic for the control system is shown in Fig. 5-7. Ordinarily, we are interested in the (squeezed) output field b that exits the ponderomotive interferometer (IFO), but we need to detect a small fraction of b to generate a control signal for damping the unstable resonance. We, therefore, insert a beamsplitter (BS) at the IFO output and use the field $u = \sqrt{R}\, b$ ($R \ll 1$) in a feedback loop. The quadrature field u is converted into a force by the transfer function $F(s)$ and $Q(s)$ converts force to quadrature fields. The velocity damping term is included in $F(s)$. $Q(s)$ contains the force-to-displacement transfer function $P(s)$ [see Eqn. (5.37)], as well as the input-output relation that converts displacement to quadrature field [see e.g. Eqns. (63) and (64) of Ref. [39]]. The majority of the squeezed field, $y = \sqrt{T}\, b$, is preserved as a squeeze source. Vacuum noise fields n_0, n_{c1} and n_{c2} enter the open ports of the beamsplitter, and must be accounted for in the total noise budget.

Defining the open-loop gain of the feedback system as

$$G(s) = -\sqrt{R}\, F(s)\, Q_\zeta(s)\,, \tag{5.38}$$

the squeezed output field $\mathbf{y}$ is given by

$$\begin{aligned} y_\zeta \;=\; & \frac{\sqrt{T}\mathcal{M}_\zeta \cdot \mathbf{a}}{1 + G(s)} + \frac{Q_\zeta \sqrt{T}}{1 + G(s)}\, \mathbf{f} \\ & + \frac{T\, G(s)}{1 + G(s)} \frac{1}{\sqrt{R}}\, (n_{c1})_\zeta - \sqrt{R}\, (n_{c1})_\zeta \,, \end{aligned} \tag{5.39}$$

where $\mathcal{M}$ is a matrix operator that converts the input field $\mathbf{a}$ to the output $\mathbf{b}$, Q converts forces into quadrature fields, and the subscript ζ denotes the projection on the quadrature to be measured. Eqn. (5.39) warrants some discussion. The first term contains the squeezed

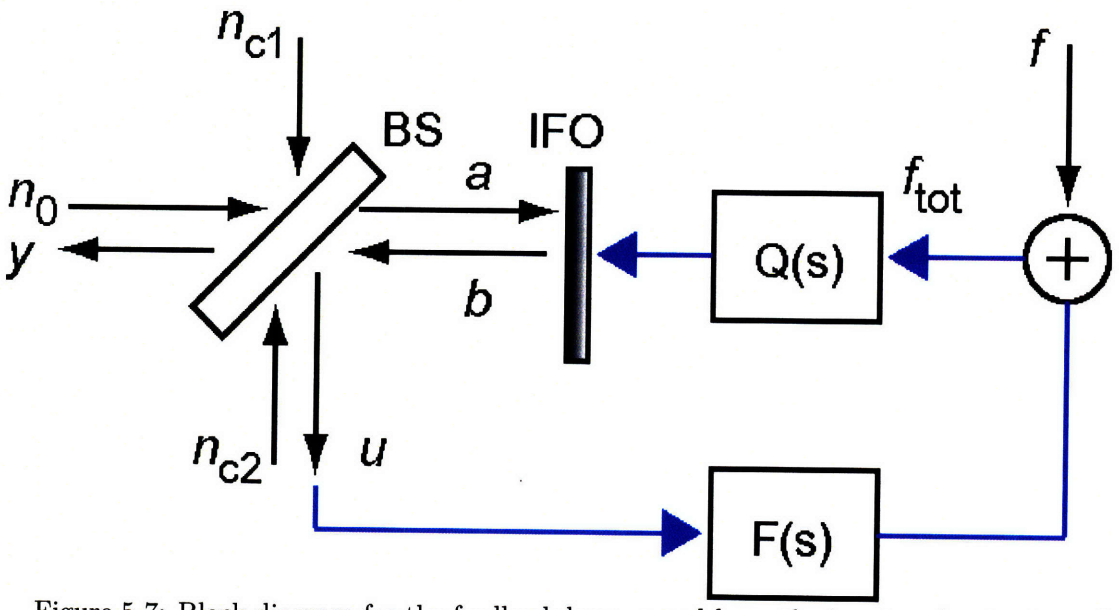

Figure 5-7: Block diagram for the feedback loop. a and b are the input and output quadrature fields; n_i are vacuum noise fields entering the different port of the beamsplitter (BS) that has power reflectivity R and transmission T. A small fraction of the output (squeezed) field $u = \sqrt{R}b$ is used to generate a shot-noise-limited error signal for a feedback loop to control the position of the differential mode of the ponderomotive interferometer (IFO), while the remainder $y = \sqrt{T}b$ is used to make sub-quantum-noise-limited measurements. The sample beam u is filtered by $F(s)$, a transfer function that converts quadrature fields into force, and $Q(s)$ converts force back into quadrature fields. f are spurious forces that act on the interferometer mirrors.

output due to the input field **a**. In order to realize the squeezing without the influence of the control system, it is necessary to make $G(s)$ as small as possible in the band where squeezing is to be measured. Similarly, when $G(s) \gg 1$, the last term dominates and R should be kept small to couple as little of the vacuum noise $(n_{c1})_\zeta$ to the output y_ζ.[3] Finally, to stabilize the optomechanical resonance, we need to introduce a damping term to $P(s)$ [implicitly included in $G(s)$]. We propose a filter transfer function that is equivalent to applying a velocity damping:

$$F = \frac{-s\gamma_d}{\sqrt{R}} \tag{5.40}$$

where γ_d is a damping constant chosen to stabilize the system. The open loop gain then becomes

$$G(s) = s\,\gamma_d \left[s^2 + \frac{\Theta^2\gamma^2}{(\gamma+s)^2 + \delta^2} \right]^{-1}, \tag{5.41}$$

In addition to stabilizing the optomechanical resonance, we must minimize the additional noise due to vacuum fluctuations that are introduced by the new beamsplitter. We consider only the newly introduced vacuum noise that is detected by the feedback detector, which is then fed back onto the position of the pendulum and thereby enters the signal detected by the squeeze detector. We neglect the correlations between these vacuum fluctuations that enter directly at the beamsplitter with those that enter through the feedback loop. This is a valid assumption for frequencies at which $|G(s)| \ll 1$, which is the case in our measurement band. Assuming that the feedback detection is shot-noise-limited, then the power spectral density of the additional noise, relative to shot noise, is

$$S_n \leq \sqrt{\left| \frac{G(s)}{1+G(s)} \right| \frac{1}{\sqrt{R}} + \sqrt{R}} \tag{5.42}$$

[see the last two terms in Eqn. (5.39), with $R \ll 1$ so that $\sqrt{1-R} \approx 1$]. Choosing 3 to 10% for the nominal value of R gives acceptable levels of loss for the squeezed output beam, while allowing for the stabilizing feedback. We note that for the case $|G(s)| > 1$, that these expressions are not valid, and a detailed calculation of the correlations must be done. The correlation between the last two terms in Eqn. (5.39) depends on the quadrature being measured to do the feedback; we assume the worst case scenario for the noise, namely that

[3] We do not combine the last two terms containing $(n_{c1})_\zeta$ because we assume that those two terms are uncorrelated. This is not true, but at worst gives an underestimation by a factor of 2 of the noise, and for the cases when $|G| \ll 1$, the error is much smaller.

the two terms add in amplitude.

In order to keep the coupling of vacuum noise n_{c1} into y_ζ at a minimum, we must make the loop gain $G(s)$ as small as possible at frequencies within the squeezing measurement band (about 100 Hz to 1 kHz), while still having sufficient gain at the optomechanical spring resonance frequency (typically 5 kHz). We achieve this by including a sharp high-pass filter in $F(s)$, typically an elliptic filter with high-pass corner frequency at several 100 Hz to preserve phase margin at the optical spring resonance. The resulting contribution to the overall noise budget is show as the curve labeled "Control noise" in Fig. 5-5, where we set $\gamma_d = 7 \times 10^4$ s^{-1}, $R = 3\%$, and a fourth-order elliptic high-pass filter with cut-off frequency at 800 Hz. A detailed analysis of the control system can be found in Ref. [56].

5.3.4 Laser noise

Laser intensity and frequency noise couple to the output port of the interferometer through imperfections and mismatch in the optical parameters of the interferometer. Analytic calculation of such noise couplings were carried out in Ref. [39]. The calculations lead to complex formulae that, in our opinion, do not provide much insight into the couplings, except the following qualitative features. For frequencies much below Θ and γ, and up to leading order of $\Theta L/c$, $\gamma L/c$ and $\delta L/c$, phase and amplitude noises both emerge in single quadratures (as a result, there exist a phase-noise-free quadrature, and an amplitude-noise-free quadrature.) The phase noise does not drive mirror motion, and emerges at the output at an orthogonal quadrature to the carrier leaking out from that port (i.e., the carrier coincides with the phase-noise-free quadrature). The amplitude noise, on the other hand, drives mirror motion, and emerges in a quadrature neither along nor orthogonal to the carrier. Different types of mismatches direct laser amplitude and phase noises into different output quadratures. Up to linear order in mismatch, the output phase (amplitude) noise can be expressed in the quadrature representation as a sum of quadrature vectors, each arising from one type of mismatch.

In full numerical results, we did not observe phase-noise-free and amplitude-noise-free quadratures, but instead found output quadratures in which contributions from one of the two laser noises has a rather deep minimum. The minimum-phase-noise and minimum-amplitude-noise quadratures do not generically agree with each other, nor do they generically agree with the minimum-quantum-noise quadrature. However, we have discovered that

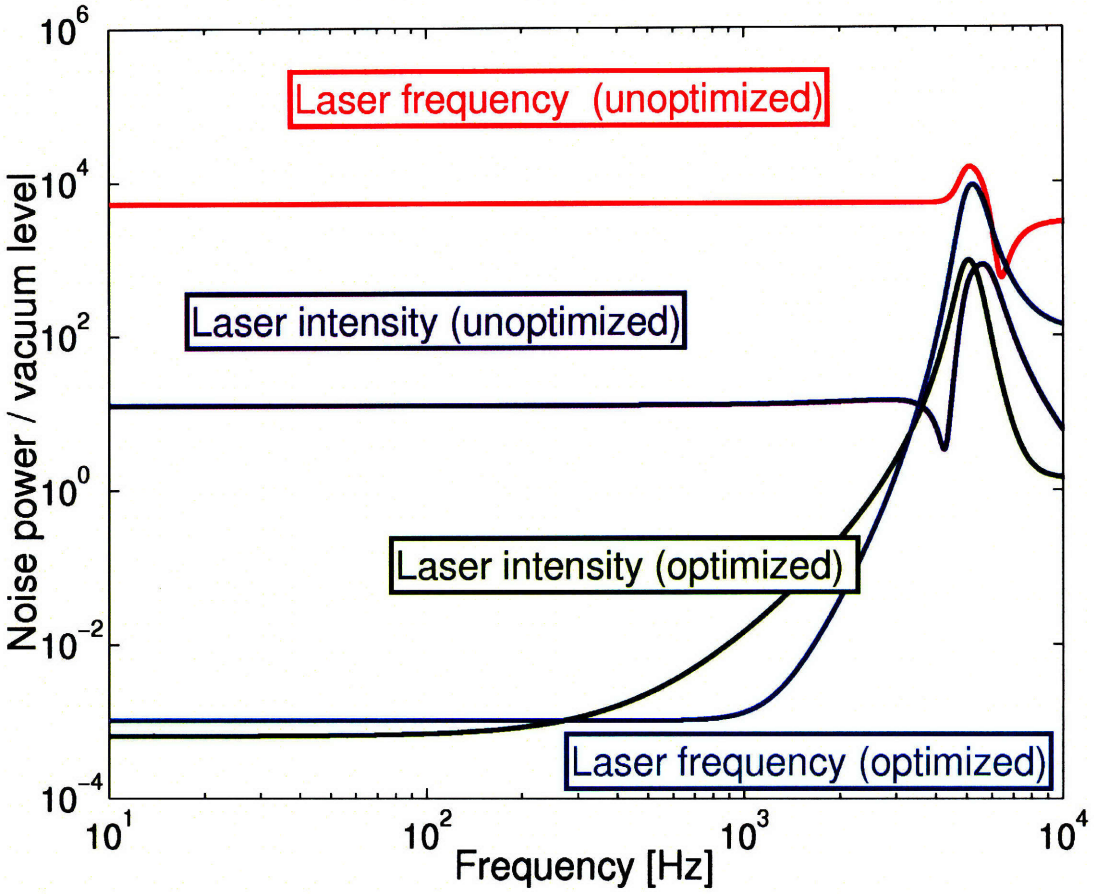

Figure 5-8: The coupling of laser noise to the antisymmetric port is shown for the unoptimized and optimized cases. The optimized case includes a Michelson detuning and intentional loss in one of the arms.

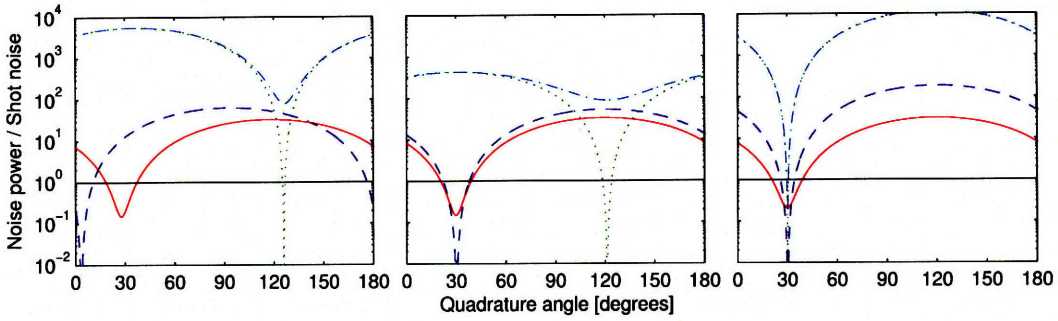

Figure 5-9: The coupling of laser and antisymmetric port noise to the output as a function of the homodyne measurement quadrature for the unoptimized case. The red curves represent the quantum optical noise, the blue curves represent laser intensity noise, the green curves represent laser phase noise and the cyan curves represent the total noise. In (a), the minimal noise quadratures for the different noise sources are not the same. In (b), the minimal noise quadratures for the laser intensity noise and the vacuum fluctuations are now the same. For this case, only a Michelson detuning has been added. In (c), the minimal noise quadratures for the laser intensity noise, laser frequency noise and the vacuum fluctuations are now the same. For this case, a Michelson detuning and a controlled loss in one arm (between the beamsplitter and the input test mass) were used.

it is possible, by intentionally introducing controlled mismatches, to modify the quadrature dependence of both of the output laser noises in such a way that both the minimum-phase-noise and minimum-amplitude-noise quadratures align with the minimum-quantum-noise quadrature. Such a procedure greatly reduces the importance of the laser noise, *as long as the noise in the minimum noise quadrature is concerned.* This is shown in Figs. 5-8 and 5-9, using our fiducial parameters in Table 5.2.

Let us describe the optimization procedure in more detail. Through the numerical simulation [39], we determine that the noise quadratures may be optimized through two steps, as shown in Fig. 5-9. The first step is to detune the Michelson from the dark fringe. The optimal position for the Michelson detuning is that which aligns the minimum-amplitude-noise quadrature to the minimum-quantum-noise quadrature. The second step is to introduce an intentional loss into one arm of the Michelson, placed artificially between the beamsplitter and one of the arm-cavity mirrors, such that both minimum-amplitude-noise and minimum-phase-noise quadratures would align with the minimum-quantum-noise quadrature. Interestingly, since the minimum-phase-noise quadrature coincides with the carrier quadrature leaking out from the output port, the resulting squeezed output light is amplitude squeezed.

As it turns out, the required artificial loss can be quite large; for our fiducial parameters in Table 5.1, the optimal loss is approximately 10%. Such a large loss noticeably limits the amount of squeezing that may be detected, but the reduction in the laser noise is necessary to measure any squeezing at all. As shown in Figs. 5-8 and 5-9, the laser amplitude noise (as measured in the squeezed quadrature) is reduced by more than 40 dB and the laser frequency noise by more than 60 dB in this process — both of them now are far below the quantum noise level.

It is difficult to predict exactly the mismatches that are present in the physical experiment. Rather than making a priori predictions for the intentional mismatch needed to optimize the noise couplings, we plan to perform this optimization empirically. We estimate that the ability to control the loss at the level of 0.1% and the detuning at the level of $10^{-4}\delta_\gamma$ is sufficient for the optimization.

Although we have greatly reduced the laser noise in the ideal quadrature, we have not reduced its overall magnitude. This presents a limitation because we must control the quadrature measurement angle to be precisely at the ideal quadrature. Small fluctuations in this measurement angle couple noise in from the orthogonal quadrature, where the noise is much larger. This is evident from the sharp features in Fig. 5-9, which shows that the margin for error in the measurement quadrature is quite narrow due to the laser frequency noise.

5.3.5 Quantum noise and losses

The quantum noise, due to output port vacuum fluctuations and optical losses, are also calculated using the noise simulation code [39]. Considering only the noise that enters through the output port, and neglecting other noise sources, including optical losses, the vacuum field is squeezed by 17 dB inside the interferometer.

Next, we include optical losses at the levels given in Table 5.1. In particular, our simulation code has automatically taken into account intracavity losses, losses due to transmission through the IMs, losses of the beamsplitter, losses into the common mode due to mismatches, and artificial losses introduced to mitigate laser noise in the detected quadrature. These together lead to a noise spectrum at the level of $\sim$ 7 dB below shot noise (see Fig. 5-5). We expect this to be the limit to measurable squeezing in most of our frequency band.

	Advantages of large value	Advantages of small value
M_E	Ease of construction Ability to sense and actuate motion	Large optical spring frequency
T_i	Large optical spring frequency	Reduce optical spring instability Reduce effective intracavity losses Higher circulating power
M_I	Ease of construction Work with existing sizes and solutions	Increase optical spring frequency [4]
I_0	Large optical spring frequency	Use available lasers Circulating power
δ_γ	Optimize $\delta_\gamma = 1/\sqrt{3}$ for largest squeezing bandwidth	Use smaller δ_γ to increase squeezing level
w	Reduce coating thermal noise	Reduce angular instability of cavity
L	For fixed beam size on mirror surfaces, longer length increases suppression of higher order spatial modes Larger mirror radii of curvature easier to manufacture	Minimize optical anti-damping

Table 5.3: Design considerations for select interferometer parameters. Here we tabulate some of the competing effects that led us to the choice of parameters listed in Table 5.1 and discussed in Sections 5.2 and 5.3.

5.3.6 Summary of design considerations

Considerations of the detailed parameters of the experiment is a sequence of trade-offs between achieving high levels of squeezing and keeping the noise couplings to a minimum. In Table 5.3 we summarize the highly intertwined and often conflicting considerations that informed the design in the preceding sections.

5.4 Summary

We have presented a design for an interferometer with movable light mirror oscillators, such that the light (and vacuum) fields circulating in the interferometer are squeezed due to the coupling of radiation pressure and motion of the mirrors. We show that even in the presence of reasonable, experimentally realizable optical losses (at the level of 10^{-5} per bounce per optic), thermal noise (associated with oscillators with intrinsic loss factors of order 10^{-7}), and classical laser noise (relative intensity noise at the level of 10^{-8} and frequency noise 10^{-4} Hz/$\sqrt{\text{Hz}}$), significant levels of squeezing can be extracted from such a device. Specifically, we find that as much as 7 dB of squeezing at 100 Hz is possible, provided great care is exerted to measure the quadrature where the laser noise coupling to the output is minimized, as shown in Fig. 5-5. We note that the squeezed state produced by this device

is far from a minimum uncertainty state (the noise in the anti-squeezed quadrature relative to the squeezed quadrature is much greater than required by Heisenberg's Uncertainty Principle). This places requirements on the stability requirements for any device to which the state is applied.

Two aspects of the design require great care: the optical performance of the high finesse, detuned arm cavities (described in Section 5.2.1); and the mechanical design of the suspended 1 gram mirror oscillators, where thermal noise must be kept at low, and pitch, yaw and longitudinal degrees of freedom must be controllable by application of external forces outside the measurement band (described in Section 5.2.5).

In the following Chapters, we describe the experimental implementation of this design, along with results from intermediate phases en route to the ultimate goal of measuring the ponderomotively squeezed output.

Chapter 6

Optomechanical experiments

We report on experimental observations of radiation-pressure induced effects in high-power optical cavities. We measure the properties of an optical spring, created by coupling of an intense laser field to the pendulum mode of a suspended mirror; and also the parametric instability (PI) that arises from the nonlinear coupling between acoustic modes of the cavity mirrors and the cavity optical mode. We also report on a stable optical trap suitable for a macroscopic mirror, wherein the dynamics of the mirror are fully dominated by radiation pressure. The technique employs two frequency-offset laser fields to simultaneously create a stiff optical restoring force and a viscous optical damping force. We show how these forces may be used to optically trap a free mass without introducing thermal noise; and we demonstrate the technique experimentally with a 1 gram mirror. The observed optical spring has an inferred Young's modulus of 1.2 TPa, 20% stiffer than diamond. The experimental work is divided into 4 parts that signify physical differences in the experiment, as described in Table 6.1. The phases of the experiment are incremental steps towards the goal of building a ponderomotive squeezer, as described in the previous chapter.

6.1 The facility

The experiments take place at the LIGO Advanced System Test Interferometer (LASTI) at MIT.

- **The laser:**

  The laser used for these experiments is of the utmost importance. It must provide

	L (m)	M (g)	Susp. Freq.	Susp. Q	Finesse	K (N/m)	$\Theta/2\pi$ (Hz)
Phase 1	1	250/2	1	10^5	1000	3×10^4	80
Phase 2	1	1/1	172	3×10^3	8000	2×10^6	5000
Phase 2.5	0.1	1/1	12.75	2×10^4	8000	4×10^4	1000
Phase 3	1	1/2	6.3	10^4	8000	5×10^5	3000

Table 6.1: Parameters for each experimental stage are given. The masses given are the reduced mass. Note that the shorter length of the cavity of Phase 2.5 dramatically increased the parametric instability of the drumhead mode of the end mirror at 100 kHz, limiting the power incident on the cavity. Phase 2.5 did not introduce any new optomechanical dynamics, so it is discussed in Chapter 7. Phase 3 was the first iteration of the experiment that implemented two cavities in an interferometer configuration.

high power levels of highly frequency and intensity stabilized light. The system used is nearly identical to the Pre-Stabilized Laser (PSL) system in use in the Initial LIGO interferometers [57]. The master-oscillator-power-amplifier (MOPA) laser, developed by Lightwave Electronics Corp., outputs approximately 8 W of continuous-wave (CW) light with wavelength of 1064 nm. The light couples through a mode cleaner with fixed mirrors that rejects light that is not in the TEM_{00} mode. The cavity is controlled through a piezo-electric element mounted on one mirror. A fraction of the transmitted light is used for intensity stabilization [58] that feeds back to the current shunt driving the laser. Another fraction passes through an acousto-optic modulator that frequency shifts the light by 160 MHz before sending it to a monolithic suspended cavity. The frequency of the laser is then stabilized to the length of this cavity. The driving signal sent to the acousto-optic modulator is provided by a voltage-controlled oscillator that may change its frequency when provided a voltage. This allows for the the bulk of the laser light, which does not pass through the acousto-optic modulator, to be tuned, while maintaining the stability provided by the suspended cavity.

- **Vacuum envelope and seismic isolation system:** The suspended-mirror cavities used in these experiments are placed within a LIGO Horizontal Access Module (HAM) chamber that is evacuated to the level of approximately 10^{-6} torr. The optics table within this chamber rests on a series of masses and springs – a vibration isolation stack that provide passive isolation from ground motion. The system also provides the capability to actively sense and stabilize the motion at the base of the stack, although this capability was not exploited until the third phase of the experiment.

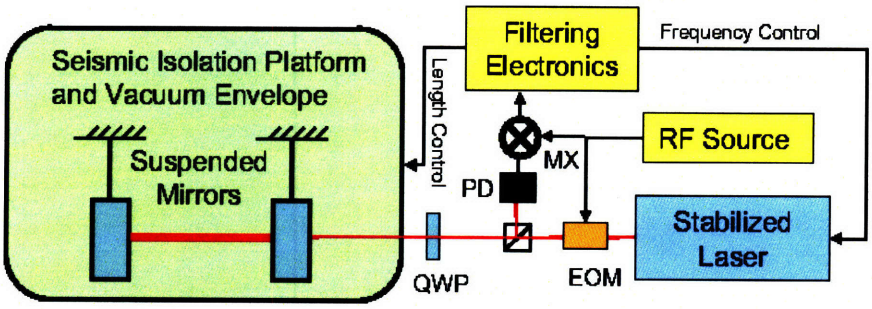

Figure 6-1: Schematic representation of the experiment, showing the 1 m long Fabry-Perot cavity suspended in vacuum. Abbreviations are acoustooptic modulator (AOM), electrooptic modulator (EOM), photodiode (PD), polarizing beam splitter (PBS), and quarter-wave plate (QWP). Most of the 10 W output of the 1064 nm Nd:YAG laser light is directed to the suspended cavity. A small fraction of is pick-off and frequency shifted by double passing through the AOM. The frequency shifted light is used to lock the laser frequency to the reference cavity resonance with high bandwidth ($>$ 500 kHz). Frequency shifting via the AOM provides a means of high speed frequency modulation of the stabilized laser output; it is an actuator for further stabilizing the laser frequency with reference to the suspended cavity. The input mirror of the cavity has a transmission of 0.63%, giving a linewidth of 75 kHz. Not shown are feedback loops actuating on the cavity length and laser frequency (via the AOM).

6.2 Phase 1 experiment

At the time of the experiment described here, the optical spring effect had been previously demonstrated on a 1.2 g mass held in a flexure mount [59]. In that experiment the mechanical resonance of the mass/flexure structure at 303 Hz was altered by 3% with the application of radiation pressure, corresponding to an optical rigidity of about 150 N/m. Optical bistability experiments had also been performed, although they were not cast in the framework of an optical spring [37]. Weak optical damping forces had also been observed previously, far below the threshold for parametric instability [36]. The results presented here appeared in Ref. [48], and were obtained nearly simultaneously with the optical spring observed at the LIGO 40 meter interferometer [60].

In the experiment performed here, 0.25 kg mirrors are suspended as pendulums with a resonant frequency of 1 Hz for the longitudinal mode (motion along the optic axis of the cavity). With detuning of the cavity, the resonance is shifted upwards by nearly 2 orders of magnitude. We also confirm the unstable nature of the resonance, and observe PI of an internal mode of the mirrors.

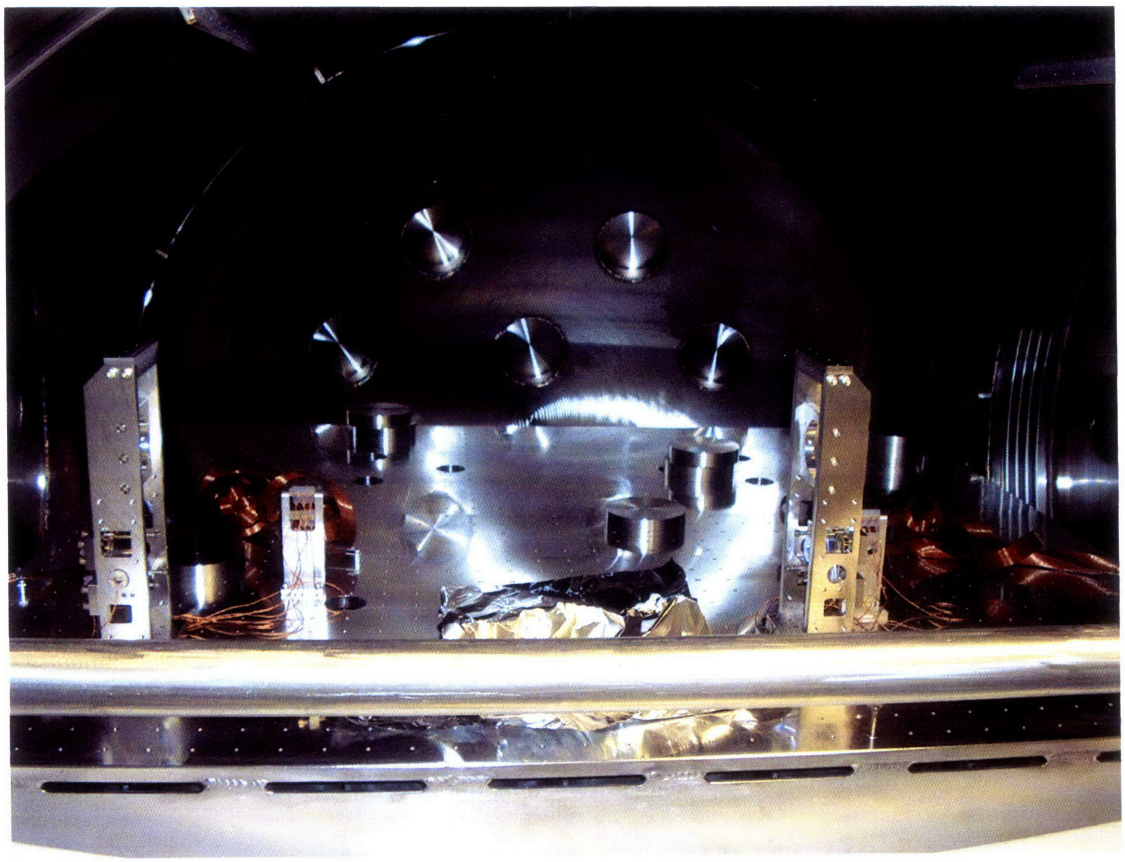

Figure 6-2: Two suspended optics located within the vacuum envelope and on the seismically isolated optical table are shown.

6.2.1 Experimental description

The experimental set-up used to observe the PI and the optomechanical rigidity is shown in Fig. 6-1. The input mirror to the cavity has a transmission of approximately $T = 0.6\%$, separated by 1 meter from the end mirror, giving a linewidth of $\gamma = 75 \times 2\pi$ kHz. The cavity mirrors are suspended as pendulums with a longitudinal resonant frequency of 1 Hz. Magnets are glued to the mirror (4 on the back surface, and 1 on each side), and devices containing both shadow sensors and coils surround each magnet. The shadow sensors consist of an LED facing a photodiode, with the magnet in between. When the mirror moves, the amount of light hitting the photodiode changes, providing a measure of the mirror's motion. Currents may be pushed through the coils to create a magnetic field that exerts a force on the mirrors via the magnets. The signals from the shadow sensors are decomposed into modes of the mirror motion (longitudinal, pitch, yaw, side-to-side), filtered, then fed back to the coils in order to damp the low frequency resonances of the suspension.

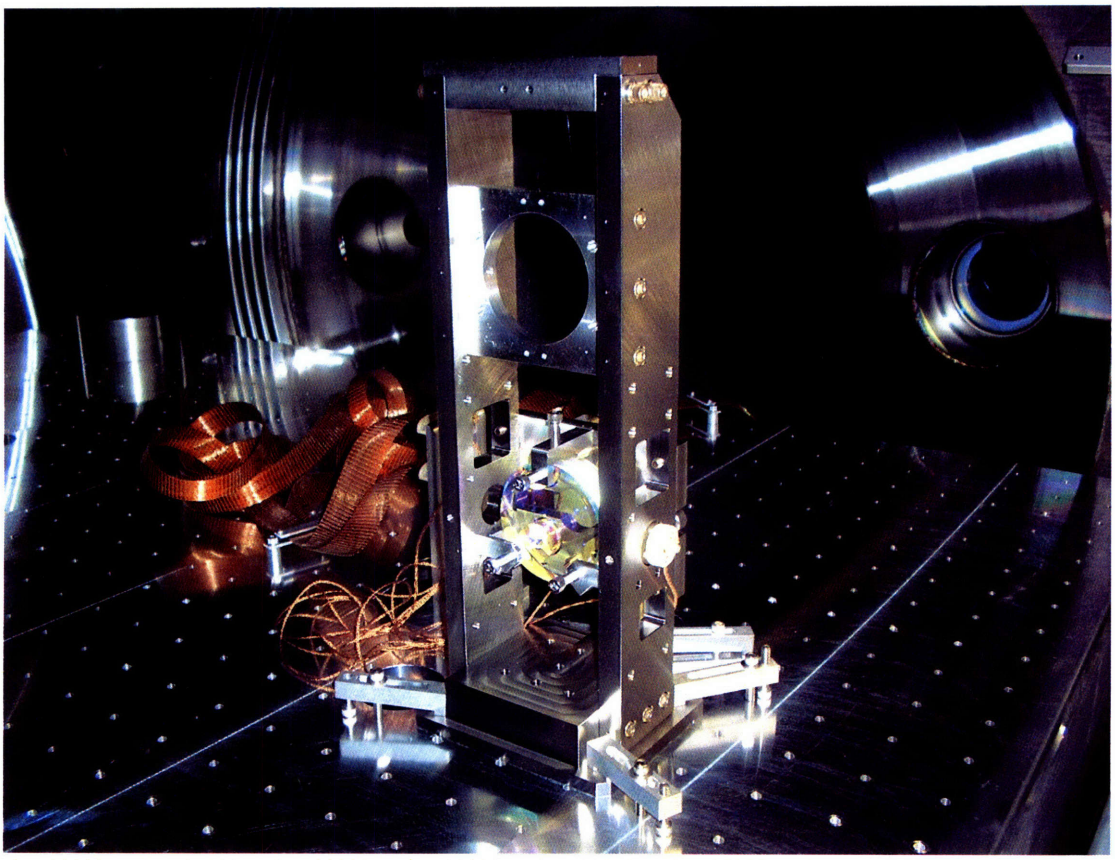

Figure 6-3: Suspended optic is shown. The suspension is identical to small optic suspensions in Initial LIGO.

Approximately 3.6 W (limited by the imperfections of the optics chain) of laser light is injected to the cavity. The light is phase modulated with an electo-optic modulator (EOM) at 25 MHz, which is used in the Pound-Drever-Hall (PDH) technique to provide a measurement of the cavity motion.

6.2.2 Parametric instability

We begin our discussion with the PI because it was the first observed effect. In recent years there has been some debate on the potential of PIs to adversely impact the performance of second generation GW interferometers [46]. The risk of PIs in future detectors arises from the high circulating power and the low mechanical loss (high quality factor, or Q) materials planned for use in future test masses. High mechanical Q materials are required to limit the effect of thermal noise on the sensitivity of the device [61].

Braginsky et al. [47] first reported on the danger of PIs in high power GW detectors.

They suggested that for kilometer-scale cavities with high circulating power and low free spectral range (FSR), a Stokes mode at the FSR could cause the cavity to become unstable. They warned that the density of mechanical modes around the FSR of the cavity could overlap with a higher order mode of the cavity, leading to instability. Application to realistic interferometers by Zhao et al. [62] has confirmed that there are likely to be modes with sufficient parametric gain to be unstable.

Parametric instabilities have been observed in resonant bar detectors with microwave resonator readouts [63] and in optical micro-cavities [64]. Kippenberg et al. observed radiation-pressure-induced parametric oscillation instabilities in ultrahigh-Q toroidal optical microcavities, at frequencies of 4.4 to 49.8 MHz and modal masses of 10^{-8} to 10^{-9} kg. The experiment reported here differs from these experiments in that it demonstrates PI at 28.188 kHz, in a suspended cavity apparatus with an effective mass of 0.125 kg. The mass and frequency regime of this experiment are of particular relevance to GW detectors and ponderomotive squeezing experiments [39, 43].

To model the effects of the PI, we recall from Eq. 3.34 that the damping rate induced by the optical spring is

$$\Gamma_{OS} = \frac{-2K_0}{M\gamma} \times \frac{1}{(1+\delta_\gamma^2-\Omega_\gamma^2)^2+4\Omega_\gamma^2}. \tag{6.1}$$

Parameterizing the PI in terms of a gain, we define

$$R = -\frac{\Gamma_{OS}}{\Gamma_M}, \tag{6.2}$$

so that $R = 0$ corresponds to no optical damping, $R = 1$ corresponds to the threshold of instability, and $R = -1$ corresponds to a doubling of the mechanical damping.

For measuring the PI, the cavity was controlled solely by feeding back the PDH error signal to the coils of the input mirror. The feedback loop is operated with typical bandwidths between 100 and 2 kHz, and the cavity is detuned by injecting an offset voltage into the PDH error signal. The drumhead mode of the mirrors at 28.188 kHz with mechanical damping rate $0.03 \times 2\pi$ Hz, is the only mode for which PI is observed. Other internal modes have poor spatial overlap with the laser beam and do not reach the threshold for PI.

To measure the value of R for this mode as a function of detuning and power, we excite the mode and measure ringup and ringdown times at varying detunings and powers,

which provides a direct measure of the damping rate. To ensure that the feedback does not interfere with the measurements, a -60 dB notch filter at 28.188 kHz is added to the servo to eliminate any interference of the servo system with the measurement of the drumhead motion of the mirror. For the cases in which $R > 1$, we allow the mode to begin oscillating and capture the ringup of the mode and fit an exponential to find the damping rate, which in turn gives the value of R. To measure values at $R < 1$, we first detune the cavity to a point where $R > 1$ and allow the mode to ring up, then quickly detune to the desired point and capture the ring down, and fit an exponential decay to find the value of R. The results of the measurements of R at various detunings, for a fixed input power, are shown in Fig. 6-4. The value of M for this mode was treated as a free parameter that was fit to the data; we found a value of 0.12 kg. The measurement of the mass of the drumhead mode show good agreement with the predicted values provided by finite element model analysis. We also measured R as a function of cavity power, with fixed detuning (set to 75% of the maximum power), and established the linear dependence on power, also showing that R goes to zero at zero injected power.

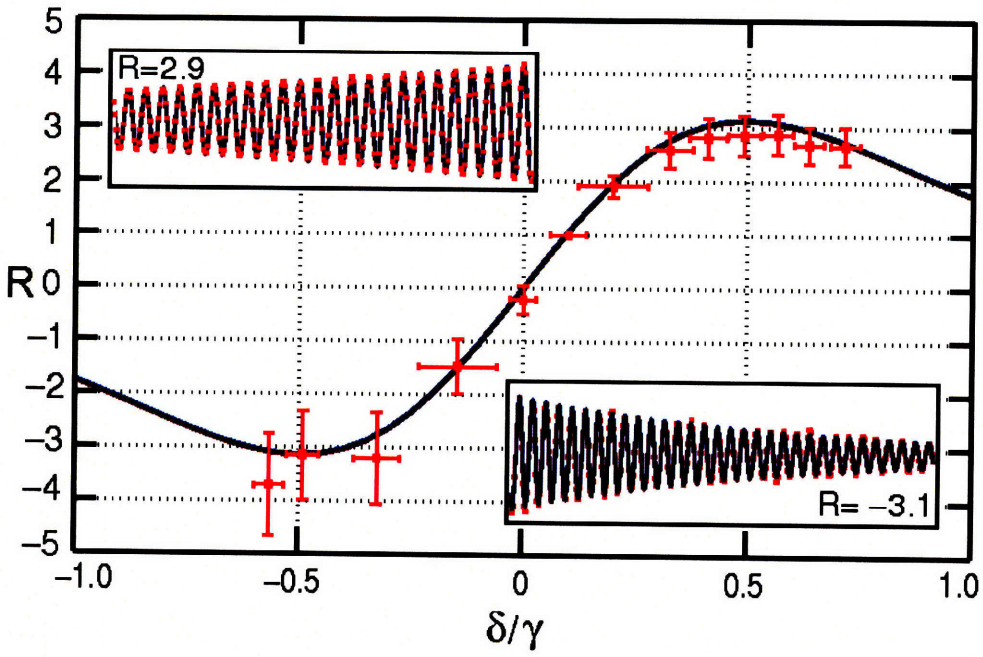

Figure 6-4: The instability measure R is plotted as a function of detuning of the cavity from resonance, for fixed input power. The solid (blue) curve is the theoretical prediction with fit parameter M; the measured data are shown as colored squares. Also shown is the power built up in the cavity, normalized to unity (green curve).

6.2.3 Optical spring

Measuring the optical spring presented some challenges. The instability of the drumhead mode must be stabilized before the measurement can be performed. To accomplish this stabilization, we modify our servo so that we tune the frequency of the laser to follow the length of the cavity at frequencies from 300 Hz to 50 kHz. The modified servo system suppresses the formation of the 28.188 kHz sidebands that induce the PI. With sufficient suppression at 28.188 kHz, the drumhead mode is not destabilized. The second difficulty is that the intrinsic motion of the mirrors at low frequencies is quite large and requires a strong servo system to hold the cavity on resonance. This has the unfortunate consequence of placing the optical spring resonance within the bandwidth of the servo system. The optical spring is characterized by injecting an excitation into the coils of the input mirror, and measuring the response to this excitation at the PDH error signal, removing the effects of the servo system.

The results from this measurement are shown in Fig. 6-5. We note that the transfer function is similar to that of a simple harmonic oscillator, with one important exception: that the resonance shows a negative damping constant (the phase *increases* by 180° at the resonance), as predicted. We suspect that the smearing out of the sharp predicted peak in the data is caused by fluctuations of the intracavity power. The measured response is, however, consistent with the theoretical prediction, with no free parameters. From the measured frequency of the optical spring resonance, we infer the optical rigidity to be $K = 3 \times 10^4$ N/m.

6.3 Phase 2 experiment

6.3.1 Experimental description

The primary modification in this stage of the experiment was the change of the cavity mirrors to provide both higher finesse, and lower mass. The input mirror was replaced by a mirror with a transmission of 0.08%, about 8 times larger than in Phase 1, resulting in an increase of a factor of 64 in the the optical rigidity, and giving a linewidth of $11 \times 2\pi$ kHz. The end mirror was also replaced with a 1 gram optic in a double suspension, as shown in Fig. 6-7. The 1 gram mirror is glued to two 300 micron diameter optical fibers, which are in turn glued to a steel ring with the same dimensions as the input mirror. The resonant

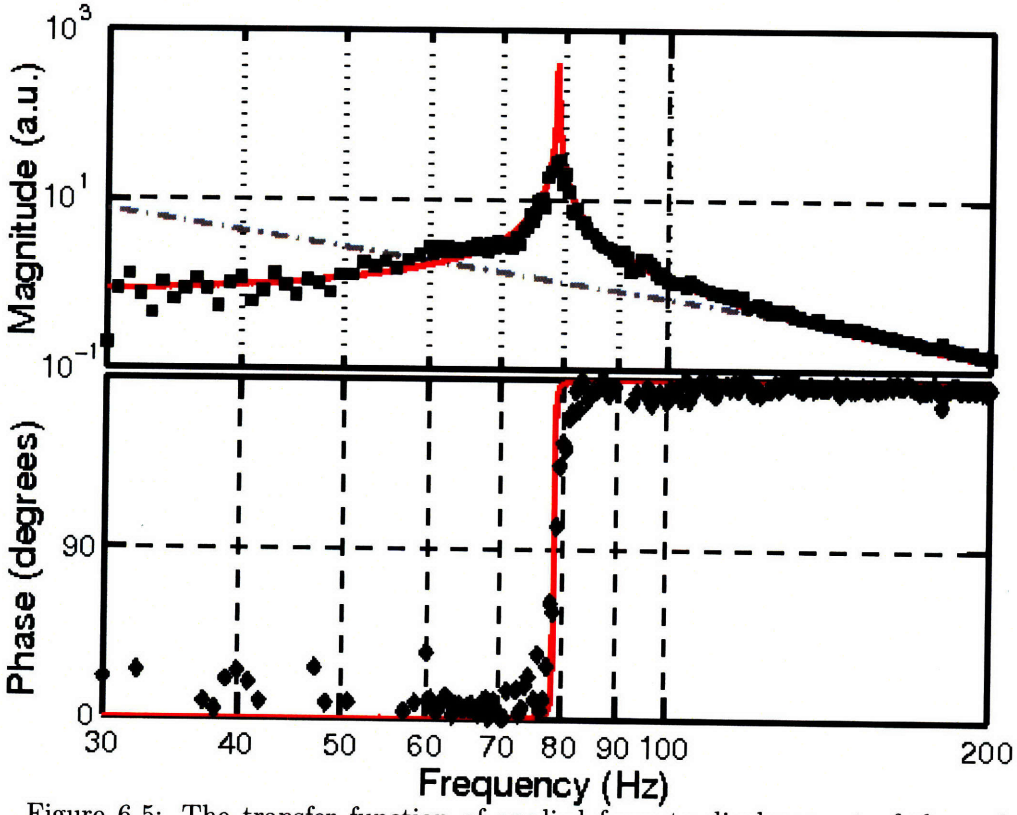

Figure 6-5: The transfer function of applied force to displacement of the end mirror of the cavity, showing the optical spring resonance. The solid (red) curve is the theoretical prediction with no free parameters, based on measurement of the intracavity power, and the quadrangles are the measured data. The phase increases from 0 to 180 degrees at the resonance, showing that the resonance is unstable.

frequency of the mirror within the ring is 172 Hz with a quality factor of 3200. The design resonant frequency was 30 Hz. During the construction of the suspension, heat was applied to cure the glue between the fibers, the mirror and the ring. The thermal expansion of steel is much larger than that of glass, however, and the ring expanded while hot, and contracted when the heat was removed after the glue was cured. The contraction left the fibers with slack, creating a bow effect that accounts for larger than expected stiffness. However, given the low mass and high optical rigidity, the expected optical spring frequency is much higher than the 172 Hz, so the experiment proceeded despite this flaw.

A more complex control system was also developed to allow for greater flexibility in the detuning of the cavity. In our experience with the Phase 1 experiment, the PDH technique only allowed us to operate at detunings of about $|\delta_\gamma| < 0.5$. In this phase of the experiment,

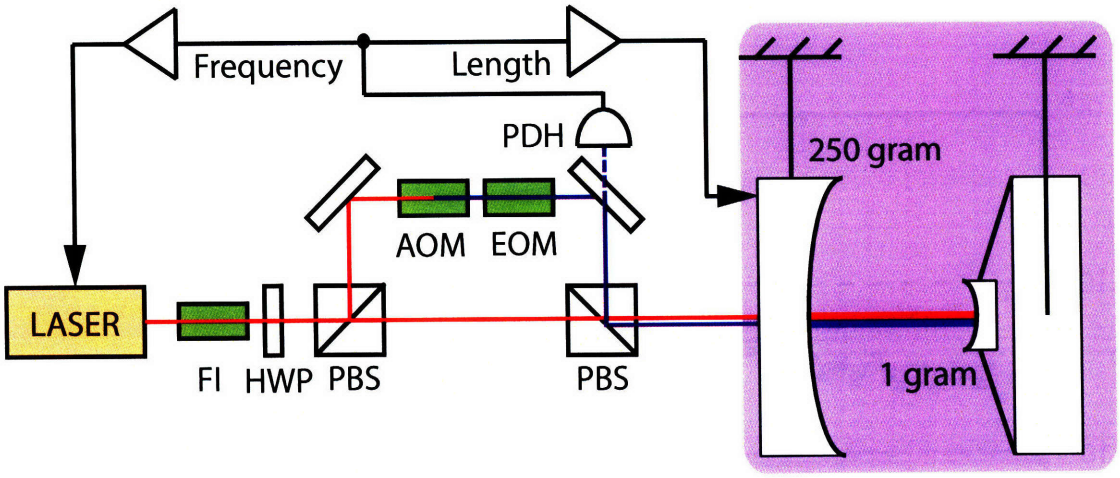

Figure 6-6: Simplified schematic of the experiment. About 3 W of $\lambda_0 = 1064$ nm Nd:YAG laser light passes through a Faraday isolator (FI) before it is split into two paths by a half-waveplate (HWP) and polarizing beamsplitter (PBS) combination that allows control of the laser power in each path. The carrier (C) field comprises most of the light incident on the suspended cavity. About 5% of the light is frequency-shifted by one free spectral range (161.66 MHz) using an acousto-optic modulator (AOM), and phase modulated by an electro-optic modulator (EOM); this subcarrier (SC) field can further be detuned from resonance to create a second optical spring. The two beams are recombined on a second PBS before being injected into the cavity, which is mounted on a seismic isolation platform in a vacuum chamber (denoted by the shaded box). A Pound-Drever-Hall (PDH) error signal derived from the SC light reflected from the cavity is used to lock it, with feedback to both the cavity length as well as the laser frequency. By changing the frequency shift of the SC, the C can be shifted off resonance by arbitrarily large detunings. The low power SC beam (blue) passes through the EOM and AOM before being recombined with the high power C beam (red).

we installed an AOM to frequency shift a fraction of the laser light, the subcarrier (SC), which was then recombined at a polarizing beamsplitter and injected into the cavity, as shown in Figure 6-6. If the frequency shift applied at the AOM is exactly equal to the free spectral range of the cavity, then both fields are simultaneously resonant. The frequency may then be slightly tuned, so that while the SC is resonant, the carrier may be arbitrarily detuned. This allows for much greater flexibility in controlling the detuning of the cavities.

6.3.2 Stiff optical spring

This stage of the experiment is an important test for many aspects of the ponderomotive squeezer. It operates with the identical mirrors and power levels that have been assumed, so it allows the extremely high optical rigidity, and the power handling capability of the

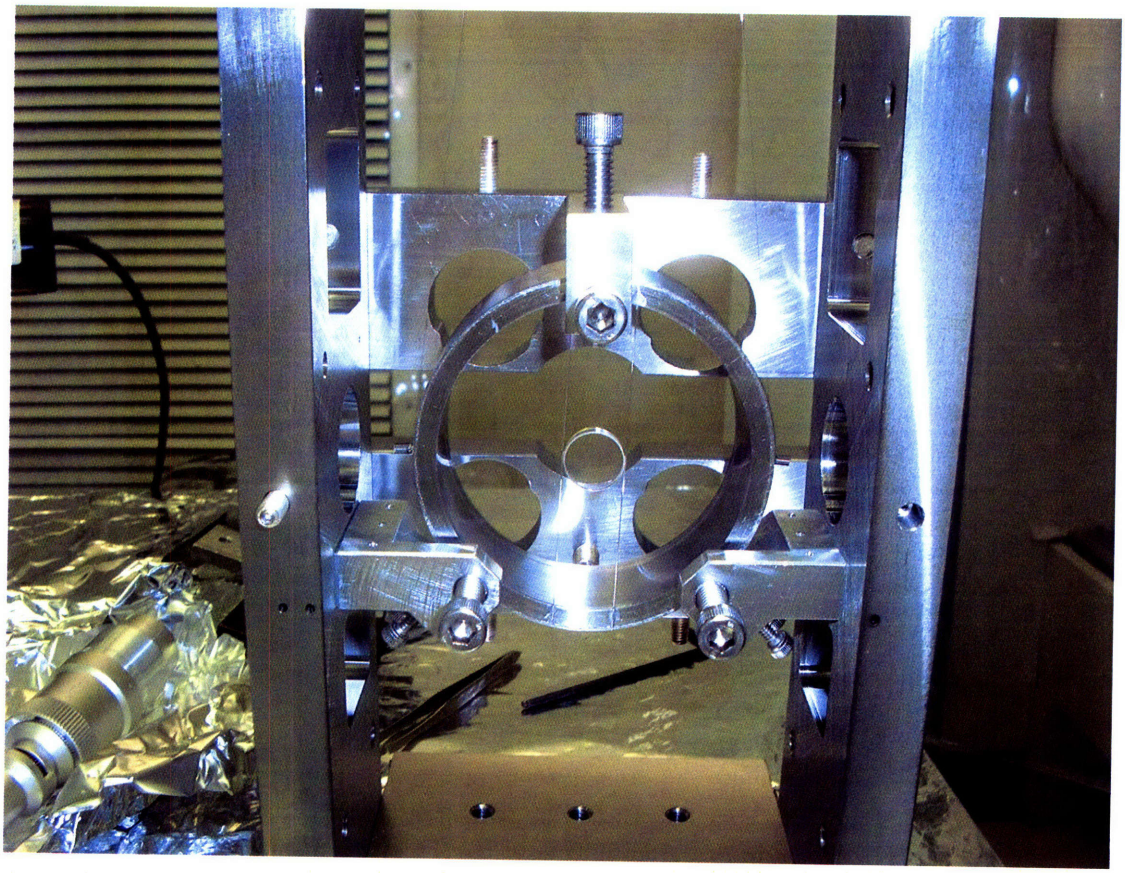

Figure 6-7: Suspension for 1 gram mirror is shown. The mirror is glue to two 300 micron diameter optical fibers, which are in turn glued to a steel shell that is itself suspended.

mirrors to be verified. It should also allow for the cavity to be operated without control in the squeezing frequency band at a few hundred Hz. To demonstrate these effects, the cavity was operated using the PDH technique on the SC, which is frequency shifted to provide $\delta_C \approx 0.5\,\gamma$. Then, the response of the system to external forces is measured as increasing power levels. At the highest input power level of about 3 W, we reach an intracavity power level of about 10 kW, comparable to the power levels in the LIGO arm cavities. There were no indications of damage to the mirrors or other negative effects at these power levels over short periods of time. No study was done of long term effects.

The 172 Hz mechanical resonance of the 1 gram mirror is shifted as high as 5 kHz (curve (a) in Fig. 6-10), corresponding to an optical rigidity of $K = 2 \times 10^6$ N/m. Consider replacing the optical mode with a rigid beam with Young's modulus E. The effective Young's modulus of this mode with area A of the beam spot (1.5 mm^2) and length $L = 0.9$ m of the cavity, is given by $E = K\,L/A = 1.2$ TPa, stiffer than any known material (but also

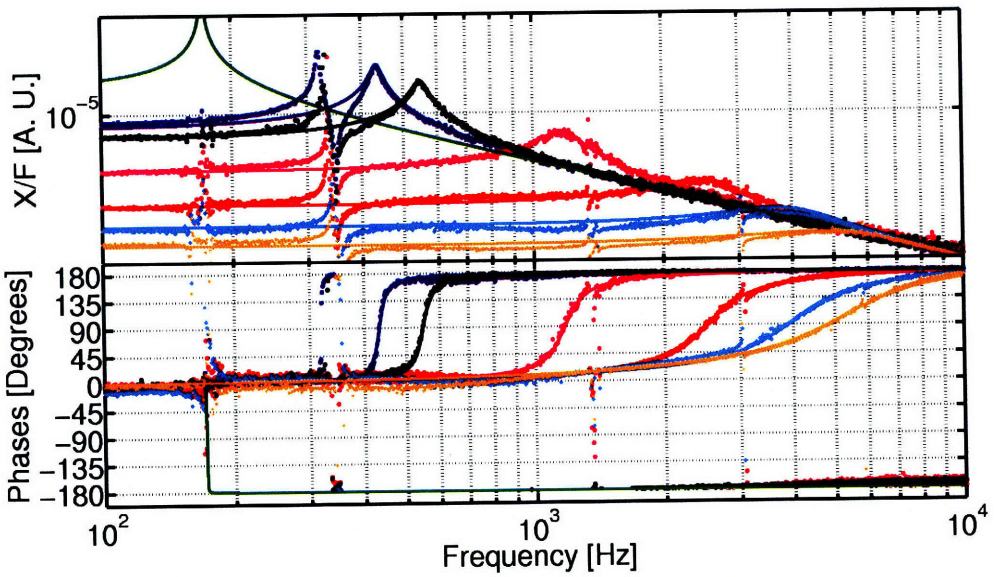

Figure 6-8: The response of the cavity to an external force applied to the end mirror is shown. The measurement is performed by injecting an excitation into the control system, and measuring the response of the cavity to the excitation. A model of the purely mechanical response is shown in green, while the other traces correspond to increasing power levels in the carrier. The feature at about 350 Hz is due to the pitch resonance of the end mirror. The feature near 170 Hz is due residual effects of the 172 Hz longitudinal resonance, and from the yaw resonance at 155 Hz. Features visible above 1 kHz are either violin modes from the suspension wire, or vibrational modes of the 300 micron fibers used in the end mirror suspension.

with very small breaking strength). We may estimate the maximum force that the cavity is capable of withstanding simply as $2P/c = 6 \times 10^{-5}$ N, where P is the intracavity power. This corresponds to roughly 0.5% of the end mirror's weight. Such extreme rigidity is required to operate the cavity without external control and to reduce the classical noise, while maintaining modest levels of squeezing. We were able to operate this cavity with narrowband control around the optical spring resonance, and at low frequency ($<$ 150 Hz), demonstrating that the cavity could be operated without control in the squeezing bandwidth. However, we defer a discussion of the control system to Section 6.4.2. Laser noise precludes the possibility of observing squeezing in the single cavity configuration.

6.3.3 Double optical spring

While we may operate the cavity without control in the squeezing bandwidth, we have shown in Section 5.3.3 that we still have residual noise from the control, so there may be

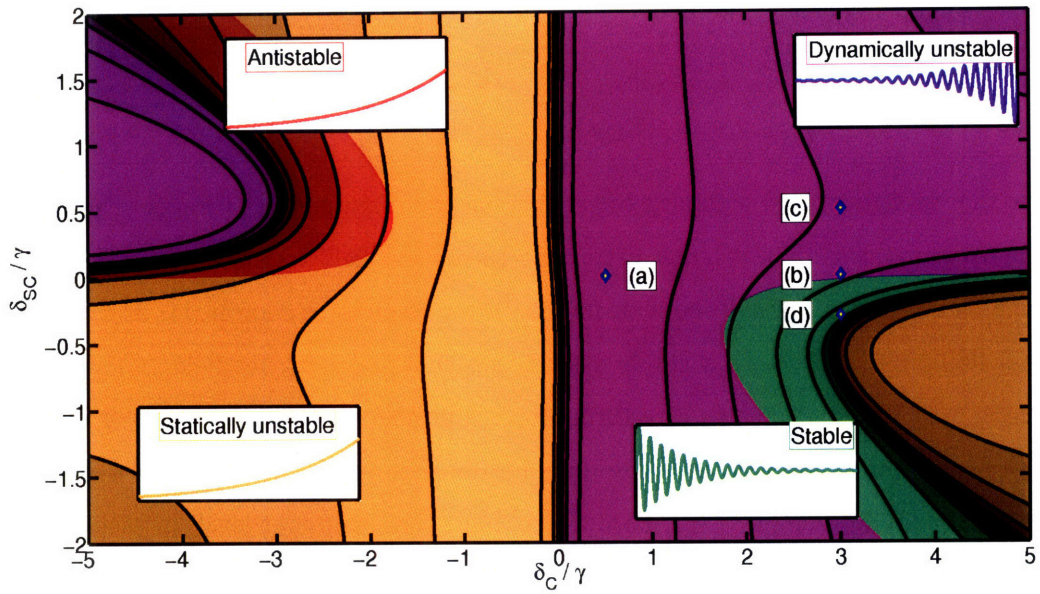

Figure 6-9: Graphical representation of the total optical rigidity due to both optical fields, as a function of C and SC detuning, for fixed input power (power in the SC field is $\sim 1/20$ the C power) and observation frequency ($\Omega = 2\pi \times 1$ kHz). The shaded regions correspond to detunings where the total spring constant K and damping constant Γ are differently positive or negative. Specifically, "stable" corresponds to $K > 0, \Gamma < 0$, "anti-stable" to $K < 0, \Gamma > 0$, "statically unstable" to $K < 0, \Gamma < 0$, and "dynamically unstable" to $K > 0, \Gamma > 0$. The (logarithmically spaced) contours shown are scaled according to K: brighter regions have larger K. The labels (a) – (d) refer to the measurements shown in Fig. 6-5.

benefits from not requiring a control system at all. However, recall that the optical spring always require stabilization because of the optical anti-damping force that arises from the finite response time of the intracavity light.

However, we show that the system may be stabilized by using two optical fields (and two optical springs) that respond on different time scales. One field should respond quickly, so that it makes a strong restoring force and only a weak anti-damping force. The other field should respond slowly, so that it creates a strong damping force, with only a minor anti-restoring force. This could be achieved with two cavities of differing bandwidths that share a common end mirror. However, it is simpler to use a single cavity and two fields with vastly different detunings. From Eqs. 3.27 and 3.34, taking $\Omega \ll \gamma$ (valid at the optical

spring resonant frequency), we find

$$\frac{\Gamma_{OS}}{K_{OS}} = \frac{2/(M\gamma)}{1+(\delta/\gamma)^2}; \tag{6.3}$$

we see that an optical field with larger detuning has less damping per stiffness. The physical mechanism for this is that at larger detunings, the optical field resonates less strongly than for smaller detunings, so the time scale for the cavity response is shorter, leading to smaller optical damping. To create a stable system, we consider a carrier field (C) with large detuning $\delta_C \approx 3\gamma$ that creates a restoring force, but also a small anti-damping force. To counteract the anti-damping, a strong damping force is created by injecting a subcarrier (SC) with small detuning $\delta_{SC} \approx -0.5\gamma$. For properly chosen power levels in each field, the resulting system is stable; we found a factor of 20 higher power in the carrier to be suitable in this case. To illustrate the behavior of the system at all detunings, the various stability regions are shown in Fig. 6-9 for this fixed power ratio. Point (d) in particular shows that the system is stable for our chosen parameters. The overall spring constant of this combined system is smaller because of the large detuning of the carrier field.

An experiment was performed to demonstrate the stable double optical spring. We already operated with a second optical field, so with the suitable distribution of power between the carrier and subcarrier, we could detune the subcarrier by inserting an offset into its PDH signal (which is sufficient for reaching the ideal detuning for maximal damping), and detune the carrier by controlling the frequency of the AOM. We operated with approximately 3 W in the carrier field, and 0.15 W in the subcarrier field. In Figure 6-10 we show response curves corresponding to various C and SC detunings. In curves (b), (c) and (d), we detune the carrier by more than the cavity linewidth since the optical spring is less unstable for large δ_C. With no SC detuning, the optomechanical resonant frequency reaches $\Omega_{\text{eff}} = 2\pi \times 2178$ Hz, shown in curve (c). Note that the optical spring is unstable, as evidenced by the phase *increase* of 180° about the resonance (corresponding to anti-damping). Next we detune the subcarrier in the same direction as the carrier, shown in curve (b), which increases the resonant frequency and also increases the anti-damping, demonstrated by the broadening of the resonant peak. For these two cases, electronic servo control is used to keep the cavity locked. If the control system is disabled, the amplitude of the cavity field and mirror oscillations grow exponentially at the optical spring frequency. Remarkably,

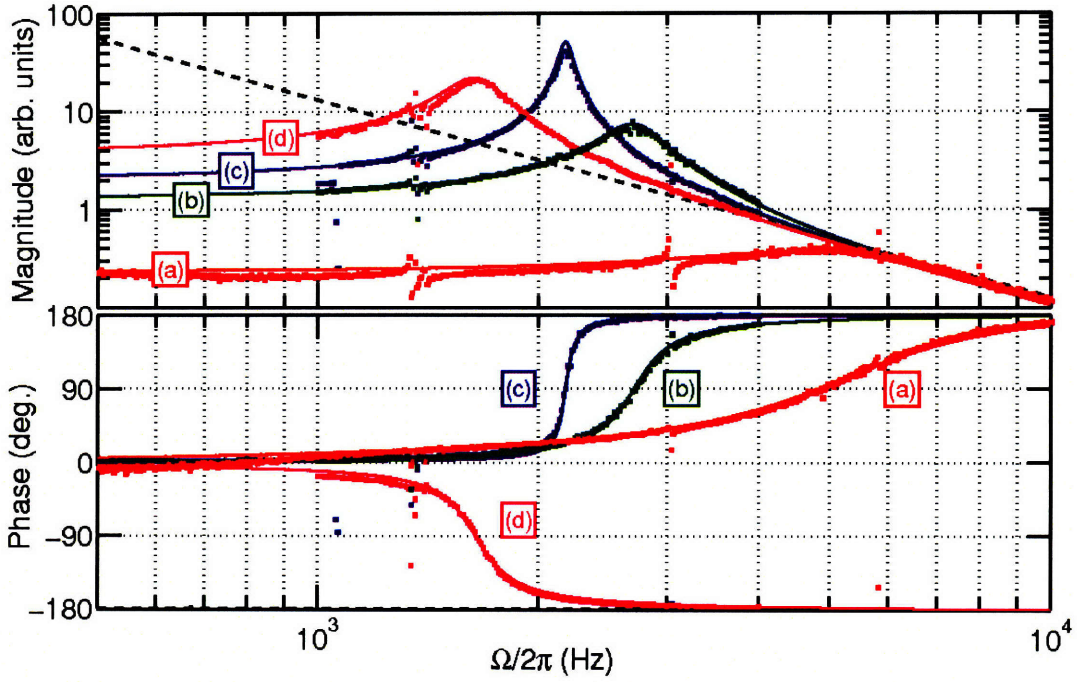

Figure 6-10: The optical spring response for various power levels and detunings of the carrier and subcarrier. Measured transfer functions of displacement per force are shown as points, while the solid lines are theoretical curves. The dashed line shows the response of the system with no optical spring. An unstable optical spring resonance with varying damping and resonant frequency is produced when (a) $\delta_C = 0.5\gamma, \delta_{SC} = 0$; (b) $\delta_C = 3\gamma, \delta_{SC} = 0.5\gamma$; (c) $\delta_C = 3\gamma, \delta_{SC} = 0$; and it is stabilized in (d) $\delta_C = 3\gamma, \delta_{SC} = -0.3\gamma$. Note that the damping of the optical spring increases greatly as the optomechanical resonance frequency increases, approaching $\Gamma_{\text{eff}} \approx \Omega_{\text{eff}}$ for the highest frequency optical spring.

when the subcarrier is detuned in the opposite direction from the carrier, the optical spring resonance becomes stable, shown in curve (d), allowing operation of the cavity without electronic feedback at frequencies above 30 Hz; we note the change in phase behavior and the reduction of the resonant frequency. The switching off of the control system was achieved by a switchable 2nd order Sallen-Key elliptic lowpass filter. The low frequency control was still necessary to counteract seismic motion. In order to maintain stability at the unity gain frequency of the servo (between 30 and 150 Hz), it is necessary that the filter have a very sharp phase response. The Sallen-Key topology allows us to create a filter with a frequency response identical to that of a damped harmonic oscillator. By tuning the frequency of the filter to match the mechanical resonant frequency of the end mirror, and giving the filter a high quality factor, we may achieve an extremely sharp phase response and maintain the

loop shape and phase below the resonant frequency. It is critical to match the frequency of the filter to the mechanical frequency in order to avoid instability caused by the peaking of the filter, which is cancelled by the notch in the optomechanical response (see Figure 6-14). These results demonstrate how the frequency and damping of the optical spring can be independently controlled in the strong coupling regime.

6.4 Phase 3 experiment

Towards the purpose of measuring ponderomotive squeezing and quantum radiation pressure noise, the experiment was upgraded to softer mechanical suspensions placed in two identical cavities in a Michelson interferometer. The softer suspension is intended to reduce the thermal noise, and the Michelson interferometer is intended to reduce the effects of classical laser noise. The fundamental frequency of the end mirrors has dropped to 6.3 Hz, below which the fiber suspensions no longer act as rods, but rather as pendulums. This limit cannot be breached because it would not allow for alignment of the pitch of the end mirrors. The pitch must be adjustable for a suspension in this regime, as the radiation pressure force at high input power deflects the mirror sufficiently to misalign the cavity. At present, we do not operate the system with a double optical spring because the beamsplitter's reflectivity is polarization dependent.

6.4.1 Experimental layout and control system

Figure 6-12 shows the experimental layout. We now outline the controls in several stages. The bulk of the control system is operated in the digital domain. The digital control system operates with a 32 kHz sampling rate, which is sufficiently fast for most, but not all of the feedback loops. In particular, the common mode feedback to the laser frequency, and the PI damping loops require special analog filters.

- Primary control concerns the three major degrees of freedom in the system: the length of each arm cavity, and the Michelson degree of freedom (the relative phase of the laser beam returning to the beamsplitter from each arm cavity). In a traditional interferometer with arm cavities arranged in a Michelson configuration with a heterodyne readout scheme, phase sidebands are placed on the input laser beam with an EOM. The frequency of these sidebands is chosen to be outside the bandwidth of the arm

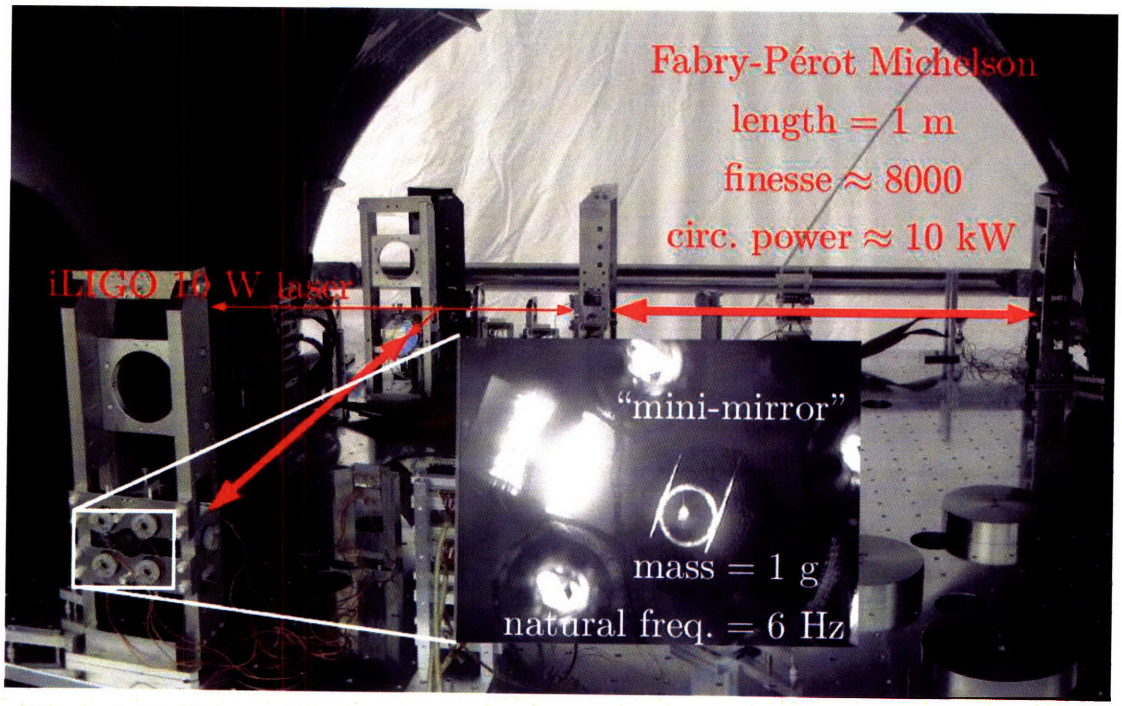

Figure 6-11: Picture of the in-vacuum layout of the Phase 3 experiment. The inset picture shows a close-up view of an end-mirror suspension when the cavity is locked.

cavities, so they do not resonate, which allows them to act as a phase reference for the carrier field. When the cavity length is not perfectly on resonance, the carrier field becomes out of phase with the sidebands, and the phase modulation (PM) Is converted to amplitude modulation (AM), which may be detected by a photodetector. The signal is then demodulated. Recall from Chapter 1 that ideally the bright port is only sensitive to common mirror motion, while the dark port is only sensitive to differential mirror motion. To allow a portion of the PM to couple to the dark port, and allow a heterodyne readout of the differential motion, a macroscopic "Schnupp" asymmetry [65] in the distance between the beamsplitter and the two input mirrors is necessary. The asymmetry, 10 cm in our case, allows for imperfect cancellation of the phase sidebands while the carrier field remains dark because of the additional phase. The asymmetry also allows for readout of the Michelson DOF at an alternative demodulation phase. The standard scheme relies on the carrier field experiencing either a 0 or π phase shift upon reflection from the arm cavities, so that there is only a signal as the cavity moves away from resonance. Unfortunately, this means that the technique works very poorly when the cavities are operated detuned. Consider

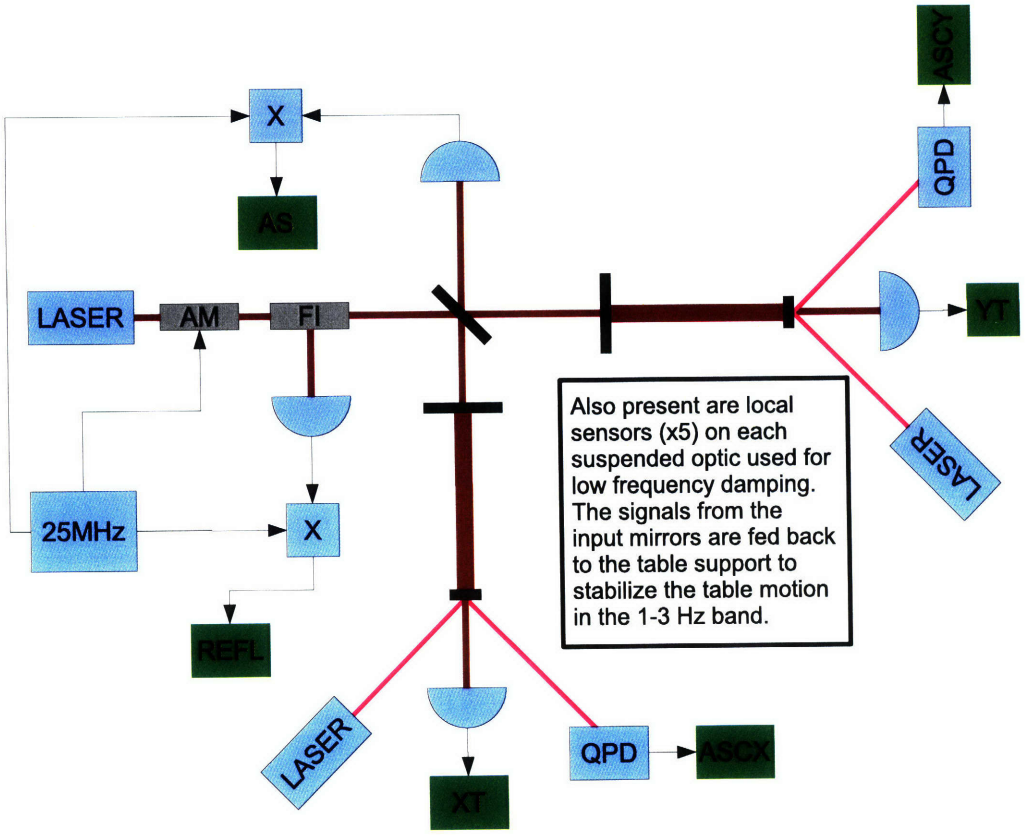

Figure 6-12: Diagram of the Phase 3 experiment. Signals used for control are shown in green. The primary length signals are generated from amplitude sidebands on the carrier light. The transmitted light through each cavity is temporarily used to acquire lock. Optical levers are used on each end mirror to sense angular motion and damp the mirror's resonances. FI refers to Faraday Isolator, AM to amplitude modulator and QPD to quadrant photodetector.

that for the case $\delta_\gamma = 1$, the carrier experiences a $\pi/2$ phase shift from the cavity, completely converting the PM to AM, destroying the sensitivity to cavity motion. To operate well at this detuning, however, we instead inject AM sidebands, which are converted entirely to phase sidebands when the cavity is operated at $\delta_\gamma = 1$. Any deviation from this position, and intensity sidebands are created, again creating a readout for the cavity motion. For any other detuning, a combination of AM and PM sidebands at the input allow for proper operation of the cavity. A detailed analysis of the technique, with construction of a "universal" modulation is outlined in Ref. [66].

One limitation to the AM technique, however, is that it does not work unless both arm cavities are maintained at $\delta_\gamma = 1$. It is extremely difficult to transition to this state when the mirrors are free swinging, because it requires that all 3 of our DOFs are in the proper position simultaneously. To ease the process, we first lock each arm cavity while allowing the Michelson DOF to remain uncontrolled. To do so, we use the transmitted light through each cavity. At $\delta_\gamma = 1$, the transmitted light provides an excellent signal for the cavity length. To acquire lock of both arm cavities quickly, we divide the signal into differential and common motion, derived from the transmitted light signals. The common motion is fed back to both the laser frequency and as a force on the input mirrors. When the mirrors swing through a resonance, typically lasting only 10 microseconds, the feedback to the laser frequency allows the cavity to stay near resonance long enough for the length feedback to lock the cavity. Once both arms are locked in this way, the Michelson degree of freedom may then be locked, and the feedback may be switched to use the demodulated heterodyne signals derived from the AM sidebands. We typically operate with 10 to 50 kHz bandwidth in the common mode feedback, with the laser feedback dominating above 1 kHz, and the length feedback below. The differential feedback is typically operated with 1 kHz bandwidth, as limited by the speed of our digital control system. The Michelson feedback is operated with about 100 Hz bandwidth.

- Secondary control concerns all auxiliary degrees of freedom in the system. First, we have found that the dominant motion of the able is the table pitching along its axes. We may use the shadow sensors of the suspended optics as a sensor for this motion, and then feed it back to the table supports. This allows for a reduction of a factor

up to about 10 in the RMS of the motion. Second, the shadow sensors themselves are used to sense the local motion of the mirror relative to its suspension cage. The signals are decomposed into pitch, yaw, longitudinal, and side-to-side motion, and each of these signals is fed back to the coil-magnet pairs to damp the low frequency resonances. The longitudinal and side-to-side modes are about 1 Hz, and the pitch and yaw modes are 0.5 to 0.7 Hz. Finally, the motion of the 1 gram mirrors can become very large because the new resonant frequency of the longitudinal mode, 6.3 Hz, is coincident with a resonant frequency of the table support structure. To counteract this, we shine a HeNe laser on each end mirror, and use a quadrant photodetector to detect the reflected beam. When the mirror moves, the signal on each quadrant varies, allowing us to detect the angular motion of the mirror (the 6.3 Hz mode couples significantly to pitch). We use narrowband feedback around each resonant frequency (6.3 Hz longitudinal, 68 Hz pitch and 38 Hz yaw) to the coil-magnet pairs to damp each resonance. The feedback greatly reduces the RMS motion of the mirror and greatly eases lock acquisition. However, once the arm cavities are locked, noise from the optical lever signal introduces broadband noise into the more sensitive primary length sensing signals. Because the primary length signals are sensitive to the angular DOFs, once the cavities are locked, we switch the angular feedback to use the length signals instead of the optical levers.

- Parametric instability damping loops are required to eliminate the instability of the drumhead motion. With the higher finesse cavities, the parametric gain R can be significantly larger then in the Phase 1 experiment, but this mode remains the only one to become unstable. We find that it is more robust to directly damp the drumhead motion of each input mirror by feeding back to the coil-magnet pairs on each mirror, using the transmitted light signals to sense the drumhead motion. We prefer to damp the mode using digital feedback, as it allows for greater flexibility, but the 27.5 kHz mode (the mirror has slightly different frequencies than the one in Phase 1) lies outside the Nyquist frequency of the control system. However, the motion at 27.5 kHz is aliased in the analog-to-digital process, and imaged in the digital-to-analog process. By taking advantage of these effects, and installing an extra aliasing filter in each of the transmitted light signals, we may heavily damp the drumhead modes and avoid instability.

6.4.2 Control issues with the optical spring

It is instructive to consider some of the control and feedback issues that arise in optomechanical systems. The Phase 3 experiment is an ideal system in which to discuss these issues because it combines the softest suspension with the most complex control topology. Suspended high finesse optical cavities present challenging control issues. Due to the flexible suspensions, these systems often exhibit motion at the level of a few microns driven by the motion of the ground at approximately 1 Hz. In our case, with a finesse of about 10^4, we require the motion between the two cavity mirrors to be less than about 10^{-11} meters, which therefore requires our control system to reduce the relative motion between the mirrors by a factor greater than 10^5. This reduction is usually accomplished with servo control of the cavity motion, feeding back to the position of the cavity mirrors, or to the laser frequency, or to some combination of the two. The addition of the optical spring dramatically alters the response of the cavity to forces applied to its mirrors, as well as to changes in the laser frequency. The change in the response, we show, can dramatically change the topology of the servo loop required to keep the cavity locked. Additionally, as discussed previously, the response of the cavity to outside disturbances is dramatically reduced. If this reduction exceeds the 10^5 factor, the cavity exhibits self-locking, in which the optical spring maintains the stability of the cavity without the need for external control.

First, we consider the case when active control of the cavity is desired, or necessary. The basic scheme is presented in Figure 6-13. Depending on the readout scheme, and the cavity detuning, the response of the cavity to displacements varies in a frequency dependent manner. However, this effect is typically counteracted electronically, and has no relevance for this discussion, so we assume that $C = 1$ for simplicity. We note that the role of the optical spring is identical to that of a feedback loop for which the feedback kernel H is identical to the optical spring constant K. First, we consider the response of the system to external forces on the end mirror. In the absence of the optical spring, the response is simply P_e, the response of the pendulum to forces. With the optical spring present, however, the response of the system to external forces becomes

$$P_e' = \frac{P_e}{1 - P_e K}, \tag{6.4}$$

and more relevant to our active control of the cavity, feedback applied to the input mirror

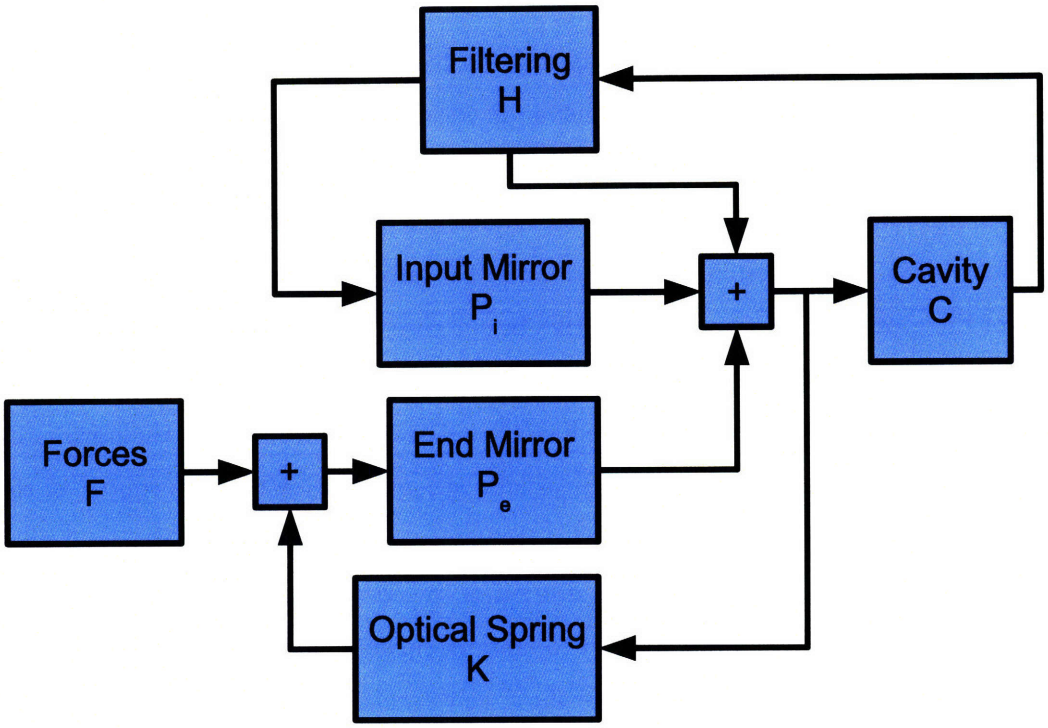

Figure 6-13: Block diagram describing the optical spring in the context of a control system is presented. P_i and P_e are the displacement to force transfer functions of the input and end mirrors, H is an electronic filter function, C is the cavity's response to mirror motion, K is the optical spring, and F are external forces applied to the end mirror.

(which is much heavier, and largely irrelevant to the optical spring) has a modified response

$$P_i' = \frac{P_i}{1 - P_e K}. \tag{6.5}$$

This modified response can have profound implications for the servo control system. In Figure 6-14, we plot the measured cavity response for three different input power levels, with the detuning of the cavity fixed, to demonstrate how the response changes as we increase K. First, we note that the response below the optical spring frequency decreases as we increase the power, as expected. Secondly, we note that the response has sharp features at 6.3 Hz (the fundamental frequency of the end mirror), 38 Hz (the yaw resonant frequency of the end mirror), and 70 Hz (the pitch resonant frequency of the end mirror). These sharp

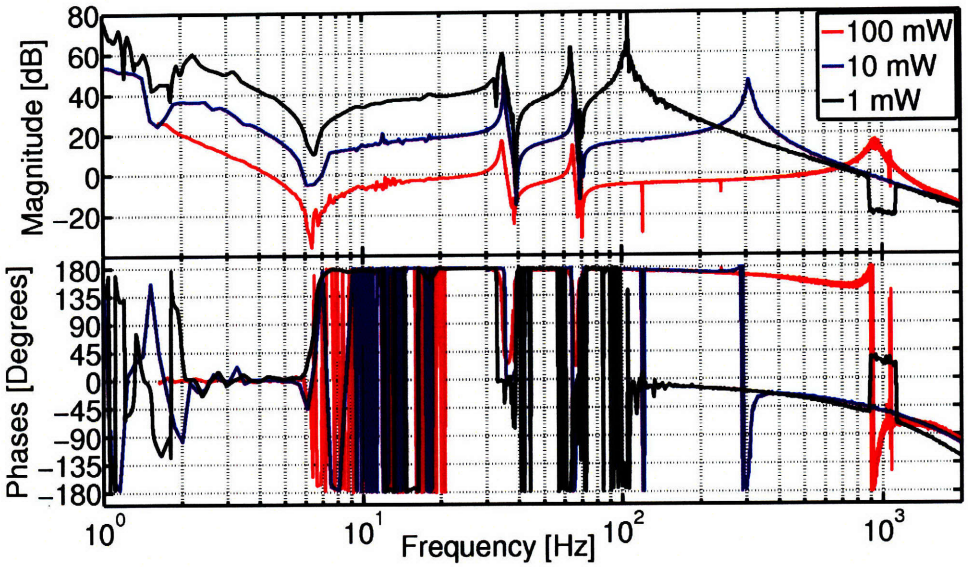

Figure 6-14: Response of the differential motion of the arm cavities to a force applied to the input mirror with an optical spring. A glitch corrupted the data near 1 kHz in the black trace. The optical spring is visible near 100 Hz (black), 300 Hz (blue) and 1 kHz (red). The phase lag above 1 kHz is due to time delays in the digital acquisition system.

notches in the response near these frequencies are present because a force applied to the input mirror couples to the optical spring, which in turn pushes on the end mirror, which excites these various modes. As a general rule, any resonance in the mechanical response of the end mirror manifests as a notch in the modified response, as P_e is in the denominator of Eq. 6.5. The presence of these notches, combined with the reduced response, can greatly complicate control of the system, as it can create additional unity gain crossings in the servo system, which can lead to instabilities. Feedback to the laser frequency experiences similar difficulties, and the response to laser feedback is given by

$$R = \frac{1}{1 - P_e K}, \tag{6.6}$$

which has identical features to those present in the input mirror feedback.

Next, we consider control strategies in the presence of an optical spring. There are two regimes that we may consider. The first is the case in which the reduction in response caused by the optical spring is large enough to require modification to the servo system, but not strong enough to exhibit self-locking. This is the most challenging regime to work in, as stabilization of the cavity is required, but the optical spring introduces additional features

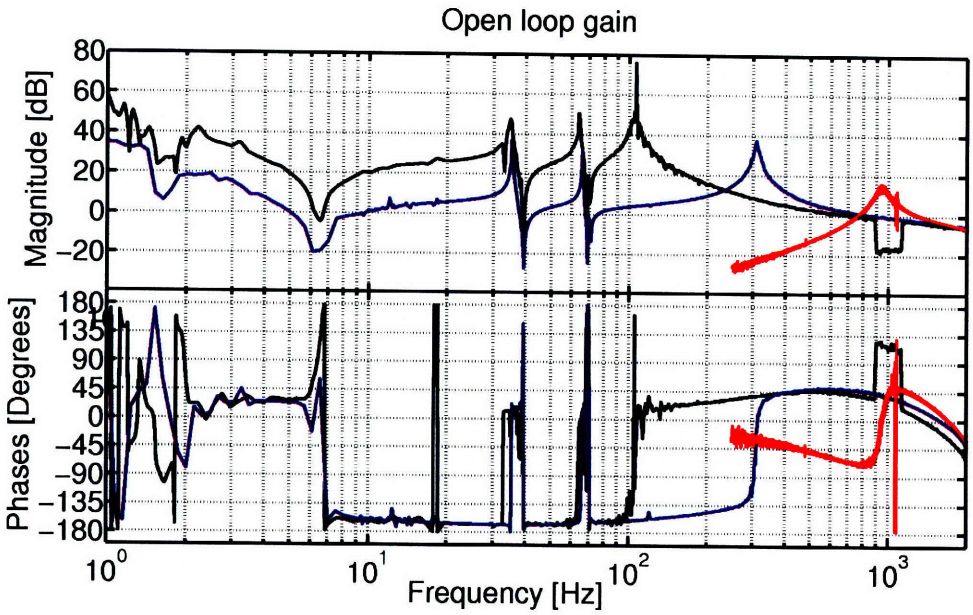

Figure 6-15: A measurement of the open loop gain of the servo control system for three levels of input power at fixed detuning are shown. The servo system for the black and blue traces are identical, while for the red trace, the compensation filter H has been modified to eliminate the gain at low frequencies.

into the response. Creating a stable servo system in the presence of these notches, while possible, creates requirements on the control system that limit the amount of stabilization that it can provide. For that reason, this regime is usually undesirable. Examples of the open loop gain for the same three input power levels is shown in Figure 6-15. Note that the red and black traces operate in this regime, and they have multiple unity gain crossings near 6, 40 and 70 Hz, corresponding to the mechanical mode frequencies of the end mirrors.

The second case is that in which the optical spring is sufficiently strong that external feedback is not required to maintain stability of the cavity. This occurs when the magnitude of K_{opt}/K_M exceeds the gain requirements for stability, which for the Phase 3 experiment, occurs with the optical spring near 1 kHz. If the previously described double optical spring technique is used to generate a stable optical spring, then the need for external control is completely negated. However, we currently do not operate in this regime because of the polarization dependence of the beamsplitter's reflectivity.

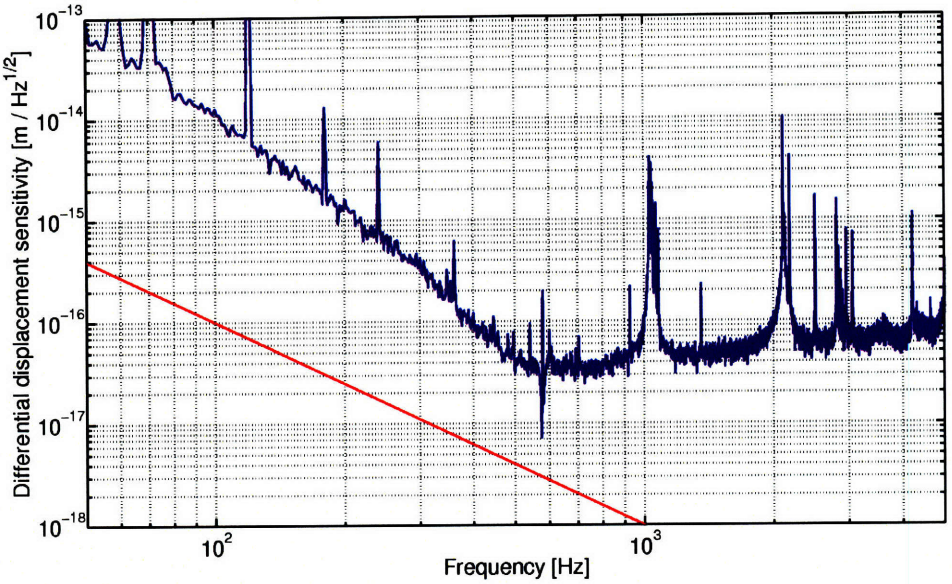

Figure 6-16: The noise level in the differential degree of freedom is given in blue, observed with 50 mW of input power and detuning $\delta_\gamma \approx 1$. The red trace indicates the nominal sensitivity required to observe squeezing or quantum radiation pressure noise with 5 W of input power. The closest approach to the required sensitivity is near 500 Hz, where the noise level is a factor of 10 too large. The large peaks near 1 and 2 kHz correspond to resonances of the fibers in the end mirror suspension. The sharp notch near 600 Hz is an artifact of the calibration. The noise above 600 Hz is created in the analog-digital conversion process. The noise below 600 Hz is not understood.

6.4.3 Current status

The system may be stably locked with all of its DOFs controlled. Work is currently underway to reduce technical noise in the system. The current sources of noise that we believe to be limitations are electronics noise and scattered light (that reflects off secondary surfaces and back into the main beam creating phase noise). It is anticipated that the thermal noise from our low Q suspensions of the end mirror precludes radiation pressure noise or squeezing to be observable. Work is currently underway to replace the end mirror with similar suspensions, but with a glass ring in place of the steel ring, and with the fibers welded to the ring and to the mirror. The current noise level in the differential degree of freedom is shown in Figure 6-16.

6.5 Summary

In this chapter, we have described experimental progress towards observation of ponderomotive squeezing, including characterization of the optical spring and parametric instability effects. In the final configuration, we operate close to the parameters assumed in Chapter 5, although at a higher noise level. In the next chapter, we explore how our experiments may be applied to the field of macroscopic quantum measurement.

Chapter 7

Cooling experiments

There has been considerable interest recently in approaching the quantum ground state of macroscopic mechanical oscillators [67–77]. "Macroscopic" in this case refers to the oscillator consisting of many individual particles, ranging from picogram oscillators to kilogram mirrors. The success of these efforts depends upon various cooling techniques that remove thermal energy that ordinarily keeps the oscillators far from the ground state. Here we discuss how the optical spring and optical damping effects, and sensitive optical readouts in general, may be useful in these efforts. In this Chapter, we first introduce the concepts of cold damping, cavity cooling and thermal dilution, then present a series of experiments demonstrating these effects.

7.1 Cold damping and cavity cooling

The most common technique for removing thermal energy in these experiments is to detect the motion that it induces, and to exert a (damping) force on the oscillator opposing it, thereby increasing its damping, but also reducing its motion and temperature. When the damping force is provided externally, the technique is called cold damping [69, 78, 79]. Alternatively, the optical damping force (or photothermal effect) may also provide the same cooling [67, 68, 70–72, 75]. There are predominantly two limits to consider. First, the oscillator may only be cooled until it becomes critically damped. A simple model of energy conservation in the system requires that

$$\Gamma_M T + \Gamma_{CD} T_{CD} = \Gamma_{\text{eff}} T_{\text{eff}}, \tag{7.1}$$

where Γ_{CD} and T_{CD} are the damping rate and temperature associated with the damping force, and $\Gamma_{\text{eff}} = \Gamma_M + \Gamma_{CD}$ and T_{eff} are the final damping rate and temperature. T_{CD} is primarily limited by the noise of the sensor, but let us assume for a moment that it is effectively 0, then we obtain

$$T_{\text{eff}} = \frac{\Gamma_M}{\Gamma_{\text{eff}}} T, \tag{7.2}$$

where T is the initial temperature. So as long as the thermal noise of the oscillator is the limitation, the effective temperature is reduced by a factor $\Gamma_M/\Gamma_{\text{eff}}$. In order to maintain a mode of oscillation, we require that $\Gamma_{\text{eff}} < 2 \times \Omega_M$, resulting in a maximum cooling ratio of twice the initial quality factor of the device. In order to reach the ground state of the oscillator, we require the minimum thermal energy to be less than the ground state energy:

$$\frac{k_B T}{2Q} < \frac{1}{2}\hbar\Omega_M. \tag{7.3}$$

The second limitation arises from the noise of the initial measurement of the oscillator's position. We may estimate the precision by assuming that the measurement is limited by the SQL. Neglecting factors of order unity, and assuming that the oscillator is nearly critically damped, the RMS uncertainty of the mirror position may be estimated as

$$x_{RMS}^2 = \frac{\hbar}{M\Omega_M}. \tag{7.4}$$

Then the number of phonons in the oscillator is (again neglecting factors of order unity)

$$N = \frac{M x_{RMS}^2 \Omega_M^2}{\hbar\Omega_M} = 1. \tag{7.5}$$

So we may expect that if the measurement device operates near the SQL, the oscillator should be able to approach the ground state. A full calculation has been performed demonstrating that the ground state can be achieved in both the cold damping and cavity cooling techniques, although with different requirements on the cavity used for detection [80]. We point out that for an experiment with typical mass of 1 gram and resonant frequency of order 1 kHz, we would require a mechanical Q of order 10^{10} to satisfy Eq. 7.3, which is a prohibitive requirement with current technology. It is clear that if we wish to approach the ground state at that mass scale, we require a more effective method of negating thermal effects.

7.2 Thermal dilution

In the LIGO interferometers, the wires in the suspensions for the optics are operated at a significant fraction of their breaking strength. This is done so that the mechanical forces acting on the mirror from the wire are as small as possible. The full equation of motion for the mirror may be written as

$$M\frac{d^2x}{dt^2} = -(k_{grav} - k_{elas})x - M\Gamma_M\frac{dx}{dt}, \tag{7.6}$$

where k_{grav} is the gravitationally induced spring constant, and k_{elas} is the spring constant induced by the internal stiffness of the suspension wire. It is shown by Saulson in Ref. [54] that the thermal force noise exerted on the mass depends only on the damping Γ_M. It is also usually the case that the quantity

$$\Phi = \frac{\Gamma_M}{\sqrt{k_{elas}/M}}, \tag{7.7}$$

the "loss angle," is roughly conserved (or at least monotonic for k_{elas}) as a function of the dimensions of the oscillator. Consequently, while a much thicker wire could be used in the LIGO suspensions to operate far from the breaking strength, doing so would greatly increase k_{elas} and therefore Γ_M, resulting in greater thermal noise. The resonant frequency is completely determined by the gravitational spring constant because $k_{grav} \gg k_{elas}$, yet the thermal noise is completely independent of the gravitational force. This allows the mechanical quality factor of the pendulum to greatly exceed the quality factor of an isolated piece of wire, thereby "diluting" its thermal noise.

We propose using a similar technique to dilute the thermal noise in our experiments. Although gravity is much too weak to be effective, the extreme stiffness of the optical spring make it an ideal candidate. The optical spring does have an associated optical damping, which must introduce extra noise. However, we note that the optical fields are not at ambient room temperature, but are instead ultimately limited by vacuum fluctuations. The vacuum fluctuations enforce the SQL, which we have shown in Eq. 7.5 allow the system to approach the ground state. A full calculation of the limitations are currently underway [81]. This technique allows us to greatly increase the cooling factor because we effectively increase the mechanical quality factor by increasing the resonant frequency

without introducing additional mechanical damping. The effectiveness of the technique with regards to suppressing thermal noise is difficult to calculate in our system. Two different models of thermal noise may be considered. In the standard viscous damping model, the frictional damping force is assumed to be viscous (proportional to velocity) in nature, and the damping is frequency independent. In an alternative model [54], the loss is modeled as a complex spring constant

$$k = k_0 e^{i\Phi}, \tag{7.8}$$

where Φ is the loss angle. In this "structural damping" case, the damping scales as Ω^{-1}, which greatly reduces the thermal noise at higher frequency. In the viscous model, the cooling factor is enhanced by a factor Θ/Ω_M, while in the structural damping case, the cooling factor is enhanced by a factor $(\Theta/\Omega_M)^2$. Unfortunately, we don't know at this time which model is correct for our system, as we have not directly observed thermal noise.

7.3 A cold all-optical trap (Phase 2)

The first cooling experiment we performed was with the stable double optical spring described in Section 6.3. To demonstrate the cooling, we operated the cavity with slightly varying detunings but fixed power levels to vary the optical damping, while maintaining a constant resonant frequency. The feedback bandwidth was limited to below 170 Hz in all cases, and heavily attenuated at higher frequencies. The limiting noise source is frequency noise of the laser that is converted into intensity fluctuations in the detuned cavity, and drives the mirror position. It is straightforward to calibrate the PDH error signal of the subcarrier by injecting a frequency excitation into the laser, and measuring the response to the excitation. We then convert to meters by the relationship

$$\frac{\Delta\omega_0}{\omega_0} = \frac{\Delta L}{L}. \tag{7.9}$$

We estimate the effective temperature of the optomechanical mode by measuring the displacement of the mirror, and equating $(1/2)Kx_{\mathrm{RMS}}^2 = (1/2)k_B T_{\mathrm{eff}}$, where x_{RMS} is the RMS motion of the mirror. The RMS motion of the mirror is determined by integrating the noise spectral density from 1500 to 2300 Hz. The displacement noise is shown in Fig. 7-1. The lowest measured temperature of 0.8 K corresponds to a reduction in N by a factor of

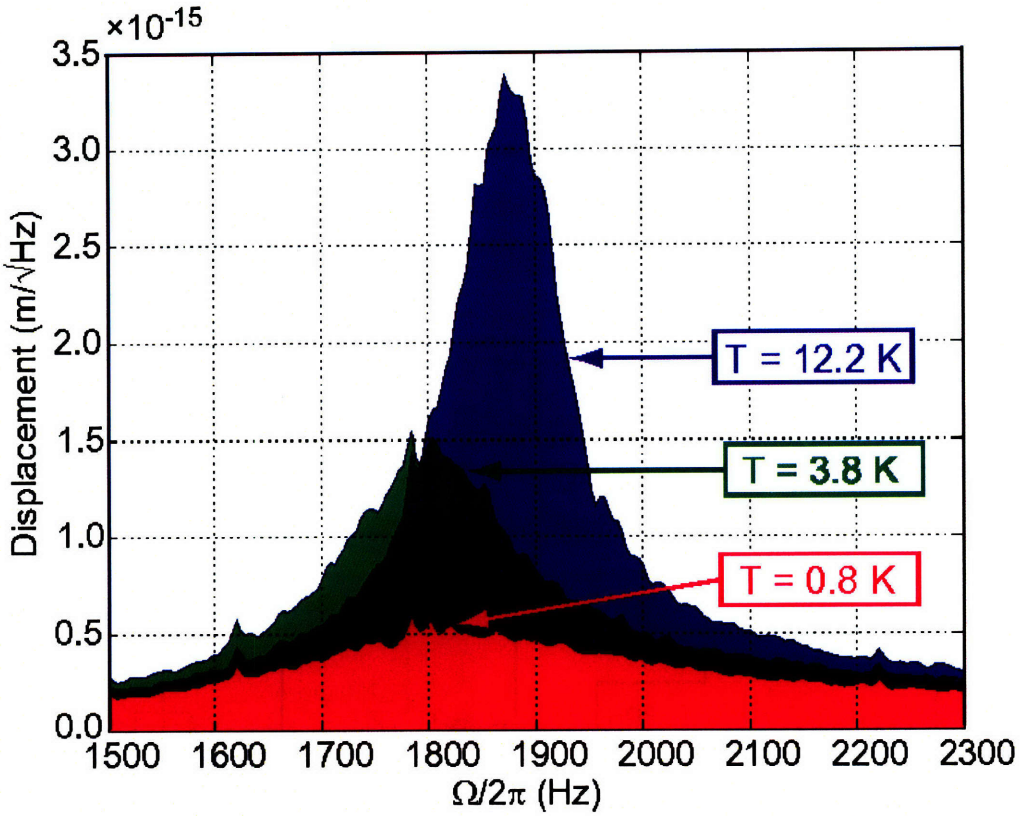

Figure 7-1: The measured noise spectral density of the cavity length is shown for several configurations corresponding to different detunings. The lowest amplitude (magenta) curve corresponds to $\delta_C \approx 3$ and $\delta_{SC} \approx -0.5$. The other (green and blue) curves are obtained by reducing δ_{SC} and increasing δ_C in order to keep Θ approximately constant, while varying Γ_{eff}. The spectrum is integrated between 1500 and 2300 Hz to calculate the RMS motion of the oscillator mode, giving effective temperatures of 0.8, 3.8 and 12.2 K. The limiting noise source here is not thermal noise, but in fact frequency noise of the laser, suggesting that with reduced frequency noise, even lower temperatures could be attained.

2.5×10^3. We point out that if we were limited by thermal noise from viscous damping, we would expect a temperature reduction closer to $Q_M \times (\Theta/\Omega_M) \approx 3 \times 10^4$. These results are reported in Ref. [73].

7.4 Cold damping of an optical spring (Phase 2.5)

From Eq. 7.9, we see that to easily mitigate the effect of laser frequency noise on a displacement measurement, one need only shorten the cavity length. Therefore, we shortened the Phase 2 cavity as much as possible, limited by the size of the suspension cages of the mirrors, to about 10 cm. A reduction in the displacement noise by a factor of 10 should imply a reduction of 10^2 in the temperature, which would increase the cooling factor to approximately 2.5×10^5. At that level, we would expect to be limited by the thermal noise of the oscillator. In order to avoid this limitation, and also to gain experience with lower frequency oscillators, we cut the optical fibers below their attachment to the mirror. This reduced the resonant frequency of the mirror to 12.75 Hz from 172 Hz, and increased its quality factor to 19,950 from 3,200, greatly reducing the thermal noise. The layout of the experiment is shown in Figure 7-2. Results from this experiment appear in Ref. [76].

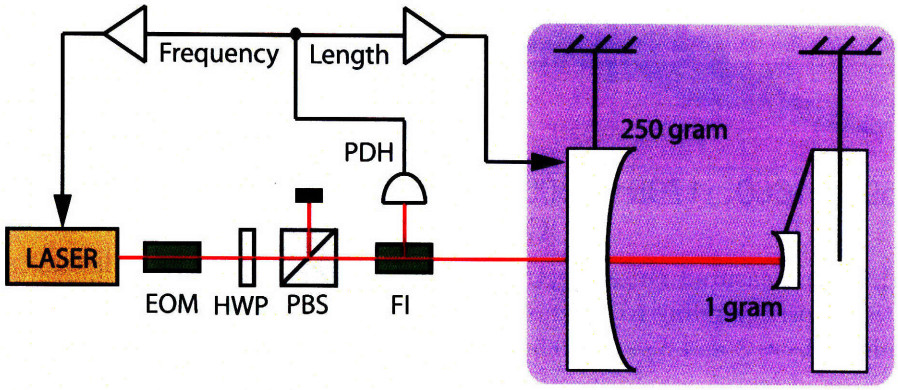

Figure 7-2: Simplified schematic of the experiment. About 100 mW of $\lambda_0 = 1064$ nm Nd:YAG laser light passes through a Faraday isolator (FI) and a half-waveplate (HWP) and polarizing beamsplitter (PBS) combination that allows control of the laser power, before being injected into the cavity, which is mounted on a seismic isolation platform in a vacuum chamber (denoted by the shaded box). A Pound-Drever-Hall (PDH) error signal derived from the light reflected from the cavity is used to lock it, with feedback to both the cavity length (actuated via magnets affixed to each suspended mirror), as well as the laser frequency.

Several factors limit the performance of this shorter cavity, however. First, the FSR of

the cavity is increased to 1.5 GHz, which is out of the range of our ability to easily produce a subcarrier. Hence, we were limited to a single optical spring. Additionally, a parametric instability of the drumhead motion of the 1 gram mirror (predicted to be 139.4 kHz by finite element analysis) at 136.8 kHz occurred at modest power levels, limiting the optical spring frequency to about 1 kHz. Unlike the input mirrors, we do not have magnets placed directly on the mirror, and we have no actuator easily capable of providing feedback at this frequency.

Despite these limitations, we are able to create a 1 kHz optical spring, which we then cold damp through active feedback. The cavity is locked off-resonance to $\delta_\gamma \approx 0.5$, to maximize the optical restoring force. The error signal for the locking servo, generated using the Pound-Drever-Hall technique [82], is split between a high bandwidth analog path fed back to the laser frequency, and a digital path fed back to the input mirror's magnet/coil actuators. The digital feedback is used at frequencies below 10 Hz to keep the cavity locked in its operating state. The analog feedback to the laser frequency is arranged so that it damps and cools the motion of the oscillator. The effective damping may be controlled by adjusting the gain of the feedback loop. Additional analog feedback is supplied to the magnet/coil actuators to damp a parametric instability of the input mirror at 28 kHz.

The noise in our experiment remains dominated by frequency noise of the laser at Θ. We estimate the effective temperature of the optomechanical mode, as determined by this noise. To determine x_{RMS} in this experiment, we first find the resonant frequency and damping of the oscillator by measuring its frequency dependent response to a driving force, shown in Fig. 7-3. In the same configuration, we then measure the noise spectral density of the error signal from the cavity, calibrated by injecting a frequency modulation of known amplitude at 12 kHz. The measured displacement spectra, as the electronic damping was varied, are shown in Fig. 7-4. Since the optical spring resonance is at $\Omega \approx 2\pi \times 1000$ Hz, we integrate the spectrum from 850 Hz to 1100 Hz to obtain an estimate of the motion of the mirror. At other frequencies, sensing noise not present on the mirror itself is dominant. To correct for the finite integration band, we assume a thermally driven displacement noise spectrum for the oscillator, given by

$$\langle x^2 \rangle = \frac{4\, k_B\, T_{\mathrm{eff}}\, \Gamma_{\mathrm{eff}}/M}{(\Theta^2 - \Omega^2)^2 + (\Omega_{\mathrm{eff}}\, \Omega/Q_{\mathrm{eff}})^2}\,, \tag{7.10}$$

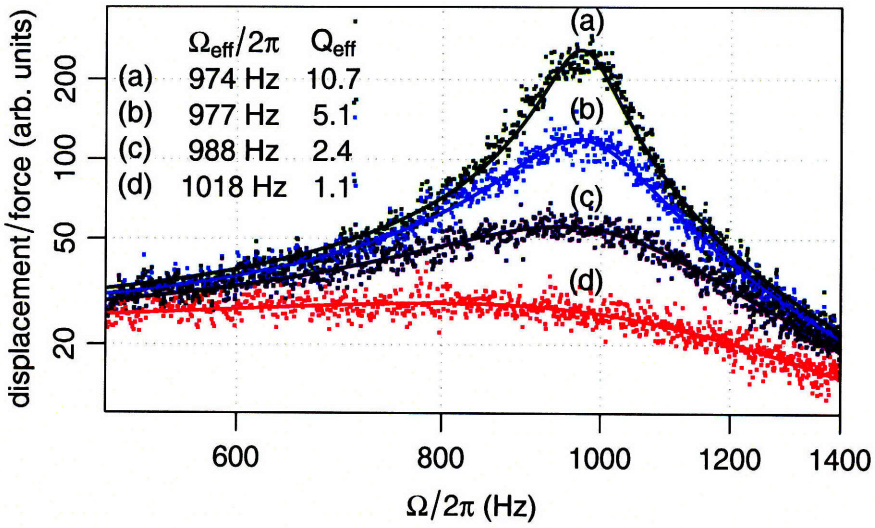

Figure 7-3: The transfer function of an applied force to mirror motion, for increasing levels of damping [curves (a) to (d)]. The force is applied via the magnet/coil actuators, and the response is measured by the PDH error signal. The points are measured data, and the lines are fitted Lorentzians from which the resonant frequency and damping constant are derived for each configuration. Statistical errors in the fit parameters are of order 1%.

and find $T_{\rm eff}$ by setting our measured spectrum integral equal to a thermal spectrum integrated over the same frequency band. The lowest temperature reached is 6.9 ± 1.4 mK. Thus the cooling factor from the ambient $T_M = 295$ K is 43000 ± 11000. Systematic error in the calibration dominates statistical error in these uncertainty estimates. We note that the mechanical quality factor was increased by a factor of about 80, from 19950 to 1.6×10^6, by optical dilution. Without an optical spring, effective temperatures below 15 mK could not have been reached given the mechanical losses of the oscillator. Further reduction of the temperature for our cavities likely requires the use of a Michelson interferometer to reject the laser noise.

7.5 LIGO cooling

While the optical spring provides a convenient method to dilute the thermal noise of our oscillators, it is by no means the only method. The essential feature to all of these schemes is a sensitive readout. The effectiveness of any technique is limited by how far the readout noise is from the SQL. The LIGO interferometers operate a factor of about 10 above the SQL

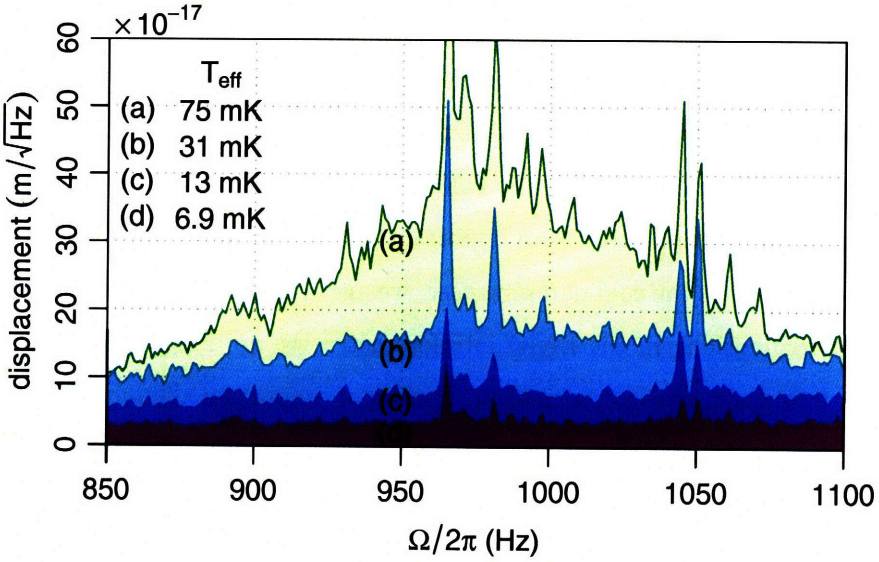

Figure 7-4: The measured noise spectral density of the mirror displacement. The curves (a) to (d) correspond to increasing gain in the damping feedback loop; for each, the parameters of the resonance are measured and depicted in Fig. 7-3. The spectra are integrated from 850 to 1100 Hz, the frequency range where the mirror motion is the dominant signal, to obtain the RMS motion of the mirror and its effective temperature. The broad limiting noise source is frequency noise of the laser. Narrow spectral features in addition to the main optical spring resonance are due to coupling of acoustically driven phase noise.

at its closest approach near 150 Hz. The mirrors of the interferometer are usually considered to behave as 0.7 Hz pendulums, yet this is only true when the mirrors are uncontrolled. When the interferometer is operating, a control system acts to lock the mirrors of each cavity to each other, in a way very similar to that of a spring. We show that with slight modifications to the control system, we may make the servo behave almost identically to a spring, thereby creating the thermal dilution.

The four mirrors of the LIGO interferometer (Fig. 7-5), each an extended object with displacement along the optical beam direction x_i ($i = 1, \ldots, 4$), are suspended as pendulums. The servo control system which keeps the interferometer mirrors at the resonant operating point is an essential component of this study. While all longitudinal and angular degrees of freedom of the mirrors are actively controlled, we limit our discussion to the differential arm cavity motion, which is the degree of freedom excited by a passing gravitational wave, and hence also the most sensitive to mirror displacements. This mode corresponds to the differential motion of the centers of mass of the four mirrors, $x_c = (x_1 - x_2) - (x_3 - x_4)$, and has a reduced mass of $M_r = 2.7$ kg. A signal proportional to differential length changes

is measured at the antisymmetric output of the beam splitter, as shown in Fig. 7-5. This signal is filtered by a servo compensation network before being applied as a force on the differential degree of freedom, by voice coils that actuate magnets affixed to the mirrors.

Although this measurement and the cold damping of an optical spring measurement both rely on a servo system, there is an important distinction in considering the calibration of the mirror motion. In the cold damping case, we are limited by laser frequency noise that drives the mirror motion. In the LIGO interferometer, we are limited by sensing noise at the resonant frequency, not mirror motion. This is an important distinction, and we show here that we require greater care in the calibration when the sensing noise is significant.

The degree of freedom that we *intend* to study as a quantum particle is the differential mirror motion x_c. However, optical measurements probe the location of the mirror surface (averaged over the optical beam), which differs from center-of-mass location due to the mirror's *internal* thermal noise), and include an additional *sensing* noise due to the laser shot noise. We combine these noises into a total displacement noise X_N, and write the output signal as

$$x_s = x_c + X_N \,. \tag{7.11}$$

The center-of-mass motion is also subject to a noise force F_N (including for example, the thermally driven motion of the mirror suspensions), and a feedback force that is proportional to x_s. The resulting equation of motion in the frequency domain is given by:

$$-M_r \left[\Omega^2 - i\,\Omega\,\Omega_p\,\phi(\Omega) - \Omega_p^2\right]\, x_c = F_N - K(\Omega) x_s \,. \tag{7.12}$$

Here $K(\Omega)$ is the frequency-domain feedback filter kernel, and the $\phi(\Omega)$ term accounts for mechanical damping. For a viscously damped pendulum with quality factor $Q_p = \Omega_p/\Gamma_p$ (Ω_p and Γ_p correspond to the real part and twice the imaginary part of the complex eigenfrequency of the pendulum), $\phi(\Omega) = 1/Q_p$. If the damping is not viscous, but instead caused by internal friction $\phi(\Omega)$ takes on a more complex form [54]. Combining Eqs. 7.11 and 7.12, we obtain the equation of motion for the center-of-mass:

$$-M_r \left[\Omega^2 - i\,\Omega\,\Omega_p\,\phi(\Omega) - \Omega_p^2 - K(\Omega)/M_r\right]\, x_c = F_N - K(\Omega) X_N \,. \tag{7.13}$$

In this experiment, we adjust the control kernel so that

$$K(\Omega)/M_r \approx \Theta^2 + i\Omega\Gamma_{\text{eff}} \tag{7.14}$$

with Θ and Γ_{eff} much larger than Ω_p and Γ_p, respectively, such that the modified dynamics of x_c are given by a damped oscillator driven by random forces:

$$-M_r[\Omega^2 - i\Omega\Gamma_{\text{eff}} - \Theta^2]x_c = F_N - K(\Omega)X_N\,. \tag{7.15}$$

The output of our experiment measures x_s, and in order to deduce true mirror motion x_c, we must consider the limiting source of noise. If noise predominantly drives the center-of-mass motion, i.e. $F_N \gg K(\Omega)\,X_N$, then $x_s \approx x_c$ (see Eq. 7.11) and the measured signal corresponds to the center-of-mass motion. However, in the case that surface or sensing noise dominates, i.e. $K(\Omega)\,X_N \gg F_N$, then a correction factor must be applied to the measured signal to deduce the center of mass motion. Taking Eqs. 7.11 and 7.15, in the limit that $F_N = 0$, we find that

$$x_c = \frac{K(\Omega)}{M_r\Omega^2}x_s. \tag{7.16}$$

If the levels of each noise X_N and F_N are not precisely known, then one can make a conservative correction by applying a factor $\max\left(1, K(\Omega)/M_r\Omega^2\right)$ to determine the worst possible center-of mass-motion, thereby accounting for the fact that the servo can inject noise back onto the oscillator. We may then determine the effective temperature of the mode

$$T_{\text{eff}} = \frac{M_r\Theta^2\delta x^2_{\text{rms}}}{k_B}, \tag{7.17}$$

where

$$\delta x^2_{\text{rms}} = \int_0^\infty \max\left(1, \frac{K(\Omega)}{M_r\Omega^2}\right)^2 S_{x_s}(\Omega)\,d\Omega \equiv \int_0^\infty S_{x_d} d\Omega\,. \tag{7.18}$$

S_{x_s} is the single-sided power spectral density of the measured motion x_s, and S_{x_d} includes the correction factor. We note that it is impossible to reliably measure the mirror motion at arbitrarily high frequencies, and the integral in Eq. 7.18 diverges in any real system. The integration therefore must be limited in its frequency band, as we later discuss.

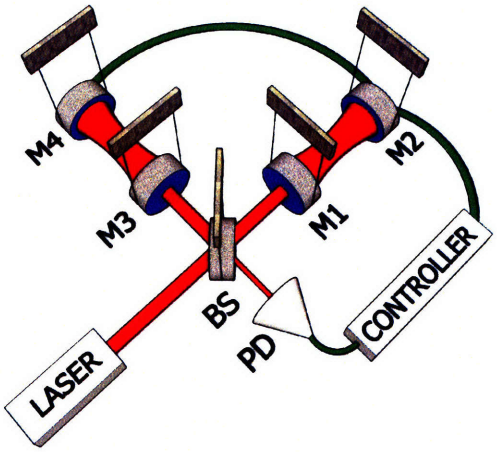

Figure 7-5: Optical layout of a LIGO interferometer. Light reflected from the two Fabry-Perot cavities formed by input and end mirrors, $M_1 - M_4$, is recombined at the beam splitter (BS). To control the differential degree of freedom, an optical signal proportional to mirror displacement is measured on the photodetector (PD), and fed back as a differential force on the mirrors, after filtering to form restoring and damping forces.

Finally, the corresponding occupation number may be determined by

$$N_{\text{eff}} = \frac{k_B T_{\text{eff}}}{\hbar \Theta}. \tag{7.19}$$

We form $K(\Omega)$ of Eq. 7.14 by convolving the position-dependent output signal with filter functions corresponding to the real and imaginary parts of the feedback kernel $K(\Omega)$. In the LIGO feedback system, there are additional filters and propagation delays that cause deviations from the ideal cold, damped spring, at high and low frequencies. Below 100 Hz, $K(\Omega)$ increases sharply to suppress seismically driven motion; at high frequencies (above a few kilohertz), $K(\Omega)$ decreases precipitously to prevent the control system from feeding shot noise back onto the test masses. However, in the frequency band important for this measurement (near the resonance), the feedback is well approximated by a spring and damping force, as shown in Fig. 7-6.

Measurement results and discussion: Fig. 7-7 shows the amplitude spectral density of mirror displacement for varying levels of cold damping. To infer the effective temperature of the mode, we must determine its effective frequency Ω_{eff} and estimate the root-mean-square displacement fluctuation δx_{RMS}. First we drive the differential mirror motion and measure the response, shown in Fig. 7-6. These response functions are fit to a damped

oscillator model; Θ and $Q_{\rm eff}$ are products of the fit. Then $\delta x_{\rm RMS}$ is computed by integrating the spectrum in the band from 100 to 170 Hz. To correct for the finite integration band, we scale the result by setting our measured spectrum equal to the integral over the same frequency band of a thermally driven oscillator spectrum,

$$S_{x_{\rm th}}(\Omega) = \frac{4k_B T_{\rm eff}\Gamma_{\rm eff}/M}{(\Theta^2 - \Omega^2)^2 + \Omega^2\Gamma_{\rm eff}^2}\,. \tag{7.20}$$

In this way, we measure a minimum effective temperature $T_{\rm eff} = 1.4 \pm 0.2\ \mu$K, corresponding to thermal occupation number $N_{\rm eff} = 234 \pm 35$. Systematic error of 15% in the calibration dominates statistical error in these uncertainty estimates. The spectra in Fig. 7-7 are predominantly limited by shot noise in the measurement band.

Cooling to the quantum limit: An interesting question arises as to whether this technique can lead to ground state cooling of the electromechanical oscillator. The continuous displacement measurement required for servo feedback does in fact introduce a small additional term to uncertainty relation for the oscillator position and momentum fluctuations, due to measurement-induced steady state decoherence. A sub-SQL noise spectrum in the vicinity of Θ can circumvent this limit [81]. This can be achieved by injection of a squeezed state into the antisymmetric port of the interferometer, for example. As classical noises are suppressed, and the squeezing becomes stronger, the oscillator approaches the ground state of the electro-optical potential well.

Future prospects with LIGO: In the coming years, two upgrades of the LIGO detectors are planned. The first, Enhanced LIGO, is presently underway with an expected completion date in 2009, and seeks to improve the sensitivity of the instruments above 40 Hz. The improvement in displacement sensitivity in the frequency band around 150 Hz, where the cold spring measurements were performed, is expected to be about a factor of 2. Subsequently, a major upgrade, Advanced LIGO, expected to be completed in 2014, should give a factor of 10 to 15 improvement in displacement sensitivity relative to that of the detector used for this work (with a concomitant factor of 4 increase in mass). In Advanced LIGO, the circulating laser power increases to 800 kW, permitting strong restoring forces to be generated optically. We expect Enhanced LIGO to reach ~ 6 times lower occupation number, approaching 40 quanta, and with Advanced LIGO, the detectors will operate at the SQL, approaching the ground state of the electro-optical potential well.

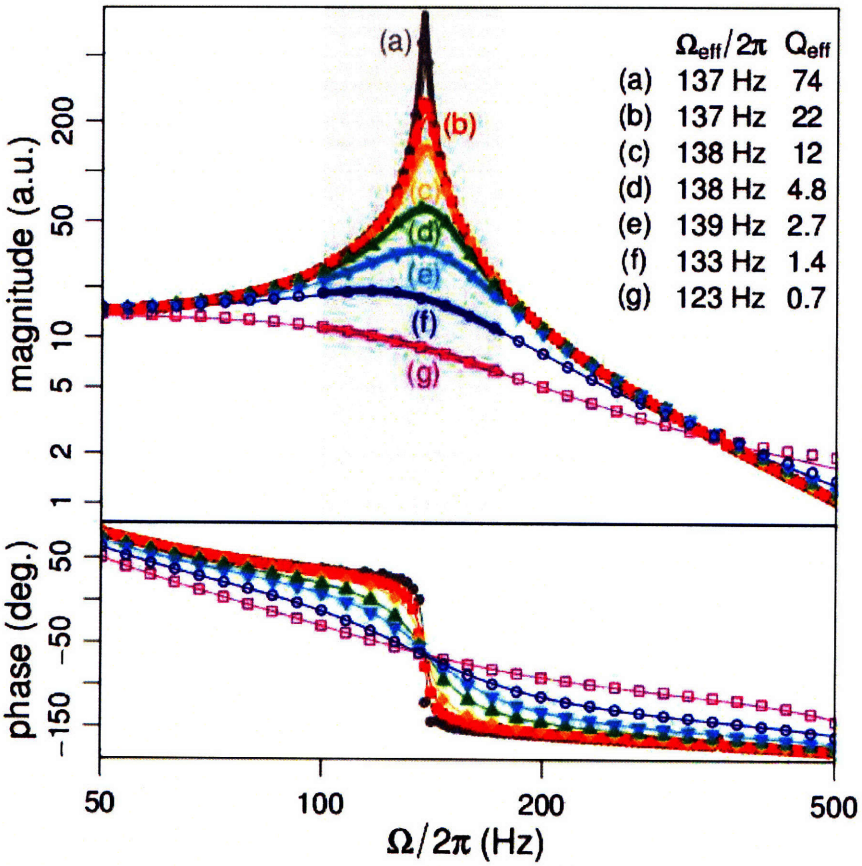

Figure 7-6: Response function of mirror displacement to an applied force, for various levels of damping. The points are measured data, the thin lines are a zero fit parameter model of the complete feedback loop, and the thick lines spanning the resonance (shown in the shaded region) are fitted Lorentzians, from which the effective resonant frequency and quality factor are derived for each configuration.

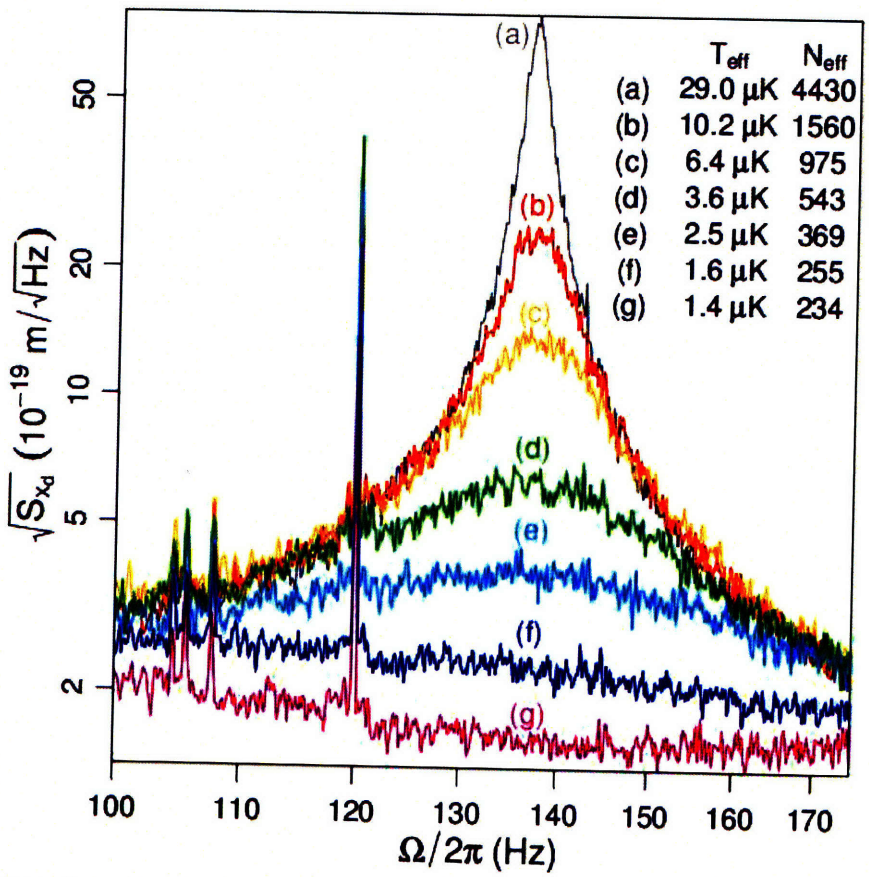

Figure 7-7: Amplitude spectral density of displacement in the frequency band of integration. The curves (from highest to lowest) were produced by applying increasingly strong cold damping to the oscillator, corresponding to the measurements of Fig. 7-6. The depression in the lowest curve is due to the shape of the background noise spectrum; the effects of the servo are corrected for according to Eqs. 7.11 – 7.18. The narrow line features between 100 and 110 Hz are mechanical resonances of auxiliary subsystems, and a 120 Hz power line harmonic is also visible.

As they approach the SQL, these devices should enable novel experimental demonstrations of quantum theory that involve kilogram-scale test masses with kilometer-scale separations [6, 12, 83]. The present work, reaching microkelvin temperatures, supplies evidence that interferometric gravitational wave detectors, designed as sensitive probes of general relativity and astrophysical phenomena, can also become sensitive probes of macroscopic quantum mechanics.

7.6 Summary

In this chapter, we have described how the experiments developed for the field of GW interferometry may also be used in the field of macroscopic quantum measurement. As a general rule, the effectiveness of a particular system is directly related to its distance from the SQL, which makes GW interferometers prime candidates for macroscopic quantum measurement experiments. We have applied optical and active feedback cooling techniques to the MIT experiments as well as to the 4 km Hanford detector.

Chapter 8

Future work

It appears that we have mostly exhausted the exploration of classical radiation pressure effects. In this section, we discuss the prospects for observing and utilizing quantum effects in GW interferometers, and for exploration of quantum mechanics in macroscopic mechanical systems.

8.1 Squeezed-input interferometers

Recent progress in squeezing technology [20–22, 24] has demonstrated that squeezers are capable of producing squeezed states that satisfy the requirements for injection into a GW interferometer. They have achieved squeezing within the entire GW frequency band, and demonstrated 10 dB reduction of shot noise. Clearly the next step is the application of a squeezer to a real GW interferometer, plans for which are already underway. The initial test has been proposed to inject squeezed light into the dark port of the Hanford 4 km detector at the conclusion of the Enhanced LIGO science run. If this test is completed successfully, there will be a strong argument for bringing squeezing to Advanced LIGO. The use of squeezed light not only allows for lower quantum noise, it also allows for identical noise performance with lower input power. This could be a significant risk reduction factor for Advanced LIGO, which may be threatened by thermally induced and parametric instabilities. Additionally, the high power level circulating in the power recycling cavity requires challenging thermal compensation. Therefore, it appears likely that squeezing will be an important tool in the field of gravitational wave detection in the coming years. It is likely that the first few implementations of squeezing in a GW interferometer will be performed without filter

cavities, although, the long term success of squeezing will likely depend upon filter cavities to provide broadband improvements.

8.2 Radiation pressure noise and squeezing

In the ponderomotive squeezing experiment, it may be quantum radiation pressure noise that is most easily observable non-classical effect. Quantum radiation pressure noise has yet to be observed in any experiment. The displacement noise sensitivity required is nearly identical to that of observing squeezing, however, it may be done without the aid of an optical spring. One unfortunate side effect of a stiff optical spring is that it suppresses the signal at the photodetector, which has the side effect of amplifying any technical noise. Most notably, light that scatters out of the laser beam reflects off any moving surface, then scatters back into the main beam. This creates significant phase noise that appears as cavity motion. The effects are severely amplified by the optical spring because the real cavity motion is suppressed, but the scattered light is not. As the technical noise sources in our system are reduced, it is likely that we will soon observe the thermal noise of our end mirror oscillators, probably precluding the observation of quantum radiation pressure noise. However, construction is currently underway of a monolithic fused silica suspension for the end mirror that should have greatly reduced thermal noise. The noise is currently about a factor of 10 too high in displacement sensitivity to allow for observation of quantum radiation pressure noise (see Figure 6-16).

Once observation of quantum radiation pressure noise is achieved, the observation of squeezing will likely require greater reductions of technical noise sources and an improved end mirror suspension, as we noted above. Additionally, Advanced LIGO should provide the capability to observe both radiation pressure noise and squeezing.

8.3 The standard quantum limit

The largest goal in the field remains the direct observation of, as well as the overcoming of, the Standard Quantum Limit. Initial LIGO remains the closest experiment to approaching the SQL in optical systems at a factor of 10 away. The prospects for reaching the SQL in a table top experiment such as the ones described in this thesis are extremely challenging, but perhaps not impossible. The biggest challenge to reaching the SQL is to find a frequency

band for which the thermal noise is sufficiently small. At low frequency, suspension thermal noise dominates with either a Ω^{-2} or $\Omega^{-5/2}$ dependence. At high frequency, coating or internal thermal noise is expected to dominate with a $\Omega^{-1/2}$ dependence. The hope is that somewhere between the two thermal noise sources, the SQL (with Ω^{-1} dependence) will be observable. Preliminary calculations suggest that it may be possible with somewhat smaller masses, of order 0.1 grams. Pursuit of this goal is of critical importance, both as a precursor to Advanced LIGO, which is expected to operate near or below the SQL, and as a path towards non-classical behavior of macroscopic masses.

8.4 Entanglement

Entanglement is a quantum mechanical phenomenon in which the state of a system becomes inseparable from the state of another system. Observation of entanglement is a strong demonstration that a system is behaving non-classically. In macroscopic optomechanical systems, there has been considerable interest in generating entanglement [84–87]. The entanglement is generated via the radiation pressure coupling, and may manifest as entanglement between the oscillator and the optical field, between two oscillators, or between two optical fields. In [88], Wipf et al. calculate that in our double optical spring configuration, the coupling of each optical field to the mirror position results in the optical fields becoming entangled. Classical noises will tend to destroy the entanglement, although it is expected that if we enter the regime where radiation pressure noise and squeezing are observable, then entanglement should also be observable, and it is not necessary to operate near the SQL. To operate our interferometer configuration with a double optical spring, however, we will need to acquire a beamsplitter that is 50% reflective for two polarizations, or to instead separate the fields only in frequency, not in polarization. Another exciting prospect is to observe entanglement between the mirror and the optical field. Preliminary calculations suggest that to achieve this goal in our system, sensitivity better than the SQL is required, making optomechanical entanglement a tantalizing, but extremely challenging goal [81,88].

8.5 Ground state cooling

Reaching the quantum ground state with a mass of order 1 gram (or even more massive) will be a symbolic milestone of quantum mechanics entering the macroscopic scale of everyday objects. However, the question then becomes "what next?" One prospect is to place the mirror into a squeezed state [89], in which its position uncertainty is less than the width of its ground state wavefunction. We have shown that the injection of squeezed light allows performance below the SQL, corresponding roughly to the ground state width. Another prospect is to observe quantum jumps in the mirror's energy state, which would require an alternative readout scheme that measures the mirror's energy as opposed to its position [90]. The requirements for this measurement are, however, likely not experimentally feasible for our mass range in the near future.

8.6 Summary

In the coming years, a broad range of experiments will approach the quantum regime in mechanical systems. It is likely that the first results will be observation of effects that may be achieved far from the SQL: quantum radiation pressure noise and squeezed vacuum and optical entanglement generated from mechanical coupling. Following these results, we hope that the systems will progress to and beyond the SQL, allowing for a broad range of tests of quantum mechanics. Advanced LIGO will likely be the quintessential system that brings many of these effects together. It will operate at or below the SQL, may benefit from input squeezed vacuum, and generate ponderomotive squeezing and quantum radiation pressure noise at a mass scale (40 kg) that exceeds the nearest competitor by many orders of magnitude, and is also capable of the direct detection of GWs.

Appendix A

Code simulation results compared to analytical calculations

In this appendeix, we consider an interferometer configuration that is shown in Fig. A-1, and in Fig. A-2 we show fields propagating in the interferometer as well as modes of motion of the mirrors. The interferometer is similar to that used in GW detection: a Michelson interferometer with Fabry-Perot cavities in each arm. All the mirrors of the interferometer are suspended as pendulums. Power-recycling is optional and is not included here. The configuration shown has a few unusual features compared with a conventional interferometer, however. First, the end mirrors of the arm cavities are a common suspended object, coated with a high-reflectivity coating on both surfaces and assumed to have an opaque substrate. Second, this cavity end mirror object is very light, with a typical mass of 1 g, and is suspended as a pendulum with resonant frequency of about 1 Hz. All remaining optics are assumed to have a mass of 250 g, and are also suspended as pendulums with a resonant frequency of 1 Hz. Third, the cavities are detuned from resonance. The configuration is designed to extract ponderomotive squeezing from the interferometer, but an alternative design with seperate end mirrors was eventually chosen and that design is detailed in Chapter 6.

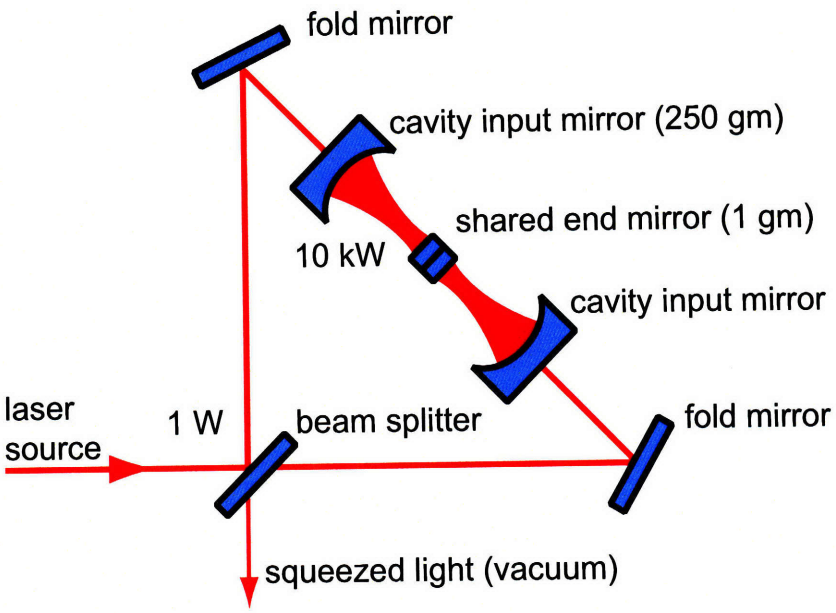

Figure A-1: Schematic of a an interferometer designed to extract ponderomotively squeezed light due to radiation-pressure-induced motion of the ultra-light shared mirror. Light from a highly intensity- and frequency-stabilized laser source is incident on the beamsplitter. High-finesse Fabry-Perot cavities in the arms of the Michelson interferometer are used to build up the carrier field incident on the end mirrors of the cavity, which are a single mechanical object.

A.0.1 Ideal optical springs

In this section we study analytically a crucial component of the interferometer design: the optical spring effect, especially in the case of two identical detuned cavities with a common end mirror. The input-output relation of this system can be obtained by carrying out our generic procedure analytically. In doing so, we extend previous results in Refs. [13, 30] to include two new features. First, we consider motions of all *three* mirrors, with mass of the input mirrors different from that of the common end mirror. Second, in our system the carrier phases incident on mirrors are different; under such a circumstance, formulas developed in Sec. 4.4 are non-trivial extensions to existing ones.

In order to make results intuitively understandable, we consider only the ideal system, with the two input mirrors completely identical, the common mirror perfectly reflective on both sides, the two cavities having exactly the same lengths, the carrier incident on both input mirrors having equal amplitude and phase, and with a perfect beamsplitter. We also ignore the free pendulum frequency, and consider the test masses to be free. Similar to

Parameter	Symbol	Value	Units
Light wavelength	λ_0	1064	nm
End mirror mass	m	1	g
Input mirror mass	M	0.25	kg
Input mirror transmission	T_i	4×10^{-4}	–
Arm cavity finesse	$\mathcal{F}$	1.6×10^4	–
Loss per bounce	–	5×10^{-6}	–
Arm cavity detuning	ϕ	10^{-5}	λ_0
Input power	I_0	1	W
BS reflectivity asymmetry	$\Delta_{\rm BS}$	0.01	–
Michelson phase imbalance	$\Delta\alpha_{\rm M}$		
Michelson loss imbalance	$\Delta\epsilon_{\rm M}$		
Input mirror mismatch	Δ_T	5×10^{-6}	–
Detuning mismatch	Δ_ϕ	10^{-7}	λ_0
Arm cavity loss mismatch	Δ_ϵ	2×10^{-6}	–

Table A.1: Select interferometer parameters and their nominal values.

ϵ	bandwidth	$(T_i + T_e)c/(4L)$
$\epsilon_{\rm L}$	bandwidth due to loss	$T_e c/(4L)$
$-\lambda$	resonant frequency	$\phi c/L$
α	characteristic quadrature rotation angle	$\arctan(\lambda/\epsilon)$

Table A.2: Quantities associated with the detuned arm cavities .

previous studies, we assume a high-finesse cavity and ignore the interaction between the motion of the input mirror and the carrier light outside the cavity. We retain terms only to the leading order in $\epsilon L/c$, $\lambda L/c$ and $\Omega L/c$, where L is the cavity length, c is the speed of light, Ω is the sideband frequency, and $(-\lambda - i\epsilon)$ is the complex optical resonant frequency of the cavity with fixed mirrors [$-\lambda$ denotes the resonant frequency and ϵ the bandwidth, defined in Table A.2; and we ignore end-mirror loss].

Differential Mode

With the above assumptions, the differential optical mode couples only to differential modes of mirror motion: those with the two input masses moving such that $x_A = -x_B \equiv x_{\rm D}$, and arbitrary x_m [see Fig. A-2]; such modes form a two-dimensional subspace of all possible motions of the three mirrors. In the ideal case, we only need to study this mode. The

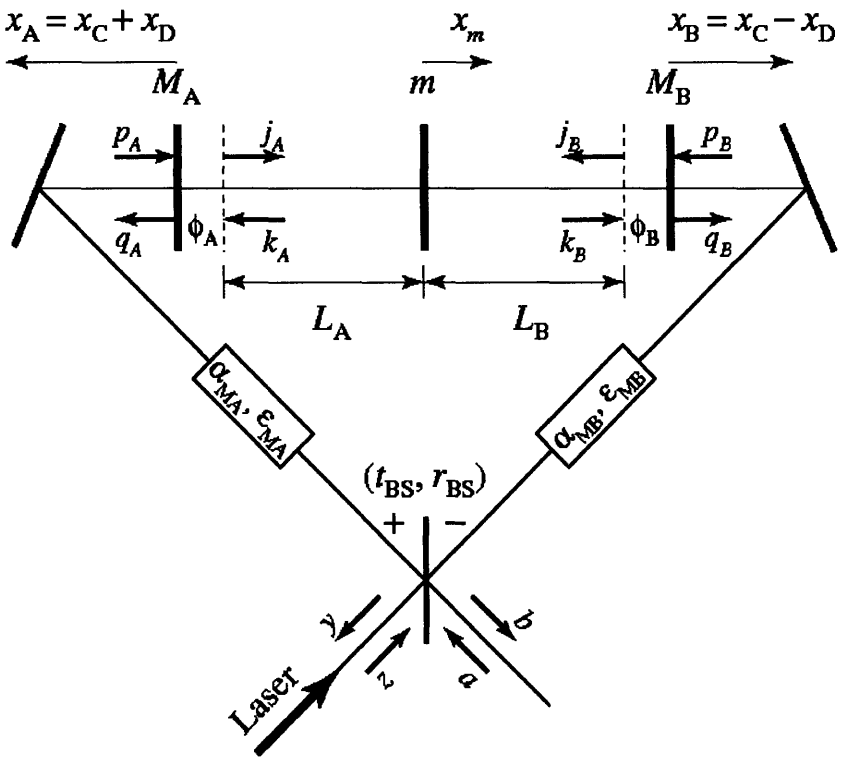

Figure A-2: Optical fields propagating in the interferometer, and modes of motion of the mirrors. In particular, $\alpha_{MA,B}$ and $\epsilon_{MA,B}$ are artificial detunings and losses one can add to the two arms of the Michelson interferometer, respectively, see Sec. A.0.2 for their significance.

differential input-output relation is given by

$$\begin{pmatrix} b_1 \\ b_2 \end{pmatrix} = \frac{1}{\mathcal{M}_D} \mathbf{R}_\alpha \left[\mathbf{C}_D \mathbf{R}_{-\alpha} \begin{pmatrix} a_1 \\ a_2 \end{pmatrix} + \mathbf{s}_D \left[x_m^{(0)} + x_D^{(0)} \right] \right], \tag{A.1}$$

with

$$\mathbf{C}_D = \begin{bmatrix} -(\Omega^2 - \lambda^2 + \epsilon^2)\Omega^2 - \lambda\iota_D & 2\epsilon\lambda\Omega^2 \\ -2\epsilon\lambda\Omega^2 + 2\epsilon\iota_D & -(\Omega^2 - \lambda^2 + \epsilon^2)\Omega^2 - \lambda\iota_D \end{bmatrix},$$

$$\mathbf{s}_D = \frac{2\sqrt{\epsilon\iota_D\Omega^2}}{L h_{SQL}^D} \begin{pmatrix} \lambda \\ -\epsilon + i\Omega \end{pmatrix}, \tag{A.2}$$

and

$$\mathcal{M}_D = \Omega^2 \left[(\Omega + i\epsilon)^2 - \lambda^2 \right] + \lambda\iota_D \,. \tag{A.3}$$

Here $x_m^{(0)}$ is the motion of a free end mirror with the same mass, $x_{\rm D}^{(0)}$ is the free differential motion of the input mirrors ($x_A^{(0)} = -x_B^{(0)} = x_{\rm D}^{(0)}$); $\alpha = \arctan(\lambda/\epsilon)$ is the carrier phase at the end mirror. The carrier incident on the input mirrors has phase 0, the carrier inside the cavity, leaving the input mirror has phase $\alpha - \phi$, while the carrier inside the cavity entering the input mirror has phase $\alpha + \phi$. The quantity $h_{\rm SQL}^{\rm D}$ is the free-mass Standard Quantum Limit associated with the differential mode, given by

$$h_{\rm SQL}^{\rm D} = \sqrt{\frac{2\hbar}{\mu_{\rm D}\Omega^2 L^2}}\,, \qquad \mu_{\rm D} \equiv 2mM/(m+2M)\,. \tag{A.4}$$

The quantity $\iota_{\rm D}$, defined by

$$\iota_{\rm D} = \frac{8\omega_0 I_c}{\mu_{\rm D} L c}\,, \tag{A.5}$$

measures the strength of optomechanical coupling [notice the dependence on carrier intensity I_c and the inverse dependence on the effective mass of the differential mode mechanical oscillator $\mu_{\rm D}$]. Roots of $\mathcal{M}_{\rm D}$ are the (complex) resonant frequencies of the coupled optomechanical system. From $\iota_{\rm D}$ we define a characteristic frequency,

$$\Theta_{\rm D} \equiv \sqrt{\iota_{\rm D}\lambda/(\epsilon^2+\lambda^2)}\,. \tag{A.6}$$

For systems with $\Theta_{\rm D} \ll \epsilon$, the two resonances are well separated, and are given approximately by $\pm\Theta_{\rm D}$ [mechanical frequency due to optical spring] and $(\pm\lambda - i\epsilon)$ [optical resonant frequency], respectively — this is indeed the regime in which we construct our experiment.

The differential optical mode couples to a two-dimensional subspace of all possible motions of the three mirrors. It is instructive to look at the motion of separate mirrors, in the regime of $\Omega \ll \epsilon$, i.e. for sideband frequencies Ω well within the linewidth of the cavities:

$$\begin{bmatrix} x_m \\ x_{\rm D} \end{bmatrix} = \frac{1}{\Theta_{\rm D}^2 - \Omega^2} \begin{bmatrix} \dfrac{\Theta_{\rm D}^2}{\Lambda^2+1} - \Omega^2 & -\dfrac{\Lambda^2\Theta_{\rm D}^2}{\Lambda^2+1} \\ -\dfrac{\Theta_{\rm D}^2}{\Lambda^2+1} & \dfrac{\Lambda^2\Theta_{\rm D}^2}{\Lambda^2+1} - \Omega^2 \end{bmatrix} \begin{bmatrix} x_m^{(0)} \\ x_{\rm D}^{(0)} \end{bmatrix}. \tag{A.7}$$

Here we have defined $\Lambda^2 \equiv 2M/m$. From Eq. (A.7), we conclude immediately that

$$x_m + x_D = -\frac{\Omega^2}{\Theta_D^2 - \Omega^2}\left[x_m^{(0)} + x_D^{(0)}\right]. \tag{A.8}$$

This change in response is exactly what happens when a free test particle is connected to a spring with mechanical resonant frequency Θ_D. Equation (A.8) reveals a crucial advantage of the optical spring — that the response of the cavity length to external disturbances (driven by seismic and/or thermal forces, e.g.) is greatly suppressed from the corresponding value for free-mass systems. Theoretically, this suppression is present even when a mechanical spring is used. However, mechanical springs introduce thermal noise, usually of much higher magnitude due to the intrinsic mechanical loss [30,91].

It is interesting to notice that the suppression of total cavity length fluctuations is achieved collectively by the end mirror and the input mirror. As we see from Eq. (A.7), [in the case of large Λ], the motion of the end mirrors x_m is suppressed from its free mass value by the factor in Eq. (A.8), while the motion of the input mirrors x_D is not influenced by the spring, since it is relatively massive. Fortunately, through the $(1,2)$ component of the matrix on the RHS of Eq. (A.7), this motion of the input mirror is imposed onto the end mirror with opposite sign, again suppressing the total cavity length fluctuations.

Now let us restrict ourselves to the regime of $\Omega < \Theta_D < \epsilon$, and study the quantum fluctuations and classical component of the output field (due to classical disturbances to the mirrors). As we shall see shortly, this regime has two crucial features: (i) the response of the output field to $x_m^{(0)} + x_D^{(0)}$, and thus length fluctuations due to seismic and thermal noise, are greatly suppressed by the optical spring and (ii) the output squeezed state is frequency-independent.

For quantum fluctuations, we have

$$\frac{\mathbf{C}_D}{\mathcal{M}_D} \to \begin{bmatrix} -1 & 0 \\ 2\epsilon/\lambda & -1 \end{bmatrix}, \tag{A.9}$$

which is frequency-independent. It is straightforward to derive that the quantum noise spectrum in the $b_\zeta \equiv b_1 \cos\zeta + b_2 \sin\zeta$ quadrature [Cf. Eq. (4.64)]:

$$S_\zeta \to 1 + \frac{2\epsilon^2}{\lambda^2} - 2\sqrt{\frac{\epsilon^2}{\lambda^2} + \frac{\epsilon^4}{\lambda^4}}\cos(2\zeta - 3\alpha). \tag{A.10}$$

In particular, terms in ϵ/λ are associated with squeezing, where the constant power squeeze factor e^{2q} ($q > 0$) is given by

$$\sinh q = |\epsilon/\lambda| \,. \tag{A.11}$$

The minimum noise spectral density ($S_\zeta = e^{-2q}$) is reached at $\zeta = 3\alpha/2$, while at $\zeta = \alpha$ and 2α the noise spectrum is equal to the vacuum level ($S_\zeta = 1$). Values of ϵ/λ corresponding to several power squeeze factors are listed in Table A.3. As shown, ϵ and λ will not differ by a factor of more than ~ 2, for typically desired squeeze factors.

Now for the classical component, given by the second term in Eq. (A.1), we have

$$\frac{1}{\mathcal{M}_{\rm D}}\mathbf{R}_\alpha \mathbf{s}_{\rm D} \rightarrow \frac{2}{L h^{\rm D}_{\rm SQL}} \sqrt{\frac{\Omega^2}{\Theta^2_{\rm D}}\frac{\epsilon}{\lambda}} \begin{bmatrix} \sin 2\alpha \\ -\cos 2\alpha \end{bmatrix} . \tag{A.12}$$

This means the entire signal due to differential displacement $x_m^{(0)} + x_{\rm D}^{(0)}$ is in the single quadrature $\zeta = 2\alpha + \pi/2$, and there is no $x_m^{(0)} + x_{\rm D}^{(0)}$ signal in the $\zeta = 2\alpha$ quadrature. Interestingly, the quantum noise in this quadrature is right at vacuum level. In addition, since $h^{\rm D}_{\rm SQL} \propto 1/\Omega$, the response of b_ζ to $x_m^{(0)} + x_{\rm D}^{(0)}$ is proportional to Ω^2 at this regime – therefore not only the motion, but also the output field, has a suppressed response to thermal and seismic noises. Note here that the suppression factor is proportional to $\sqrt{I_c}$ (since $\theta_{\rm D} \propto \sqrt{\iota_{\rm D}} \propto \sqrt{I_c}$) – because motion is suppressed by I_c, while the optical sensing of mirror motion is enhanced by $\sqrt{I_c}$. Now suppose we introduce a noisy force which induces a spectral density S_x^N on a free mass, then the output classical noise will be

$$S_\zeta^N = 4\frac{\Omega^2}{\Theta_D^2}\frac{\epsilon}{\lambda}\sin^2(\zeta - 2\alpha)\frac{S_x}{L^2(h^{\rm D}_{\rm SQL})^2} \,. \tag{A.13}$$

At the minimum quantum noise quadrature, $\zeta = 3\alpha/2$, we have

$$\begin{aligned} S^N_{3\alpha/2} &= \frac{2\epsilon}{\lambda}\left[1 - \frac{\epsilon}{\sqrt{\lambda^2+\epsilon^2}}\right]\frac{\Omega^2}{\Theta_D^2}\frac{S_x}{L^2(h^{\rm D}_{\rm SQL})^2} \\ &\leq 0.6\frac{\Omega^2}{\Theta_D^2}\frac{S_x}{L^2(h^{\rm D}_{\rm SQL})^2} \,, \end{aligned} \tag{A.14}$$

where the inequality is obtained by taking maximum over all ϵ and λ. We note that because of the suppression factor Ω^2/Θ^2, the classical noise S_x^N can be much higher than the free-mass Standard Quantum Limit while still allowing the interferometer to generate squeezed

vacuum!

Squeeze Factor (dB)	3	7	10	20
ϵ/λ	0.58	1.13	1.42	2.12

Table A.3: Relationship between power squeeze factor and ϵ/λ, see Eq. A.11.

Common Mode

We now consider the common optical mode, which couples with motion of the input mirrors corresponding to $x_A = x_B \equiv x_C$. This mode is irrelevant to an ideal interferometer with identical arms and perfect contrast. In reality, however, the common mode *will* influence the output via couplings induced by differences (mismatch) between the two cavities, for example. Such effects can be quite important near the common-mode optomechanical resonance.

The input-output relation of the common mode, similar to that of the differential mode [cf. Eq. (A.1)], is given by:

$$\begin{pmatrix} y_1 \\ y_2 \end{pmatrix} = \frac{1}{\mathcal{M}_C}\mathbf{R}_\alpha \left[\mathbf{C}_C\mathbf{R}_{-\alpha}\begin{pmatrix} z_1 \\ z_2 \end{pmatrix} + \mathbf{s}_C x_C^{(0)}\right], \tag{A.15}$$

with [cf. Eq. (A.2)]

$$\mathbf{C}_C = \begin{bmatrix} -(\Omega^2 - \lambda^2 + \epsilon^2)\Omega^2 - \lambda\iota_C & 2\epsilon\lambda\Omega^2 \\ -2\epsilon\lambda\Omega^2 + 2\epsilon\iota_C & -(\Omega^2 - \lambda^2 + \epsilon^2)\Omega^2 - \lambda\iota_C \end{bmatrix},$$

$$\mathbf{s}_C = \frac{2\sqrt{\epsilon\iota_C\Omega^2}}{L h_{SQL}^C}\begin{pmatrix} \lambda \\ -\epsilon + i\Omega \end{pmatrix}, \tag{A.16}$$

and [cf. Eq. (A.3)]

$$\mathcal{M}_C = \Omega^2\left[(\Omega + i\epsilon)^2 - \lambda^2\right] + \lambda\iota_C\,. \tag{A.17}$$

h_{SQL}^C, the SQL associated with the common mode, is given by [cf. Eq. (A.4)]

$$h_{SQL}^C = \sqrt{\frac{2\hbar}{\mu_D\Omega^2 L^2}}, \quad \mu_C = 2M\,. \tag{A.18}$$

$\Delta_{(k)}$	$C_{(k)}$	$\varphi^{\mathrm{C}}_{(k)}$
$\dfrac{\Delta\epsilon}{\epsilon}$	$-\dfrac{\epsilon\lambda}{\epsilon^2+\lambda^2}$	$2\alpha+\pi/2$
$\dfrac{\Delta\epsilon_{\mathrm{L}}}{\epsilon}$	$-\dfrac{\epsilon}{\sqrt{\epsilon^2+\lambda^2}}$	α
$\dfrac{\Delta\lambda}{\lambda}$	$\dfrac{\epsilon\lambda}{\epsilon^2+\lambda^2}$	$2\alpha+\pi/2$
$\Delta\alpha_{\mathrm{M}}$	1	$2\alpha+\pi/2$
Δ_{BS}	0	
$\Delta\epsilon_{\mathrm{M}}$	$-\frac{1}{2}$	2α

Table A.4: Transfer function from carrier to differential output [see Eq. (A.29)], in the leading-order approximation. The same coefficients apply to phase-noise coupling, i.e., $N^{\mathrm{P}}_k = C_{(k)}$, $\varphi^{\mathrm{P}}_k = \varphi^{\mathrm{C}}_{(k)}$, in the low-frequency regime [see Eq. (A.33)].

The quantity ι_{C} is given by [cf. Eq. (A.5)]

$$\iota_{\mathrm{C}} = \frac{8\omega_0 I_c}{\mu_{\mathrm{C}} L c}\,. \tag{A.19}$$

For the common mode, we have a optomechanical resonant frequency of [cf. Eq. (A.6)]

$$\Theta_{\mathrm{C}} \equiv \sqrt{\iota_{\mathrm{C}}\lambda/(\epsilon^2+\lambda^2)}\,, \quad \text{if } \Theta_{\mathrm{C}} \ll \epsilon\,. \tag{A.20}$$

This frequency is in general much lower than its differential-mode counterpart, with

$$\frac{\Theta_{\mathrm{C}}}{\Theta_{\mathrm{D}}} = \sqrt{\frac{\iota_{\mathrm{C}}}{\iota_{\mathrm{D}}}} = \sqrt{\frac{\mu_{\mathrm{D}}}{\mu_{\mathrm{C}}}} = \sqrt{\frac{m}{m+2M}}\,. \tag{A.21}$$

A.0.2 Laser coupling to the antisymmetric port due to mismatch

Mismatch between the optical parameters of the two arm cavities, as well as imbalance in the beamsplitter reflection/transmission ratio and imperfect contrast of the Michelson interferometer, can couple the carrier and also the noise sidebands on the laser to the differential detection port. For each arm, A and B, we denote the true value of the kth

$\Delta_{(k)}$	$N^{A}_{(k)}$	$N^{A}_{(k)}(\Theta_C \to 0)$	$\varphi^{A}_{(k)}$
$\frac{\Delta\epsilon}{\epsilon}$	$\frac{\epsilon^2\left[\epsilon^2(\Omega^2+\Theta_C^2)^2+4\lambda^2\Theta_C^4\right]^{1/2}}{\lambda(\epsilon^2+\lambda^2)(\Omega^2-\Theta_C^2)}$	$\frac{\epsilon^3}{\lambda(\epsilon^2+\lambda^2)}$	$2\alpha - \arctan\frac{2\lambda\Theta_C^2}{\epsilon(\Omega^2+\Theta_C^2)}$
$\frac{\Delta\epsilon_L}{\epsilon}$	$\frac{\epsilon^2}{\lambda\sqrt{\epsilon^2+\lambda^2}}$	$\frac{\epsilon^2}{\lambda\sqrt{\epsilon^2+\lambda^2}}$	α
$\frac{\Delta\lambda}{\lambda}$	$\frac{\epsilon\left[(\lambda^2\Omega^2-\epsilon^2\Theta_C^2)^2+4\epsilon^2\lambda^2\Theta_C^4\right]^{1/2}}{\lambda(\epsilon^2+\lambda^2)(\Omega^2-\Theta_C^2)}$	$\frac{\epsilon\lambda}{\epsilon^2+\lambda^2}$	$2\alpha + \arctan\frac{2\epsilon\lambda\Theta_C^2}{\lambda^2\Omega^2-\epsilon^2\Theta_C^2}$
$\Delta\alpha_M$	$-\frac{\left[\lambda^2(\Omega^2-\Theta_C^2)^2+4\epsilon^2\Theta_C^4\right]^{1/2}}{\lambda(\Omega^2-\Theta_C^2)}$	-1	$2\alpha - \arctan\frac{2\epsilon\Theta_C^2}{\lambda(\Omega^2-\Theta_C^2)}$
Δ_{BS}	$\frac{2\epsilon\Omega^2}{\lambda(\Omega^2-\Theta_C^2)}$	$\frac{2\epsilon}{\lambda}$	2α
$\Delta\epsilon_M$	$\frac{\left[\left[(\epsilon^2+\lambda^2)\Omega^2-(2\epsilon^2+\lambda^2)\Theta_C^2\right]^2+\epsilon^2\lambda^2\Theta_C^4\right]^{1/2}}{2\lambda\sqrt{\epsilon^2+\lambda^2}(\Omega^2-\Theta_C^2)}$	$\frac{\sqrt{\epsilon^2+\lambda^2}}{2\lambda}$	$\alpha - \arctan\frac{\epsilon\lambda\Theta_C^2}{(\epsilon^2+\lambda^2)\Omega^2-(2\epsilon^2+\lambda^2)\Theta_C^2}$

Table A.5: Laser amplitude noise coupling into the dark port, in the leading-order approximation and low-frequency regime [see Eq. (A.33)].

quantity by its nominal value plus contributions due to imperfections, i.e.

$$X_{(k)A,B} = X_{(k)} \pm \frac{1}{2}\Delta X_{(k)}\,. \tag{A.22}$$

Here the index k refers to the type of imperfection being considered. The beamsplitter asymmetry is characterized by

$$\Delta_{\rm BS} = t_{\rm BS}^2 - r_{\rm BS}^2\,. \tag{A.23}$$

Michelson imperfections can be characterized by the difference in the phase shifts and losses when light travels from the beamsplitter to the input mirrors of the two arms:

$$\alpha_{\rm MA,B} = \alpha_{\rm M} \pm \frac{1}{2}\Delta\alpha_{\rm M}\,, \qquad \epsilon_{\rm MA,B} = \epsilon_{\rm M} \pm \frac{1}{2}\Delta\epsilon_{\rm M}\,. \tag{A.24}$$

In addition to $\Delta_{\rm BS}$, $\Delta\alpha_{\rm M}$ and $\Delta\epsilon_{\rm M}$, which concern the beamsplitter, we consider the following contributions to mismatch between the arms,

$$T_{i\rm A,B} \equiv T_i \pm \frac{1}{2}\Delta_T\,, \tag{A.25}$$

$$T_{e\rm A,B} \equiv T_e \pm \frac{1}{2}\Delta_\epsilon\,, \tag{A.26}$$

$$\phi_{\rm A,B} \equiv \phi \pm \frac{1}{2}\Delta_\phi\,, \tag{A.27}$$

that is, mismatch between input mirror power transmissivities, end mirror losses and cavity

detuning, respectively. We replace these with the following more convenient quantities:

$$\frac{\Delta\epsilon}{\epsilon} = \frac{\Delta_T}{T_i + T_e}, \quad \frac{\Delta\epsilon_{\rm L}}{\epsilon} = \frac{\Delta_\epsilon}{T_i + T_e}, \quad \frac{\Delta\lambda}{\lambda} = \frac{\Delta_\phi}{\phi}. \tag{A.28}$$

[See Table A.2 for definitions of ϵ, $\epsilon_{\rm L}$ and λ.]

In the remainder of this section, we give the transfer functions from the carrier light (DC), laser amplitude fluctuations and laser phase fluctuations to the differential output port, to first order in the mismatch (recall that ideally, in the absence of imperfections, these common-mode inputs do not appear in the differential output port). We keep our formulae to the leading order in $\{\Omega L/c, \epsilon L/c, \lambda L/c\}$, and ignore the *averaged* losses, $\epsilon_{\rm L}$ and $\epsilon_{\rm M}$ (but not $\Delta\epsilon_{\rm L}$ and $\Delta\epsilon_{\rm M}$). We refer to this as the *leading-order approximation.* Furthermore, in order to keep the analytical results understandable, we work only in the regime of $\{\Omega, \Theta_{\rm C}\} \ll \{\Theta_{\rm D}, \lambda, \epsilon\}$, which we shall refer to as the *low-frequency regime.*

Definitions and assumed values for $\Delta_{\rm BS}$, $\Delta\alpha_{\rm M}$, $\Delta\epsilon_{\rm M}$, $\Delta_{\rm T}$, Δ_ϕ, and Δ_ϵ are given in Table A.1.

The Carrier

The transfer function from the carrier to the differential output can be written as

$$\sum_k \Delta_{(k)} C_{(k)} \begin{pmatrix} \cos\varphi^{\rm C}_{(k)} \\ \sin\varphi^{\rm C}_{(k)} \end{pmatrix}, \tag{A.29}$$

where definitions of $\Delta_{(k)}$, values of $C_{(k)}$ and $\varphi^{\rm C}_{(k)}$ are listed in Table A.4, assuming the carrier at the beamsplitter is in the first (amplitude) quadrature.

Contributions listed in Table A.4 can all be obtained from simple considerations. First, since each field that interferes at the beamsplitter is scaled by one transmission and one reflection coefficient factor, $\Delta_{\rm BS}$ does not contribute to the output carrier light at the differential port. Then, for all mismatches except the loss, one only has to notice that when the arm cavities are lossless, carrier light with amplitude D and phase $\varphi = 0$ returns to the beamsplitter with amplitude reduced to $(1 - \epsilon_{\rm M})$, and quadrature rotated by $2\alpha + 2\alpha_{\rm M}$. As a consequence, the differential output port gets $(D/2)(-\Delta\epsilon_{\rm M}) = (-\Delta\epsilon_{\rm M}/2)D$ in the $\varphi = 2\alpha$

quadrature (factor of 2 due to the beamsplitter), and

$$\begin{aligned} & (D/2)\Delta[2\alpha + 2\alpha_{\rm M}] \\ = & \left[\frac{\epsilon\lambda}{\epsilon^2+\lambda^2}\left(-\frac{\Delta\epsilon}{\epsilon}+\frac{\Delta\lambda}{\lambda}\right)+\Delta\alpha_{\rm M}\right]D \end{aligned} \tag{A.30}$$

in the orthogonal quadrature, $\varphi = 2\alpha + \pi/2$. The effect of the loss mismatch can be understood when we decompose the (complex) reflectivity of the cavity into a sum of two components:

$$\begin{aligned} \frac{\sqrt{R_e}e^{2i\phi}-\sqrt{R_i}}{1-\sqrt{R_iR_e}e^{2i\phi}} &= \frac{1+i\lambda/\epsilon}{1-i\lambda/\epsilon}-\frac{\epsilon_{\rm L}}{\epsilon}\frac{2}{1-i\lambda/\epsilon} \\ &= e^{2i\alpha}-\frac{\epsilon_{\rm L}}{\epsilon}\frac{2\epsilon}{\sqrt{\epsilon^2+\lambda^2}}e^{i\alpha} \end{aligned} \tag{A.31}$$

Here we see that the loss $\epsilon_{\rm L}$ creates an output at the $\varphi = \alpha$ quadrature, so an imbalance in loss $\Delta\epsilon_{\rm L}$ will contribute

$$\left(-\frac{\Delta\epsilon_{\rm L}}{\epsilon}\frac{\epsilon}{\sqrt{\epsilon^2+\lambda^2}}\right)D \tag{A.32}$$

in the $\varphi = \alpha$ quadrature in the differential output port.

Amplitude (Intensity) and Phase (frequency) Noise

Under our simplifications, the laser amplitude noise z_1 and phase noise z_2 couple to single (yet frequency dependent) quadratures in the differential output port, as parametrized by

$$\begin{aligned} \sum_k \Delta_{(k)} \quad \Bigg[& N^{\rm A}_{(k)} \begin{pmatrix} -\sin\varphi^{\rm A}_{(k)} \\ \cos\varphi^{\rm A}_{(k)} \end{pmatrix} z_1 \\ + & N^{\rm P}_{(k)} \begin{pmatrix} -\sin\varphi^{\rm P}_{(k)} \\ \cos\varphi^{\rm P}_{(k)} \end{pmatrix} z_2 \Bigg] . \end{aligned} \tag{A.33}$$

Measurement of the output quadrature $b_\zeta \equiv b_1\cos\zeta + b_2\sin\zeta$ will include the laser noise:

$$\sum_{(k)} \Delta_{(k)} \left[N^{\rm A}_{(k)} z_1 \sin(\varphi^{\rm A}_{(k)} - \zeta) + N^{\rm P}_{(k)} z_2 \sin(\varphi^{\rm P}_{(k)} - \zeta)\right] . \tag{A.34}$$

In particular, the output quadrature $\zeta = \varphi^{\rm A(P)}_{(k)}$ is not sensitive to the k-th contribution of laser amplitude (phase) noise [note that we have switched the notation for φ from that of

Eq. (A.29)].

As it also turns out, in the leading-order approximation and the low-frequency regime, $\left[N^{\mathrm{P}}_{(k)}, \varphi^{\mathrm{P}}_{(k)}\right] = \left[C_{(k)}, \varphi_{(k)}\right]$. Considering the different ways φ appears in Eqs. (A.29) and (A.33), this means the phase noise coupled to the differential output port remains orthogonal to the carrier. This can be argued for easily: since phase modulations on the carrier do not drive mirror motion, the propagation of phase noise is not affected by the optical spring. Amplitude modulations, on the other hand, do drive mirror motion and therefore should couple to the differential port in a dramatically different way. We tabulate the quantities $N^{\mathrm{A}}_{(k)}$ and $\varphi^{\mathrm{A}}_{(k)}$ in Tab. A.5, from which we can see that the amplitude-noise coupling has features around the common-mode optical-spring resonant frequency, Θ_{C}.

Evading Laser Noise by Artificial Asymmetry

For realistically achievable symmetry between the two arms, laser noises turn out to be the dominant noise source to our squeezer. Here we discuss a novel way of mitigating laser noise coupling by introducing *artificial asymmetries*. According to the approximate results (in the leading-order approximation and low-frequency regime) obtained in the previous section, both amplitude and phase noise emerge from single quadratures (as vector sums of contributions from different mechanisms). We can, therefore, eliminate the laser noise totally, up to this order, if we make both of them emerge from the same quadrature $\zeta + \pi/2$, and make sure that the orthogonal quadrature, ζ, has a sub-vacuum noise spectrum. At our disposal are two asymmetries that we can adjust manually: $\Delta\alpha_{\mathrm{M}}$ and $\Delta\epsilon_{\mathrm{M}}$.

At any given sideband frequency Ω, for a generic set of other asymmetries, it is always possible to make both laser noise sources emerge at the $\zeta + \pi/2$ quadrature (and, therefore, to vanish at the ζ quadrature), by adjusting $\Delta\alpha_{\mathrm{M}}$ and $\Delta\epsilon_{\mathrm{M}}$, if the following *non-degeneracy condition* is satisfied:

$$\begin{aligned} & \Delta_{\mathrm{laser}}(\Omega, \zeta) \\ \equiv\ & \det \begin{bmatrix} \sin(\varphi^{\mathrm{A}}_{\alpha_{\mathrm{M}}} - \zeta) N^{\mathrm{A}}_{\Delta\alpha_{\mathrm{M}}} & \sin(\varphi^{\mathrm{A}}_{\Delta\epsilon_{\mathrm{M}}} - \zeta) N^{\mathrm{A}}_{\Delta\epsilon_{\mathrm{M}}} \\ \sin(\varphi^{\mathrm{P}}_{\alpha_{\mathrm{M}}} - \zeta) N^{\mathrm{P}}_{\Delta\alpha_{\mathrm{M}}} & \sin(\varphi^{\mathrm{P}}_{\Delta\epsilon_{\mathrm{M}}} - \zeta) N^{\mathrm{P}}_{\Delta\epsilon_{\mathrm{M}}} \end{bmatrix} \\ \neq\ & 0 . \end{aligned} \tag{A.35}$$

[See Eq. (A.33).]

According to Tables A.4 and A.5, laser phase noise emerges in a frequency-independent quadrature, but the amplitude noise does not. This means the elimination of laser noise must be frequency-dependent, and we can only choose one particular frequency for perfect laser noise evasion. However, if $\Omega \gg \Theta_C$ is also satisfied, then the frequency-dependence goes away. We consider this special case, and choose a detection quadrature of $\zeta = 3\alpha/2$, i.e., the one with minimum quantum noise. From Tabs. A.4 and A.5, we get

$$\Delta_{\text{laser}}\left(\Omega, \frac{3}{2}\alpha\right)\Big|_{\Theta_C \to 0} = -\frac{\epsilon}{4\sqrt{\epsilon^2 + \lambda^2}} \neq 0\,. \tag{A.36}$$

Since the carrier always emerges $\pi/2$ away from the phase noise, it emerges in exactly the same quadrature we propose to detect. In this way, the laser-noise-evading squeezer always produces *squeezed light with amplitude squeezing.*

Finally, we note that, due to possible higher-order corrections, laser noise evasion may not be as perfect as predicted by our first-order approximation, even at a single frequency. The amount of *residual* laser noise, as well as the exact level of the deliberate asymmetries we introduce, must be given by a more accurate calculation.

A.0.3 Comparison between analytical calculations and numerical simulations

In Table A.1, we list the parameters used in modelling our interferometer. An important feature of the numerical code is that it can handle imperfections in the optics quite naturally, while for analytical techniques the solution becomes complicated rather dramatically when more ingredients are added. To fully test this feature, we constructed a test case with realistic imperfections. The imperfections included were those mentioned in Sec. A.0.2. Using the parameters listed in Table A.1, we calculate the noise at the differential port due to quantum fluctuations entering from this port and from lossy mirrors, as well as laser amplitude and phase fluctuations entering from the symmetric port.

In Figs. A-3 and A-4, we show the calculated noise levels from numerical simulations in curves, while those from the analytical treatment are shown as solid points. The agreement between the two sets of calculations is reassuring. Now we discuss these noise spectrum in more details. In Fig. A-3, we plot noises due to vacuum fluctuations entering from the dark port (light curve and points), and due to vacuum fluctuations entering from mirror losses

(dark curve and points). In both results, there is a rather dramatic resonant feature around the differential-mode optical-spring resonant frequency, at $\Theta_D \approx 8\,\mathrm{kHz}$, as can be expected from Sec. A.0.1. The rather weak but still noticeable feature around the common-mode optical-spring resonant frequency $\Theta_C \approx 360\,\mathrm{Hz}$ is solely due to optical parameter mismatch. In Fig. A-4, we show laser amplitude (light curve and dots) and phase (dark curve and points) noises; we have introduced artificial asymmetries α_M and ϵ_M, with values obtained empirically using the numerical simulation code, such that both laser noise sources are evaded to a roughly maximal extent at 1 kHz. For this reason, contributions to the results shown here are largely higher order, and we cannot hope to explain them using results obtained in Sec. A.0.2. Here we do observe dramatic features around both the differential-mode and the common-mode optical-spring resonances.

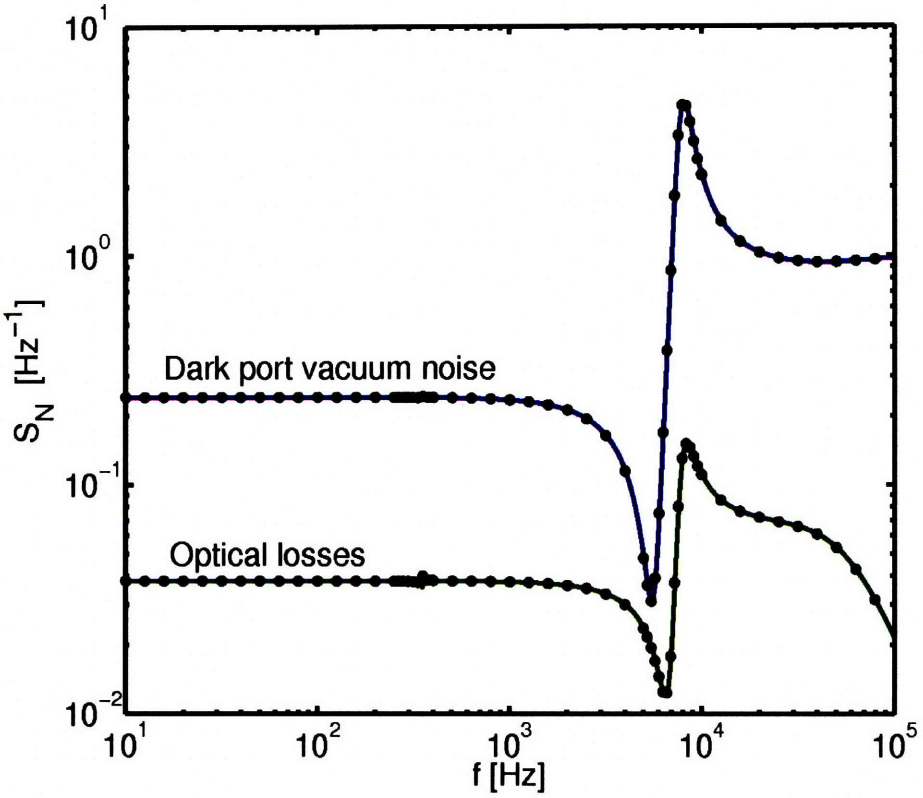

Figure A-3: Spectra of noise power at the output port of the ponderomotive interferometer, normalized to the vacuum noise level. The noise power is dimensionless, as compared to vacuum; a pure vacuum (or shot noise) corresponds to unity. The lines are results of the simulation code, while the data points are values calculated from the corresponding analytic calculations. The vacuum noise level of the light exiting the antisymmetric port is shown. The solid (blue) curve shows the vacuum noise due to the (unsqueezed) vacuum fluctuations that enter via the antisymmetric port of the interferometer; the dashed (green) plot represents the noise due to the vacuum fluctuations that enter via other optical losses in the system. At all frequencies where the vacuum noise power is below unity, the vacuum modes exiting the interferometer are squeezed due to radiation-pressure effects. For the squeezing to be useful, all noise couplings must yield a lower noise power than the squeezed vacuum. All parameters are listed in Table A.1.

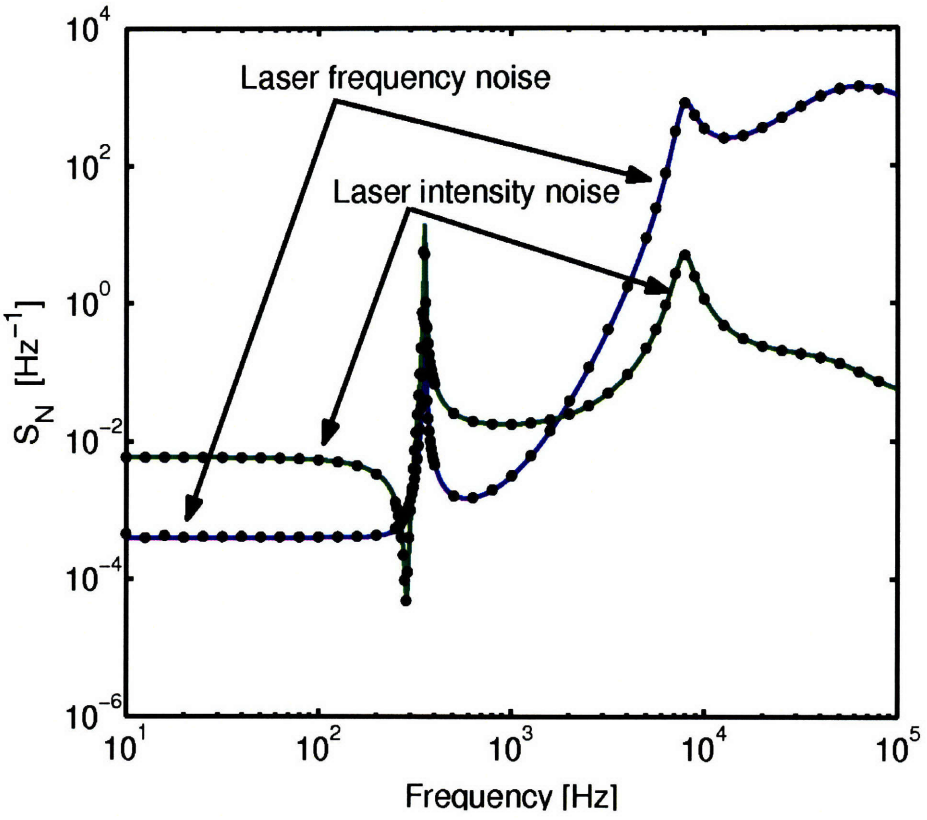

Figure A-4: Spectra of noise power at the output port of the ponderomotive interferometer, normalized to the vacuum noise level. The noise power is dimensionless, as compared to vacuum; a pure vacuum (or shot noise) corresponds to unity. The lines are results of the simulation code, while the data points are values calculated from the corresponding analytic calculations. We show the coupling of laser frequency (solid, blue) and laser amplitude (dashed, green) noise fields to the output port, as calculated by the simulation code. Noise levels of $10^{-4}\,\mathrm{Hz/Hz^{1/2}}$ for frequency noise and $10^{-8}\,\mathrm{Hz^{-1/2}}$ for amplitude noise are assumed at the input to the interferometer; all other parameters are listed in Table A.1.

Appendix B

Electronics diagram

Here we show block diagrams to the core electronics of the experiment. Almost all of the feedback used in the system passes through the digital control system, a prototype of the system to be used in Advanced LIGO, and detailed in Ref. [92]. Documents are available at the LIGO Document Control Center [93] with the reference numbers given. The frequency feedback to the laser is the only current analog feedback path specific to this experiment.

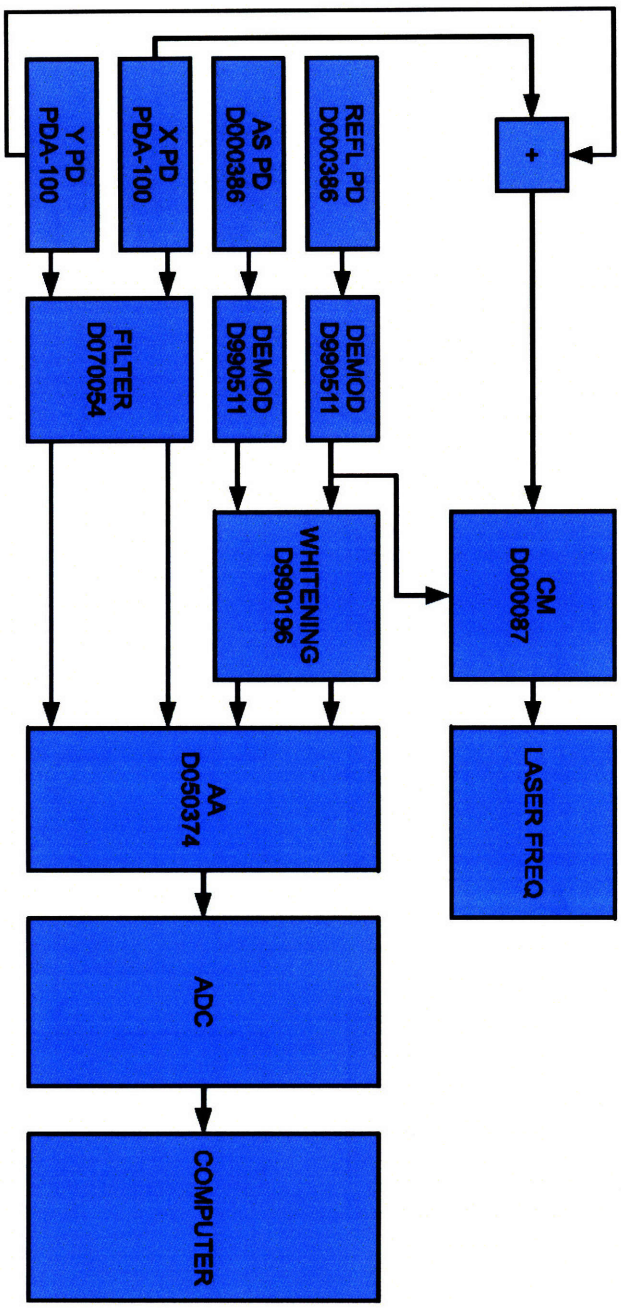

Figure B-1: Length sensing and control (LSC) electronics. REFL and AS PD are the photodetectors at the reflected and anti-symmetric ports. X and Y PD are photodetectors that detect the light transmitted through each cavity. DEMOD demodulates the radio frequency error signals to DC. FILTER and WHITENING prepare the signal for digitization. AA (anti-alias) is a filter that prevents high frequency signals from appearing in-band. CM (common-mode servo board) filters the error signal for the common degree of freedom of the cavities before feeding it back to the laser frequency.

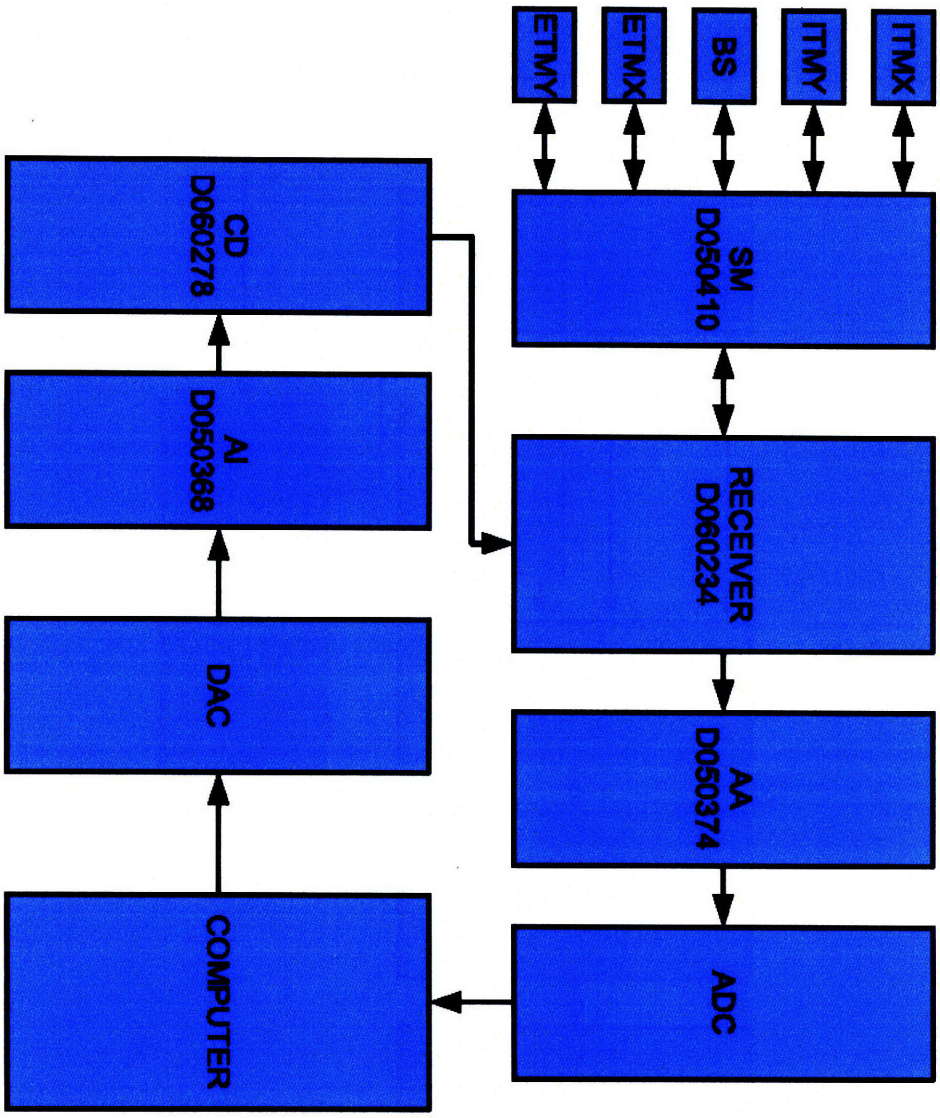

Figure B-2: Suspension electronics. I/ETMX/Y are the input and end mirrors of the X and Y cavities. BS is the beamsplitter. The optics interface with a Satellite Module (SM). The signals from the shadow sensors interface with the RECEIVER before passing through the AA filter and being digitized. Length control signals are interfaced back to coils on the optics through the RECEIVER and SM, after being anti-imaged (AI) and generating a current in the coil driver (CD).

Bibliography

[1] http://www.ligo.caltech.edu/;
http://www.virgo.infn.it/;
http://www.geo600.uni-hannover.de/;
http://tamago.mtk.nao.ac.jp/

[2] P. Fritschel, "Second generation instruments for the Laser Interferometer Gravitational-wave Observatory (LIGO)," in *Gravitational Wave Detection, Proc. SPIE* **4856-39**, p. 282, 2002.

[3] Advanced LIGO Team, "Advanced LIGO Reference Design," LIGO-060056-08-M.

[4] A. Buonanno, Y. Chen, and N. Mavalvala, "Quantum noise in laser-interferometer gravitational-wave detectors with a heterodyne readout scheme," Phys. Rev. D **67**, 122005 (2003).

[5] T. Corbitt and N. Mavalvala, "Quantum noise in gravitational-wave interferometers: Overview and recent developments," Proceedings of SPIE, *Fluctuations and Noise in Photonics and Quantum Optics*, Santa Fe, NM, **5111**, 23 (2003).

[6] J.H. Kimble, Y. Levin, A.B. Matsko, K.S. Thorne and S.P. Vyatchanin, "Conversion of conventional gravitational-wave interferometers into QND interferometers by modifying their input and/or output optics," Phys. Rev. D **65**, 022002 (2002).

[7] C. M. Caves, "Quantum-mechanical radiation-pressure fluctuations in an interferometers," Phys. Rev. Lett. **45**, 75 (1980).

[8] C. M. Caves, "Quantum-mechanical Noise in interferometers," Phys. Rev. D **23**, 1693 (1981).

[9] R. W. P. Drever, "The detection of gravitational waves," D. G. Blair, ed., Cambridge University Press, Cambridge, England (1991).

[10] J. Mizuno, "Comparison of optical configurations for laser-interferometer gravitational-wave dtectors," Ph.D. thesis, Max-Planck-Institut für Quantenoptik, Garching, Germany (1995).

[11] J. Mason and P. Willems, "Signal extraction and optical design for an advanced gravitational-wave interferometer," Appl. Opt. **42**, 1269 (2003); K. A. Strain, G. Muller, T. Delker, D. H. Reitze, D. B. Tanner, J. E. Mason, P. Willems, D. Shaddock, M. B. Gray, C. Low-Mowry, and D. E. McClelland, "Signal and control in dual-recycling laser interferometer gravitational-wave detectors," Appl. Opt. **42**, 1244 (2003).

[12] A. Buonanno and Y. Chen, "Quantum noise in second-generation signal-recycled laser interferometric gravitational wave detectors," Phys. Rev. D **64**, 042006 (2001).

[13] A. Buonanno and Y. Chen, "Quantum noise in second generation, signal-recycled laser interferometric gravitational-wave detectors," Phys. Rev. D **64**, 042006 (2001).

[14] V. B. Braginsky and F. Ya. Khalili, "Gravitational wave antenna with QND speed meter" Phys. Lett. A **147**, 251 (1990); V. B. Braginsky, M. L. Gorodetsky, F. Ya. Khalili, K. S. Thorne, "Dual resonator speed meter for a free test mass," Phys. Rev. D **61**, 044002 (2000).

[15] P. Purdue and Y. Chen, "Practical speed meter designs for QND gravitational-wave interferometers," Phys. Rev. D **66** 022001 (2002).

[16] R. E. Slusher, L. W. Holberg, B. Yurke, J. C. Mertz, and J. F. Valley,"Observation of squeezed states generated by four-wave mixing in an optical cavity," Phys. Rev. Lett. **55**, 2409 (1985).

[17] L.-A. Wu, H. J. Kimble, J. L. Hall, and H. Wu, "Generation of squeezed states by parametric down-conversion," Phys. Rev. Lett. **57**, 2520 (1986).

[18] S. Schiller, G. Breitenbach, S. F. Periera, T. Müller and J. Mlynek, "Quantum statistics of the squeezed vacuum by measurement of the density matrix in the number state representation," Phys. Rev. Lett. **77**, 2933 (1996).

[19] K. Schneider, M. Lang, J. Mlynek, S. Schiller, "Generation of strongly squeezed continuous-wave light at 1064 nm," Opt. Exp. **2**, 59 (1998).

[20] H. Vahlbruch et al., "Observation of Squeezed Light with 10-dB Quantum-Noise Reduction ," Phys. Rev. Lett. **100**, 033602 (2008).

[21] H. Vahlbruch et al., "Coherent Control of Vacuum Squeezing in the Gravitational-Wave Detection Band," Phys. Rev. Lett. **97**, 011101 (2006).

[22] K. McKenzie, D. A. Shaddock, D. E. McClelland, B. C. Buchler, and K. Lam, "Experimental demonstration of a squeezing-enhanced power-recycled Michelson interferometer for gravitational-wave detection," Phys. Rev. Lett. **88**, 231102 (2002).

[23] H. Vahlbruch et al., "Demonstration of a squeezed-light-enhanced power- and signal-recycled Michelson inteferometer," Phys. Rev. Lett. **95**, 21102 (2005).

[24] K. Goda, O. Miyakawa, E. E. Mikhailov, S. Saraf, R. Adhikari, K. McKenzie, R. Ward, S. Vass, A. J. Weinstein, and N. Mavalvala, "A Quantum-Enhanced Prototype Gravitational-Wave Detector," Nature Physics **4**, 472 (2008).

[25] J. Harms, Y. Chen, S. Chelkowski, A. Franzen, H. Vahlbruch, K. Danzmann, R. Schnabel, "Squeezed-input, optical-spring, signal-recycled gravitational-wave detectors," Phys.Rev. D **68**, 042001 (2003).

[26] K. Lam, T. C. Ralph, B. C. Buchler, D. E. McClelland, H.-A. Bachor, and J. Gao, "Optimization and transfer of vacuum squeezing from an optical parametric oscillator," J. Opt. B **1**. 469 (1999).

[27] M. Xiao, L.-A. Wu, and H. J. Kimble, "Precision measurement beyond the shot noise limit," Phys. Rev. Lett. **59**, 278 (1987).

[28] T. Corbitt, N. Mavalvala, S. Whitcomb, "Optical cavities as amplitude filters for squeezed fields," Phys. Rev. D **70**, 022002 (2004).

[29] J. Harms, Y. Chen, S. Chelkowski, A. Franzen, H. Vahlbruch, K. Danzmann, R. Schnabel, "Squeezed-input, optical-spring, signal-recycled gravitational-wave detectors," Phys. Rev. D **68**, 042001 (2003).

[30] A. Buonanno and Y. Chen, "Scaling law in signal recycled laser-interferometer gravitational-wave detectors," Phys. Rev. D **67**, 062002 (2003).

[31] C. M. Caves and B. L. Schumaker, "New formalism for two-photon quantum optics. I. Quadrature phases and squeezed states," Phys. Rev. A **31**, 3068 (1985).

[32] B. S. Schumaker and C. M. Caves, "New formalism for two-photon quantum optics. II. Mathematical foundation and compact notation," Phys. Rev. A **31**, 3093 (1985).

[33] K. S. Thorne, *300 Years of Gravitation*, edited by S. W. Hawking and W. Israel (Cambridge Universtiy Press, Cambridge, 1987), p. 369 and p. 380.

[34] É. É. Flanagan, "Sensitivity of the laser interferometer gravitational wave observatory (LIGO) to a stochastic background, and its dependence on the detector orientations," Phys. Rev. D **48**, 389 (1993).

[35] B. Allen and J.D. Romano, "Detecting a stochastic background of gravitational radiation: Signal processing strategies and sensitivities," Phys. Rev. D **59**, 102001 (1999).

[36] V. B. Braginsky, Yu. I. Vorontsov and F. Ya. Khalili, Sov. Phys.-JETP **46** 705 (1977).

[37] A. Dorsel, J. D. McCullen, P. Meystre, E. Vignes, and H. Walther, "Optical Bistability and Mirror Confinement Induced by Radiation Pressure," Phys. Rev. Lett. **51**, 1550 (1983).

[38] V. B. Braginsky, M. L. Gorodetsky, F. Ya. Khalili, "Optical bars in gravitational wave antennas," Phys. Lett. A **232** 340 (1997).

[39] T. Corbitt, Y. Chen, and N. Mavalvala, "Mathematical framework for simulation of quantum fields in complex interferometers using the two-photon formalism," Phys. Rev. A **72**, 013818 (2005).

[40] M. W. Regehr, "Signal extraction and control for an interferometric gravitational wave detector," Ph.D. thesis, California Institute of Technology, 1995; M. W. Regehr, J. E. Mason, and H. Yamamoto, "Twiddle: A program for analyzing interferometer frequency response," LIGO-T990022-00-R.

[41] A. Freise, G. Heinzel, H. Lueck, R. Schilling, B. Willke, and K. Danzmann, "Frequency-domain interferometer simulation with higher-order spatial modes," Class. Quant. Grav. **21**, S1067 (2004).

[42] B. Bhawal, M. Evans, M. Rakhmanov, V. Sannibale, and H. Yamamoto, "The LIGO end-to-end simulation program," Proc. Moriond workshop on gravitational-waves and experimental gravity (2003).

[43] T. Corbitt, Y. Chen, F. Khalili, D. Ottaway, S. Vyatchanin, S. Whitcomb and N. Mavalvala, "Squeezed-state source using radiation-pressure-induced rigidity," Phys. Rev. A **73**, 023801 (2006).

[44] Purdue and Y. Chen, "Analysis of a quantum nondemolition speed-meter interferometer," Phys. Rev. D **66** 122004, (2002).

[45] S. Chelkowski, H. Vahlbruch, B. Hage, A. Franzen, N. Lastzka, K. Danzmann, and R. Schnabel, "Experimental characterization of frequency-dependent squeezed light," Phys. Rev. A **71**, 013806 (2005).

[46] S.E. Strigin and S.P. Vyatchanin, "Analysis of parametric oscillatory instability in signal recycled LIGO interferometer with different arms," Phys. Lett. A **365**, 10 (2006).

[47] V. B. Braginsky, S. E. Strigin, and S. P. Vyatchanin, "Parametric oscillatory instability in Fabry-Perot interferometer," Phys. Lett. A **287**, 331 (2001).

[48] T. Corbitt, D. Ottaway, E. Innerhofer, J. Pelc, N. Mavalvala, "Measurement of radiation-pressure-induced optomechanical dynamics in a suspended Fabry-Perot cavity," Phys. Rev. A **74**, 021802 (2006).

[49] J. Sidles and D. Sigg, "Optical Torques in Suspended Fabry-Perot Interferometers," submitted to Phys. Lett. A (2004).

[50] B. Abbott et al. (LIGO Scientific Collaboration), "Detector description and performance for the first coincidence observations between LIGO and GEO," Nucl. Instrum. Meth. **A517**, 154 (2004).

[51] G. Harry, T. Corbitt, M. Freytsis, D. Ottaway, and N. Mavalvala, "Mechanical loss of laser-welded fused silica fibers," Rev. Sci. Instrum. **77**, 023906 (2006).

[52] G. González, "Suspensions thermal noise in the LIGO gravitational wave detector," Class. Quant. Grav. **17**, 4409 (2000).

[53] H. B. Callen and R. F. Greene, Phys. Rev. **86** 703 (1952).

[54] P. R. Saulson, "Thermal noise in mechanical experiments," Phys. Rev. D **42**, 2437 (1990).

[55] G. M. Harry, A. M. Gretarsson, R. Saulson, S. E. Kittelberger, S. D. Penn, W. J. Startin, S. Rowan, M. M. Fejer, D. R. M. Crooks, G. Cagnoli, J. Hough, and N. Nakagawa, "Thermal noise in interferometric gravitational wave detectors due to dielectric optical coatings," Class. Quantum Grav. **19**, 897 (2002).

[56] T. Corbitt, Y. Chen, D. Ottaway, and N. Mavalvala, "Control system for damping the unstable optomechanical resonance in the ponderomotive interferometer," LIGO-T050140-00-R.

[57] R. Abbott and P. King., "Control system design for the LIGO pre-stabilized laser," LIGO-P010037-00-C.

[58] J. Rollins, "Intensity stabilization of a Solid-State Laser for Interferometric Gravitational Wave Detectors," MA thesis, Massachusetts Institute of Technology (1999).

[59] B. S. Sheard, M. B. Gray, C. M. Mow-Lowry, D. E. McClelland and S. E. Whitcomb, "Observation and characterization of an optical spring," Phys. Rev. A, **69**, 051801 (2004).

[60] O. Miyakawa, R. Ward, R. Adhikari, M. Evans, B. Abbott, R. Bork, D. Busby, J. Heefner, A. Ivanov, M. Smith, R. Taylor, S. Vass, A. Weinstein, M. Varvella, S. Kawamura, F. Kawazoe, S. Sakata, and C. Mow-Lowry, "Measurement of optical response of a detuned resonant sideband extraction gravitational wave detector," Phys. Rev. D **74**, 022001 (2006).

[61] P. Saulson, "Thermal noise in mechanical experiments," Phys. Rev. D **42**, 2437 (1990).

[62] C. Zhao, L. Ju, J. Degallaix, S. Gras, and D. G. Blair, "Parametric Instabilities and Their Control in Advanced Interferometer Gravitational-Wave Detectors," Phys. Rev. Lett. **94**, 121102 (2005).

[63] B. D. Cuthbertson, M. E. Tobar, E. N. Ivanov, and D. G. Blair, "Parametric back-action effects in a high-Q cyrogenic sapphire transducer," Rev. Sci. Instrum. **67**, 2345 (1996).

[64] T. J. Kippenberg, H. Rokhsari, T. Carmon, A. Scherer and K. J. Vahala, "Analysis of Radiation-Pressure Induced Mechanical Oscillation of an Optical Microcavity," Phys. Rev. Lett, **95**, 033901 (2005).

[65] M. W. Regehr, F. J. Raab, and S. E. Whitcomb, "Demonstration of a power-recycled Michelson interferometer with Fabry-Perot arms by frontal modulation," Optics Letters **20**, 1507 (1995).

[66] S. Ackley, "Construction and Characterization of a Universally Tunable Modulator," BS Thesis, Massachusetts Institute of Technology (2008).

[67] C. H. Metzger, K. Karrai, "Cavity cooling of a microlever," Nature **432**, 1002 (2004).

[68] O. Arcizet, P.-F. Cohadon, T. Briant, M. Pinard, and A. Heidmann, "Radiation-pressure cooling and optomechanical instability of a micromirror," Nature **444**, 71 (2006).

[69] D. Kleckner, D. Bouwmeester, "Sub-kelvin optical cooling of a micromechanical resonator," Nature **444**, 75 (2006).

[70] S. Gigan, H. Böhm, M. Paternostro, F. Blaser, G. Langer, J. Hertzberg, K. Schwab, D. Bäuerle, M. Aspelmeyer, and A. Zeilinger, "Self-cooling of a micromirror by radiation pressure," Nature **444**, 67 (2006).

[71] A. Naik, O. Buu, M. D. LaHaye, A. D. Armour, A. A. Clerk, M. P. Blencowe, and K. C. Schwab, "Cooling a nanomechanical resonator with quantum back-action," Nature**443**, 193 (2006).

[72] A. Schliesser, P. Del'Haye, N. Nooshi, K. J. Vahala, and T. J. Kippenberg, "Radiation Pressure Cooling of a Micromechanical Oscillator Using Dynamical Backaction," Phys. Rev. Lett. **97**, 243905 (2006).

[73] T. Corbitt, Y. Chen, E. Innerhofer, H. Müller-Ebhardt, D. Ottaway, H. Rehbein, D. Sigg, S. Whitcomb, C. Wipf, and N. Mavalvala, "An All-Optical Trap for a Gram-Scale Mirror," Phys. Rev. Lett. **98**, 150802 (2007).

[74] M. Poggio, C. L. Degen, H. J. Mamin, and D. Rugar, "Feedback Cooling of a Cantilever's Fundamental Mode below 5 mK," Phys. Rev. Lett. **99**, 017201 (2007).

[75] J. G. E. Harris, B. M. Zwickl, and A. M. Jayich, "Stable, mode-matched, medium-finesse optical cavity incorporating a microcantilever mirror: Optical characterization and laser cooling," Rev. Sci. Instrum. **78**, 013107 (2007).

[76] T. Corbitt, C. Wipf, T. Bodiya, D. Ottaway, D. Sigg, N. Smith, S. Whitcomb, and N. Mavalvala, "Optical dilution and feedback cooling of a gram-scale oscillator to 6.9 mK," Phys. Rev. Lett. **99**, 160801 (2007).

[77] C. M. Mow-Lowry, A. J. Mullavey, S. Goßler, M. B. Gray, and D. E. McClelland, "Cooling of a gram-scale cantilever flexure to 70 mK with a servo-modified optical spring," Phys. Rev. Lett. **100**, 010801 (2008).

[78] S. Mancini, D. Vitali, P. Tombesi, "Optomechanical Cooling of a Macroscopic Oscillator by Homodyne Feedback," Phys. Rev. Lett **80**, 688 (1998).

[79] P. F. Cohadon, A. Heidmann, M. Pinard, "Cooling of a Mirror by Radiation Pressure," Phys. Rev. Lett. **83**, 3174 (1999).

[80] C. Genes, D. Vitali, P. Tombesi, S. Gigan, and M. Aspelmeyer, "Ground-state cooling of a micromechanical oscillator: generalized framework for cold damping and cavity-assisted cooling schemes," Phys. Rev. A **77**, 033804 (2008).

[81] Y. Chen et al., "Creation of a quantum oscillator by classical control," to be submitted to Phys. Rev. Lett. (2008).

[82] R. W. P. Drever, J. L. Hall, F. V. Kowalski, J. Hough, G. M. Ford, A. J. Munley, and H. Ward, Appl. Phys. B **31**, 97 (1983).

[83] H. Müller-Ebhardt, H. Rehbein, R. Schnabel, K. Danzmann, and Y. Chen, "Entanglement of macroscopic test masses and the Standard Quantum Limit in laser interferometry," Phys. Rev. Lett. **100**, 013601 (2007).

[84] S. Bose, K. Jacobs, and P.L. Knight, "Preparation of nonclassical states in cavities with a moving mirror," Phys. Rev. A **56**, 4175 (1997).

[85] W. Marshall, C. Simon, R. Penrose, and D. Bouwmeester, "Towards Quantum Superpositions of a Mirror," Phys. Rev. Lett. **91**, 130401 (2003).

[86] S. Mancini, V. Giovannetti, D. Vitali, and P. Tombesi, "Entangling Macroscopic Oscillators Exploiting Radiation Pressure," Phys. Rev. Lett. **88**, 120401 (2002).

[87] J. Zhang, K. Peng, and S.L. Braunstein, "Quantum-state transfer from light to macroscopic oscillators," Phys. Rev. A **68**, 013808 (2003).

[88] C. Wipf, T. Corbitt, Y. Chen, and N. Mavalvala, "A route to observing ponderomotive entanglement with optically trapped mirrors," arXiv:0803.4001v1 (2008).

[89] M. P. Blencowe and M. N. Wybourne, "Quantum squeezing of mechanical motion for micron-sized cantilevers," Physica B **280**, 555 (2000).

[90] J. D. Thompson, B. M. Zwickl, A. M. Jayich, Florian Marquardt, S. M. Girvin, and J. G. E. Harris, "Strong dispersive coupling of a high-finesse cavity to a micromechanical membrane," Nature **452**, 900 (2008).

[91] V.B. Braginsky, F.Ya. Khalili, "Low noise rigidity in quantum measurements," Phys. Lett. A **257**, 241 (1999).

[92] J. Heefner, "Squeezing Experiment System Wiring," LIGO-D060294.

[93] http://admdbsrv.ligo.caltech.edu/dcc/